JPL Quarterly Technical Review

Volume 1 July 1971 Number 2

Papers on:
Bioengineering
Control and Guidance
Environmental Sciences
Fluid Mechanics
Lunar Exploration
Particle Physics
Propulsion
Radio Astronomy
Structural Engineering
Telecommunications

Abstracts of:
Technical Reports
Technical Memorandums
JPL Quarterly Technical Review
Open Literature Reporting

Jet Propulsion Laboratory/California Institute of Technology

JPL Quarterly Technical Review
Volume 1, Number 2

Jet Propulsion Laboratory
California Institute of Technology
4800 Oak Grove Drive
Pasadena, California 91103

Prepared Under Contract NAS 7-100
National Aeronautics and Space Administration

JPL Quarterly Technical Review

Volume 1 July 1971 Number 2

Contents

Bibliography of Current Reporting

A Comparison Between Planar and Nonplanar Free-Flight Data

P. Jaffe

Environmental Sciences Division

Results from the first program designed to explore the difference between the planar and nonplanar dynamic stability coefficient, using the JPL developed bi-planar wind-tunnel free-flight system, are presented. Two widely different configurations, a blunt 60-deg half-angle cone and a sharp 10-deg half-angle cone were tested. The overall accuracy of the data was extremely high and firmly demonstrates the capability of the technique. Although no dramatic difference in the coefficients was apparent from the data, which was limited in number, they do suggest that there is a favorable increase in the coefficient as the motion becomes more nonplanar.

Introduction

Predicting the angle-of-attack history of a body exhibiting nonplanar motion from planar data can be erroneous since it presupposes that there are no aerodynamic coupling forces and further requires that the conventional aerodynamic forces which are observable in the planar mode are the same in the nonplanar mode. The investigation of this last requirement was the main purpose of an experimental program conducted in the JPL Supersonic Wind Tunnel using a refined nonplanar free-flight system. Specifically, the program was directed toward the question of whether the dynamic stability coefficient is different in the two modes. For this investigation two widely different configurations were chosen: a short, blunt 60-deg half-angle cone and a sharp 10-deg half-angle cone. This article presents the results of this test program.

Test Operation

The basis of the testing technique is to launch models upstream into the oncoming flow with a pneumatic gun (Reference 1). In the case of nonplanar flight, the models are released with an initial angle of attack, yaw angular velocity, and spin rate. The proper combination of these three initial conditions will produce any desired nonplanar motion. The

motion is recorded with a high-speed 35-mm movie camera operating at about 2000 frames per second. Two views of the model in flight are obtained by splitting the schlieren strobe light and directing the two beam halves through the test section, 60 deg apart, by means of a complex mirror system (References 2 and 3). Generally, about 250 frames of data are obtained for a flight. Each pair of angles from a frame set is measured and mathematically transformed to a vertical and horizontal set. Nominal accuracies are 0.2 deg for the slender models and 0.5 deg for the blunt bodies. In addition to this data, an independent measurement of the model's spin rate is obtained by means of either a fiber optics lens system mounted inside the tunnel, which transmits a picture of the model's base to an outside camera, or a stripe painted on the model.

The data is processed in a manner similar to the procedure used in a ballistic range, which is to numerically fit the angle data with the tricylic equation of motion (Reference 4). From this fit the static stability coefficient (C_{m_α}), the dynamic stability coefficient ($C_{m_q} + C_{m_{\dot{\alpha}}}$), and the magnus moment coefficient ($C_{m_{p_\alpha}}$) are obtained. The drag coefficient (C_D) is independently obtained from the model's translational history.

The 60-deg blunt body test was conducted principally at Mach 3.97 with a few shots at Mach 1.65. The 10-deg cone test was performed at Mach 4.56. The diameters of the blunt models and of the sharp cones were 3.81 and 2.54 cm (1.5 and 1.0 in.), respectively. The models were designed to optimize the number of pitch cycles and angle-of-attack decay during a flight. This is accomplished by constructing them with a dense core and a light plastic exterior shell; in the case of the blunt cones, gold was used for the cores. Typical weights for the models were 28 g for the 60-deg cones and 10 g for the 10-deg cones. The blunt cones were launched at spin rates varying from zero to 35 rev/s. The 10-deg cone spin rates were from 90 to 135 rev/s (resonance was about 60 rev/s).

A representative α–β plot (angle of attack versus angle of yaw) from both tests is shown in Figures 1 and 2 along with a frame of movie data from each flight. The stars are the raw data points obtained from the movie frames and the smooth curves are from the fit equations. The standard rms angle-of-attack deviations were about 0.4 deg for the 10-deg cone flights and 0.9 deg for the blunt body flights.

Test Results

Before proceeding to the dynamic stability data, it is wise to first investigate the drag and static stability results since they provide a gage as to the quality of the data. The drag and static stability coefficients are the results of first-order driving forces and can be obtained much more accurately than the dynamic stability coefficient which is the result of second-order forces. If the static data from a flight looks good, confidence in the value of the dynamic stability coefficient is increased.

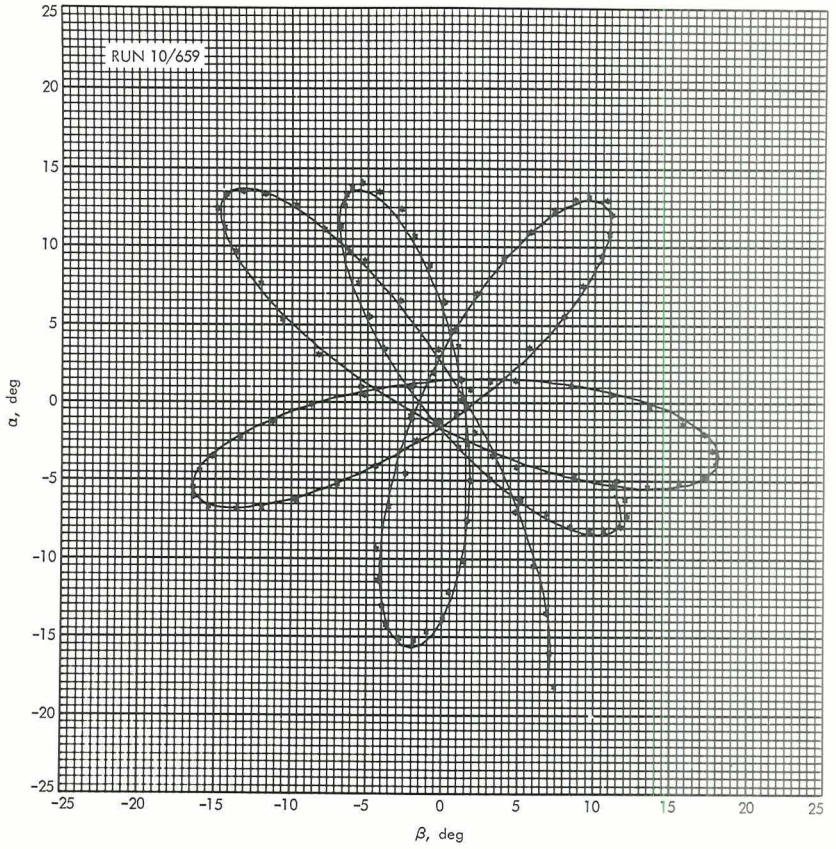

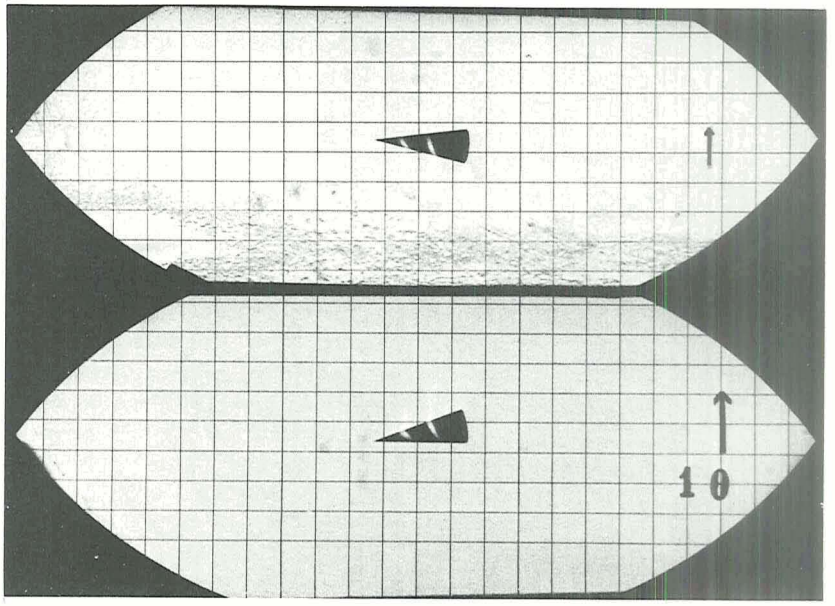

Figure 1. Representative 10-deg cone data

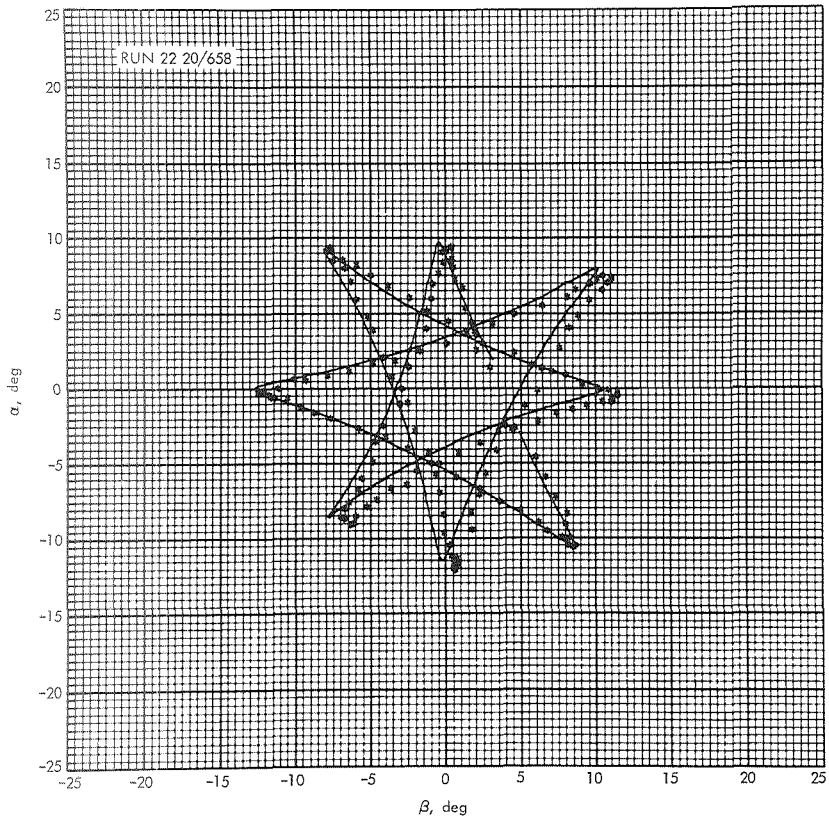

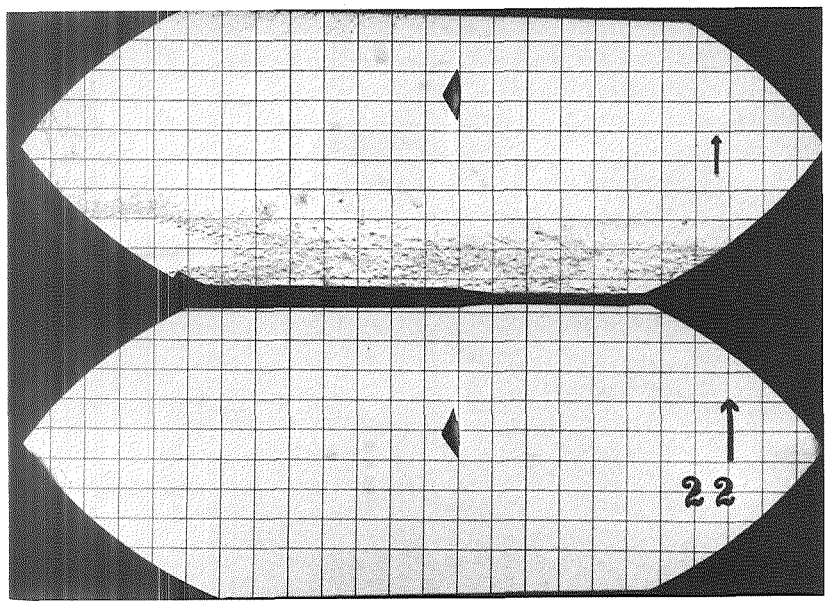

Figure 2. Representative 60-deg blunt body data

The drag and stability data are best correlated with the mean-square resultant angle of attack, δ^2, which is defined as

$$\delta^2 = \frac{\int_0^x (\eta^2)\, dx}{x}$$

where η is the resultant angle of attack and x is the relative distance between the model and free-stream. It has been shown that if a body has local drag coefficient of the form $C_D = C_{D_0} + k\eta^2$, then the effective drag coefficient is $C_{D_{\text{eff}}} = C_{D_0} + k\delta^2$. Figure 3 contains the effective drag data from both tests. The data consistency for both configurations is excellent, particularly the 10-deg cone where the deviation is less than 0.25%. The data also exhibit straight-line correlations with δ^2, which means that the drag coefficients for both configurations are quadratic functions of the angle of attack.

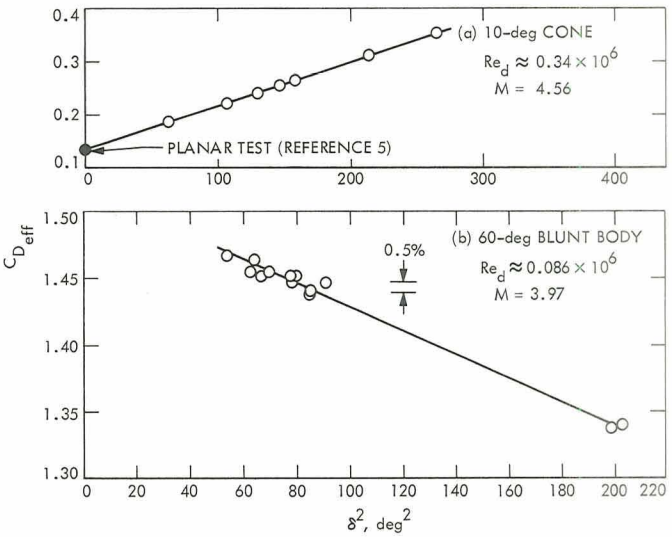

Figure 3. Drag results

Figure 4 contains the static stability data from both tests as a function of δ^2. The 10-deg cone data does not vary with δ^2, indicating that the pitching moment is dependent upon the angle of attack (at least through the region tested). The data deviation from the mean is excellent, less than 0.5%. The blunt body data shows a large increase in the static stability coefficient at large δ^2's, indicating a highly nonlinear pitching moment. From an examination of the flights themselves, it appears that the coefficients are more accurate than the scatter on the plot would indicate. Part of the problem is due to the use of δ^2 as the correlator since it is not necessarily the proper one for a nonlinear pitching moment. A vehicle experiencing the same δ^2 during both planar and circular flights

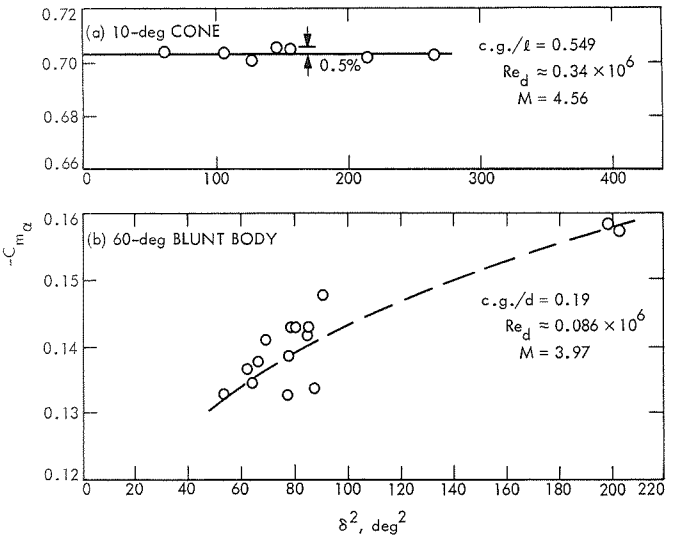

Figure 4. Static stability results

will not necessarily have the same effective static stability coefficients for both of them. This has been demonstrated for the case of a cubic pitching moment ($C_m = C\alpha + k\alpha^3$), where the appropriate correlator for an arbitrary nonplanar flight is a much more complicated function than δ^2 (Reference 4). Another factor that might relate to the scatter of the data is the "phase difference"; i.e., there appears to be a difference between the time the amplitude nodes generated by the fit equation occur and those formed by the raw data occur. (See Run 22, Figure 2, for an example.) After extensive study of this problem, it is now believed to be primarily the result of the combination of a highly nonlinear pitching moment and a trim angle due to an offset center of gravity (c. g.). Fortunately, both the correlator problem and the phase problem have a rather small influence on the values of the aerodynamic coefficients obtained from the data reduction, and although the scatter of the data is larger than it should be, it is still quite small. Nevertheless, efforts to reconcile the differences are continuing.

The dynamic stability data for both configurations are presented as a function of δ^2 in Figure 5 and as a function of roll rate to velocity ratio (p/V) in Figure 6. This last parameter relates to the degree to which the motion is nonplanar and is merely a first attempt to use a nonplanar correlation parameter. When presented as a function of δ^2 (Figure 5), particularly in the case of the blunt body, the data does not correlate well. However, presented as a function of p/V, the correlation for both configurations is substantially improved. Interestingly, both sets of data for two completely different configurations demonstrate the same trend of an increase in the dynamic stability (a more negative dynamic stability coefficient is favorable) as the roll rate is increased to a point, and then

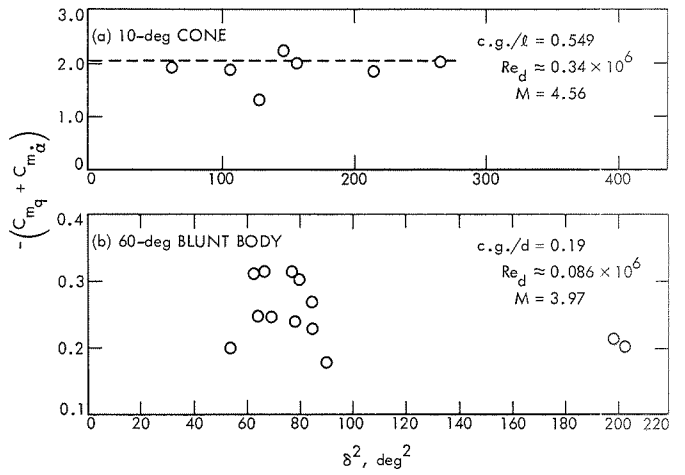

Figure 5. Dynamic stability data as a function of the mean-square resultant angle of attack

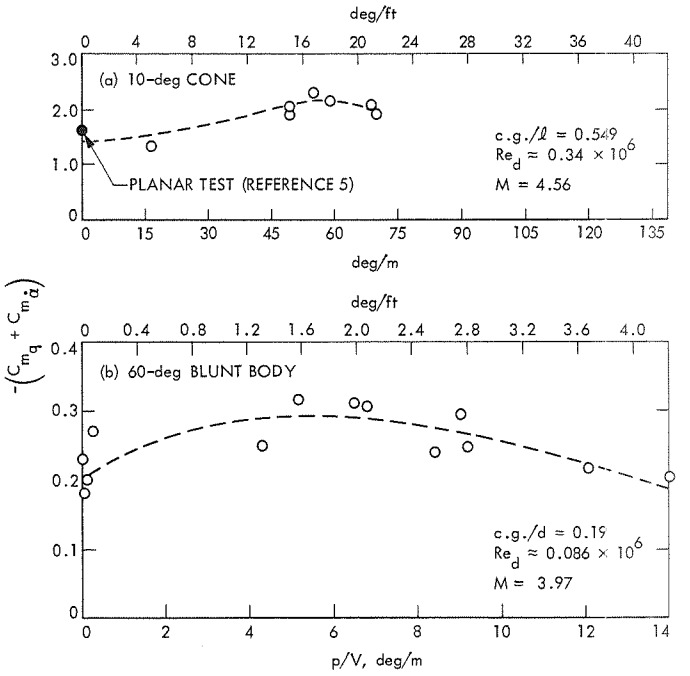

Figure 6. Dynamic stability data as a function of the roll to velocity ratio

a decrease in the dynamic stability. The fact that the dynamic stability coefficient changes with roll means that it is dependent upon the type of motion the body is undergoing, which is contrary to the traditional supposition that it is only dependent upon the angle of attack. It should be mentioned, however, that in order to investigate this subject thoroughly and obtain definitive conclusions much more data is required. More work oriented toward defining the key parameters, which determine dynamic stability, is needed.

References

1. Dayman, B., Jr., *Free-Flight Testing in High-Speed Wind Tunnels,* AGARDograph 113. Advisory Group for Aerospace Research and Development, North Atlantic Treaty Organization, Paris, May 1966.
2. Prislin, R. H., and Holway, H. P., "A Wind Tunnel Free-Flight Testing Technique for Nonplanar Motion of Spinning Models," AIAA Paper 66-774, Sept. 1966.
3. Jaffe, P., "Planetary Entry Flight Dynamic Research," in *Supporting Research and Advanced Development,* Space Programs Summary 37-62, Vol. III, pp. 218–222. Jet Propulsion Laboratory, Pasadena, Calif., Apr. 30, 1970.
4. Murphy, C. H., *Free-Flight Motion of Symmetric Missiles,* BRL Report 1216. Ballistic Research Laboratory, Aberdeen Proving Ground, Md, July 1963.
5. Jaffe, P., and Prislin, R. H., *Effect of Boundary-Layer Transition on Dynamic Stability,* Technical Report 32-841. Jet Propulsion Laboratory, Pasadena, Calif., Mar. 1, 1966. (Reprinted from *J. Spacecraft Rockets,* Vol. 3, No. 1, pp. 46–52, Jan. 1966.)

Aerodynamics of Vehicles in Tubes

D. W. Kurtz

Environmental Sciences Division

Currently many transportation systems are being studied which require vehicles to operate in tunnels under conditions of high blockage. As a consequence, a great deal of interest is being generated in the aerodynamic characteristics of such transportation systems. Model testing should be performed to better understand the aerodynamic aspects of such systems. This article presents a brief description of a facility that was constructed to study these systems and some of the initial results which have been obtained to date.

Introduction

Currently many transportation systems are being studied which require vehicles to operate in tunnels (tubes) under conditions of high blockage (vehicle frontal area occupying a significant portion of the tunnel cross-sectional area). When this condition exists, the vehicle drag can be one to two orders of magnitude greater than the value in free air. In addition, the air velocities in the tunnel ahead of and behind the vehicle can be an appreciable ratio of the vehicle velocity. A proper understanding of these aerodynamic characteristics is necessary in order to efficiently design systems utilizing vehicles in tunnels, which in turn will make it possible to choose an optimum transportation system. In conjunction with theoretical studies by the Aeronautics Department at the California Institute of Technology, an experimental program was initiated at JPL on the aerodynamics of vehicles traveling in tubes.

Facility

Currently operational is a 21.5-m (70-ft)[1] long, 5.3-cm (2-in.) diameter, vertically oriented aluminum tube that utilizes gravity to propel the test

[1] Values in customary units are included in parentheses after values in SI (International System) units if the customary units were used in the measurements or calculations.

Figure 1. Installation of VICS-70 facility

models. This facility, referred to as VICS-70 (vehicles in constrained spaces), and two typical models are shown in Figure 1.

The 21.5-m (70-ft) tube replaces an original 9.8-m (32-ft) long, 5.3-cm (2-in.) diameter, vertically oriented Plexiglas tube that was used to develop the necessary testing techniques for the more advanced, high-precision facility now in operation. The 21.5-m (70-ft) tube is instrumented along its length with magnetic-coil pickups which are triggered when magnets in the model pass each station and indicate model position along the tube as a function of time. This configuration yields data from which model velocity, acceleration, and drag can be determined. Wall pressure ports are provided for recording the pressure history along the

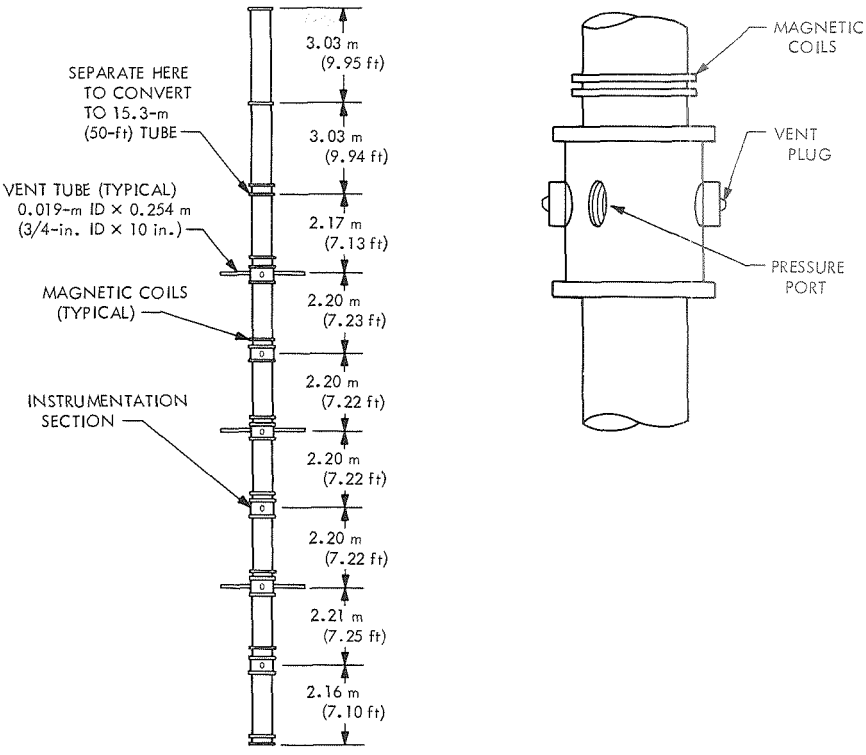

Figure 2. Schematic of VICS-70 facility

tube. The tube is aligned to within ±0.4 mm (±0.015 in.) over the 21.5-m (70-ft) length. A schematic of the tube is shown in Figure 2.

The present facility is a very versatile one; several geometric characteristics of the 21.5-m (70-ft) tube are readily alterable. The tube length can be decreased to 15.3 m (50 ft) or effectively increased up to an infinite length by placing restrictions or orifices at the exit. Tube lengths shorter than 15.3 m (50 ft) require that sections of the tube be removed, and hence necessitate tube realignment upon their replacement. Venting ports are provided along the entire length of the tube. The interior walls of the tube are aerodynamically smooth but controlled roughness of the walls can be introduced. It can be pressurized up to 1.03×10^6 N/m^2 (150 psi) and can use different fluids to obtain data through a wide range of Reynolds numbers. A model launcher is used, when testing at atmospheric pressure, to vary the initial velocity of the test models up to 15 m/s (50 ft/s). Also, the flow velocity in the tube at the time of model launch can be controlled in order that equilibrium test conditions can be obtained as soon as possible. To date, only circular cross-section models equipped with fine Teflon centering skids have been tested. The effects of model eccentricity in the tube and several models traveling simultaneously in the tube can be investigated.

Experimental Results

Drag

The effects of tube length and model blockage on the drag coefficient of the models tested are appreciable. Test section length effects are presented for three blockage ratios in Figure 3. (See Table 1 for definitions of symbols used.) It should be pointed out, however, that some Reynolds number effects are superimposed. Here, the drag coefficient is based on the model velocity relative to the test section wall. The drag coefficient in free air is about 0.5. Model length effects are important but to a lesser degree. This effect is not nearly as strong for higher blockage models and diminishes as models become very long. Nose and tail shapes exhibit distinct, although minor, effects on the drag coefficient. Streamlined nose

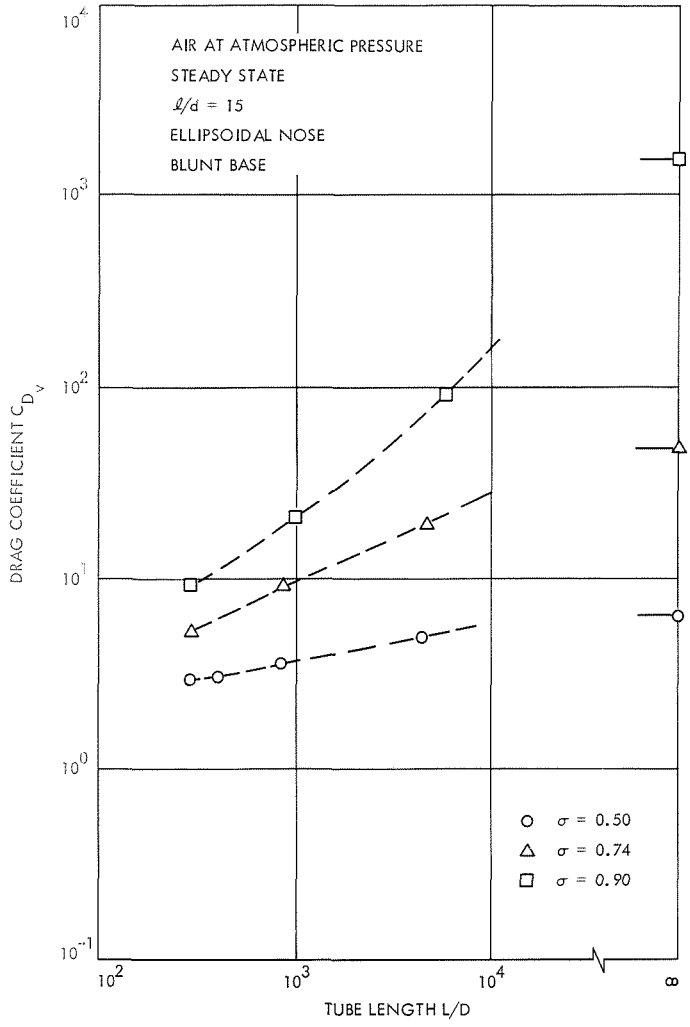

Figure 3. Variation of drag coefficient with tube length for three blockage ratios

Table 1. Nomenclature

a	model cross-sectional area, m^2
d	model diameter, m
C_{D_v}	drag coefficient based on the model velocity relative to the tube, $C_{D_v} = \text{drag} \Big/ \frac{1}{2}\rho v^2 a$
L/D	ratio of tube length to tube diameter
ℓ/d	ratio of model length to model diameter
Re_{d_v}	Reynolds number based on the model velocity and model diameter, $Re_{d_v} = \rho v d/\mu$
v	model velocity relative to the tube, m/s
μ	viscosity of test gas, $N\text{-}s/m^2$
ρ	density of test gas, kg/m^3
σ	ratio of model cross-sectional area to tube cross-sectional area (sometimes expressed in percent)

and tail sections resulted in about a 10% drag reduction on models with a blockage ratio of 0.5 but little or no reduction on models with a 0.9 blockage ratio.

The average velocity of the flow ahead of (and behind) the model increases with the blockage ratio and decreases with the tunnel length. The drag which the model experiences is a direct result of this since it must move (or attempt to move) part of this column of air surrounding it.

The drag coefficient is quite sensitive to test Reynolds number in the lower Reynolds number region (Figure 4). However, the drag coefficient becomes much less sensitive at Reynolds numbers that are near full-scale conditions.

Pressure Signature of Model Traveling in Tube

Experimental investigations performed to date on tube–vehicle systems indicate that the near-field flow is quite complex even for the ideal case; i.e., steady-state, incompressible-flow conditions. The characteristics of the near-field flow (flow extending from just ahead of the model to just aft of the model) can, in part, be inferred from the pressure distribution along the tube as the model passes. The experimental data show the near-field flow to consist of many clearly distinct regions. As few as four and as many as seven of these regions have been observed in each model pressure signature. A sample of a pressure signature at the test section wall in the vicinity of a 50% blockage model traveling at its equilibrium

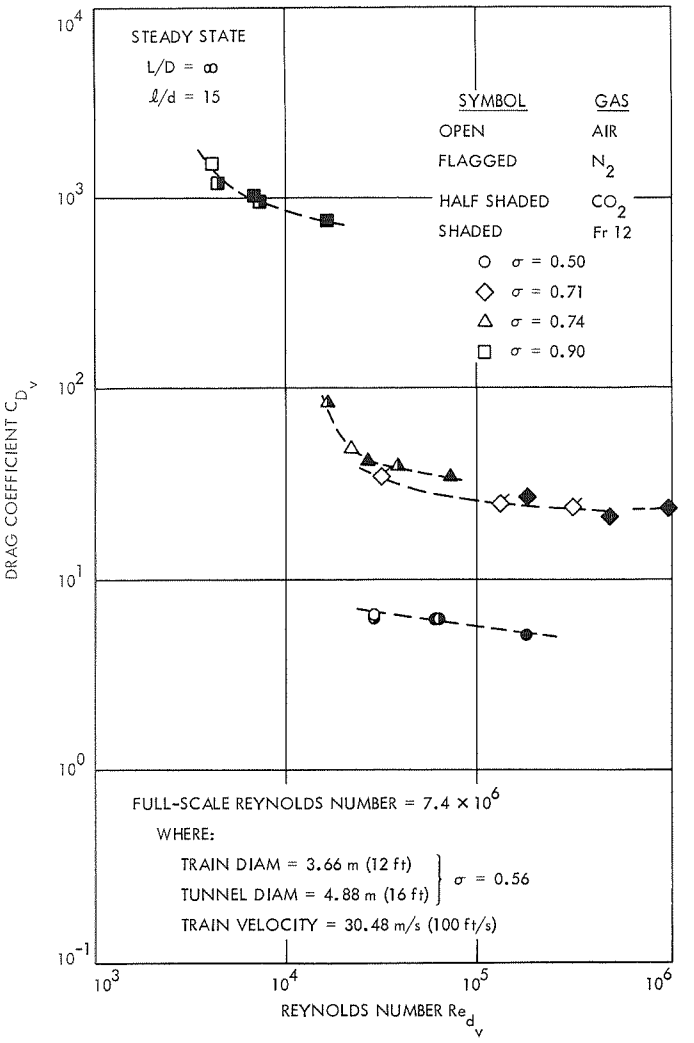

Figure 4. Variation of drag coefficient with Reynolds number for three blockage ratios

velocity is presented in Figure 5. Although recorded on a time scale, the figure has been converted to a pressure distribution along the test section in order to indicate the relative position of the model. Regions 1 and 6 indicate the pressure gradient in the test section due to the flow ahead and behind the model, respectively. Region 1 is essentially pure pipe flow, whereas Region 6 has certain wake effects embedded in the flow. Region 2 is representative of the Bernoulli pressure drop as the flow velocity increases over the nose of the model. Region 3 is the pressure gradient along the model length. Sometimes this occurs as a definite two-slope region, indicating the possible existence of laminar and turbulent flow regimes. Region 4 is usually present but to varying degrees. It is due to an over-expansion of the flow at the model base and acts

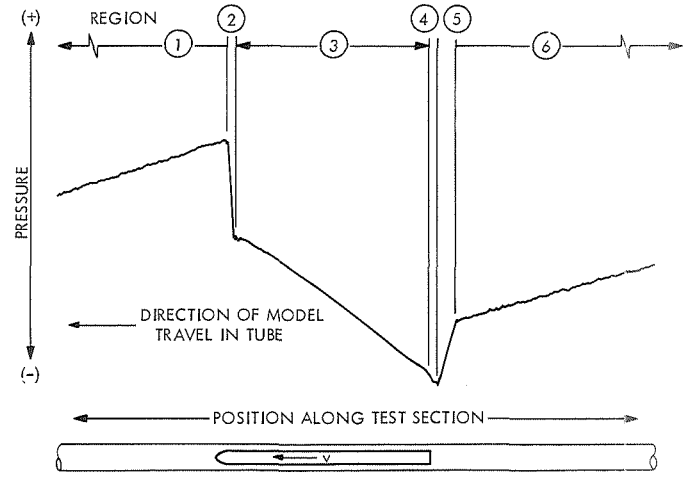

Figure 5. Sample of a pressure distribution along the tube in the vicinity of a 50% blockage model

to increase the drag. Region 5 is the pressure recovery as the flow velocity decreases to downstream conditions.

A great deal of useful information can be obtained from the model's pressure signature, such as:

(1) Velocity of flow in tube.

(2) Bernoulli pressure drop over model nose.

(3) Effective flow skin friction coefficient along model and tube immediately surrounding model.

(4) Pressure drop of flow expanding over base of model.

(5) Pressure recovery in flow downstream of model base.

(6) Effect of model wake on pipe flow friction factor.

The characteristics of the model pressure signature are greatly affected by the model blockage ratio. The tube length affects the signature to a smaller degree. For the 50% blockage model, there is both a relatively large initial pressure drop and a large pressure recovery. For the 90% case, the pressure gradient due to friction along the model and tube is the dominant characteristic of the pressure signature.

The pressure drop over the nose of the vehicle is about as would be expected from simple Bernoulli considerations for the 50% blockage model, but becomes increasingly larger than expected as the model blockage increases. The pressure recovery downstream of the model decreases as the model blockage increases in a manner not far off from the decrease expected from strict theoretical considerations.

Effective friction factors on the model and along the tube wall immediately surrounding the model can be inferred from the pressure signature of the model. Based upon the limited data analyzed to date, it appears that the concentric pipe flow approach is better than the flat plate approach. Not enough data have been analyzed to determine if there are significant effects on the friction factor due to the variables investigated (tube length, model length, model blockage, and gas).

Aerobraking of High-Speed Ground Transportation Vehicles

W. Marko

Environmental Sciences Division

A JPL-sponsored aerodynamic testing program has been initiated to perform initial investigations on the effectiveness of a series of aerodynamic brakes on a long cylindrical body. The development of the experimental program is presented in this article and a description of the model and test configuration is given. Preliminary results from a low subsonic wind tunnel test using three standard test techniques are also discussed. A moving-model drop-wire facility has been constructed and initial testing is currently underway. This data, which more correctly simulates the viscous interactions of the model with the ground plane, will be compared with the wind tunnel data and used to develop analytical prediction methods.

Introduction

The significant amounts of kinetic energy present in high-speed ground transportation vehicles present serious problems during both normal and emergency operation. Friction braking systems adequate for trains operating at normal speeds, as well as some proposed nonfriction systems, are complicated by heat dissipation systems that become even larger as speeds increase. However, additional braking can be obtained by aerodynamic brakes, or panels, which can be attached to the train and extended when necessary. All energy is dissipated directly to the air and complicated coolers are not required. In addition, since aerodynamic forces are proportional to the square of velocity, this type of braking rapidly increases in effectiveness as speed increases. While the effect of a single brake located near the front of a vehicle can be estimated with confidence, little is known of the effects of a cascade of such brakes spaced along the entire length of a long vehicle.

The flow disturbances created by a brake are expected to decrease the effectiveness of any succeeding brakes. Recommendations have been made in References 1 and 2 that an aerodynamic testing program be

undertaken in this area. Because such a small amount of reliable information is available, a very simple experiment was developed utilizing idealized models to yield useful preliminary results that can be applied to evaluation of the potential of aerodynamic braking as well as to indicate specific configurations of most promise for further investigation.

Approach

Scale model aerodynamic tests are usually performed in wind tunnels. In such cases where the vehicle in its normal operation travels near the ground, the ground boundary is simulated by the insertion of a ground board in the wind tunnel, thereby minimizing the influence of slow-speed flow near the tunnel wall (boundary layer). Another wind tunnel technique is to mount two identical models in the unobstructed test area, one as the mirror image of the other. Both techniques provide only an imperfect simulation of the ground interaction effects and attempts have been made with varying success to improve the ground board technique by removing the boundary layer or providing a moving ground belt.

In the main efforts of this program, a direct approach to the interaction problem has been undertaken because the turbulence induced by the extended brakes complicates the problem and makes the need for a more accurate simulation more important. This is achieved by using a moving model while the ground plane is stationary. This first generation experimental program uses a 15.24-m (50-ft)[1] vertical guide wire in close proximity to a ground plane and on which simple models of train-like vehicles (long, circular cylinders) with arrays of extended brakes slide by means of bearings on the model axis of symmetry. Braking effectiveness of the arrays will be determined by model velocity measurements under near-equilibrium conditions; high-speed photography will be used to investigate local flow conditions on the model. A range of Reynolds numbers will be obtained by varying the model velocity and the model diameter. These tests are to be augmented by small-scale wind tunnel tests.

Wind Tunnel Test Configuration

To minimize the length of the entire program, work was begun on the small-scale wind tunnel tests while construction of the drop-wire apparatus was under way. These wind tunnel tests and the drop-wire apparatus are now complete. The wind tunnel model is shown in Figures 1 and 2. It is a basic cylindrical model which simulates a train consisting of four 25.908-m (85-ft) cars at a scale of 0.00854. The model length and diameter

[1] Values in customary units are included in parentheses after values in SI (International System) units if the customary units were used in the measurements or calculations.

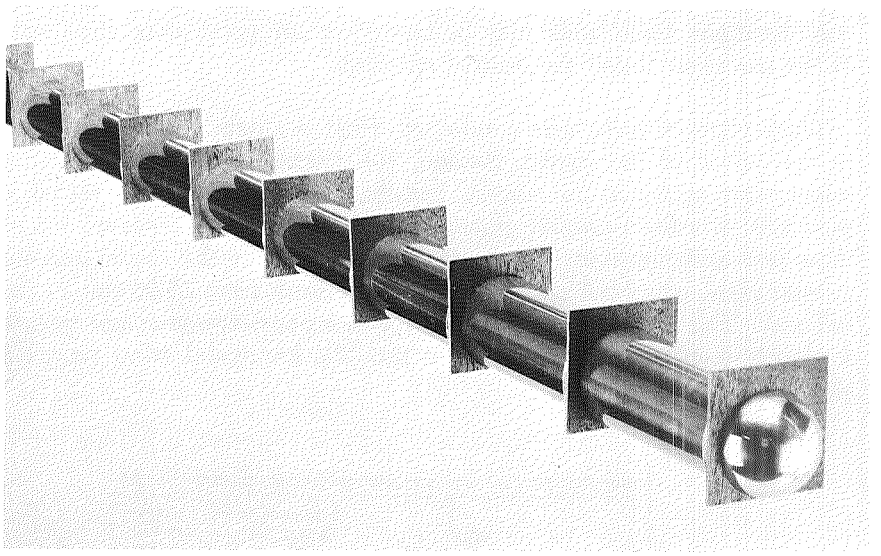

Figure 1. Wind tunnel model with brakes

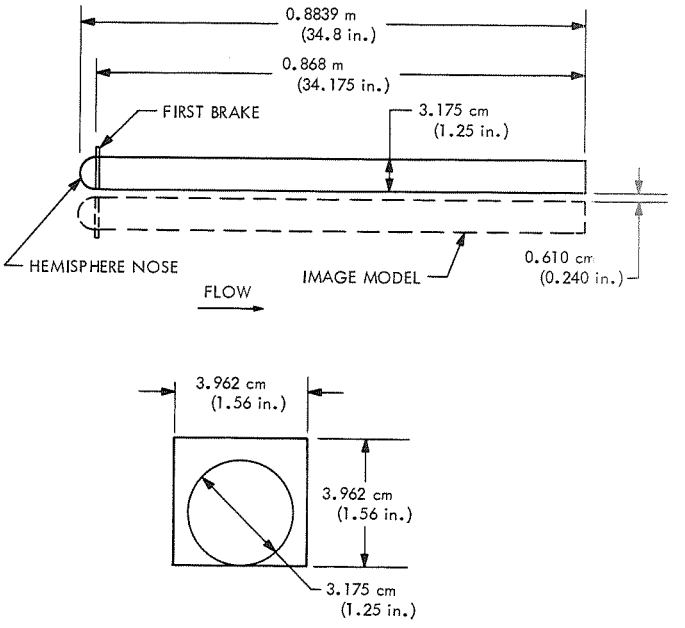

Figure 2. Schematic of wind tunnel model

are 0.8839 m (34.8 in.) and 3.175 cm (1.25 in.), respectively. The rectangular aerodynamic brakes were designed to approximate realistic full-scale brakes and were also satisfactory from wind tunnel blockage considerations. Each brake may be located at any point along the length of the model to obtain the desired spacings.

Three types of tests were conducted. First, a single model was tested in the center of the tunnel. Second, the original model and a mirror image were tested in the tunnel. Finally, a single model was tested in proximity to a fixed ground plane. Brake spacings were repeated for all three test configurations. The basic distance between the model and the ground plane was 0.305 cm (0.12 in.) scaled down from 35.56 cm (14 in.) full scale. This figure was doubled for the distance between image models. A sketch of a typical installation in the JPL low-speed wind tunnel is shown in Figure 3.

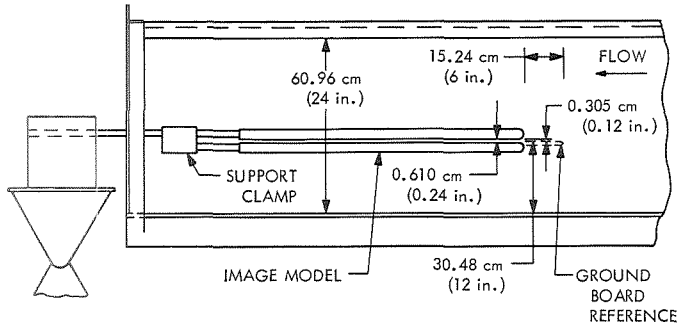

Figure 3. Wind tunnel model installation

Preliminary Results and Discussion

The primary wind tunnel measurement, axial force, was made with an internal three-component strain gage balance. Normal force and pitching moment were also recorded. Data have been reduced to a drag coefficient based on the model cylindrical cross-sectional area of 7.917 cm^2 (1.23 $in.^2$), which is approximately the same as that for one brake.

Figure 4 shows a typical data plot of the drag coefficient C_D as a function of the number of brakes installed on the model at a spacing of 12.7 cm (5 in.). All data with the exception of the first brake point may be faired smoothly. Differences between the image and ground plane models clearly illustrates the problem of selecting the proper method of testing, in a wind tunnel, a vehicle moving over a fixed surface. All of the results of the wind tunnel test will not be discussed here. However, some effects are noteworthy. Three complete sets of brake spacings were tested: 7.62, 12.70, 15.24 cm (3, 5, and 6 in.). The total drag on the four-car train model was highest for the 7.62-cm (3-in.) brake spacing because

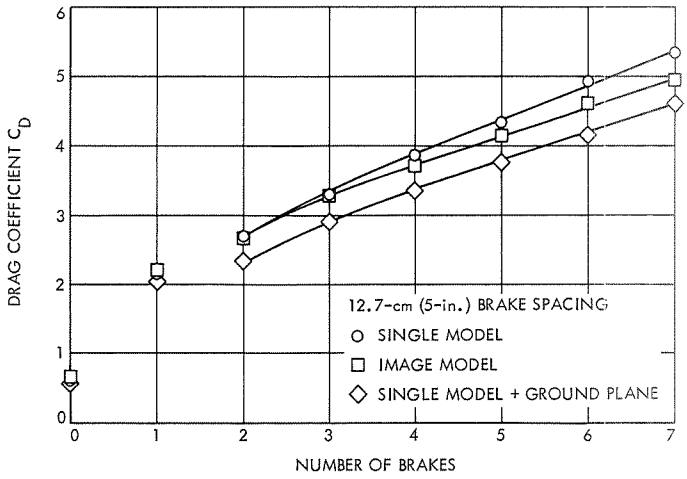

Figure 4. Effect of brake additions

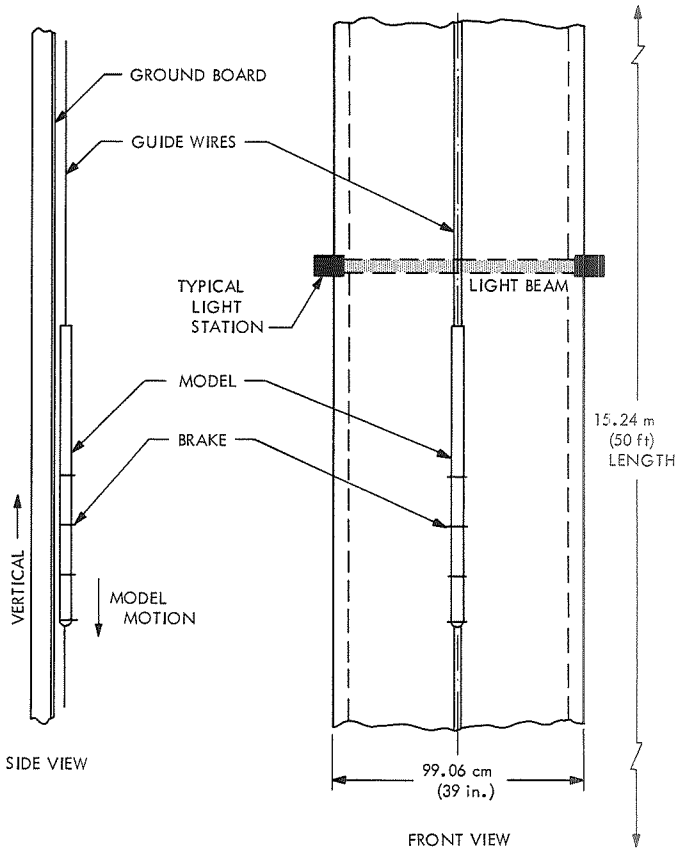

Figure 5. Drop-wire installation

of the greater total number of brakes, twelve as compared to seven for the 12.7-cm (5-in.) spacing. However, the drag increment per brake is actually less for a 7.62-cm (3-in.) spacing. Other tests concerned the effect of brake venting in an attempt to add high-energy air to each succeeding brake in the cascade. The result was a decrease in drag when 10 and 15% of the surface area of each brake was ventilated. Increasing the clearance between the model and the ground plane resulted in drag increases which approach the data obtained for the single model in free air.

The wind tunnel test completes the supporting information necessary for evaluating the drop-wire program. The primary data, with the moving model, is now being obtained on the drop-wire system shown in schematic form in Figure 5. To operate, the model is raised to the top of the wire guides and released. During the fall, the model interrupts the light beams, and sensors register the time and distance for the model's passage. Velocity and corresponding drag coefficient may be calculated from these data. Model drops will be made with and without a ground plane for varying brake spacings. A range of Reynolds numbers will be obtained by varying model terminal velocity and model diameter. Comparison of these data with those of the wind tunnel experiment is expected to give significant insight into the problem of brake effectiveness beyond that of the first brake with a minimum of ground plane viscous interactions.

References

1. *Development of Nonfriction Braking Systems for High Speed Trains*, No. YM-2811-K-3. Cornell Aeronautical Laboratory, Inc., Vehicle Research Department, Buffalo, N.Y., Apr. 1970.
2. *High Speed Rail Systems Study by TRW Systems*. TRW Inc., Redondo Beach, Calif., 1969.

Nitric Oxide Emission Studies of Internal Combustion Engines

F. H. Shair

California Institute of Technology

J. H. Rupe

Propulsion Division

This article reports on the methods and results of preliminary experiments that have been conducted with an ASME–CFR (American Society of Mechanical Engineers–Committee on Fuel Research) engine in order to determine the effect of fuel composition on the emission characteristics of an internal combustion engine. Initial emphasis was placed upon a comparison of the nitric oxide emissions within the exhaust for various mixtures of natural gas and gasoline. A pneumatically driven atomizer permitted the CFR engine to be operated with gasoline fuel–air ratios down to 0.05. At fuel–air ratios below 0.05, misfiring occurred when either natural gas or gasoline fuels were used. In a natural gas–gasoline fuel mixture, the nitric oxide concentration in the emissions decreased almost linearly with increasing concentration of natural gas, based on a fuel–air ratio near 0.063. It is shown, for the limited conditions investigated, that the concentration of NO_x in the exhaust (on the basis of mass discharged for unit work done) is always less when natural gas is the fuel, except for a limited range of operation at very lean equivalence ratios where misfiring precluded a direct comparison. However, the emissions were never reduced by more than ½, and were limited to approximately 20% over a substantial part of the equivalence ratio range ($1.0 < 0 < 1.3$).

Introduction

The development of a low pollution engine for automotive applications that will meet or surpass the 1975–1980 standards set forth in the California Pure Air Act of 1968 (AB 357) is fraught with compromise. Proposals varying from minor modification of the internal combustion engine, including add-on devices for exhaust gas treatment, to outright substitution with, for example, external combustors (fossil-fueled steam engines) or electric cars (ultimately based on nuclear reactors as an

energy source) are many and varied. Although the latter approach may ultimately be implemented, it seems clear that the current national investment in the internal combustion engine and the substantial half-life (3 to 5 yr, assuming 100% changeover for all new units starting at some arbitrary time) of this system dictates a near-term solution based on the former approach. Thus, it is essential that the potential improvements that are available with minor engine modifications (preferably suitable for retrofit to existing vehicles) and/or fuel composition be thoroughly evaluated. It was to this end that a series of experiments were initiated as a part of the activity of the "Low Pollution Vehicle Study Group," which includes JPL staff and California Institute of Technology (Caltech) faculty. The bulk of the experimental work is being carried out by Caltech students.

In view of the recent interest in the use of natural gas (NG) as a substitute for gasoline, the first set of experiments was devised to compare emission characteristics from a given engine when run alternately on gasoline and natural gas. Previous results have demonstrated substantial improvements for multicylinder engines where manifolding (1) introduces severe complications for liquid-fueled systems (based on normally aspirated carburetors), and (2) enhances mixing for gaseous-fueled systems. These results may be more representative of manifolding effects than "composition"; hence, an investigation to determine whether or not composition *per se* would materially alter emission characteristics was initiated.

The results reported here are concerned only with the formation of NO_x as a function of inlet fuel composition for a given set of engine operating conditions. Analogous measurements of CO, CO_2, and unburned hydrocarbons were also obtained but these results are not included in this report.

These initial experiments have shown that mixtures of natural gas and gasoline do not produce a significant synergistic effect and that replacing gasoline with natural gas results in reductions in *peak* levels of about 24% in terms of NO_x in grams per kilowatt-second (g/kW-s) (see discussion of results for this extrapolation). However, the reduction in available power is substantial. Further, it is shown that with *well-atomized* gasoline, it would be possible to control mixture ratio so as to achieve even lower NO_x emissions at greater efficiencies with gasoline than with natural gas.

It should be emphasized that these results in themselves cannot preclude the desirability of utilizing natural gas in internal combustion engines. As noted above, the emissions of NO_x *are* reduced, and it can be argued that the compromises associated with reduced power output can be offset by reductions in hydrocarbon reactivity index for emissions from natural gas combustion. Any particular conversion must also con-

sider such factors as economy of operation, availability of natural resources, and fuel supply and distribution.

It is noted that these observations are for a limited set of operating conditions and are therefore restricted by those limits.

Experimental Methods

The experiments reported here were conducted with an ASTM–CFR (American Society of Mechanical Engineers–Committee on Fuel Research) single cylinder engine running throttleless (full throttle) at a constant 900 rev/min. The engine was motored except when brake-horsepower measurements were being made. Initial testing was done with a compression ratio of 7 and with a constant spark advance of 10 deg.

The original variable float level carburetor was replaced by a fuel injection system to allow the blending of air, natural gas, and gasoline. To this end the induction system was modified to incorporate a pneumatically driven liquid atomizer of conventional design (Spraying Systems Company Model No. 1A). The atomizer was operated so as to assure a mean drop size less than 20 μm[1] and to yield a mixture that would behave essentially like a gas. In addition it was mounted in a tube bolted directly to the inlet flange of the engine so that liquid deposition on walls was minimized.

Provisions were made to vary the composition of the fuel from 100% gasoline to 100% natural gas in an attempt to (1) evaluate the potential of the so-called mixed or dual systems that are being proposed (Reference 1), and (2) determine whether or not adding small amounts of natural gas to gasoline could yield disproportionate benefits for a fuel comprised of a mixture of natural gas and gasoline. For these latter experiments the working fluid for the pneumatic atomizer became a mixture of natural gas and compressed air (infinitely variable from 0 to 100% natural gas) so that the atomization characteristics of the gasoline were maintained nearly constant. Thus, in summary, the induction system provided a common source for the injected fuel which could be composed of any ratio of natural gas/gasoline at any desired fuel–air ratio. The system will also be utilized in future experiments to evaluate the effects of mean drop size *per se* on combustion and emission characteristics.

Fischer–Porter rotameters were used to monitor the mass flow rates. A disc brake torquemeter was installed to allow measurement of the output power developed by the engine. A mixing tank (with a volume equal to approximately 35 cylinder volumes) was installed in the exhaust line to eliminate problems of concentration stratification.

[1]Presumed from manufacturer's specifications alone; not proven.

On-line analysis of the exhaust products was achieved with a high-speed, quadrapole, mass spectrometer (E.A.I. Quad 300) monitoring the effluent from a sampling probe installed downstream of the mixing tank. This system was used to measure, with relative precision, the concentrations of NO, CO, CO_2, CH_4, and C_2H_6.

In order to aid in the measurements of the higher hydrocarbon emissions, a Carle Model 9000 gas chromatograph (with a flame ionization detector) was also arranged so as to permit on-line sampling of the exhaust. The electrical signals from the gas chromatograph were: (1) integrated by means of an Infotronics Model CRS-100 digital integrator, and (2) displayed on a Hewlett-Packard Model 7127A strip chart recorder. This system is providing excellent data on hydrocarbon emissions, but, as indicated previously, this information is not included in this report.

As shown in Figure 1 a control panel is used to control and monitor flow rates of air and fuels flowing to the CFR engine; the disc brake and the on-line mass spectrometer are in the background, whereas the on-line gas chromatograph system (although present) is not visible in the picture.

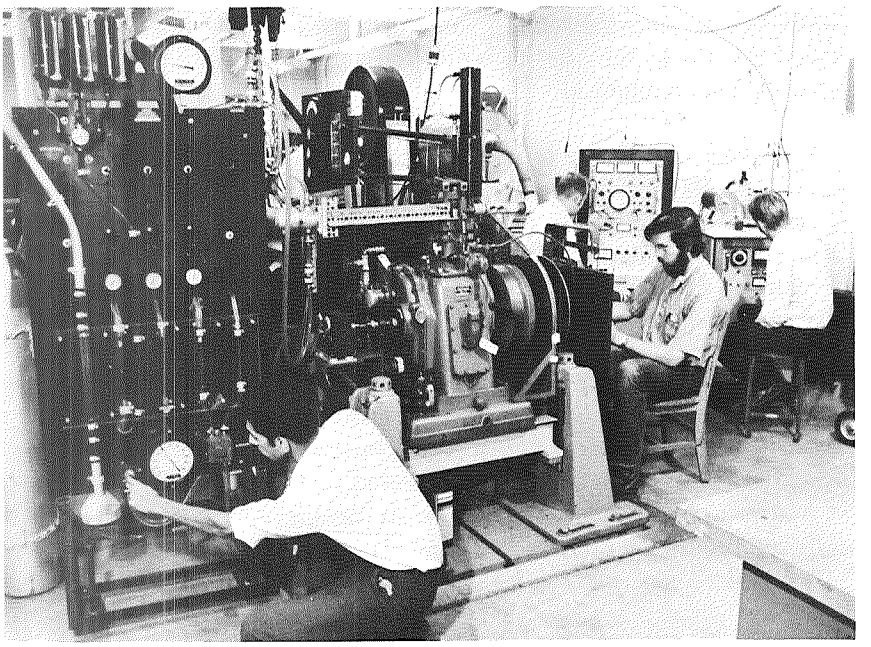

Figure 1. CFR engine and instrumentation for determining exhaust emissions

Experimental Results

The concentration of NO_x in the exhaust versus fuel–air ratio for this engine is shown in Figure 2; the curve with a maximum at approximately

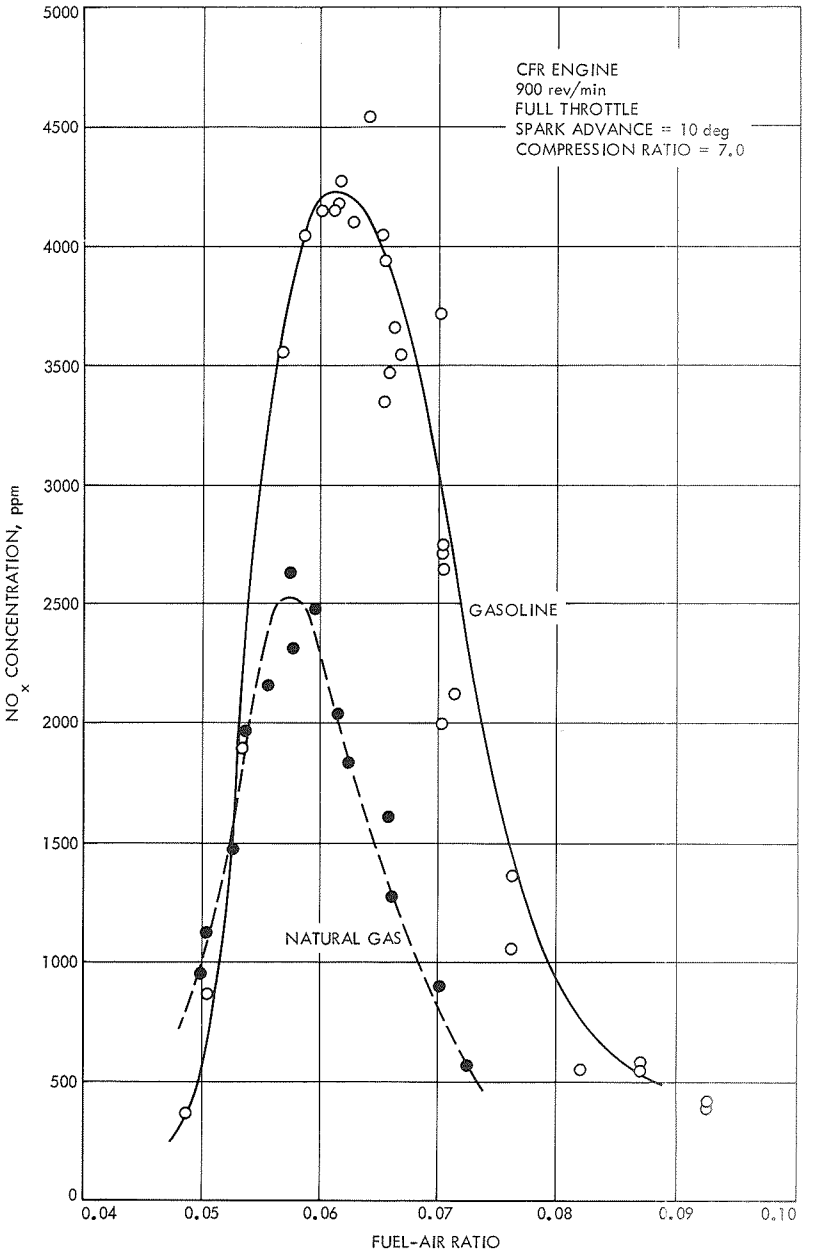

Figure 2. NO_x concentration in exhaust of an internal combustion engine burning natural gas or gasoline

4200 ppm is that obtained for several gasolines purchased at random from local outlets, whereas the other curve is for natural gas, nominally composed of 90% CH_4 + 9% C_2H_6 + residual CH + H_2. The stoichiometric fuel–air ratio for these gasolines is near 0.0645 and for natural gas is 0.0578. Where there is overlap, there is good agreement between

these results and those reported previously (for example, see Figure 4 of Reference 2).

Figure 3 indicates how the concentration of NO_x varies with the percent of natural gas in the fuel. These data are being analyzed with respect to theoretical models put forth by Newhall (Reference 3) and by Lavoie, Heywood, and Keck (Reference 4). Tests are planned to determine the comparable lean limit equivalence ratio associated with the original CFR carburetor system.

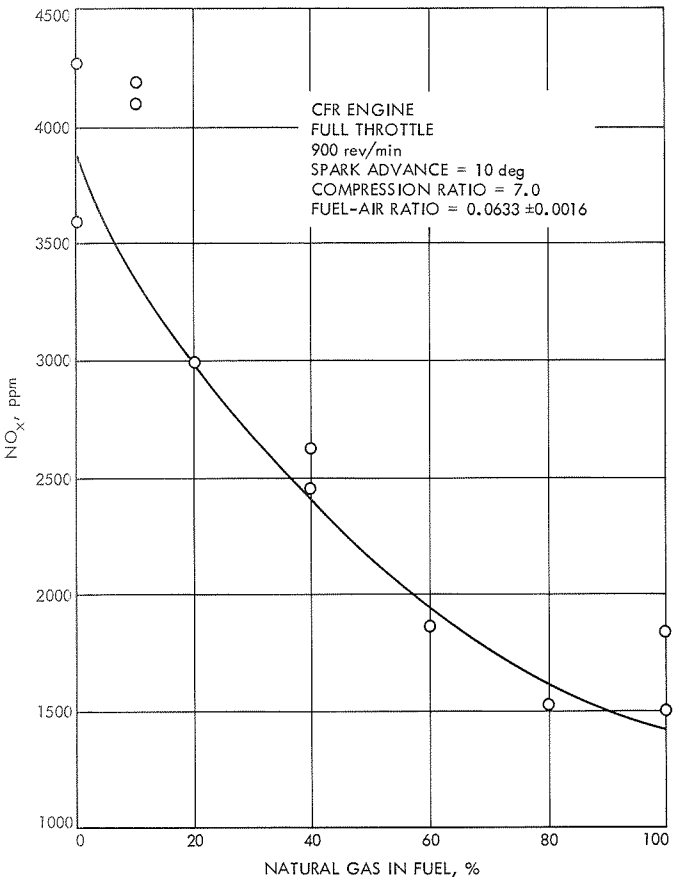

Figure 3. NO_x concentration in exhaust of an internal combustion engine burning mixtures of gasoline and natural gas

A comparison of engine performance, in terms of brake horsepower and specific fuel consumption versus fuel–air ratio, for natural gas and gasoline is presented in Figure 4. Clearly, the characteristic reduction in horsepower and the associated increase in specific fuel consumption (which is partially offset by the increase in heat of combustion) when burning natural gas are not negligible. Therefore, a proper comparison

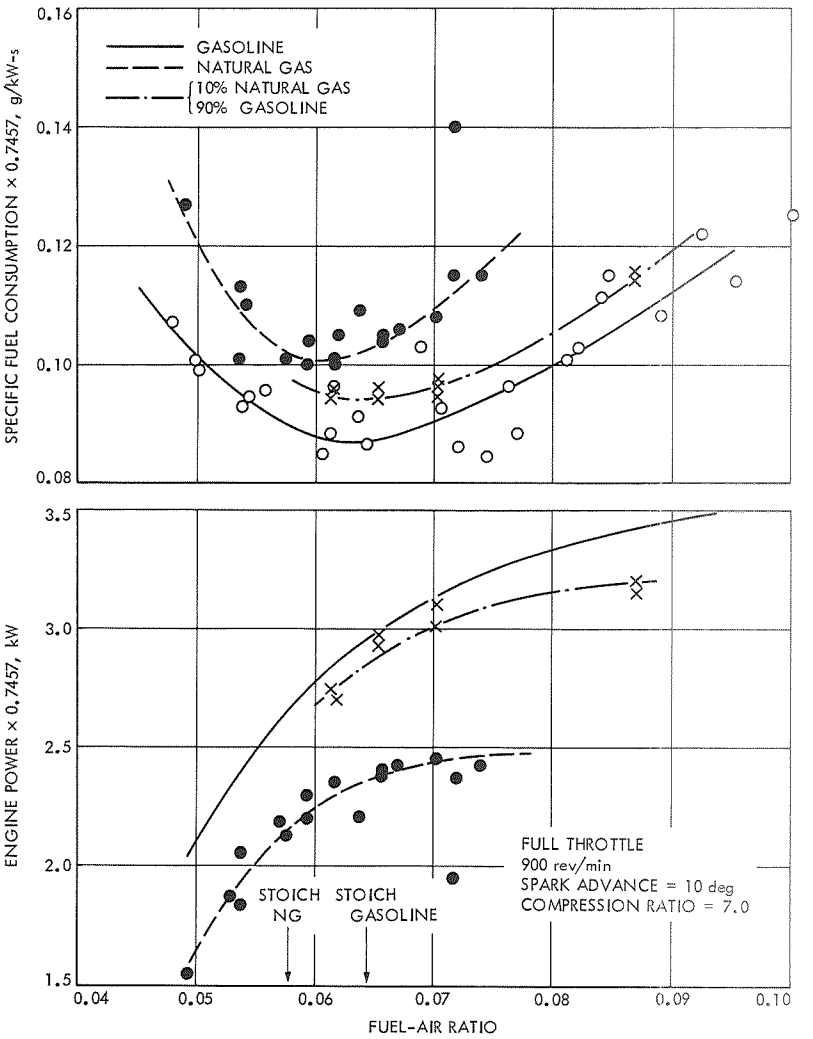

Figure 4. CFR engine performance with gasoline and natural gas

of the emission characteristics of these two fuels should incorporate the effects of this compromise.

It should be emphasized that Figures 2 and 3 deal exclusively with NO_x formation; other data are being reduced wherein consideration is given to the photochemical reactivity associated with the hydrocarbon product distribution.

Discussion of Results

When these data are presented as in Figure 2, it is observed that: (1) gasoline produces substantially greater quantities of NO_x than does natural gas for fuel–air ratios greater than about 0.057; (2) for fuel–air

ratios leaner than about 0.057, the emission levels for these two fuels are similar; and (3) for fuel–air ratios less than about 0.053, gasoline actually produces lower emission levels than does natural gas. Thus, it can be argued that emission levels for natural gas are similar to gasoline for lean fuel–air ratios but substantial reductions in NO_x formation are available for fuel-rich operation—even though, as illustrated in Figure 4, the compromises in terms of fuel economy (cost) and horsepower (engine size) are costlier for fuel-rich operation. It follows, then, that with well-atomized gasoline, the benefits to be derived by substituting natural gas for gasoline as an automotive fuel must stem from operation in the fuel-rich condition, not the lean condition, as is commonly stated.

It is of interest to point out that these conclusions must be modified somewhat if the comparison is based on the equivalence ratio rather than the fuel–air ratio. Thus, when the concentration data of Figure 2 are converted to an emissions rate, in terms of NO_x in grams per hour (g/h), and the comparison of emissions and engine performance portrayed as a function of fuel equivalence ratio[2] (as illustrated in Figures 5 and 6), it can be seen that the emission levels for natural gas always fall below those for gasoline. Further, substitution of natural gas for gasoline produces a nearly constant 28–30% reduction in available horsepower over the entire range of equivalence ratios, and the compromise associated with fuel economy is no longer so mixture ratio dependent—except that it is "desirable" to operate at or near equivalence ratio unity where the penalty, in terms of increased specific fuel consumption, for converting to natural gas is limited to approximately 14%.

It is interesting to note that, on an equivalence ratio basis, the lean stability limit for the "well-atomized" gasoline system is even lower than that for natural gas. Hence, the potential for controlling emissions by operation with "Lean air–fuel mixture carburetion . . . achievable by means of air–fuel mixture homogenation," as concluded by Kopa (cf Reference 5), is also demonstrated in these experiments with the CFR engine. Note that a similar conclusion is not strictly true when natural gas is the fuel. As seen in Figure 5, substantial amounts of NO_x are still being produced at the lean stability limit and it follows therefore that the only way to reduce these emissions further is to operate in the relatively rich region where the fuel–air equivalence ratios exceed approximately 1.18.

If the data of Figures 5 and 6 are combined to reflect the emission rate in terms of the work done, as shown in Figure 7, then the relative advantages associated with substitution of natural gas for gasoline are further reduced. It can be seen that if the comparison is made at their respective maxima, natural gas produces approximately 76% as much

[2]Fuel equivalence ratio ϕ is equal to the fuel–air ratio divided by the stoichiometric fuel–air ratio.

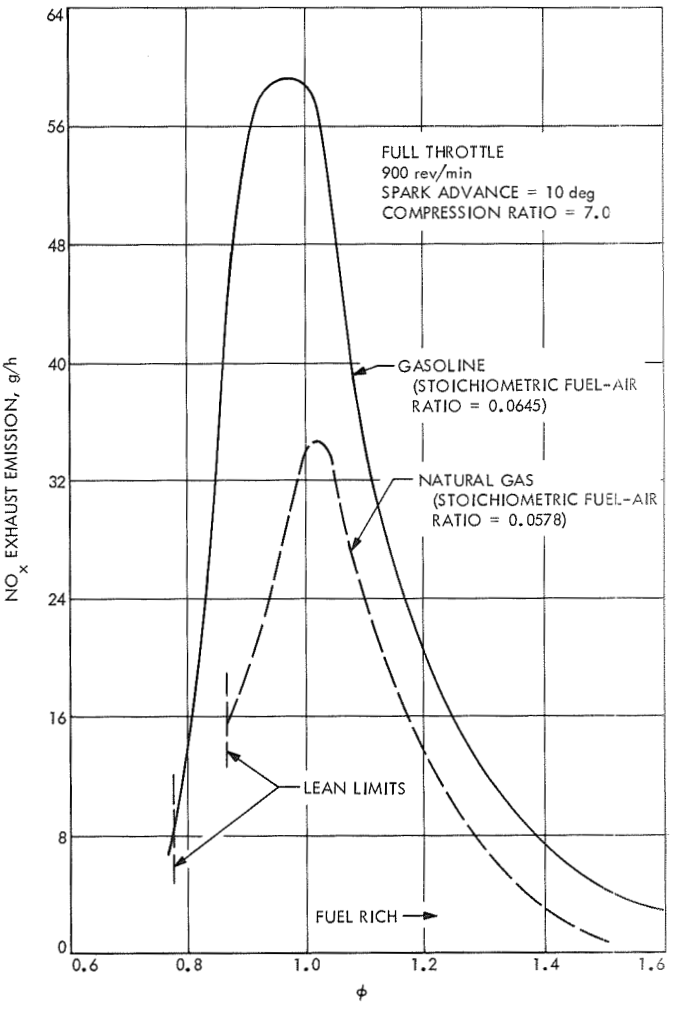

Figure 5. NO_x emission from CFR engine for two fuels

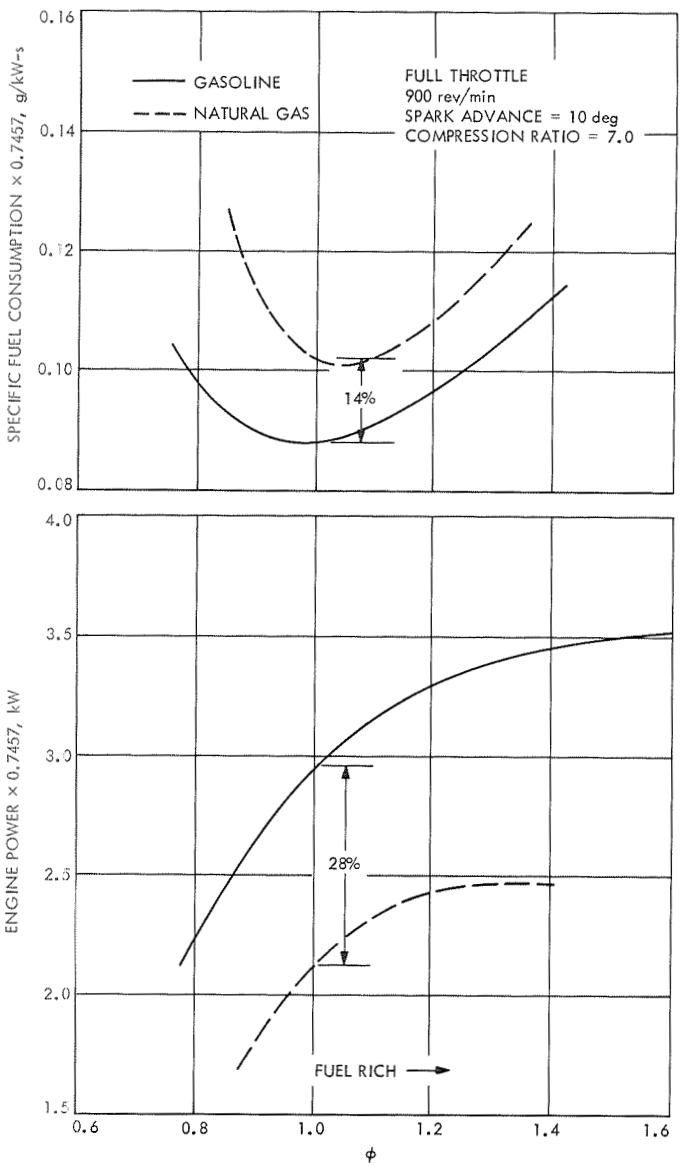

Figure 6. CFR engine performance as a function of fuel equivalence ratio with gasoline and natural gas

NO_x as does gasoline. However, this ratio rises to approximately 90% over most of the fuel-rich region.

The "relative" emission rates for the two fuels is illustrated in Figure 8, where it can be seen that gasoline always produces more NO_x. However, the difference is only about 8% at the minimum and does not exceed 20% for a rather broad range of equivalence ratios. Further, the data do not allow a comparison at the lean limit where the ratio would

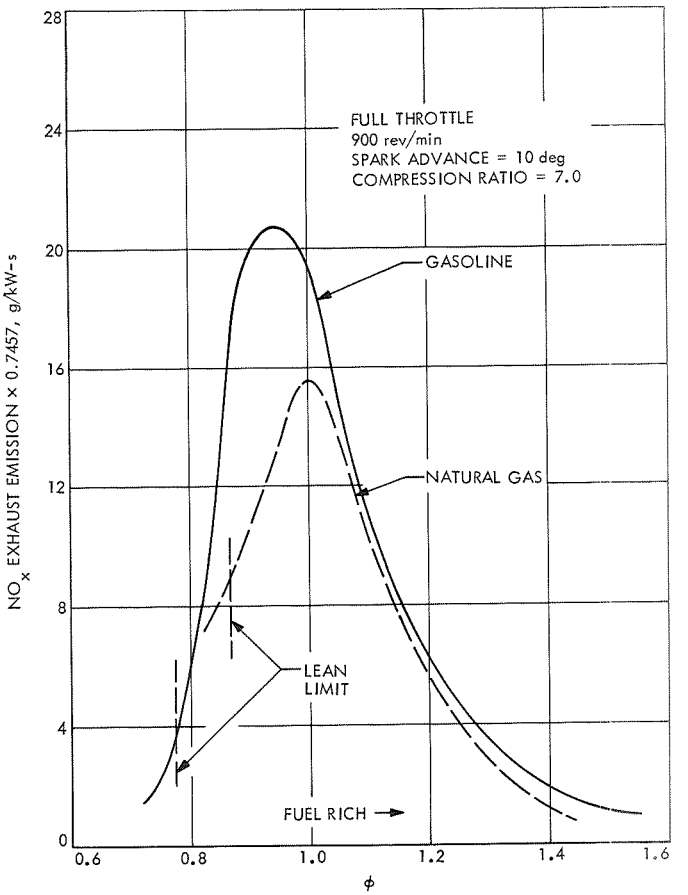

Figure 7. NO_x emission as a function of fuel equivalence ratio from CFR engine for two fuels

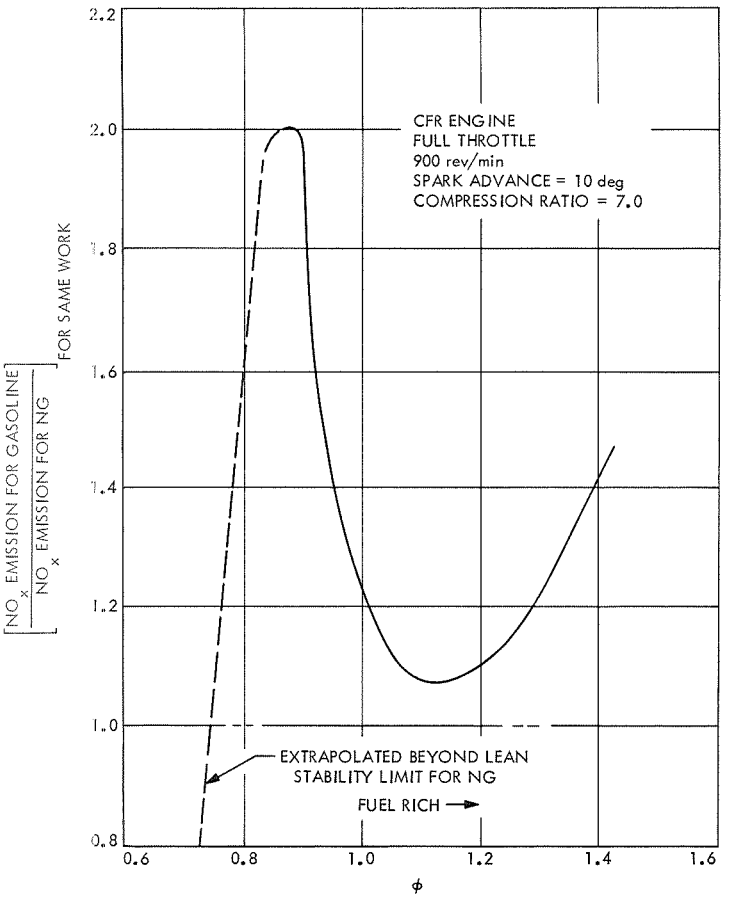

Figure 8. **Relative NO_x emission for gasoline and natural gas fuels doing same work**

(apparently) be less than 1.0. One should also note that in the fuel-rich regions the absolute emission levels are small for both fuels (see Figure 7).

Conclusions

Preliminary results of this study have shown that:

(1) The substitution of natural gas for gasoline as the fuel for an internal combustion engine:

(a) Yields fractional reductions in peak NO_x emissions for a given amount of work done.

(b) Compromises available horsepower by about 28%.

(c) Imposes a requirement that the engine be run rich (not lean) in order to minimize NO_x.

(2) The lean stability limit equivalence ratio for gasoline is less than that for natural gas if an efficient atomizer is utilized.

(3) The figure-of-merit for any pollutant cure must reflect the useful work done.

(4) Mixtures of natural gas and gasoline do not produce any appreciable synergistic effect insofar as reduction of NO_x is concerned.

References

1. McJones, R. W., and Corbeil, R. J., "Natural Gas Fueled Vehicle Exhaust Emissions and Operational Characteristics," SAE Paper 700078, presented at the Automotive Engineering Congress, Detroit, Mich., Jan. 12–16, 1970.
2. Eyzat, P., and Guibet, J. C., *A New Look at Nitrogen Oxide Formation in Internal Combustion Engines,* SAE Report 680124. Society of Automotive Engineers, New York, 1968.
3. Newhall, H. K., "Kinetics of Engine-Generated Nitrogen Oxides and Carbon Monoxide," presented at the 12th Symposium (International) on Combustion, the Combustion Institute, Pittsburgh, 1968.
4. Lavoie, G. A., Heywood, J. B., and Keck, J. C., "Experimental and Theoretical Study of Nitric Oxide Formation in Internal Combustion Engines," *Combustion Science and Technology,* Vol. 1, pp. 313–326, 1970.
5. Kopa, R. D., "Control of Automotive Exhaust Emission by Modifications of the Carburetion System," SAE Paper 660114, presented at the Automotive Engineering Congress, Detroit, Mich., Jan. 10–14, 1966.

An All-Carbon Radiating Nozzle for Long-Burning Solid Propellant Motors

R. L. Bailey and J. I. Shafer

Propulsion Division

Three 27-kg solid propellant motors have been static-fired in three tests to demonstrate the feasibility of using nozzles based on all-carbon composite materials for long-burning, high-performance solid rocket propulsion systems suitable for planetary orbit-insertion applications. The successful completion of these firings represents a significant advancement in long-burning solid propellant motor technology in that: (1) the motor burning times are comparable to those required for space missions; (2) the nozzle weights are about 0.4–0.6 that estimated for equivalent flight-weight ablative nozzles; and (3) unlike the ablative nozzles, the all-carbon radiating nozzles can be reused without, or with only very limited, refurbishment. Additionally, thermal analysis indicates that the nozzle design is acceptable when applied to a scaled-up 355-kg motor with a total burning time of 150 s (the desired time). The all-carbon radiating nozzle design, fabrication, testing, and analysis activities are described in this article.

Introduction

For solid propellant motors to meet the requirements of attitude-stabilized spacecraft for planetary orbiter missions, they must have both high performance and abnormally long burning times of up to 125–250 s (References 1–3). For a given motor, as the burning time is increased, one intuitively believes that a non-ablating radiative nozzle would, at some point, prove to be superior (lighter) than the ablative nozzles now in use. This assumes, of course, that the nozzle can be efficiently isolated, or insulated, from its thermally sensitive rocket motor chamber and that the severe thermal environment can be made acceptable to nearby spacecraft components.

A non-ablating radiative nozzle that utilizes all-carbon composite materials recently developed by industry has been designed and fabricated.

Feasibility tests have been conducted on a 27-kg (60-lb)[1] flight-weight solid propellant motor having a burning time of about 45 s. Ultimately, a scaled-up version of the nozzle will be used in a demonstration firing, at simulated altitude, of a 355-kg (780-lb) orbit insertion motor with a burning time of 150 s. (An artist's rendering of the demonstration motor with the proposed all-carbon nozzle is given in Reference 4.)

Nozzle Design

Carbon filaments belong to a class of materials typically prepared from synthetic (e.g., rayon) fibers that, under controlled thermal decomposition in an inert atmosphere (i.e., pyrolysis), yield the desired carbon class of filaments. When advantageous, the carbon filaments may be graphitized in order to orient the carbon crystal structure to alter mechanical and thermal properties in preferred directions.

Carbon (graphite) filaments have been available for some time. However, the all-carbon composite class, i.e., the carbon (graphite) filaments or cloth in a carbon (graphite) matrix, is quite new, and there are several preparation processes under development by various manufacturers. The nozzle design described here capitalizes on the unusual properties of these carbon composites.

The mechanical strength and elongation of these materials increase with increasing temperature up to and above 3030 K (5000°F). The mechanical and thermal properties are anisotropic; e.g., heat transfer across the fibers is significantly lower than that along the fibers. The tensile and compressive strengths are reasonably high, but the interlaminar shear, at present about 1380 N/cm^2 (2000 psi), is the weakest property and strongly influenced the design. These materials, as fabricated, are somewhat porous (density of about 1.44 g/cm^3 versus 1.9 for high-density bulk graphite), but the strong reinforcement fibers contribute markedly to toughness, an important factor during handling and ignition of the motor.

In the chemically reducing atmosphere typical of solid rocket combustion gases, these composites are relatively inert so nozzle erosion was expected to be low. Sublimation temperature reportedly is about 3922 K (6600°F), well above the flame temperature of the propellant system used for the design.

The nozzle assembly (Figure 1) includes a laminated nozzle body of pyrolyzed graphite tape fabricated by the rosette pattern technique, a high-density graphite insert for the throat for maximum erosion resistance, and a laminated conical transition section of graphite tape oriented

[1]Values in customary units are included in parentheses after values in SI (International System) units if the customary units were used in the measurements or calculations.

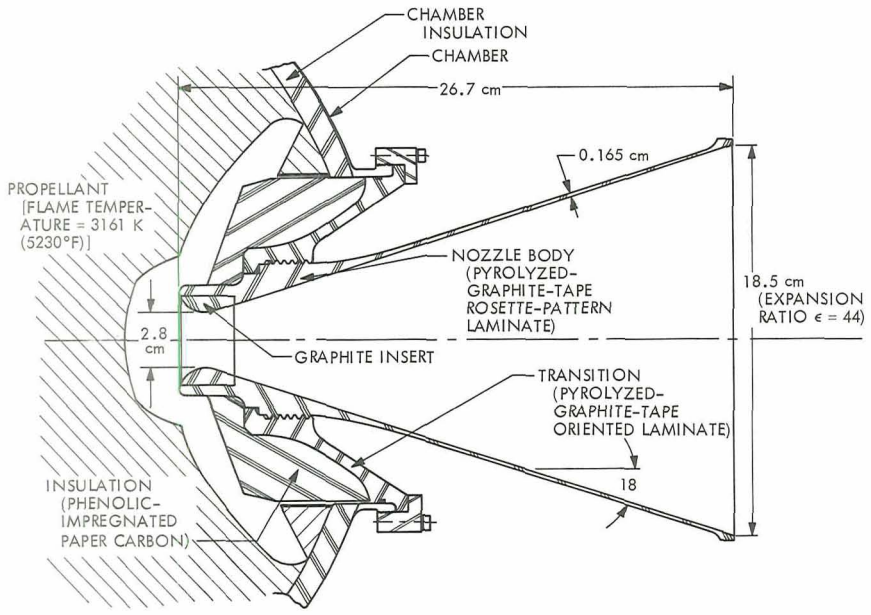

Figure 1. Configuration of all-carbon nozzle for feasibility testing

to minimize heat transfer. The transition, when mated to the chamber, supports the nozzle in a submerged position. Its gas seal at the chamber is a silicone O-ring; the seal at the threaded nozzle joint is a graphite gasket and ceramic cement. The thickness of most of the expansion cone is only 0.165 cm (0.065 in.), the minimum that could be fabricated with confidence at the time the nozzle was produced.

In the design philosophy adopted, the extremely hot nozzle was retained by providing a long enough heat path along the conical transition section such that the heat-treated chamber would not be weakened unacceptably during the heating transient of the required burning time. Obviously, the transition section, with this design requirement, must be insulated on its lateral surface from propellant combustion gases of 3161-K (5230°F) temperature. A low-density (0.9-g/cm^3) ablative composite based on a phenolic-impregnated paper carbon serves as insulation.

Nozzle Fabrication

Success of the all-carbon nozzle work depended strongly on the knowledge and experience of industry, especially regarding material choice and nozzle fabrication procedures; design and feasibility testing were JPL's responsibility. Early development efforts were based on a filament-wound graphite nozzle body, but it was found that, during a late processing step (high-temperature graphitizing), significant cracks or delaminations developed or porosity proved to be unacceptably high

in the pyrolyzed part. Subsequently, Reflective Laminates, a division of Fansteel, Inc., succeeded in producing satisfactory nozzle components by using graphite cloth in place of the filament-wound graphite.

Materials and procedures were specially designed for the fabrication of the carbon-to-carbon bonded structures. During processing, the interlaminar bond strengths are reduced, and the shrinkage stresses of the components increase. Therefore, procedures had to be tailored to process the components through these critical cycles without producing cracks or delaminations. The fabricator reported that the final part must be stress-relieved if interlaminar shear values in excess of 1380 N/cm^2 (2000 psi) are to be produced.

Figure 2 illustrates the method used for producing the oriented laminated transition and the rosette-pattern laminated nozzle body. In essence, the procedure for producing these components consists of: (1) making a large flat-plate laminated block and a thick-walled rosette-patterned laminated cone out of graphite cloth impregnated with phenolic resin, (2) rough-machining the two components from the block and cone, (3) subjecting these components to temperature pyrolyzing cycles, and (4) machining the components to their final configuration. The laminates are oriented in the block to increase the thermal resistance between the inside and outside diameters of the transition. The rosette pattern

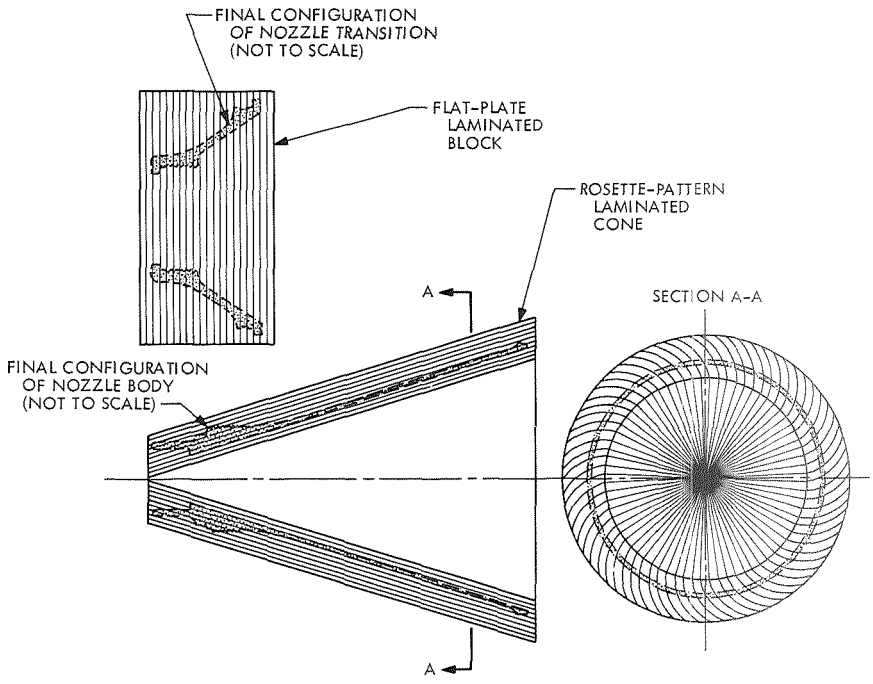

Figure 2. Layup step in nozzle transition and body fabrication

in the thick cone helps minimize shrinkage stresses and delaminations during the pyrolyzing steps.

The selection of a preimpregnated graphite cloth for making the block and thick-walled cone of Figure 2 was based on special requirements to produce uniform pyrolyzed components. The fabric must be selected for weave conditions and thermal stability of the fibers. The impregnating resin must have good char-forming characteristics with minimum shrinkage during polymerization. The resin solids content, volatiles, and flow must be carefully controlled in the preimpregnated stage. The product meeting those requirements was a highly heat-treated graphite cloth impregnated with a phenolic resin with a solids content of 20–30% and a maximum volatile content of 4%; the cured minimum density was 1.4 g/cm^3.

To obtain the required minimum density in the block and cone, several debulking cycles were performed at increasing pressures, but at temperatures low enough to prevent cure in the preimpregnated material. The block and cone were then cured at high pressure at 436 K (325°F) and subsequently post-cured at 506 K (450°F).

Following cure, the individual nozzle components were rough-machined, radiographed for cracks or delaminations, and subjected to a series of pyrolyzation cycles that carbonized the resin. Reimpregnation with a phenol-furfurol-based material after each cycle gradually raised the component density to that required. A final graphitization cycle was performed at 3030 K (5000°F).

The components were again radiographically inspected for cracks or delaminations and were then machined to finished dimensions. Another radiography inspection preceded the assembly of the components into the final configuration.

Static-Firing Test Results

The two finished nozzles were subjected to a total of three static-firing tests using flight-weight motors; the test conditions and results are summarized in Table 1. During the first test, conducted March 26, 1970, using nozzle SN-1, much of the nozzle body operated in a "white hot" mode for approximately 35 s of the 47-s burning time. After the firing, an inspection revealed no cracks or delaminations in the all-carbon transition and nozzle body sections and only small delaminations in the phenolic-impregnated paper carbon insulation. The nozzle was, in fact, judged to be in such good condition that it was subjected to another static firing test without refurbishment.

Table 1. Static-firing test conditions and results

Item	All-carbon nozzles			Ablative nozzle
	Test 1 (SN-1)	Test 2 (SN-1)	Test 3 (SN-2)	
Propellant weight, kg	26.65	25.42	26.65	27.57
Simulated altitude, km	Sea level	Sea level	15.90	15.90
Motor burning time, s	47	45	48	20
Nozzle expansion ratio ϵ	53.5	40.3	40.4	35
Maximum chamber pressure, N/cm^2	196.6	146.3	157.4	172.5
Nozzle weight, kg				
Initial	1.069	0.909	0.987	1.981
Final	0.928	0.869	0.924	1.776
Throat diameter, cm				
Initial	2.533	2.920	2.916	4.445
Final	2.635	2.998	2.954	4.465

The second firing resembled the first, except that the nozzle throat diameter was increased in order to test the motor and nozzle at pressure conditions closer to those desired for the ultimate flight application. The motor performed as expected. However, after an estimated 30–35 s of burning, a small rectangular hole (ultimately about 2.5 cm × 5 cm) developed in one side of the exit cone, at an expansion ratio $\epsilon \cong 9$, just downstream from the nozzle attachment ring plane. Since thrust was not being measured, the hole had no adverse effect on the motor performance. After sectioning the nozzle, the thickness at the edge of the hole was found to average 0.095 cm (compared with a fabricated thickness of 0.165 cm); no change in the internal diameter of the nozzle was noted. It was concluded that, since the nozzle was exposed to the air during the test, rapid oxidation on the outer surface of the cone resulted in the weak area and subsequent formation of the hole. It is believed that the nozzle would not have failed if the atmosphere had been inert or absent. The rest of the nozzle, especially the transition section, showed no abnormal effects after a cumulative 91 s of testing.

A third test, using nozzle SN-2, was made under simulated altitude conditions in order to test the high-expansion-ratio cone at full flow and to verify that the cone thickness, without oxygen exposure, would remain unchanged. Figure 3, a photograph taken about 30 s into the firing, shows the nozzle exhausting downward into the diffusor and illustrates the typical temperature gradient along the expansion cone. This nozzle was also found to be in excellent condition after testing, as shown in Figure 4. No cracks, delaminations, or changes in cone thickness from oxidation could be detected upon post-fire inspection. It is currently planned to refire this nozzle.

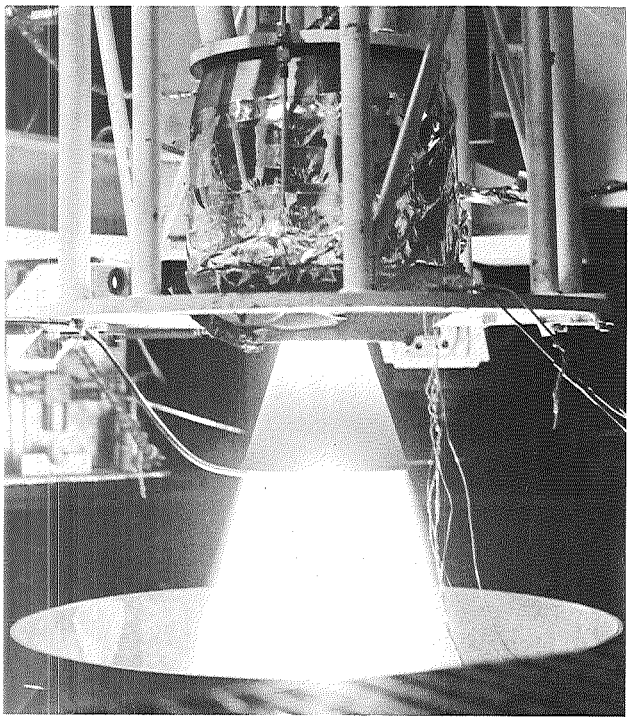

Figure 3. All-carbon nozzle during simulated altitude firing

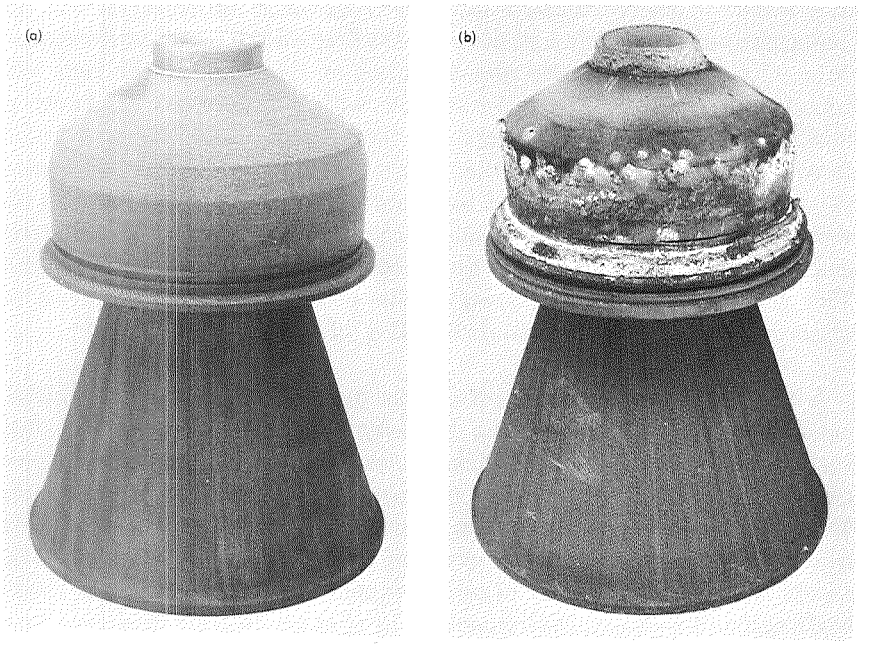

Figure 4. All-carbon nozzle (a) before and (b) after simulated altitude firing

These all-carbon nozzles are about the same size as the flight nozzle used successfully on the JPL Syncom apogee kick motor (SR-12-1). Typical 1964 test results of the Syncom nozzle are also presented in Table 1 for comparison purposes. The Syncom motor used an ablative nozzle that was fabricated with a randomly oriented carbon–phenolic material. It was approximately 100% heavier than the all-carbon nozzles. It should also be noted that the Syncom nozzle could be used for only *one* motor firing of *20-s* duration.

Figure 5 illustrates the nozzle surface temperature variation with time as measured by two infrared radiometers during the second SN-1 firing and the SN-2 firing at altitude. During the SN-1 nozzle test, the radiometers were focused at station 1, where $\epsilon = 7$ (i.e., about 2.5 cm downstream from the nozzle-to-transition joint). During the SN-2 nozzle test, one radiometer was focused at station 1 and the other was focused at station 2, where $\epsilon \cong 27$ (i.e., 7.6 cm upstream of the nozzle exit). The maximum temperature measured at station 1 was about 1845 K (2860°F); that at station 2 was about 1666 K (2540°F). These values agree within about 55–83 K (100–150°F) to the predicted temperatures at those stations – good agreement considering the limited data available on the thermal properties of these newly developed materials and the radiometer accuracies under the test conditions.

Conservative calculations were made to determine whether radiation losses would contribute significantly to a loss in specific impulse. They

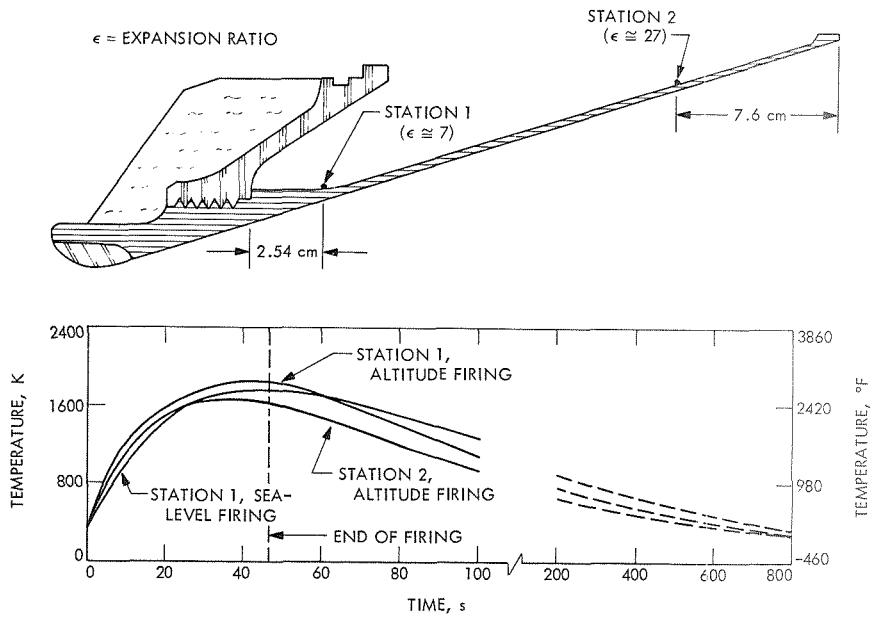

Figure 5. Measured nozzle surface temperatures during and after static firing of flight-weight motor

showed that: (1) such losses, based on measured heat fluxes from the nozzle, did not exceed 0.6%; and (2) total nozzle heat losses did not exceed 1.2%, a typical value for small ablative flight-weight nozzles. A separate determination of the loss in specific impulse due to combustion gases flowing radially outward through the relatively porous walls of the nozzle cone revealed that such a loss was insignificant ($< 0.1\%$). Thus, the use of all-carbon radiating nozzles would not appear to have a deleterious effect on motor performance.

Thermal Analysis of Scaled-Up Nozzle

Ultimately, a 355-kg motor utilizing a scaled-up version of these all-carbon nozzles will be tested. In preparation for the firing of this motor with a 150-s burning time, a thermal analysis of a full-sized nozzle was made. Basically, the design used the same materials and concepts as those of the small-nozzle design. However, a sandwich-type heat shield [i.e., 1.3-cm-thick, low-density (0.08-g/cm^3) carbon felt between aluminum plates, each 0.051 cm (0.020 in.) thick] was introduced to protect the aft end of the motor case. In addition, a 0.63-cm-thick (0.25-in.-thick) layer of low-density carbon felt was incorporated as a thermal barrier between the transition and nozzle cone. The thermal model was set up and analyzed by Dr. L.-C. Wen of JPL, using the CINDA computer program, which is capable of handling combined conduction, convection, and radiation for transient and steady-state conditions.

Figure 6 plots the predicted temperature versus time at five stations on the nozzle body and five stations on the conical transition member. The calculations indicate that, at the end of burning, the nozzle cone temperature will vary from 2390 K (3842°F) near its junction with the transition to 1140 K (1592°F) near the nozzle exit. The transition member easily provides the pronounced temperature gradient needed to protect the chamber. The temperature of the chamber at the nozzle attachment point is expected to be only 375 K (215°F), an acceptable design value. The aluminum heat shield at node 184 should reach 547 K (525°F), well below its melting point. The temperature of the shielded case will rise an insignificant amount due to heat from the nozzle; e.g., node 150 should rise about 1–2 K.

Separate computer runs revealed that motor burning times up to 200–225 s are feasible with the indicated basic design for very small increases in insulation weight, provided the chamber pressures are kept low. It is of interest to note that the total nozzle, including insulation and heat shield, is estimated to weigh 9.8 kg (21.5 lb). That weight can be compared with 16.6 kg (36.5 lb) for a lightweight ablative nozzle designed as an alternative to the all-carbon nozzle.

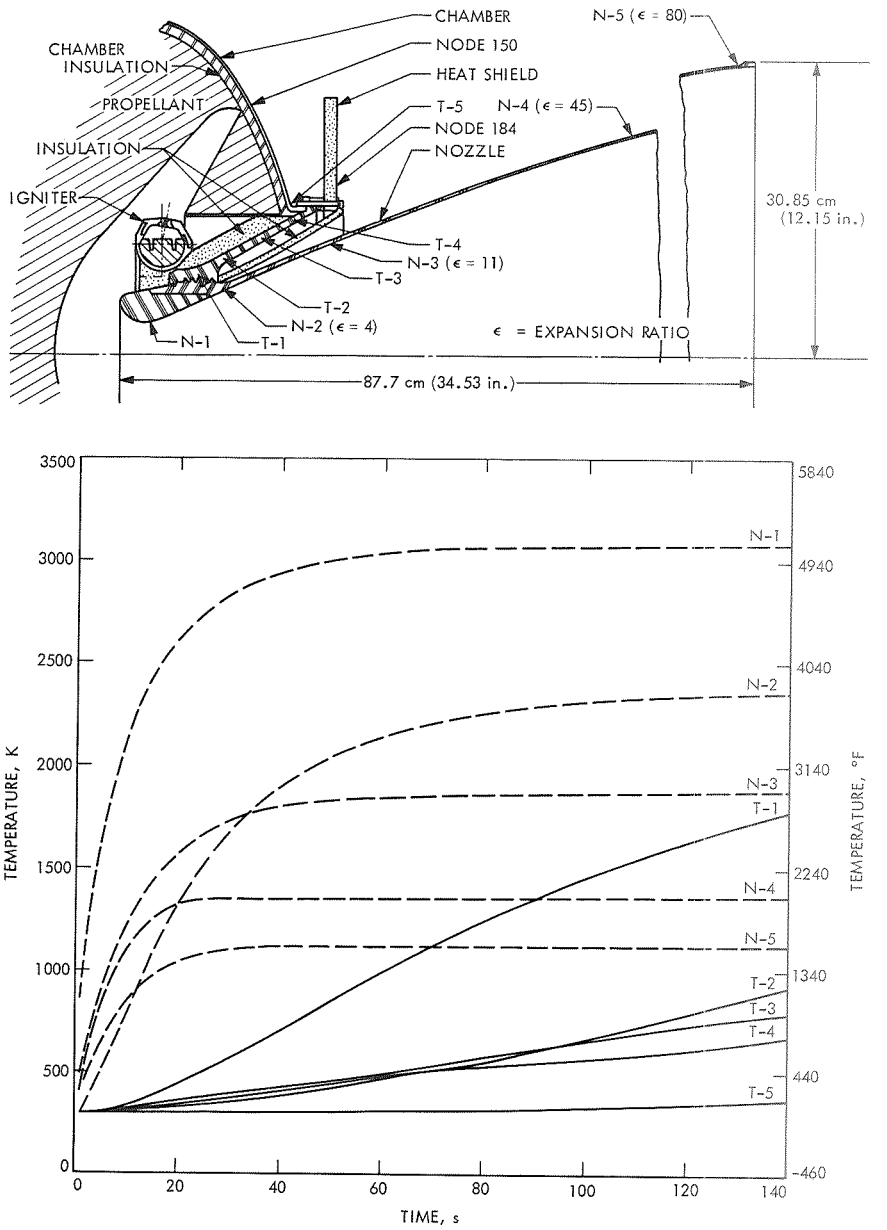

Figure 6. Predicted nozzle temperatures during firing of 355-kg demonstration motor

Conclusions

From the information obtained thus far, it can be concluded that:

(1) Fabrication technique is a critical factor affecting the integrity of all-carbon nozzles; Reflective Laminates has demonstrated a satisfactory technique for nozzles of the size tested.

(2) An all-carbon nozzle can be reused several times, which, in effect, compensates for its initial high cost.

(3) The use of submerged all-carbon radiating nozzles for high-performance solid propellant motors is technically feasible and very promising.

References

1. Robillard, C. L., and Cork, M. J., "Mission Analysis for Solid Propellant Motors on Unmanned Spacecraft," AIAA Paper 68-815. American Institute of Aeronautics and Astronautics, 1290 Avenue of the Americas, New York, N. Y. 10019.

2. Don, J. P., and Shafer, J. I., "Outer Planet Orbiter Propulsion," CPIA Publication 196, Vol. I. Chemical Propulsion Information Agency, Johns Hopkins University, 8621 Georgia Ave., Silver Spring, Md.

3. Shafer, J. I., "Long-Burning-Time Motors for High Incremental-Velocity Maneuvers at Low Acceleration," CPIA Publication 188, Vol. I. Chemical Propulsion Information Agency, Johns Hopkins University, 8621 Georgia Ave., Silver Spring, Md. (Confidential).

4. Shafer, J. I., Strand, L. D., and Robertson, F. A., "Low Acceleration Rate Ignition for Spacecraft," in *JPL Quarterly Technical Review*, Vol. 1, No. 1, pp. 35–44. Jet Propulsion Laboratory, Pasadena, Calif., Apr. 1971.

Mariner Mars 1971 Orbiter Propulsion Subsystem Type Approval Test Program

J. F. Stocky

Propulsion Division

A new propulsion subsystem was used on the *Mariner* Mars 1971 orbiter spacecraft to provide the necessary impulse for trajectory corrections, Mars orbit insertion, and Mars orbit trim maneuvers. The type approval test program that provided the functional, structural, and environmental qualification of this subsystem and demonstrated its performance margin in excess of flight mission requirements is described. A brief discussion of the problems encountered is included.

Introduction

The *Mariner* Mars 1971 spacecraft is designed to use the basic vehicle employed on previous *Mariner* (fly-by) missions with the incorporation of a new and larger propulsion subsystem (Figure 1) to decelerate the spacecraft from a hyperbolic approach trajectory and place it into an elliptical orbit about Mars. The schematic diagram of this pressure-fed, bipropellant subsystem is shown in Figure 2. A regulated supply of filtered nitrogen gas is used to expel the hypergolic fuel (monomethylhydrazine) and oxidizer (nitrogen tetroxide), each of which is contained in a Teflon expulsion bladder, from the propellant tanks through a filter to the rocket engine. Braided, Teflon-lined, flexible hoses are used to permit gimballing of the rocket engine to provide spacecraft pitch–yaw control. Positive isolation of the pressurant and propellants is achieved with explosively actuated gate valves, which are actuated by ground commands.

Because this propulsion subsystem was new and different from those previously used, it was required that it be subjected to a type approval (TA) test program. Successful completion of this test program would then qualify the subsystem for the 9-mo mission for which it was designed.

Components identical to those used on the flight spacecraft were employed in the assembly of the propulsion subsystem to be used for

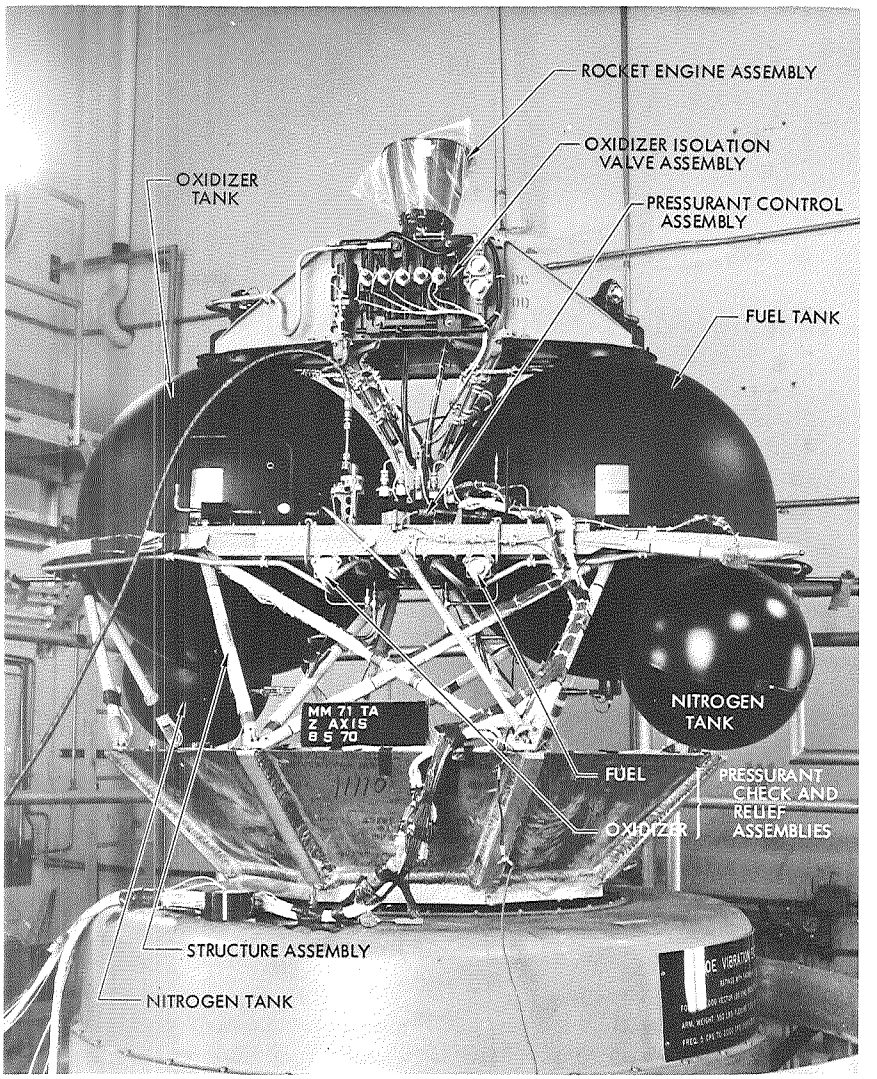

Figure 1. Fueled and pressurized TA propulsion subsystem ready for vibration

the type approval test program. After assembly this test subsystem was subjected to the same flight acceptance tests to which the flight subsystems were exposed.

The TA test program was conceived and conducted to demonstrate functional and structural margin and performance capability in excess of that which will be required of those subsystems to be used for the flight mission. To this end the test conditions listed below were planned.

(1) Higher level and increased duration for mechanical vibration.

(2) Operation at extreme temperature limits.

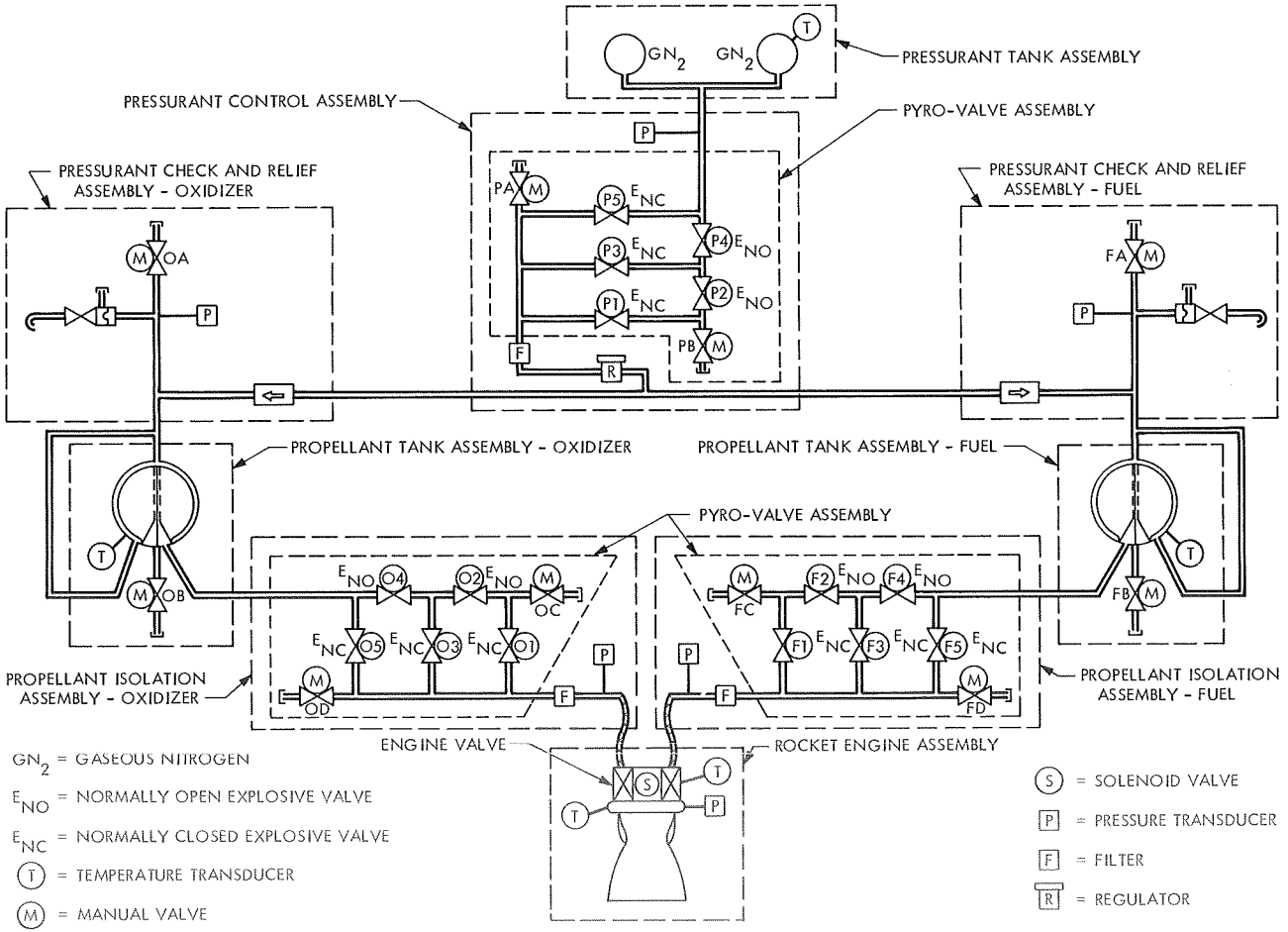

Figure 2. Schematic of *Mariner* Mars 1971 propulsion subsystem

(3) Two-mission duty cycles.

(4) Extra handling and servicing.

(5) Additional functional and component checks.

(6) Other extended operating limits, such as high tank pressures, extreme non-operating temperatures, and extreme engine valve temperatures prior to firing.

Description of Events

The sequence of the TA program was as listed below.

(1) Component acceptance tests.

(2) Flight acceptance tests of subassemblies, conducted to verify proof of workmanship, quality, and performance characteristics of the subassemblies.

(3) Flight acceptance tests of the propulsion subsystem, which included the tests listed below.

  (a) Subsystem fabrication and assembly.

  (b) Proof pressure test.

  (c) External leakage test.

  (d) Functional test (regulator, valves).

  (e) Vibration test, loaded with solvents to simulate propellant mass.

  (f) Acoustic test, simulating launch environment.

  (g) Bladder leakage test.

  (h) External leakage test.

  (i) Functional test.

  (j) External leakage test.

The above tests were the same as those that all flight subsystems experienced prior to the actual mission. Then, to simulate mission conditions, Test Series 1 and 2, as outlined in Tables 1 and 2, were performed.

Test Series 1 and 2 simulated two-mission duty cycles. The fact that the pyro valves were irreversible in operation precluded a complete simulation, so the sequences were folded, as shown in Tables 1 and 2. The total engine firing time of each test series exceeded that expected for flight. Therefore, the engine, filters, bladders, and service valves demonstrated margin in capacity and cycle capability. The extra handling and servicing required for two propellant loadings and unloadings

Table 1. Test Series 1 (high temperature)

Test sequence	Simulated mission sequence
1. Propellant vibration (3 axes)	Launch
2. Installation in vacuum chamber	2-wk coast
3. Open and close engine valve	Liquid line vent
4. Pyro valves open (-1 series)	Pyro valves open (-1 series)
5. 8-s firing	Midcourse 1 firing
6. 1-day hold	1-wk coast
7. Pyro valves close (-2 series)	Pyro valves close (-2 series)
8. 1-day hold	6-mo coast
9. Pyro valves open (-3 series)	Pyro valves open (-3 series)
10. 10-s firing	Midcourse 2 firing
11. 1-day hold	20-day coast
12. 900-s firing	Orbit insertion firing
13. 2-day hold	2- to 4-day coast
14. 0.4-s firing	Orbit trim 1 firing
15. 3-day hold	2- to 4-day coast
16. 40-s firing	Orbit trim 2 firing
17. Not performed	Coast Pyro valves close Orbit planet

qualified the techniques and subsystem in the case of offloading propellants for repairs prior to launch. The engine was heated to 338.7 K (150°F)[1] prior to the first midcourse firing, approximately 11 K (20°F) hotter than that predicted from solar radiation; the subsystem was heated to 303.7 K (87°F), near the maximum of its specified range [305.4 K (90°F)] and 6.7 K (12°F) warmer than that predicted for the first midcourse maneuver. Cold propellants were then loaded for Test Series 2, and the propellants were at 280.3 K (45°F) at the time of the orbit insertion firing, compared to an expected temperature of 297 K (75°F). These temperature extremes were intended to demonstrate margin for bladder collapsing, engine valve operation, check valve operation, and the operation of other temperature-sensitive components. Saturated propellants were not used for testing, since analysis had shown that the predicted level of saturation at the time of orbit insertion would be well

[1]Values in customary units are included in parentheses after values in SI (International System) units if the customary units were used in the measurements or calculations.

Table 2. Test Series 2 (low temperature)

Test sequence	Predicted mission sequence
1. Not performed	Launch through midcourse 2 firing
2. 900-s firing	Orbit insertion firing
3. 3-day hold	2- to 4-day coast
4. 16-s firing	Orbit trim 1 firing
5. 1-day hold	2- to 4-day coast
6. Not performed	Orbit trim firing / Coast
7. Pyro valves close (-4 series)	Pyro valves close (-4 series)
8. 1-day coast	Orbit planet
(End of nominal sequence)	
9. Pyro valves open (-5 series)	Margin demonstration operations
10. 10-s firing	
11. 1-day coast	
12. 20-s firing	

below the threshold required to affect performance. The orbit insertion firing of Test Series 2 was performed with propellant tank pressures initially 17 N/cm^2 (25 psi) higher than expected, simulating tank heating or regulator gas leakage.

Results and Conclusions

Two problem areas were discovered in the subsystem TA program. A beryllium tube supporting one of the pressurant tanks failed during vibration with solvents. This occurred at the resonant frequency of the pressurant tanks, and was due to a higher than expected tank response. The pressurant tank support tubes were replaced with steel tubes and were qualified. The oxidizer check valve partially opened during the first engine firing of Test Series 1, and the oxidizer tank supplied propellant in a blowdown mode. Operation for later engine firings was satisfactory. A detailed component test program determined the cause of the check valve sticking to be interference between the Teflon poppet and the metal poppet guide, due to oxidizer absorption and thermal growth of the poppet. Predicted temperatures during the actual mission are 19.3 K (35°F) lower than the check valve temperature at the time of the observed sticking. This, combined with the fact that momentary sticking would have little possibility of degrading the mission, resulted in the decision to not change the flight check valves.

All other components functioned as expected. All specification requirements were satisfied. Reliability of the propulsion subsystem was demonstrated and all interfacing equipment, such as pyro, thermal, structure, and support equipment, operated and functionally interfaced satisfactorily.

Prediction of Lipid Uptake by Prosthetic Heart Valve Poppets From Solubility Parameters

J. Moacanin and D. D. Lawson

Propulsion Division

H. P. Chin, E. C. Harrison, and D. H. Blankenhorn

University of Southern California

Most prosthetic heart valves currently implanted consist of a silicone rubber poppet situated within a metallic cage. Recent reports indicate that gradual deterioration of the poppet can occur and lead to serious valve malfunction. Physical changes (variance) observed in recovered prostheses include discoloration, swelling, and cracking. A major cause of variance is believed to be lipid accumulation. This article presents an assessment of the solubility of lipids in silicone rubber and other commonly used poppet materials. The analysis is based on solubility parameter theory that is based on principles derived from thermodynamic considerations. The results of this analysis predict that highly polar compounds, such as phospholipids or proteins, should not be present in silicone rubber poppets, which is in agreement with observations.

Introduction

Most prosthetic heart valves currently implanted consist of a silicone rubber poppet situated within a metallic cage. Recently, reports have indicated that gradual deterioration of the poppet can occur and lead to serious valve malfunction (References 1–6). Physical changes (variance) observed in prostheses recovered at autopsy or surgery include discoloration, swelling, and cracking; these may be accompanied by alterations in resiliency and specific gravity (References 1, 2, 4, 7, and 8).

A major cause of variance is believed to be lipid accumulation. Several laboratories have reported that all blood lipids are found in implanted valves, and occur in roughly the proportions usually found in human plasma (References 3, 6, 9, and 10). In our recent studies, however, no phospholipids or lipoproteins were found in any of the silicone poppets that were assayed, while the other lipids occurred in widely varying

proportions (Reference 11). These results strongly suggested that lipid infiltration is selective and that it may be influenced by the poppet material.

This article deals with an assessment of the solubility of lipids in silicone rubber and other commonly used poppet materials. The analysis is based on solubility parameter theory that is based on principles derived from thermodynamic considerations. The results of this analysis predict that highly polar compounds, such as phospholipids or proteins, should not be present in silicone rubber poppets, in agreement with observations.

Solubility Parameters for Poppet Materials and Lipids

In general, solubility, or miscibility, of two substances is to be expected if there is a decrease in the free energy of mixing, viz.,

$$\Delta F_{mix} = \Delta H_{mix} - T\Delta S_{mix}$$

Inasmuch as the entropy of mixing ΔS_{mix} is always positive (i.e., $-T\Delta S_{mix} < 0$), the enthalpy of mixing ΔH_{mix} will virtually determine solubility. The latter term for non-polar substances is positive and its magnitude is proportional to the difference of the respective solubility parameters δ (i.e., square root of the cohesive energy density):

$$\Delta H_{mix} \sim (\delta_1 - \delta_2)^2$$

Thus, the closer the solubility parameter values, the smaller the ΔH_{mix} will be and, consequently, the greater the decrease in ΔF_{mix} (References 12 and 13). For polar substances and those with strong tendency for hydrogen bonding, the definitions are somewhat tenuous. However, semi-empirical correlations are possible nevertheless. It follows from the above considerations that a lipid will dissolve in the poppet polymer material if the respective values are close to each other. Equal δ values, of course, will favor solubility most. However, mutual miscibility will exist for a range of values in the vicinity of the polymer solubility parameter δ_p. This range will depend in general on the particular polymer, but as a rule of thumb solubility will be likely for lipids whose solubility parameters δ_l are in the range $\delta_l = \delta_p \pm 2$. Inasmuch as the solubility parameter is a measure of intermolecular forces, it defines a number of molecular characteristics besides solubility. Consequently, there are a variety of methods to determine its value. Heats of vaporization data are commonly used for compounds which can be volatilized, whereas for polymers δ is usually determined indirectly from swelling measurements. For this work, literature data were used when available (Reference 14). However, for lipids such information could not be found. For these, estimates were made using semi-empirical correlations between the solubility parameter and refractive index (Reference 15).

Table 1 shows δ values for silicone rubber and other polymeric materials that are being used for valve poppets, whereas Table 2 shows values for a variety of lipids.

Table 1. Solubility parameters for poppet materials (References 14 and 16)

Material	Repeat unit	Density, g/cm³	(calories/cm³)$^{1/2}$
Poly(tetrafluoroethylene)	$-CF_2-CF_2-$	2.3–2.4	6.2
Poly(dimethylsiloxane)	$-\overset{\displaystyle CH_3}{\underset{\displaystyle CH_3}{\overset{|}{Si}}}-O-$	1.13	7.3–7.6
Poly(ethylene), high density	$-CH_2-CH_2-$	0.99	7.9–8.4
Poly(propylene)	$-\overset{\displaystyle CH_3}{\overset{|}{CH}}-CH_2-$	0.90–0.94	8.2
Poly(ethylene terephthalate)	$-\overset{\displaystyle C_6H_4-COO-}{\overset{|}{COOCH_2CH_2-}}$	1.46	9.7–10.7
Poly(methyltrifluoropropylsiloxane)	$-\overset{\displaystyle CH_3}{\underset{\displaystyle C_2H_4CF_3}{\overset{|}{Si}}}-O-$	1.4	8.5–11.0
Poly(formaldehyde), crystalline	$-CH_2-O-$	1.50	10.2–11.0

Discussion and Analysis

Most of the available information on the effect of blood on valve materials pertains to poly(dimethylsiloxane) elastomer, because most valves currently implanted have poppets made from this material. This elastomer contains about 20% silica filler. However, the powder, being crystalline and dispersed in the elastomer matrix, is very impermeable and is rather inaccessible to blood constituents. Thus, lipid uptake must be controlled by the properties of the elastomeric matrix, which has a solubility parameter δ of about 7.5.

Examination of Table 2 shows that δ values for lipids fall in two groups: for the weakly polar lipids, such as cholesteryl esters, triglycerides, and cholesterol, δ is about 9; whereas for the more polar phospholipids, δ is in excess of 16. Likewise, solubility parameters for proteins are again high, i.e., $\delta > 18$. It is apparent that δ for the first group is less than 2 units from that for the silicone elastomer and, consequently, well within the range necessary for miscibility. On the other hand, both phospholipids

Table 2. Solubility parameters of possible blood lipids estimated from refractive index data (Reference 15)

Lipids	$(\text{calories/cm}^3)^{1/2}$
Cholesterol and esters:	
Cholesteryl palmitate	8.4
Cholesteryl oleate	8.4
Cholesteryl stearate	8.4
Cholesterol	8.9
Triglycerides, α-glycerol ether esters and fatty acids (tripalmitin, tristearin, selachyl dioleate, oleic acid, stearic acid)	8.0 to 8.3
Lipid soluble vitamins	8.6 to 10.9
Hydrocarbon lipids (isoprene based and related alcohols)	8.2 to 8.5
Lipid bases (phosphorous and nitrogenous materials)	>16
Proteins	>18
Water	23

and proteins are far outside this range and therefore are insoluble. These considerations provide a straightforward explanation for our observations on recovered silicone rubber valve poppets (Reference 11), which showed the presence of the first group of lipids and absence of both phospholipids and proteins in poppets after implantation.

It has been reported that the extent of the vulcanization procedure affects lipid uptake (Reference 9). Vulcanization should not have a significant effect on δ, whereas it may greatly affect the crosslink density and the sol fraction, i.e., amount of soluble silicone. For given δ, the maximum (i.e., equilibrium) extent of swelling depends on these two factors (Reference 17). In general, a decrease in crosslink density and increase in sol content (both likely consequences of insufficient vulcanization) will increase the tendency to swell, or, in other words, favor lipid uptake. A similar effect may result from chemical degradation caused by excessive heating during vulcanization.

There is little information on variance in poppets made from other materials. We have examined recently two poly(formaldehyde) poppets which were implanted for rather short times. The results are preliminary but it was interesting to note that even though there appeared to be little foreign matter, some organic phosphorus was detected in one of the poppets. The δ value of near 11 for poly(formaldehyde) makes this result plausible, but it is still sufficiently far from 16, the value for phospholipids, to expect significant infiltration.

For the fluorosilicone elastomer we were able to arrive only at a range for δ. Calculations gave a low value, whereas solubility experiments (Reference 18) favor higher values. The higher value also seems to support the much lower lipid uptake for this elastomer as compared to silicone (Reference 9). Fluorosilicones would therefore appear to be promising. But their undesirably high density precludes their use in conventional configurations because for proper functioning the overall poppet density must approximate that of blood. Fluorocarbons have low δ, and their density is very high. Hydrocarbons such as poly(ethylene) and poly(propylene) do not have a favorable δ. However, their density is acceptable, and the highly crystalline forms of these polymers should be more impervious to lipids than silicone.

The presence of certain lipids and the absence of phospholipids and protein from silicone elastomer poppets is thus explained from considerations of solubility properties. However, the mechanism by which these lipids reach and infiltrate the poppet remains unknown. Lipids are present in plasma as spherical lipoprotein complexes that vary in size from a few hundred to perhaps 5000 Å and contain from about 1 to as much as 50% protein. The physico–chemical properties of lipoproteins appear to be dominated by the protein moiety, which suggests that their surface must be covered by protein. When the protein content is insufficient to form a monomolecular surface layer, it is believed that then the surface consists of a mixed protein-phospholipid layer, the latter being oriented with their charged groups at the surface (see, for example, References 19 and 20).

The silicone surface, like any foreign body in contact with blood, becomes covered with a protein layer. Inasmuch as lipid components exhibit considerable equilibration and exchange among the different lipoprotein classes (Reference 20), it is likely that they would behave similarly with respect to the protein layer on the silicone. Once on the surface, their solubility, which is higher in silicone than in plasma, will provide the necessary driving potential for permeation into the elastomer.

The importance of the blood flow to lipid uptake is suggested by the fact that most known cases of poppet variance are for the aortic valve; the blood flow velocity through this valve is the highest. The importance of the flow profile to the rate of collision with a surface has been analyzed in detail for the case of platelet deposition (Reference 21). Also, high shear forces would tend to deform lipoproteins and consequently increase the surface area, with the possible destruction of the continuity of the protein layer, thus favoring lipid deposition upon collision with the polymer surface. The fact that *in vitro* tests using lipid mixtures could not duplicate the extent of *in vivo* uptake (Reference 6) suggests that surface wetting by proteins and/or phospholipids is necessary for spreading of lipids at the surface. The importance of spreading at the surface could

be tested by studying *in vitro* the effect of various emulsifying and emulsion-breaking agents on lipid uptake.

Acknowledgment

The authors thank R. F. Landel and J. D. Ingham, JPL, for their comments and suggestions regarding this study.

References

1. Starr, A., Pierie, W. R., Raible, D. A., Edwards, M. L., Siposs, G. G., and Hancock, W. D., *Circulation,* Vol. 33, Supplement I, p. I-115, 1966.
2. Laforet, E. G., *New Eng. J. Med.*, Vol. 276, p. 1025, 1967.
3. Pierie, W. R., Hancock, W. D., Koorajian, S., and Starr, A., *Ann. N. Y. Acad. Sci.*, Vol. 146, p. 345, 1968.
4. Roberts, W. C., and Morrow, A. G., *Am. J. Cardiol.*, Vol. 22, p. 614, 1968.
5. Lee, S. J. K., Zaragoza, A. J., Callaghan, J. C., Couves, C. M., and Sterns, L. P., *Circulation,* Vol. 41, p. 479, 1970.
6. McHenry, M. M., Smeloff, E. A., Fong, W. Y., Miller, G. E., Jr., and Ryan, P. M., *J. Thorac. Cardiovasc. Surg.*, Vol. 59, p. 413, 1970.
7. Bonnabeau, R. C., and Lillehei, C. W., *J. Thorac. Cardiovasc. Surg.*, Vol. 56, p. 258, 1968.
8. Hameed, K., Ashfaq, S., and Waugh, D. O. W., *Arch. Pathol.*, Vol. 86, p. 520, 1968.
9. Carmen, R., and Kahn, P., *J. Assoc. Adv. Med. Instr.*, Vol. 314, p. 14, 1969.
10. Noiret, R., Penther, P., Bensaid, J., Beaumont, J. L., and Lenegre, J., *J. Athero. Res.*, Vol. 8, p. 975, 1968.
11. Chin, H. P., Harrison, E. C., Blankenhorn, D. H., and Moacanin, J., *Circulation,* Vol. 43, Supplement I, p. I-51, May 1971.
12. Hildebrand, J. H., and Scott, R. L., *The Solubility of Nonelectrolytes,* 3rd Edition. Reinhold Publishing Co., New York, 1950.
13. Gardon, J. L., "Cohesive Energy Density," in *Encyclopedia of Polymer Science and Technology,* Vol. 3, p. 844. Interscience Publishers, Inc., John Wiley & Sons, Inc., New York, 1965.
14. Burrell, H., and Immergut, B., "Solubility Parameter Values," in *Polymer Handbook.* Edited by J. Brandrup and E. H. Immergut. Interscience Publishers, Inc., John Wiley & Sons, Inc., New York, 1966.

References (contd)

15. Lawson, D. D., and Ingham, J., *Nature*, Vol. 223, p. 614, 1969.

16. Lewis, O. G., *Physical Constants of Linear Homopolymers*. Springer-Verlag, New York, 1968.

17. Flory, P. J., *Principles of Polymer Chemistry*, Chapter XIII. Cornell University Press, Ithaca, N. Y., 1953.

18. Lewis, F. M., *Rubber Chem. Technol.*, Vol. 35, p. 1222, 1962.

19. Hashim, S. A., Felch, W. C., and Van Itallie, T. B., "Lipid Metabolism," in *Handbook of Physiology, Circulation*, Chapter 34. Edited by W. F. Hamilton and P. Dow. American Physiological Society, Washington, D. C., 1963.

20. Cornwell, D. G., "Lipoproteins," in *Lipids and Lipidoses*, pp. 168–189. Edited by G. Schettler. Springer-Verlag, New York, 1967.

21. Friedman, L. I., Liem, H., Grakowski, E. F., Leonare, E. F., and McCord, C. W., *Trans. Am. Soc. Arti. Int. Org.*, Vol. 16, p. 63, 1970.

Resequencing of the Structural Stiffness Matrix to Improve Computational Efficiency

R. Levy

Telecommunications Division

Improved computational efficiency and reduction in core storage requirements in large-capacity structural-analysis computer programs are achieved by taking advantage of the typical sparseness in the stiffness matrix. In many cases, the favorable effects can be enhanced by resequencing the interconnecting terms of the stiffness matrix. This produces a relatively large empty region that can be bypassed and a relatively small, compact region that is moved into the core for computations.

In the past, the goal of resequencing has been to minimize the stiffness matrix bandwidth. A favorable alternative resequencing procedure that has the goal of reducing the matrix wavefront is described in this article. Comparisons are supplied to show the relative compactness that can be achieved for practical structural models with wavefront sequencing and with bandwidth sequencing. Examples show that wavefront sequencing can produce a savings in the time required for subsequent decomposition of the stiffness matrix.

Introduction

Conventional finite-element analysis of structures is typically implemented by any of the several currently available computer program packages that perform matrix interpretive analysis. When the structure to be analyzed entails many degrees of freedom, it becomes important to develop the analytical model to fit efficiently within the computer program capacity and to avoid excessive computation time for processing. Ground-based radar antenna structures in the 26-m and larger classes are practical examples from a wide range of structures that contain 1000 or more degrees of freedom for which judicious modeling can provide substantial computational benefits.

Large-capacity computer programs for structural analysis operate most efficiently when the computational procedure is formulated to capitalize on the typical sparseness of the structural stiffness matrix. Sparseness is

used to advantage by confining the computational operations to a compact region densely populated with non-zero coefficients and by omitting operations for the empty region in which the coefficients are zero. Consequently, it is often desirable to reorder a given stiffness matrix to make the region for computations as compact as possible and to make the empty region as large as possible. Traditionally, the compactness of the stiffness matrix has been measured by the matrix bandwidth, but an apparently more efficient equation-solving approach has been formulated to perform the computations within the region delineated by the matrix wavefront (Reference 1). The wavefront approach is attractive because the maximum wavefront is often considerably less than the maximum bandwidth, and it can never be greater.

The purpose of resequencing for an analytical model of a particular structure is to minimize the number of degrees of freedom that determine the maximum of the bandwidth or the wavefront of the stiffness matrix. Frequently, the number of degrees of freedom per node is approximately the same for all nodes. Therefore, it is reasonable to perform resequencing on the basis of the nodes and nodal connectivity, which is considerably simpler than resequencing on the basis of degrees of freedom and stiffness matrix connectivity. Algorithms of Rosen (Reference 2), Akyuz and Utku (Reference 3), and Cuthill and McKee (Reference 4) were designed to reorder nodes for bandwidth reduction. An algorithm to be described here has been found effective for wavefront reduction. A recent independent development by King (Reference 5), although described differently, appears to be related to the present method.

Resequencing procedures, either for bandwidth or wavefront reduction, do not ensure achievement of the optimal sequence. Results could be considered acceptable if there is an improvement from an initial sequencing in a local optimum sense, rather than convergence to an absolute minimum in a global sense. For this reason, it is sometimes useful to perform resequencing several times, with each cycle starting from a different initial sequence. This provides the opportunity to select the most favorable of the several local minimums that will be developed from the various cycles.

Wavefront Counting

The wavefront at a row of the nodal connectivity matrix is the number of active columns that follow the diagonal element; a column becomes active at the row containing the first entry for that column, and it remains active until that column is absorbed into the diagonal of the connectivity matrix. As shown in Figure 1, wavefront counting is accomplished by drawing heavy vertical lines for each column, beginning at the row at which the column becomes active and ending at the diagonal. To obtain the wavefront at each row, it is necessary only to count the heavy lines crossing each row.

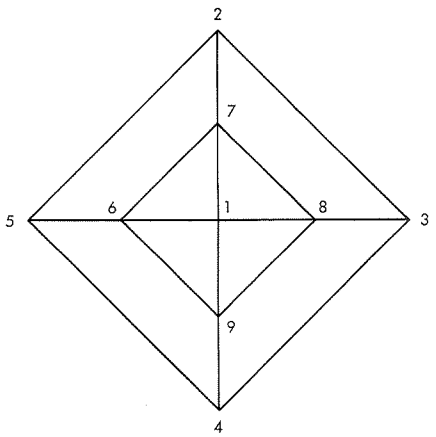

(a) EXAMPLE STRUCTURE

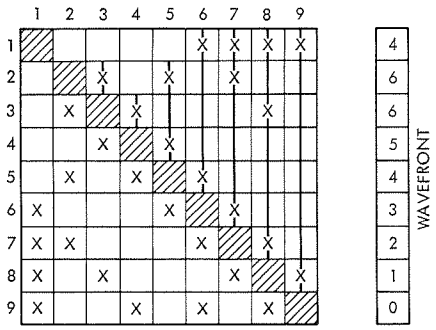

(b) NODAL CONNECTIVITY MATRIX

Figure 1. Wavefront counting example

Alternatively, the wavefront at any row can be computed as equal to the wavefront at the preceding row, plus the number of new columns that become active. If the column corresponding to the row is currently in the wavefront, then the wavefront is reduced by one. The subtraction is made to account for columns that leave the wavefront by virtue of reaching the diagonal. This method of wavefront counting is explained for the rows of Figure 1a as follows:

Row 1: The wavefront is 4, because columns 6–9 become active at this row and the wavefront at the non-existent preceding row is defined to be 0.

Row 2: Columns 3 and 5 become active; therefore, the wavefront is $2 + 4 = 6$.

Row 3: Column 4 is added to the active list; because Column 3 was in the wavefront, 1 is subtracted. Therefore, the wavefront is $6 + 1 - 1 = 6$.

Rows 4–9: All columns have been activated (matrix has filled), and no new columns can enter the wavefront. Therefore, at each row 1 is subtracted from the preceding wavefront, since one column always reaches the diagonal and leaves the wavefront.

The isolated column to the right of the connectivity matrix in Figure 1b gives the wavefront at the row. The maximum wavefront is 6, which occurs at both the second and third rows. It will be shown that this can be reduced by resequencing.

Wavefront Sequencing

A resequencing approach that is recommended here for its conceptual simplicity can be called a "minimum growth" method. That is, assuming that resequencing has already been used to identify the nodes that will constitute the new first i nodes, the node to be selected as the new $(i + 1)$th node is the one for which the wavefront at the $(i + 1)$th node will represent the smallest increase with respect to the wavefront at the ith node. In accordance with the alternative method just described for wavefront counting, the increase can be a positive integer, zero, or negative unity. Very often, any one of several nodes will give the same minimum wavefront increase for the $(i + 1)$th node, and, when this happens, the first node encountered is chosen. This tends to make the new sequencing as close as possible to the original. The question remains, of course, as to how to choose the node to be first in the new sequence. The choice could be based upon one of the following alternatives:

(1) Choose the node that will give the minimum wavefront for the first row. This is equivalent to choosing the node with the minimum number of connections. Break ties by picking the first node encountered.

(2) When the connectivity matrix involves n nodes, perform resequencing n times, picking each node in turn to be the first. At the end, select the most favorable of the n sets of resequences. This method is feasible if the number of nodes is not excessive.

(3) Perform resequencing k (where $k \leq n$) times. Each time, pick at random the node that is to be first. This procedure is suggested if n is very large; nevertheless, more than one cycle of resequencing should be tested for possible improvements.

(4) Assign one particular node to be the first in accordance with prior inspection and reasoning.

The resequencing operations can be conveniently organized in a tableau format for manual execution. This format employs the original nodal connectivity matrix and a new table listing the change in wavefront for each possible selection of the next node to be placed in the new

sequence. Tableau resequencing will be demonstrated for the structure of Figure 1. Figure 2 shows the progressive changes (heavy lines) in the combined tableau as each next node is selected to be placed within the new sequence. For clarity, the figure is subdivided into the stages associated with selecting one successively ascending node at a time. The general procedure that is employed repetitively for selection of the successive nodes is described below.

Wavefront Change Table Operations for Figure 2

Step 1: Enter the number of the new node that is about to be selected in the new sequence heading list.

Step 2: Count the number of new connections at each row. This is equal to the sum of the entries in the connectivity matrix that do not occur at columns already in the wavefront. The columns that are in the wavefront are identified by vertical lines previously drawn through these columns. The change in wavefront at each row is the sum of the new connections. The change is reduced by one if the row is already in the wavefront. Enter the change in wavefront in the column of the node to be selected and opposite the associated row.

Step 3: Select the smallest change in wavefront from the column of wavefront changes (first occurrence in case of ties). Circle the row entry and draw a horizontal line across the wavefront change table. This is the new row to be placed in the sequence. Add the wavefront change to the preceding wavefront and enter the value at the space provided at the bottom of the table.

Connectivity Matrix Operations for Figure 2

Step 1: Strike the column of the node just selected (a double line used in Figure 2). Enter the new sequence number at the bottom of this column in the space provided.

Step 2: Strike the row of the node just selected.

Step 3: Strike all unstruck columns that have connections in this row.

Additional Notes on Figure 2

Stage 1: The first node is selected with the objective of minimum wavefront in the first row of the new sequence. Original node 2 is the first one encountered with the minimum number of 3 connections. Original node 2 becomes the new first node, the wavefront at the new first row of the connectivity matrix is 3, and columns 3, 5, and 7 of the connectivity matrix become activated.

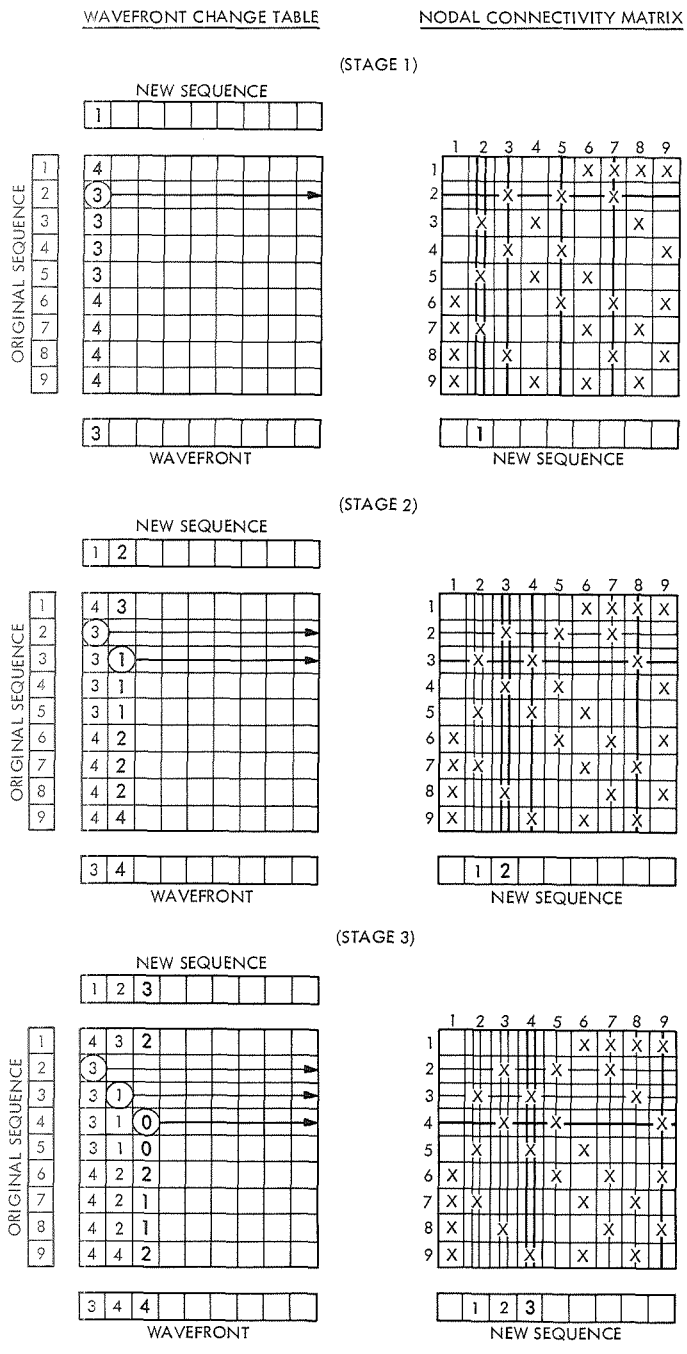

Figure 2. Tableau resequencing example

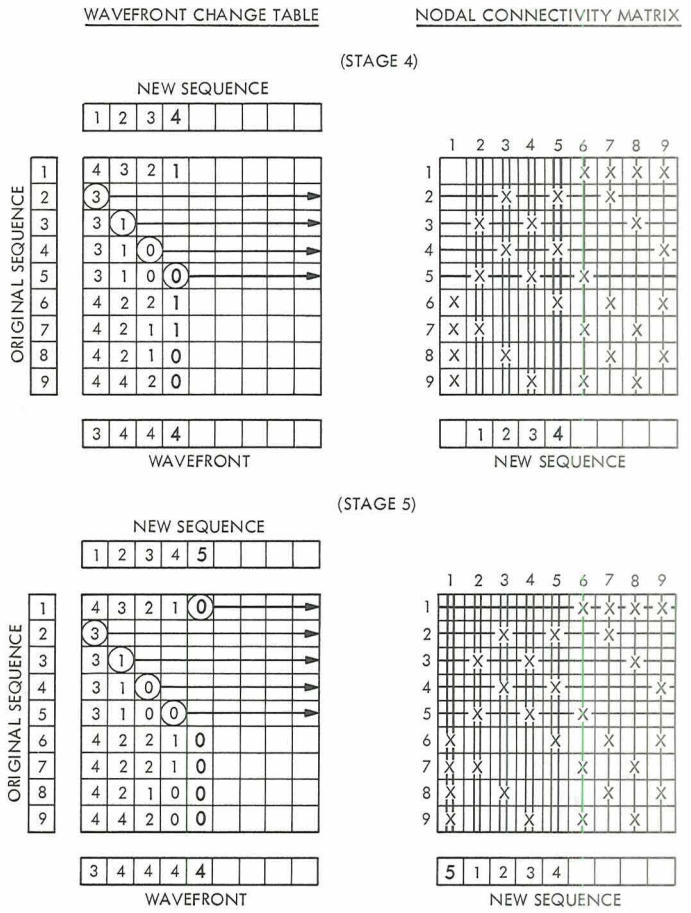

Figure 2 (contd)

Stage 2: Original node 3 causes columns 4 and 8 to become activated, but node 3 has been activated previously; thus, the net increase in wavefront is only one. Original node 3 becomes the new second node. Columns 4 and 8 are added to the active list, and column 3 leaves the wavefront.

Stage 3: Original node 4 activates column 9, but there is no net increase in wavefront because column 4 was in the wavefront. Original node 4 becomes the new third node, and column 4 leaves the wavefront.

Stage 4: Original node 5 activates column 6, but there is no net increase in wavefront because column 5 was in the wavefront. Original node 5 becomes the new fourth node, and column 5 leaves the wavefront.

Stage 5: Original node 1 does not activate any additional columns, but there is no net decrease in wavefront because column 1 was not on the active list. Original node 1 becomes the new fifth node.

At the completion of stage 5, there are no remaining columns to be activated, and the wavefront has filled the connectivity matrix. The remaining nodes can be added to the new sequence in arbitrary order, and the wavefront will decrease by unity at each successive stage.

Results and Conclusions

Tableau resequencing can be performed without difficulty for matrices with orders of 20 to 30. When the order becomes much larger, the tableau becomes cumbersome, and it is advisable to perform resequencing by computer. A program has been written to automate the procedure by performing essentially the same operations as those for executing the tableau. The largest model for which the program has been used to date has a connectivity matrix with over 500 nodes. In one test of the program for this model, the initial sequencing was developed by inspection and study of the connectivity. The maximum wavefront was 43. One resequencing computer cycle reduced the initial maximum wavefront to 30. In another test, the initial sequencing was scrambled at random, which produced a maximum wavefront of 92. One computer cycle reduced this to 40. As the result of six additional computer cycles, the maximum wavefront was reduced to 27; in these, the starting node for each cycle was chosen at random.

On the UNIVAC 1108 Exec-8 computer, the computation time for this structure averaged about 15 s/cycle. For a structure with 75 nodes, the program averaged more than 2 cycles/s. The computation time per cycle varies considerably, depending upon how quickly the connectivity matrix fills or upon the number of nodes processed before it can be determined that the current cycle is to be aborted because there will be no reduction of an existing maximum wavefront.

Table 1 shows some additional comparisons for resequencing tests to reduce either bandwidth or wavefront. These tests were performed for

Table 1. Effects of resequencing on bandwidth and wavefront[a]

Component type	Nodes	Initial size		Size after resequencing	
		Bandwidth	Wavefront	Bandwidth	Wavefront
Antenna pedestal	56	40	20	23	11
Quadripod	66	41	18	16	8
Coarse grid reflector	83	73	30	24	12
Azimuth–elevation reflector	466	200	52	75	29
Polar reflector	506	—	92	—	28

[a]Bandwidth sequencing method described in Reference 2; wavefront sequencing method described in this article.

the analytical models of structural components used on ground-based radar antenna systems. The table shows that, after sequencing, the wavefront tends to be less than half of the bandwidth, which can provide definite computational advantages in subsequent analysis. The savings in computation time depends to some extent on the type of analytical problem to be solved and the efficiency of the approach used to process the stiffness matrices. For statics problems, comparisons have shown that about 20% savings in stiffness matrix decomposition time could be achieved by using wavefront sequencing instead of bandwidth sequencing. In eigenvalue problems, the possible savings appears to be considerably greater. Table 2 shows a few cases from Table 1 where the comparable decomposition times were available for both types of sequencing.

Table 2. Stiffness matrix decomposition times

Component type	Problem type	Decomposition time, s	
		Bandwidth sequencing	Wavefront sequencing
Coarse grid reflector	Statics	10.4	7.5
Azimuth–elevation reflector	Statics	260.1	215.2
	Eigenvalue	3604.5	635.4

The experience with the computer program indicates that minimum growth sequencing is effective, rapid, and capable of producing worthwhile economies. The savings occurs in the reduction or elimination of lengthy effort to study a particular structural model for the purpose of generating an acceptable sequencing pattern, as well as in the reduction of computation time as the result of processing a relatively compact stiffness matrix.

References

1. Melosh, R. J., and Bamford, R. M., "Efficient Solution of Load-Deflection Equations," *J. Struct. Div., Proc. ASCE*, Vol. 95, No. ST4, pp. 661–676, Apr. 1969.
2. Rosen, R., "Matrix Bandwidth Minimization," *Proceedings of the 23rd National Conference of the ACM*, p. 585. Brandon/Systems Press, Inc., New Jersey, 1968.
3. Akyuz, F. A., and Utku, S., "An Automatic Node-Relabeling Scheme For Bandwidth Minimization of Stiffness Matrices," *AIAA J.*, Vol. 6, No. 4, pp. 728–730, Apr. 1968.
4. Cuthill, E., and McKee, S., *Reducing the Bandwidth of Sparse Symmetric Matrices,* Applied Mathematics Laboratory Technical Note

References (contd)

AML-40-69. Naval Ship Research and Development Center, Washington, D.C., June 1969.

5. King, I. R., "An Automatic Reordering Scheme For Simultaneous Equations Derived From Network Systems," *Int. J. Numer. Meth. Eng.*, Vol. 2, pp. 523–533, 1970.

On the Statistical Distribution of Spacecraft Maximum Structural Response

J.-N. Yang

Engineering Mechanics Division

In most aerospace engineering applications, the finite number of flight data accumulated in the past is not sufficient to characterize nonstationary random excitations resulting from each flight event, such as booster engine ignition or burnout. In this article, a direct statistical analysis of spacecraft maximum structural response is performed and the spacecraft structural reliability is obtained. It is found that the Gumbel Type I asymptotic distribution of maximum values provides a reasonably good statistical model for spacecraft maximum structural responses. The current approach makes it possible to perform the reliability-based optimum design of spacecraft structures.

Introduction

Flight data taken on a number of past flights indicate that major spacecraft excitations and responses resulting from booster engine ignition or booster engine shutdown are nonstationary random processes (e.g., References 1 and 2). These excitations not only are highly transient but may also produce some of the most severe spacecraft vibrations in the entire mission. A typical example taken from Reference 2 is given in Figure 1 in which three sample functions of nonstationary random processes applied at the base of the launch vehicle are given. In Figure 1, two random forcing processes resulting from two booster engines have been converted into a resultant thrust process $F(t)$ and a bending moment process $M(t)$.

For the reliability prediction and the design of spacecraft structures, the rigorous random vibration approach, unfortunately, suffers from a number of difficulties as follows:

(1) The number of sample functions accumulated from past flights for the same type of booster engine is not sufficient for the statistical characterizations of $F(t)$ and $M(t)$, as well as their correlations. Thus far, 27 samples are available.

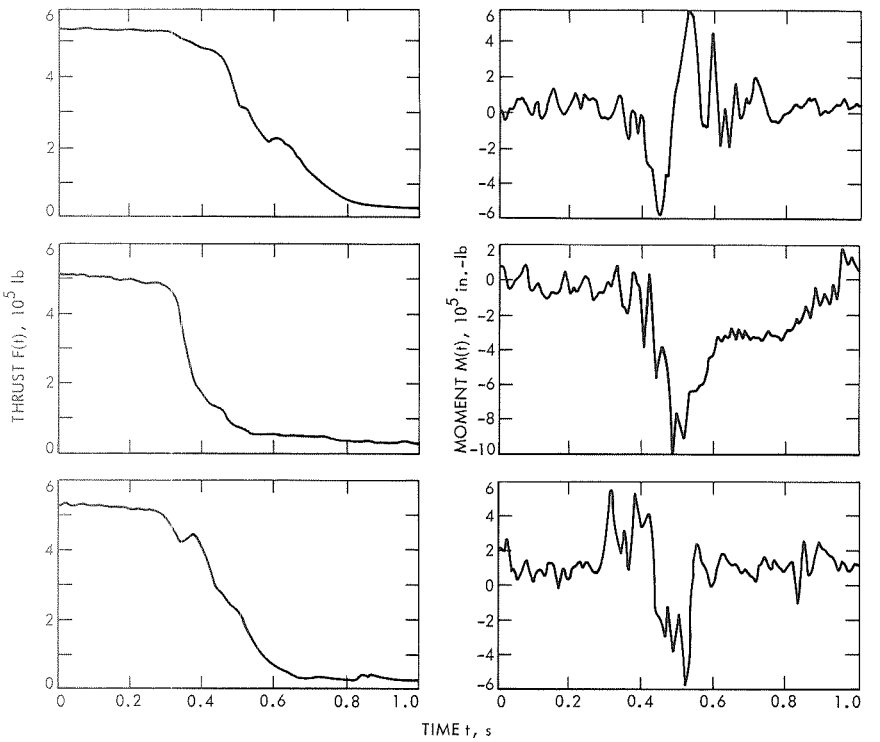

Figure 1. Typical sample function of nonstationary random excitation (from Reference 2)

(2) Because of the complexity of the entire space vehicle structure and the excessive computational cost involved, the redesign of the spacecraft structure is usually made separately from the vehicle, using the resulting six random acceleration processes, $g_i(t), i = 1,2,\cdots,6$, at the spacecraft/boost vehicle (S/BV) interface as input excitations for approximation (Reference 1). Therefore, even if the number of samples is sufficient to characterize random excitations $F(t)$ and $M(t)$, the computer storage space required for all the digitized data of covariance functions $K_{g_i g_j}(t_1, t_2)$, or generalized spectra $S_{g_i g_j}(\omega_1, \omega_2)$, of all the six random processes, $g_i(t)$, $i = 1,2,\cdots,6$, may easily exceed the computer capacity. Furthermore, the numerical operations involved in computing the statistics of responses and response derivatives, such as covariance functions, are quite involved. Preliminary investigation indicates that the cost of spacecraft redesign (many cycles of redesign) becomes intolerable when the rigorous random vibration approach is employed.

(3) The prediction of structural reliability or failure, such as the first excursion probability, under nonstationary random excitations is still in the primitive stage. Hence, the final reliability figure usually

involves two kinds of approximations: (a) the approximation of known random processes, such as gaussian processes, to the actual processes, and (b) the approximation made in estimating the reliability from the response statistics.

It is due to these theoretical, as well as practical, difficulties that other possible approaches appear to be highly desirable. In fact, some attempts have been made from the viewpoint of deterministic analysis. The premise of deterministic analysis approaches, so far, is to obtain an upper bound of the maximum response under a specified class of excitations. In this connection, the upper bound of the maximum structural response based on the excitation energy (Reference 3), the response envelope in the frequency domain analysis (References 1 and 4), and the response envelope in the time domain analysis (Reference 5) should be mentioned. Although the foregoing deterministic analyses provide useful information for structural design, there are two inherent discrepancies: (1) the upper bound obtained may be too high and there is no indication of how conservative it may be, and (2) the estimated upper bound is not associated with any probability statement. Since the excitations are random processes, the probability statement is important in design.

It has been realized that the source of randomness in excitations is due to the fact that the properties of rocket motors are associated with considerable statistical variation. Thus, a sample of a rocket motor generates a sample of random excitations which, in turn, produces a sample value of maximum response at certain points of the spacecraft. Hence, there is a one-to-one correspondence between the maximum spacecraft response and the property of the rocket motor. Since the underlying physical process describing how the ignition or shutdown of the random rocket motor is related to the random excitation processes is not clear, the assumption of certain types of nonstationary random processes, such as random processes obtained by passing a modulated short noise through a filter (Reference 1), is difficult to be justified. It, therefore, appears that a direct statistical analysis of the spacecraft maximum response may be a reasonable approach when 27 sample functions are available.

Statistical Analysis of Maximum Response

The advantages of the direct statistical analysis of spacecraft maximum responses can be summarized as follows: (1) the cost of analysis and redesign is within practical limitation, (2) the accuracy of the reliability estimate increases as the number of samples increase, and (3) it admits to a reliability-based optimum design of spacecraft structures.

Let the structural system of the space vehicle be characterized by a linear time invariant operator L, which relates the spacecraft stress

response vector $\mathbf{Y}(t)$, consisting of component $\mathbf{Y}_k(t)$, $k = 1,2,\cdots$, to the excitation vector process $\mathbf{X}(t)$ through the following equation:

$$L[\mathbf{Y}(t)] = \mathbf{X}(t) \tag{1}$$

where $\mathbf{X}(t)$ consists of the thrust process $F(t)$ and the bending moment process $M(t)$ at the base of the launch vehicle, i.e.,

$$\mathbf{X}(t) = [F(t)\ M(t)]'$$

When the redesign of spacecraft structures is separated from the space vehicle, L represents the spacecraft characteristics and

$$\mathbf{X}(t) = [g_1(t)\ g_2(t) \cdots g_6(t)]'$$

is the acceleration vector process at the S/BV interface.

The stress response vector $\mathbf{Y}(t)$ can be written as

$$\mathbf{Y}(t) = \int_0^t \mathbf{h}(t - \tau)\,\mathbf{X}(\tau)\,d\tau \tag{2}$$

or

$$\mathbf{Y}(t) = \frac{1}{2\pi}\int_{-\infty}^{\infty} \mathbf{H}(\omega)\mathbf{X}(\omega)e^{-i\omega t}d\omega \tag{3}$$

in which $\mathbf{h}(t)$ and $\mathbf{H}(\omega)$ are, respectively, the impulse response matrix and the frequency response matrix or transfer matrix. Both $\mathbf{h}(t)$ and $\mathbf{H}(\omega)$ are Fourier transform pairs, and they are functions of natural frequencies, modes, generalized masses, and dampings of the structure (e.g., Reference 1). $\mathbf{X}(\omega)$ is the Fourier transform of $\mathbf{X}(t)$. The solution of Equation 2 is referred to as the time domain analysis, while the solution of Equation 3 is referred to as the frequency domain analysis.

Let $\mathbf{X}^j(t)$, $\mathbf{X}^j(\omega)$, and $\mathbf{Y}_k^j(t)$ represent the jth samples of $\mathbf{X}(t)$, $\mathbf{X}(\omega)$, and $\mathbf{Y}_k(t)$, respectively, where $\mathbf{Y}_k(t)$ is the spacecraft stress response at point k. The absolute maximum, $\mathbf{Z}$, of $\mathbf{Y}_k(t)$ for $t \geq 0$ is a random variable whose jth sample value $\mathbf{Z}_j$ follows from Equations 2 and 3 as

$$\mathbf{Z}_j = \max_t \left| \mathbf{Y}_k^j(t) \right| = \max_t \left| \int_0^t \mathbf{h}_k(t - \tau)\mathbf{X}^j(\tau)\,d\tau \right| \tag{4a}$$

$$= \frac{1}{2\pi} \max_t \left| \int_{-\infty}^{\infty} \mathbf{H}_k(\omega)\mathbf{X}^j(\omega)e^{-i\omega t}\,d\omega \right| \tag{4b}$$

where $\mathbf{H}_k(\omega)$ and $\mathbf{h}_k(t)$ are the kth row of $\mathbf{H}(\omega)$ and $\mathbf{h}(t)$, respectively.

Then, rearrange $\mathbf{Z}_j$, $j = 1,2, \cdots, 27$, in an ascending order such that $\mathbf{Z}_1 \leq \mathbf{Z}_2 \cdots \leq \mathbf{Z}_{27}$.

Some investigations (Reference 6) indicate that when the excitation $\mathbf{X}(t)$ is nonstationary gaussian, the distribution of the peaks or troughs within a time interval $[0,T]$ is approximately the Weibull distribution, which is a distribution of exponential type. Furthermore, large peaks or troughs, being of particular interest in design, are approximately independent; and if the number of peaks or troughs in the response history approaches infinity, the asymtotic distribution of the maximum response $\mathbf{Z}$ can be shown (References 6 and 7) to follow the Gumbel Type I asymptotic distribution of maximum values as follows:

$$F_{\mathbf{Z}}(x) = \Pr[\mathbf{Z} \leq x] = \exp\{-\exp[-\sigma(x - \mu)]\}$$
$$\sigma > 0, -\infty \leq x \leq \infty, -\infty \leq \mu \leq \infty \tag{5}$$

where $F_{\mathbf{Z}}(x)$ is the distribution function of the maximum stress response $\mathbf{Z}$, and σ and μ are distribution parameters.

If the samples $\mathbf{Z}_1, \mathbf{Z}_2, \cdots, \mathbf{Z}_{27}$ follow the distribution of Equation 5, they should be scattered around a straight line when plotted on Gumbel extreme-value probability paper. The empirical distribution function $F_m(Z_k)$ for the sample values $\mathbf{Z}_1, \mathbf{Z}_2, \cdots, \mathbf{Z}_{27}$ can be established as

$$F_m(Z_k) = (k - 0.5)/n \tag{6}$$

where n is the total number of samples and is equal to 27 herein.

The first quadrant of a preliminary design of a spacecraft is shown schematically in Figure 2 (four quadrants are symmetrical). Sample values of maximum stresses $\mathbf{Z}_1, \mathbf{Z}_2, \cdots, \mathbf{Z}_{27}$ in each structural member, due to 27 samples of excitation vector $\mathbf{X}(t)$ at the base of the launch vehicle during the stage 1 shutdown, are computed. These sample values are then plotted on both the Gumbel extreme-value probability paper and the cumulative probability paper; five of these typical plots are given in Figure 3. In Figure 3, members 1 and 2 are capsule members, members 3 and 4 are spacecraft members, and member 5 is a member supporting the fuel tank (see Figure 2). All the plots indicate that the Gumbel Type I asymptotic distribution of maximum values is a reasonably good model. Results of the Kolmogorov–Smirnov test (e.g., Reference 8) indicate that the hypothesis that the sample data of maximum stress responses in each member follow the distribution of Equation 5 can be accepted at least at the 20% level of significance.

Other distribution functions, such as normal, lognormal, Weibull, and gamma, etc., have been tried; it was found that the plots associated with

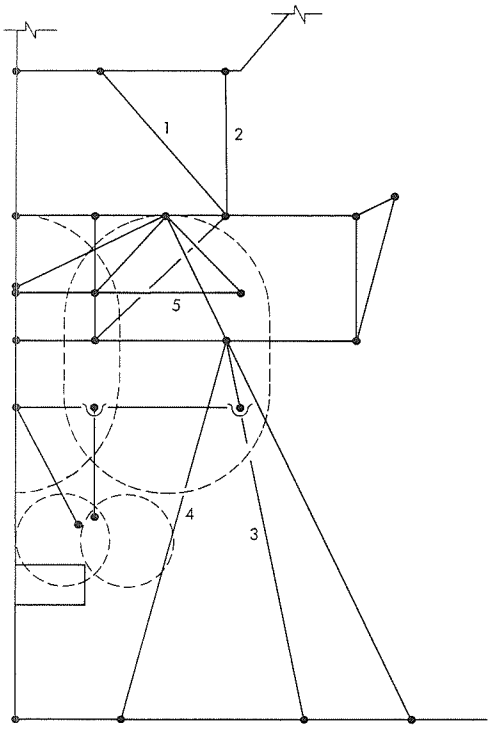

Figure 2. Schematic configuration of a spacecraft

these distributions exhibit a clear departure from linearity, and the associated Kolmogorov–Smirnov statistics are higher than those associated with the distribution of Equation 5. This is an indication that Equation 5 may be the best to fit the samples of maximum stress response. Indeed, the Gumbel Type I asymptotic distribution of maximum values (Equation 5) is a logical choice for the maximum response in approximation, although the conditions for the distribution that peaks are independent and that the number of peaks approaches infinity are not satisfied. In fact, some investigators (Reference 9) in earthquake engineering have shown that Equation 5 provides a reasonable statistical model for maximum structure response due to earthquakes, where the conditions for the distribution are clearly violated. Gumbel has also shown problems (Reference 7) where the distribution conditions are not satisfied but where the distribution of Equation 5 is a good model.

The probability of first excursion failure p_k of the kth structural member follows from Equation 5 as

$$p_k = \int_{-\infty}^{\infty} (1 - \exp\{-\exp[-\sigma_k(x - \mu_k)]\}) f_k(x)\, dx \qquad (7)$$

where $f_k(x)$ is the probability density of the ultimate strength of the kth member, and σ_k and μ_k are the associated distribution parameters which

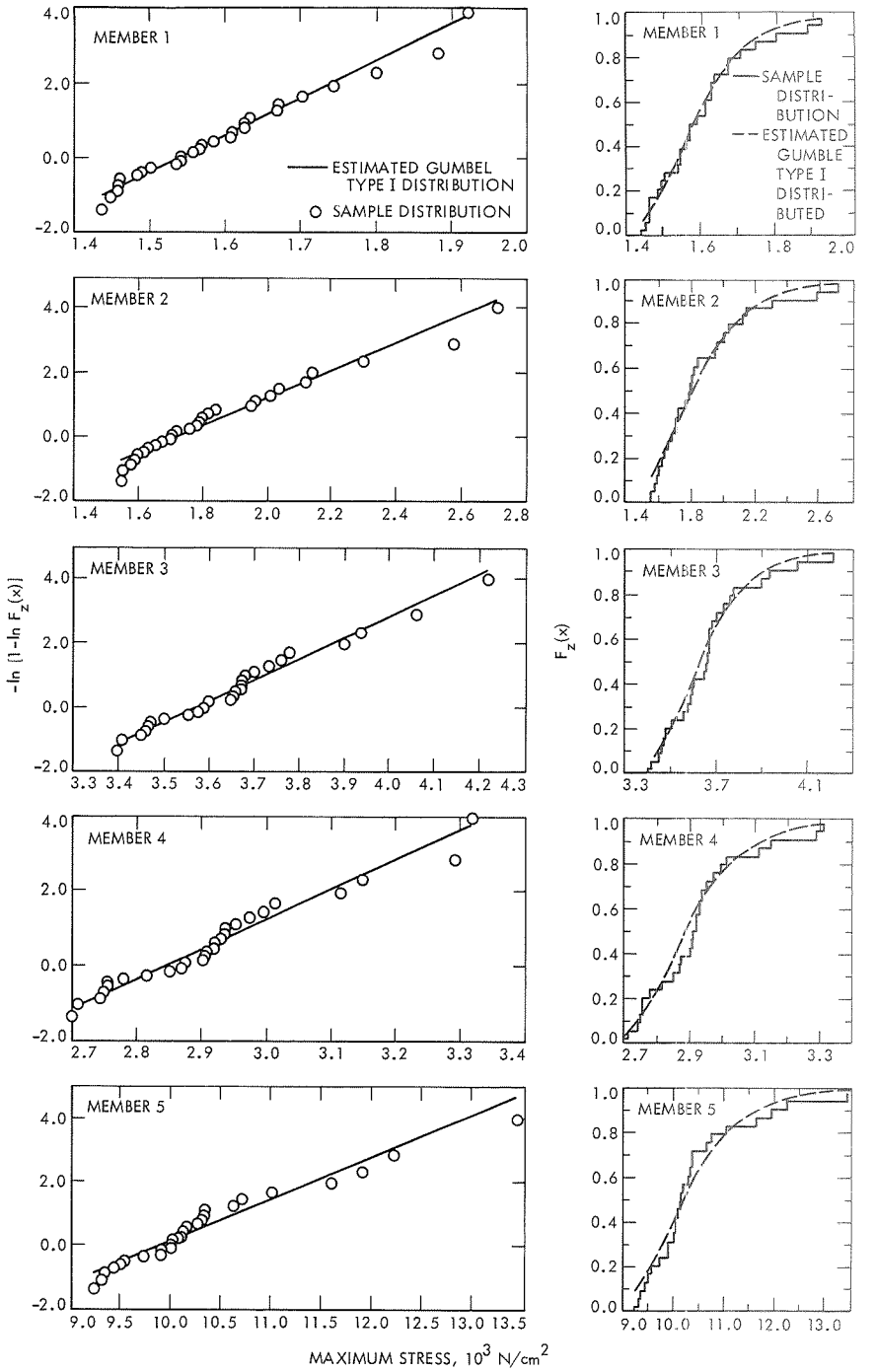

Figure 3. Distribution of maximum stress response

can easily be estimated from Figure 3. The material used for each structural member of the spacecraft (Figure 2) is aluminum with a mean ultimate strength of 20.68×10^3 N/cm^2. Results of this analysis indicate that the probability of failure of each member is negligibly small except member 5, which has a probability of failure 0.45×10^{-6}, when the statistical dispersion of the ultimate strength of aluminum is negligible.

It follows from Equation 4 that the computation of 27 samples of maximum stress response $\mathbf{Z}_j$, $j = 1,2, \cdots, 27$, for each structural member requires neither heavy computational effort nor excessive storage in computer. In fact, using the fast Fourier transform, $\mathbf{Z}_j$ can easily be computed (Equation 4b). Therefore, the cost involved in computing the structural reliability, Equation 7, as well as redesign of spacecraft structures, is within practical limitation.

While it is not difficult to compute structural reliability, one can proceed to perform the reliability-based optimum design of spacecraft structures (e.g., Reference 10), and minimize the structural weight subject to the constraint that the overall probability of failure of the spacecraft p_f should be less than certain value p_a. The feasibility of incorporating the notion of reliability in optimum design is another advantage of the current approach. It should be mentioned that much research work remains to be done before the rigorous nonstationary random vibration approach can be incorporated in optimum structural design.

Conclusion

Under nonstationary random excitations resulting from booster engine shutdown, a direct statistical analysis of spacecraft maximum responses is performed and the spacecraft structural reliability is obtained. It is found that the Gumbel Type I asymptotic distribution of maximum values provides a reasonably good statistical model for spacecraft maximum responses. The current approach makes it possible to perform the reliability-based optimum design of spacecraft structures.

Acknowledgment

The author gratefully acknowledges valuable information and discussions by B. K. Wada and J. Garba of the Jet Propulsion Laboratory.

References

1. Marx, M. H., et al., "Evaluation of Techniques for Estimating Titan III-C Flight Loads," paper presented at the AIAA 3rd Communication Satellite Systems Conference, Los Angeles, Calif., Apr. 6–8, 1970.

References (contd)

2. *Titan Launch Vehicle—Stage I Thrust Transient Data Book*, MCR-70-8. Martin Marietta Corp. Aerospace Group, Denver, Colo., Jan. 1970.

3. Drenick, R. F., "On the Model-Free Design of a Seismic Structure," *J. Eng. Mech. Div., Proc. ASCE,* Vol. 96, No. EM4, pp. 483–493, Aug. 1970.

4. Shinozuka, M., "Maximum Structural Response to Seismic Excitations," *J. Eng. Mech. Div., Proc. ASCE,* Vol. 96, No. EM5, pp. 729–738, Oct. 1970.

5. Yang, J.-N., and Heer, E., "On Maximum Dynamic Response and Proof Testing," Preprint 1372, presented at the ASCE Annual Meeting on Structural Engineering, Baltimore, Md., Apr. 19–23, 1971, to appear in *J. Eng. Mech. Div., Proc. ASCE,* Aug. 1971.

6. Shinozuka, M., and Yang, J.-N., "Peak Structural Response to Nonstationary Random Excitation," *Proceedings of the AIAA/ASME 12th Structural, Structural Dynamics and Materials Conference, Anaheim, Calif., Apr. 19–21, 1971.*

7. Gumbel, E. J., *Statistics of Extremes.* Columbia University Press, New York, 1958.

8. Lindgren, B. W., *Statistical Theory.* The Macmillan Company, New York, 1962.

9. Wirsching, P. H., and Yao, J. T. P., "Distribution of Response to Simulated Earthquakes," *J. Eng. Mech. Div., Proc. ASCE,* Vol. 96, No. EM4, pp. 515–519, Aug. 1970.

10. Heer, E., and Yang, J.-N., "Structural Optimization Based on Fracture Mechanics and Reliability Criteria," *AIAA J.,* Vol. 8, No. 4, pp. 621–628, Apr. 1971.

JPL Quarterly Technical Review Volume 1, Number 2 July 1971

Use of Pulsar Signals As Clocks

P. Reichley, G. Downs, and G. Morris

Telecommunications Division

The pulses of energy from pulsars are regarded as ticks from a clock. By comparing this pulsar clock with an earth-based atomic clock, several variations in the pulsar clock's frequency are noted. The major effect is due to the motion of the atomic clock in relation to the pulsar clock and contains information on the pulsar's position, elements of the earth's orbit, and solar relativistic effects. Another effect is the slowly varying frequency of the pulsar clock and contains information on the physics of the pulsar. In this article, the measurements of these effects and their present and future applications are discussed.

Introduction

One of the remarkable properties of pulsars is the emission of periodic pulses of energy. The periods of the known pulsars vary from 0.033 to 4 s. The periods are also slowly increasing with a typical value of 200 ns/yr. If these pulses are regarded as ticks of a clock, this pulsar clock can be calibrated with great accuracy.

Shortly after the discovery of pulsars, a program was started in order to see how well these pulsar clocks could be calibrated. The Venus Deep Space Station (DSS 13) at Goldstone is an ideal environment in which to conduct the measurements. The low-noise maser receiver and the high-rate sampling ability of the station are ideally suited to the measurements. The S-band operating frequency also minimizes charged-particle effects on the received pulse train.

The observations of the arrival times of the pulses are made using a 26-m parabolic reflector at a frequency of 2388 MHz. The atomic clock used to record the time-of-arrivals is a cesium standard, which is compared monthly with the master clock at the National Bureau of Standards.

The observational technique has been described elsewhere (References 1 and 2) and will not be described here. The sampling resolution of the pulses is typically on the order of 100 μs.

The determination of the arrival time for each pulse is accomplished by correlation techniques. The signal-to-noise ratio for the pulses is improved by coherently adding at least 500 pulses. The pulse is then correlated with a template which approximates the pulse shape. The determination of the arrival time has been described more fully in References 1 and 2. Typically, they have a standard deviation on the order of 100 μs.

An initial application of the pulsar clock was the synchronization of earth-based clocks. The application of this technique to the Deep Space Network seemed attractive since only an antenna to receive and a correlator are needed, i.e., a passive measurement. The technique is not presently competitive with the moon-bounce technique, due to the present limitation on sampling resolution and the noise on the pulses. Work is currently being done to develop a technique to sample the pulses faster.

The determination of the pulsar's positions and period characteristics has proved of value to the scientific community. Several groups of optical observers have used our positions and periods to try to detect pulsars optically. The period characteristics have been used by the scientific community to try to explain some of the physics of pulsars.

An attempt has also been made to measure the sun's gravitational red shift. The magnitude of the effect is easily within the measurement accuracy but has so far eluded detection due to correlation problems. A technique to eliminate these correlations and make a definitive measurement is currently being worked on.

With improved sampling resolution, elements of the earth's orbit can be improved. At present most of the measurable parameters are better measured by planetary radar. The parameter of the earth's orbit that can best be measured by pulsar clocks is the orientation of the orbit with respect to the celestial sphere. These measurements are currently made using a combination of optical and radar measurements.

Problem Formulation

The period characteristics of the ticks from the pulsar clocks, as observed at Goldstone, are different from those of the emitted ticks. Of interest are the differences, as well as the period characteristics, of the emitted ticks. The differences between the emitted and received period

characteristics can all be attributed to the motion of Goldstone in the inertial frame of the solar system (within measurement accuracy).

The inertial frame used for the calculations is a right ascension–declination system for the epoch 1950.0 centered at the barycenter of the solar system. The ephemeris used to describe the motion of the geocenter about the barycenter is JPL ephemeris DE-69 (Reference 3). The motion of Goldstone about the geocenter, the conversion from ET (ephemeris time) to UTC (universal time coordinated), and the reduction to the epoch 1950.0 were computed by means of standard equations using parameters developed at JPL (Reference 4).

To remove the effects of Goldstone's motion, the arrival times of the ticks were reduced to the barycenter of the inertial frame. The line element used to make the reduction is the Robertson isotropic line element which is consistent with DE-69. This allows us to account for relativistic effects on the arrival times, such as delay in the solar gravitational field and the red shift of the atomic clock as it moves in the solar gravitational field.

The pulsar's angular position is needed in order to make the reduction to the barycenter. Changes in the period due to changes in the relative distance between the barycenter and the pulsar are indistinguishable from the emitted period for motion on the order of galactic rotation (Reference 2). This is not true if the distance varies in a rapid (in the galactic sense) manner such as if the pulsar were in orbit. Proper motion and distance can also be detected in a manner similar to optical techniques.

The period characteristics are described by means of a polynomial that is equivalent to a Taylor series expansion of the period. The period is given as a function of time from some initial epoch. This form of representation is convenient since other models can be related to our model by simply comparing the derivatives.

A mathematical model has been constructed which includes all of the above-mentioned effects as free parameters. This model is used to predict the time-of-arrival of ticks at the barycenter of the inertial frame. These predictions are compared with the observations and the model is then differentially corrected by least-squares techniques.

Currently, 20 pulsars are being observed on a regular basis. Solutions of the parameter sets for 12 pulsars have been obtained (References 2 and 5), and work is continuing on the remaining 8, as well as on the first 12 for improved solutions. Since the major solar system effects on the arrival times of the ticks are tied to the earth's motion about the sun, a year's worth of data is typically required to obtain a minimal correlation solution.

Results

Specific numerical values for the results that were obtained in this study are given in References 2 and 5. Our main interest here will be with the precision of the results and the limits of this precision. Our discussion will be limited to only typical results and not for any one pulsar.

Regarding position determination, definitive results have been obtained for angular position only. After a year's worth of data, the typical limitation is the accuracy of the ephemeris of 0.1 seconds of arc in right ascension and declination. This limitation is due to the uncertainty in reducing the data to the inertial frame. The typical relative uncertainty is on the order of a few hundredths of a second of arc. Bounds have been determined for proper motion and distance (Reference 6). A typical lower bound for the distance is on the order of 50 light years and a typical upper bound on proper motion is on the order of 0.1 seconds of arc per year. These measurements are limited by the noise on the arrival-time data.

The period characteristics of most pulsars are described quite well by a simple polynomial, i.e., a constant plus a linear term. The constant term corresponds to the period at some epoch and the linear term corresponds to the rate of change of the period. The uncertainty in the period determinations is typically a few parts in 10^{11} (a few hundredths of a nanosecond). The uncertainty in the rate of change determinations is typically a few parts in 10^3 ($\sim 10^{-17}$ seconds per second). The accuracy in determining period characteristics is limited by noise on the time-of-arrival data and the length of the data span. There are two pulsars for which the linear model does not describe their period characteristics. They are discussed in the next section.

Definitive results have not been obtained in our attempts to measure relativistic effects. A highly correlated measurement of the gravitational red shift of the sun was obtained (Reference 7), which agrees with theory to within a few percent. The limitation on the measurement was the use of data from one pulsar only. By using as many pulsars as possible, the correlation of the result could be reduced significantly. An attempt was made to measure the time delay of the ticks of the pulsar clock as they passed through the sun's gravitational field. However, the accuracy in arrival time needed to make the measurement was not achieved. The basic limitation was noise on the data.

Discussion

The noise on the data has been blamed for the basic limitation in the majority of the measurements discussed in the previous section. The noise

can be thought of as having two components, discrete and random. The random component is due to the random noise that is inherent in the received signal. This causes random errors in the measurements of the pulse arrival times. For pulsars with stronger signals, the discrete component of measurement error shows up. Since there is a limit to the speed at which the pulses can be sampled, the error then becomes dependent on the length of time between samples.

Currently, work is being done on methods in which to reduce the noise. The obvious solution to the discrete component is to sample at a rate fast enough such that the noise is indeed random. Therefore, equipment which will sample at a faster rate is being designed and constructed. The random noise can also be reduced somewhat. As mentioned in the introduction, the arrival times are estimated by correlating an approximate pulse shape with the data. These estimates can be improved by correlating with the true pulse shape. By adding all the pulses for a particular pulsar and using this as the "true" pulse shape, it is hoped that this improvement can be attained. Just such a technique is currently being worked on.

As mentioned in the last section, the limitation to angular position determination was the accuracy of the ephemeris, mainly the rate of precession. If the measurement accuracy of the data can be improved, then this limitation would disappear for then the rate of precession can be solved for.

The length of the data span was mentioned as the limitation in the determination of period characteristics. The solution to this, of course, is to take data for a long time. But this, then, opens the door to other unknowns which must be solved for. It has been observed that two pulsars do not have a period described by a linear period model. These two pulsars are described by higher-order polynomials. It is predicted that other pulsars will also exhibit this behavior. The measurement of the quadratic term, or second derivative, is important in determining the radiation process of pulsars. Our estimates show (Reference 2) that for some of the pulsars which are being observed, this effect should be observable after approximately 5 yr.

Another error source that will show up over a length of time is the uncertainty in planetary masses. Since the inertial frame used in the data reduction is solar system barycentric, it involves all the planetary masses. If there is significant error in a planet's mass, this effect will show itself in a period of time roughly comparable to half of the planet's period of revolution. Much care must be exercised in solving for these effects, especially the longer period ones. Galactic rotation could contribute similar effects. This means that measurements should be taken for at least two periods of a particular planet's orbit before an attempt is made to improve its mass determination.

As mentioned, there are two pulsars whose period characteristics are not described by linear polynomials. A more accurate description would be that they are not described by polynomials at all. The periods of the Crab Nebula pulsar and the Vela pulsar are not only not described by polynomials but also exhibit discrete jumps in their periods (see, for example, Reference 5). These effects are ideal for determining the physics of the pulsars themselves but make them very unreliable as pulsar clocks. These pulsars are believed to be much younger than other pulsars and to be in an unstable state. All the other pulsars have exhibited stable periods for the 3 yr that they have been under observation.

There are other applications of pulsars in determining the unknowns of the galaxy and the solar system. The observation of dispersive effects on the pulsar signals has yielded information on the electron content of the interstellar medium. The observations of scintillations on the signals has yielded information on the size and density of electron clouds and their movements. Some scintillation measurements have been made (Reference 8) and more are being planned.

It is concluded that the calibration of pulsar clocks is indeed a useful concept, and that there is a wealth of knowledge that can be gleaned in the process.

References

1. Downs, G. S., Morris, G. A., and Reichley, P. E., "Average Pulsar Energies at Centimeter Wavelengths," *Nature*, Vol. 222, No. 5200, pp. 1257–1258, June 28, 1969.

2. Reichley, P. E., Downs, G. S., and Morris, G. A., "Time-of-Arrival Observations of Eleven Pulsars," *Astrophys. J.*, Vol. 159, pp. L35–L40, Jan. 1970.

3. O'Handley, D. A., Holdridge, D. B., Melbourne, W. G., and Mulholland, J. D., *JPL Development Ephemeris Number 69*, Technical Report 32-1465. Jet Propulsion Laboratory, Pasadena, Calif., Dec. 15, 1969.

4. Melbourne, W. G., Mulholland, J. D., Sjogren, W. L., and Sturms, F. M., Jr., *Constants and Related Information for Astrodynamic Calculations, 1968*, Technical Report 32-1306. Jet Propulsion Laboratory, Pasadena, Calif., July 15, 1968.

5. Reichley, P. E., and Downs, G. S., "Observed Decrease in the Period of Pulsar PSR 0833-45," *Nature*, Vol. 222, No. 5190, pp. 229–230, Apr. 19, 1969.

6. Reichley, P. E., "Pulsar Astrometrics and Period Characteristics," *Proceedings of International Symposium on Pulsars and High Energy Activity in Supernovae Remnants, Accademia Nazionale de Lincei, Rome, Dec. 1969.*

References (contd)

7. Reichley, P. E., "Tests of General Relativity Using Pulsars," *Proceedings of Conference on Experimental Tests of Gravitational Theories, California Institute of Technology, Pasadena, Calif., Nov. 1970* (in press).

8. Downs, G. S., and Reichley, P. E., "Observations of Interstellar Scintillations of Pulsar Signals at 2388 MHz," *Astrophys. J.*, Vol. 163, pp. L11–L16, Jan. 1, 1971.

Characteristics of a Cigar Antenna

S. A. Brunstein and R. F. Thomas

Telecommunications Division

Dual-frequency propagation experiments will be performed using the Deep Space Network 64-m antennas and the *Mariner* Venus–Mercury 1973 and *Viking* orbiter 1975 spacecraft. For such experiments, the 64-m antennas must be capable of receiving and transmitting at S-band and simultaneously receiving at X-band. One possible configuration involves placing an X-band feed inside the S-band feed horn.

A cigar (metallic-disc-on-rod) antenna was investigated for this application because this type of antenna is physically thin and would have minimal effect on the radiation from the S-band feed horn. A cigar antenna design obtained using new phase velocity data is described in this article. The new phase velocity measurements were required when it was found that the available published data for disc-on-rod structures were in error. The new measurements and the experimental results obtained with the resulting design are also described.

Introduction

Dual-frequency propagation experiments will be performed using the Deep Space Network 64-m antennas and the *Mariner* Venus–Mercury 1973 and *Viking* orbiter 1975 spacecraft (Reference 1). For these experiments, the 64-m antennas must be capable of receiving and transmitting at S-band and simultaneously receiving at X-band.

Several configurations are being investigated to implement this capability. One involves a coaxial feed in which an X-band radiator is placed inside the S-band feed horn on the centerline. The obvious requirement is that the X-band device must be diametrically small to avoid distortion of the fields in the S-band horn. The X-band feed must also have a radiation pattern that is very similar to that of the S-band feed (Reference 2) in order to achieve essentially identical aperture efficiencies at both frequencies.

Investigation of antenna types that could be used led to the class of long, thin, endfire antennas typified by the polyrod (dielectric) antenna (Reference 3, pp. 16–23). These antennas are slow-wave structures that achieve their gain by length rather than by aperture size. Scale-model experiments showed that this type of antenna of the approximate required size could be placed in the S-band feed horn with negligible effect on the radiation pattern. Specifically, it was decided to investigate a relatively little known form known as the cigar or disc-on-rod antenna. This antenna, essentially a metallic analogue to the polyrod antenna, was chosen because of concern for the effect on S-band system noise temperature if a dielectric rod was introduced into the S-band horn. A cigar antenna is shown in Figure 1.

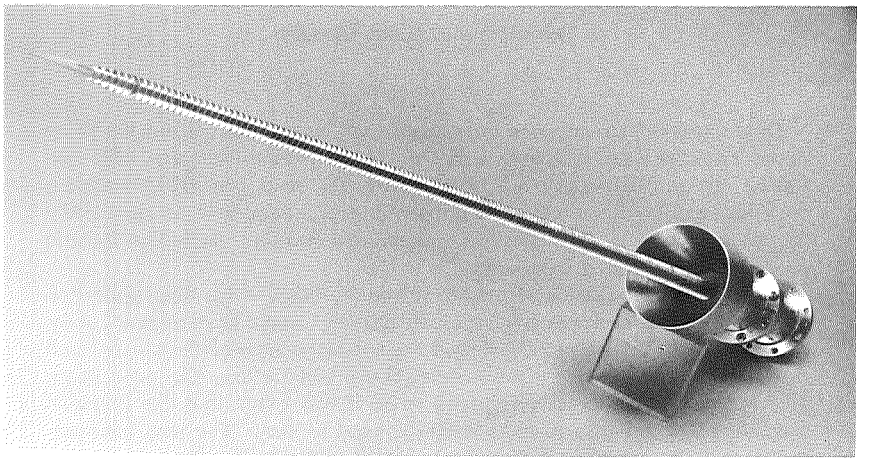

Figure 1. Cigar antenna

General design criteria for lengths, phase velocities, etc., required to achieve a given result with a slow-wave endfire antenna are thoroughly discussed by Jasik in Reference 3. Jasik also discusses phase velocity as a function of physical dimensions of disc-on-rod structures, based on the work of Simon and Weill (Reference 4). Based on the material in Reference 3, investigation of a cigar antenna was begun.

However, the initial results achieved with the cigar antenna did not meet expectations. Since the general phase velocity design criteria had been amply proven in polyrod antennas, the phase velocity data for the disc-on-rod structures became suspect; thus, an experimental program was undertaken to obtain new phase velocity measurements for these structures.

Phase Velocity Measurements

Phase velocity measurements were performed by three different techniques over a frequency range of 7–10 GHz. In all cases, the disc-on-rod

structure was fed from a circular X-band waveguide, excited by the linearly polarized TE_{11} mode. The inside diameter of the waveguide was 3.477 cm. The first disc of the disc-on-rod structure was located in the waveguide aperture. No discs were inside the waveguide, but the support rod extended several centimeters into the waveguide, and the disc-on-rod structure was supported by two thin Micarta discs inside the waveguide. The disc-on-rod structures had disc diameters ranging from 1.397 to 2.159 cm, with center-to-center spacings of 0.635, 0.953, and 1.270 cm. Two support rod diameters were used: 0.635 and 0.953 cm. The discs had a thickness of 0.0762 cm in all cases. Although difficulty was experienced with spatial harmonics throughout the measurements, the results were sufficiently conclusive to demonstrate that the data of Simon and Weill are substantially in error.

Measurements were first performed by moving a large metal plate with a hole for the cigar structure along the cigar and measuring the relative phase of the reflected energy with a Hewlett–Packard network analyzer to establish the wavelength on the cigar. The results of this measurement appeared to disprove Simon and Weill, so further investigation was felt to be in order.

The next technique used a small probe to measure the relative phase along a cigar structure that was terminated into free space with a taper; the last technique was identical, except that the cigar was terminated into a block of microwave absorber.

All of the measurement techniques suffered from the usual problem whereby the methods upset the fields sufficiently to affect the measurements. The difficulty was especially acute when the velocities on the structure approached the free-space velocity. Nevertheless, all three sets of measurements showed substantial agreement, and the results were quite different from those of Simon and Weill. The belief in the correctness of the measurements is substantiated by the fact that the cigar antenna designed from these data worked precisely as anticipated.

The results of the measurements are shown in Figure 2, along with the curves of Simon and Weill. The parameter limits for which the results are considered valid are shown on the figure. During the course of the measurements, it was found that the phase velocities were reasonably well-behaved until either the spacing of the discs or the diameter of the support rod approached 0.25 wavelengths. At values greater than about 0.21 wavelengths, the data became quite erratic, and it appears that the phase velocity is not a smooth function of physical dimensions above this value. Values smaller than 0.15 wavelengths were not investigated, nor were the effects of disc thickness.

The data shown by the points on Figure 2 did not justify more than a single phase velocity curve. It appears that the disc spacing does not

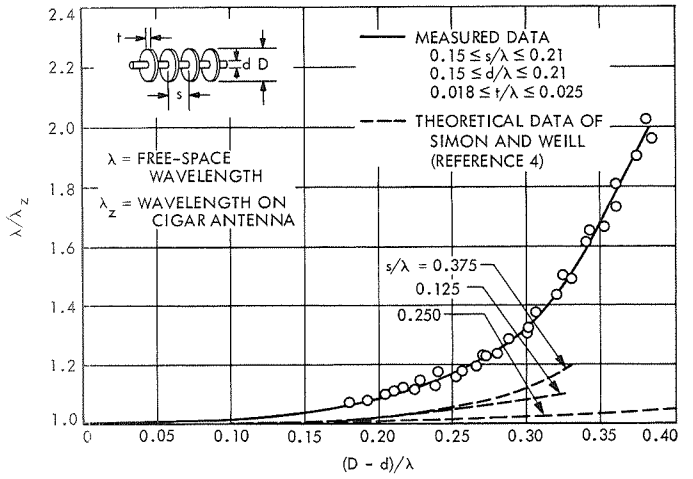

Figure 2. Ratio of free-space wavelength to wavelength on the cigar antenna as a function of normalized disc depth

significantly affect the phase velocity within the parameter limits shown. Significant data could not be taken below $(D - d)/\lambda = 0.18$ because of the measurement problems previously indicated. Certainly, the assumption of the point at zero seems justified, but the curve between there and the first data point must remain suspect.

Cigar Antenna Design

Using the general phase velocity criteria for a low-sidelobe endfire slow-wave antenna of about 22-dB gain (Reference 3), a cigar antenna was designed. Some empirical manipulation of the disc diameter in the constant velocity section where the velocity is near the free-space value was necessary to achieve the best results, indicating that the interpolated region of the phase velocity curve may indeed be in error, although certainly not grossly so.

The final design is shown in Figure 3. The waveguide inside diameter in regions A through E is 3.477 cm; in region I, it is tapered linearly to 8.192 cm. This small flare was found to substantially reduce the wide-angle radiation. The diameter of the center conductor in region A is linearly tapered from a point to 0.635 cm. The diameter in region B is constant at this value. In region C, the diameter tapers linearly to 1.415 cm. Region D is constant at this value, and region E has a diameter of 1.080 cm. The center conductor dimensions were determined empirically such that a low voltage standing-wave ratio would be achieved.

The disc-on-rod structure begins at the right side of region F in Figure 3. With the exception of the taper at the radiating end, it consists entirely of discs of thickness 0.0762 cm, spaced 0.625 cm, on a rod of

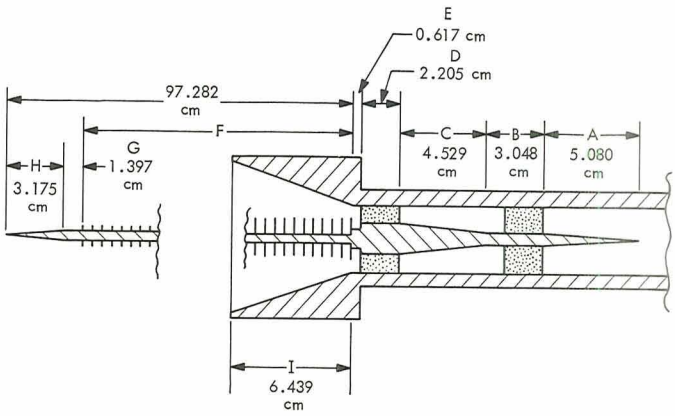

Figure 3. Cigar antenna physical configuration

diameter 0.625 cm. The first disc at the right of region F has a diameter of 1.704 cm. The disc diameter is tapered linearly over a length of 10.160 cm to a diameter of 1.549 cm and over a further distance of 45.72 cm to a diameter of 1.080 cm. This diameter is then held constant over a length of 33.020 cm. The disc diameter is then linearly tapered into the support rod over a distance of 3.810 cm. Region G has the constant diameter of the support rod, and, in region H, the diameter is linearly tapered to a point. The cigar is supported by foam plugs with a dielectric constant of about 1.02.

Experimental Results

The antenna was fed with a linearly polarized TE_{11} mode in the circular waveguide, and radiation pattern and voltage standing-wave ratio measurements were taken. Results were found to be good over the range of 7–9 GHz.

A typical radiation pattern is shown in Figure 4. While only the *H*-plane pattern is shown, the *E* and *H* planes are virtually identical over the main lobe and very similar over the full sphere. In both planes, radiation beyond an angle of 50 deg is more than 40 dB below the peak of the beam, except near 7 GHz, where it is down about 35 dB.

Directivity and beam efficiency were computed by pattern integration over the full sphere. While the directivity of 21.5 dB is significantly less than the 22.5-dB measured gain of an X-band feed horn, it is shown in Figure 5 that, at the edge of the Mars Deep Space Station antenna subreflector (29-deg included angle), the same amount of energy is included in the beam of the cigar as in the beam of the feed horn, and that the beam efficiencies are quite similar over the entire subreflector. This leads to the assumption that, while the beam shapes are different, the antenna efficiency will be essentially the same with either feed.

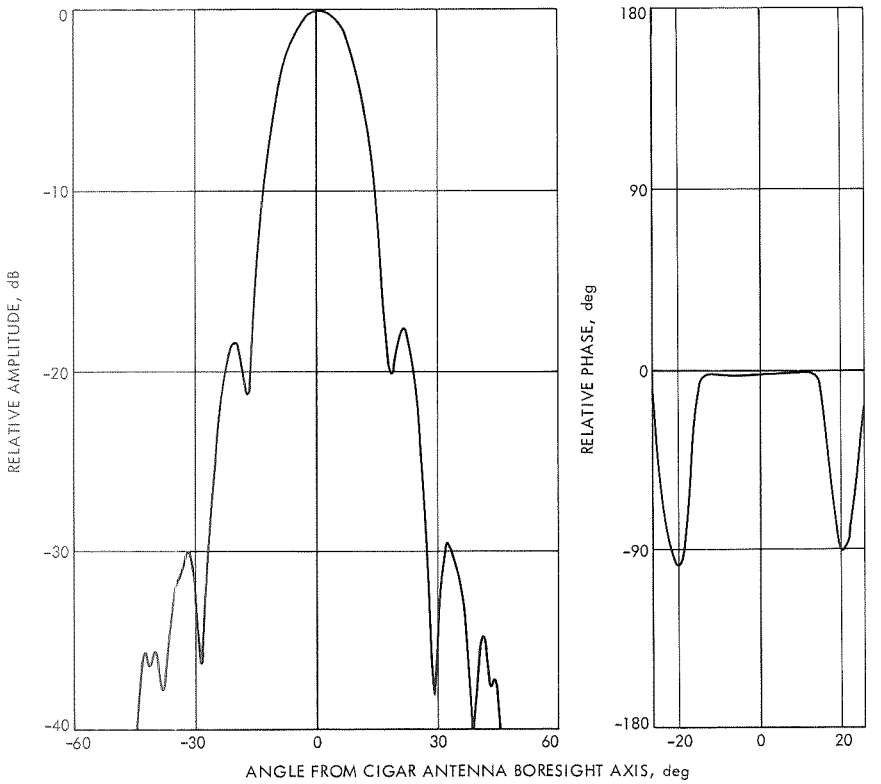

Figure 4. Relative amplitude and relative phase as functions of angle from the cigar antenna boresight axis (typical of both *E* and *H* planes at 8500 MHz)

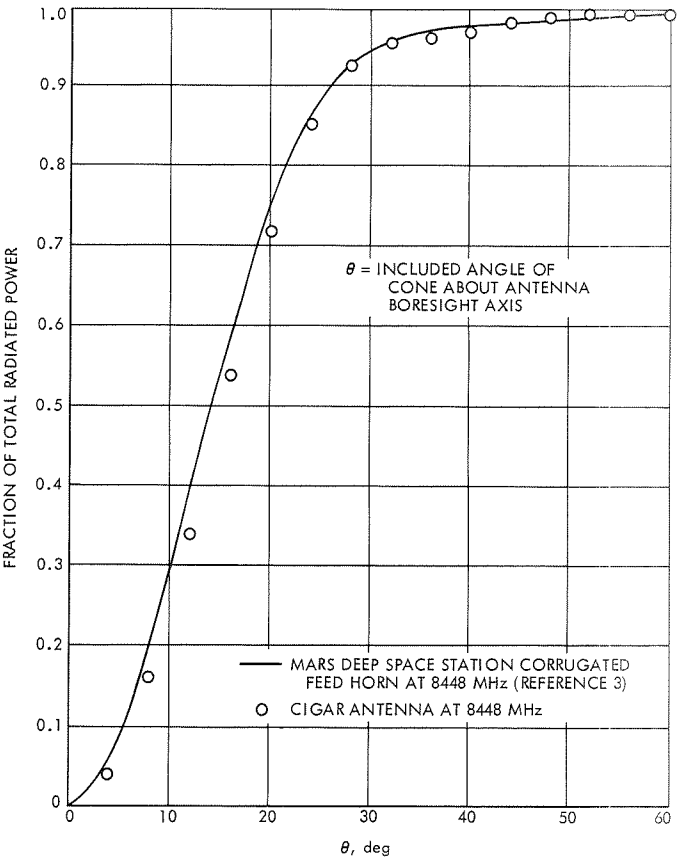

Figure 5. Fraction of the total radiated power contained in a cone about the antenna boresight axis

It must be pointed out that no actual gain measurements have yet been made with the cigar, and nothing is yet known of the possible losses on the disc-on-rod structure. Integration of the X-band horn pattern gave a directivity of 22.5 dB, in good agreement with measurements. This gives confidence in the pattern integration technique, providing the radiator is virtually lossless.

Figure 6 shows the 10-dB bandwidth, phase center location, and voltage standing-wave ratio of the cigar antenna as functions of frequency. Of

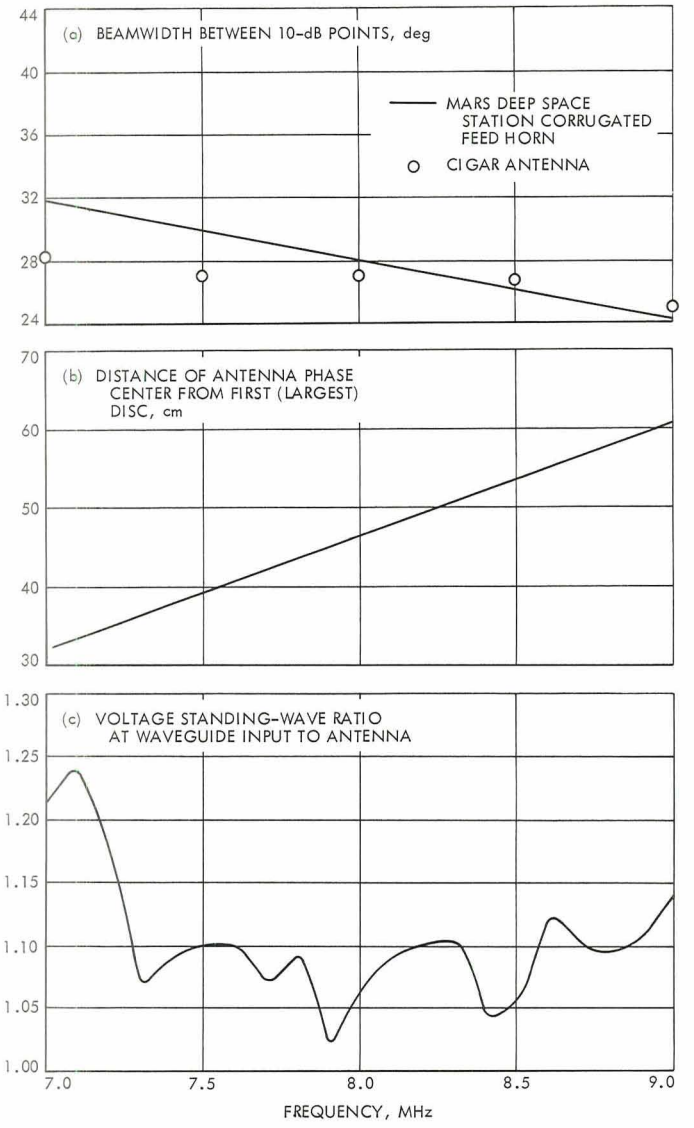

Figure 6. 10-dB beamwidth, phase center location, and voltage standing-wave ratio of cigar antenna as functions of frequency

particular interest is the virtual frequency independence of the beamwidth compared to the usual inverse frequency relationship demonstrated by the curve for the feed horn. Unfortunately, the phase center is not as well-behaved.

Conclusions

The phase velocity curves of Simon and Weill are in error. Using the phase velocity curves generated experimentally, a cigar antenna can be designed with good gain and sidelobe characteristics. If the losses on the disc-on-rod structure are small, the cigar will make a good feed device for cassegrain antennas or a good medium-gain lightweight antenna for other applications.

References

1. Levy, G., Dickinson, R., and Stelzried, C., "S/X Band Experiment," in *Supporting Research and Advanced Development,* Space Programs Summary 37-61, Vol. III, pp. 93–95. Jet Propulsion Laboratory, Pasadena, Calif., Feb. 28, 1970.
2. Brunstein, S. A., "A New Wideband Feed Horn with Equal E and H Plane Beamwidths and Suppressed Sidelobes," in *The Deep Space Network,* Space Programs Summary 37-58, Vol. II, pp. 61–64. Jet Propulsion Laboratory, Pasadena, Calif., July 31, 1969.
3. Jasik, *Antenna Engineering Handbook,* Chap. 16. McGraw-Hill Book Company, Inc., New York, 1961.
4. Simon, J. C., and Weill, G., "A New Type of Endfire Antenna," *Ann. Radioelectricite,* Vol. 8, p. 183, 1953 (in French).

Improvements in Deep-Space Tracking by Use of Third-Order Loops

R. C. Tausworthe

Telecommunications Division

Third-order phase-locked receivers have not yet found wide application in deep-space communications systems because the second-order systems now used have performed adequately on all past spacecraft missions. However, a survey of the doppler profiles for future missions shows that an unaided second-order loop may be unable to perform within reasonable error bounds. This article discusses the characteristics of a simple third-order extension to present second-order systems that will not only extend their doppler-tracking capability, but will widen the pull-in range, decrease pull-in time, lower the voltage-controlled oscillator noise detuning when no signal is present, and lessen the susceptibility to voltage-controlled oscillator drift.

Introduction

Second-order phase-locked receivers, used both in spacecraft and in ground tracking stations, have performed their function so satisfactorily that, up until now, there has been little or no reason to consider the installation of a more complicated system. Their performance characteristics have become well-understood, analyzable, and easily optimized relative to almost any criterion in a straightforward, well-defined way. Their capability to track incoming signals over a great range of signal levels and doppler profiles and to maintain lock and coherence at very low signal-to-noise ratios has become an accepted engineering fact.

As the more difficult deep space missions come into being, however, there is a corresponding stringency of requirements placed on the tracking instrument, as well as corresponding need to reevaluate the best ways of performing the tracking function technically, economically, and operationally. The *Mariner* Mars 1971 orbital missions and the *Pioneer F* Jupiter flyby mission, for example, have doppler rate profiles that may cause up to 30-deg steady-state phase error in the unaided second-order

loops now implemented. Such stress in receivers decreases the efficiency with which command or telemetry data are detected (by 1.25 dB at 30 deg), makes acquisition of lock difficult and faulty, and increases the likelihood of cycle slipping and loss of lock.

The way to avoid these problems is clear: eliminate or diminish the offending loop stress. This can be done by widening the loop bandwidth, by programming the uplink and downlink frequencies to correct these effects, or by increasing the order of the tracking loop. Widening the loop bandwidth increases loop noises; hence, it cannot be accepted as a general solution for the diminution of loop stress. Programming the uplink frequency and ground station local oscillator in accordance with the predicted doppler profile is certainly a valid solution, but it is costly to implement and introduces difficulty in reducing the two-way doppler data for navigation purposes. It also may require accurate predicts during critical phases of a mission where an *a priori* doppler profile is uncertain.

A third-order loop, however, will track the actual phase deviations presented to it without the need for accurate predicts. Raising the order of the loop to three would thus seem to be an ideal, even if only partial, solution because of its simplicity and possible economic factor.

The basic characteristics of third-order phase-tracking systems have been known since the first works of Jaffee and Rechtin (Reference 1), but these systems have not found wide application in the past due to what seemed to be poor acquisition and stability characteristics. Design seemed more complicated and was not well-understood. However, these potential problems have been overcome to the extent that a loop of the third order can now out-perform a second-order loop not only in its ability to track a frequency ramp with practically zero phase error, but also in its ability to acquire lock more quickly and from greater offsets. Even when synthesized with imperfect integrators within the loop filter, the third-order system will out-perform a perfect second-order system by orders-of-magnitude improvement in steady-state phase error, lock-in time, and pull-in range. One further advantage to the third-order system is that there is less of a requirement for the long time constants dictated by the high loop gains needed in the second-order loop to maintain small tracking errors.

Other advantages are that the loop filter configuration is a simple extension of presently mechanized loops, so required modification is minor; the role of the receiver operator subsequent to lock is essentially eliminated; several bandwidths are not needed to acquire rapidly; and frequency drifts in the loop voltage-controlled oscillator (VCO) cause essentially no degradation in performance. This last advantage may

remove the need to have the VCOs in ovens and thereby further extend the usefulness of the system.

Third-Order Loop Synthesis

When minimizing the total transient distortion plus noise variance by the Wiener filtering technique (Reference 1), one is led to the following optimum loop filter for tracking an input phase acceleration $\theta(t) = \Lambda_0 t^2/2$:

$$F(s) = \frac{1 + \tau_2 s}{\tau_1 s} + \frac{1}{2\tau_1 \tau_2 s^2}$$

Values are chosen so the parameter $r = AK\tau_2^2/\tau_1$ is equal to 2. In usual notation, A refers to the rms input signal amplitude and K is the loop gain. The first part of this filter resembles that used in the second-order loop (Reference 2). Based on this resemblance, one may conceive (References 3 and 4) a two-stage loop design: acquisition by the second-order loop to avoid any of the problems that a third-order system out of lock might supposedly have, and subsequent addition of the other pole to remove loop stress. As will be shown, such a configuration is particularly useful for unattended receivers; henceforth, it will be referred to as a *hybrid* design.

However, perfect integrators are not usually practical, so modifications are necessary. The loop filter to be considered in the remainder of this article may be synthesized in many ways, three designs of which are shown in Figure 1. These all have the same transfer function,

$$F(s) = \frac{1 + \tau_2 s}{1 + \tau_1 s} + \frac{1}{(1 + \tau_1 s)(\delta + \tau_3 s)}$$

With the same loop transfer function, the designs operate identically once the loop is locked; they differ in their lock-in transient behaviors, however, because of the possibly different initial capacitor voltages. If all C's are shorted at $t = 0$, they are again identical (within limits introduced by hardware imperfections). However, when the loop is operating as a hybrid, i.e., as second order (C_2, or C_2 and C_3 shorted) during the acquisition phase and third order (C_2, or C_2 and C_3 released) after lock, Circuit I exhibits a different transient phenomenon than do Circuits II and III because of the placement of the capacitors.

In a Circuit I hybrid, the charge on C_1 at the end of the acquisition phase is related to the loop frequency mistuning, $\Omega_0 = 2\pi\Delta f$. It causes the transient shown in Figure 2 in the third-order loop, which, if too large, can knock the loop irrecoverably out of lock. Such a characteristic leads to the conclusion that *Circuit I is not generally suitable for hybrid loop design.* Circuits II and III, however, exhibit no such transient away from lock and thus make excellent hybrids.

CIRCUIT I: EXTENSION OF SECOND-ORDER LOOP BY ADDITION OF ONE INTEGRATOR

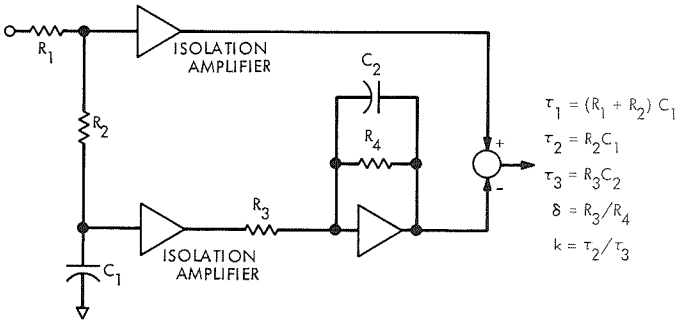

CIRCUIT II: EXTENSION OF SECOND-ORDER LOOP BY ADDITION OF TWO INTEGRATORS

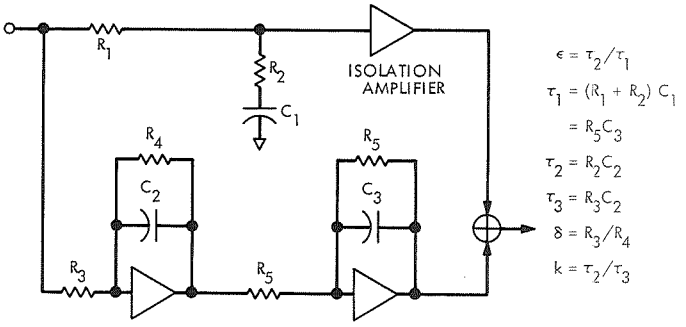

CIRCUIT III: NOT AN EXTENSION OF USUAL SECOND-ORDER LOOP

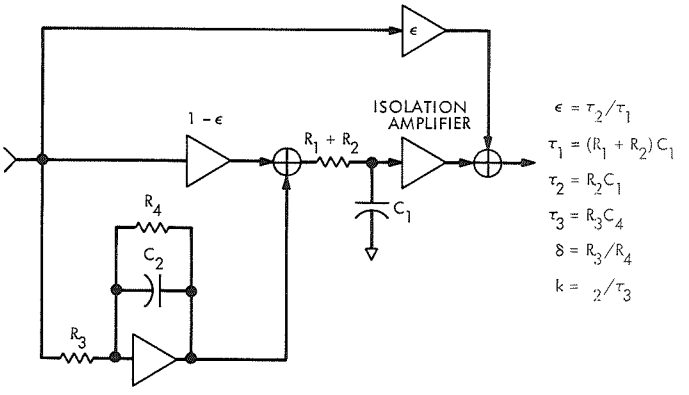

Figure 1. Third-order loop filters

The two-sided noise bandwidth in the simplified, but usual, case $\epsilon = \tau_2/\tau_1 \ll 1$ and $\delta \ll 1$ is given by

$$w_L = \frac{r}{2\tau_2}\left(\frac{r-k+1}{r-k}\right)$$

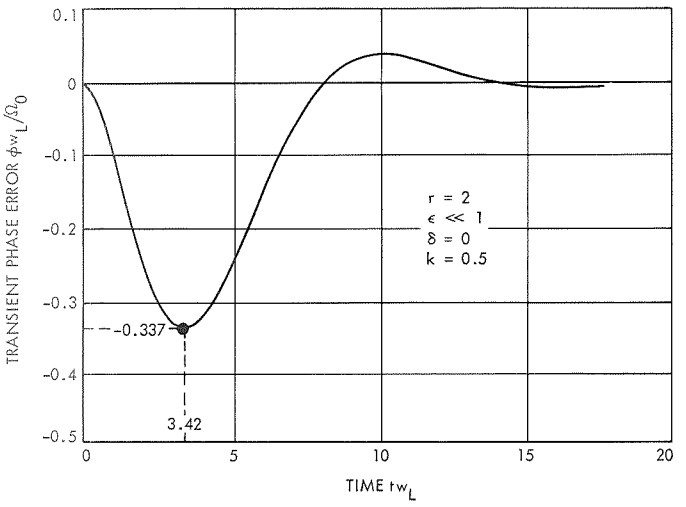

Figure 2. Circuit I hybrid loop transient caused by final lockup voltage on C_1

The parameter k is the time-constant ratio τ_2/τ_3. As compared with the loop bandwidth formula of the second-order loop, the simplified expression above is only slightly increased in complexity, and, of course, the two merge to the same result as $k \rightarrow 0$.

The primary determining factors of w_L are still τ_2 and r, just as in the second-order loop. The phase error variances of any two loops due to input noise are, of course, the same as long as their loop bandwidths are the same.

Acquisition and Lock-In Behavior

The phase-plane technique, which is useful in visualizing the lock-in behavior of second-order loops (Reference 5), does not readily extend the same advantage to third-order systems, partly because there are *three* initial conditions—phase, frequency, and frequency rate—needed to specify a unique trajectory, and partly because this trajectory lies in a three-dimensional, difficult-to-imagine, hyperplane. By analogy, however, one still can visualize that, if there is a beat frequency between the incoming sinusoid and the VCO, there will be a small dc voltage at the detector output tending to force the loop toward lock. The extra integration in the loop accumulates this force, accelerating the loop toward lock. There is thus an understandable reduction in the time required to reach the zero-beat lock-in region, and there is a corresponding increase in the loop pull-in-frequency range, as compared to that with a second-order system.

If loop damping is not set properly, the great velocity acquired by the loop phase and the momentum associated with the two integrations of the error may carry the loop frequency error past the lock region, perhaps out of lock so rapidly that recovery is not possible. Proper setting of the system roots can reduce this velocity through the zero-beat region enough to prevent frequency overshoot or irrecoverable loss of lock. In fact, if the loop has no underdamped roots, there is no transit past the zero-beat region.

The theory developed for computing the pull-in range of a second-order loop is easily extended to account for effects in the third-order loop; *there is an enhancement in the acquisition range by approximately the square root of the added integrator dc gain.* In fact, experimental evidence (Figure 3) verifies this formula exceedingly well all the way out to the point where IF filtering or minute equipment bias imperfections begin to limit the loop pull-in.

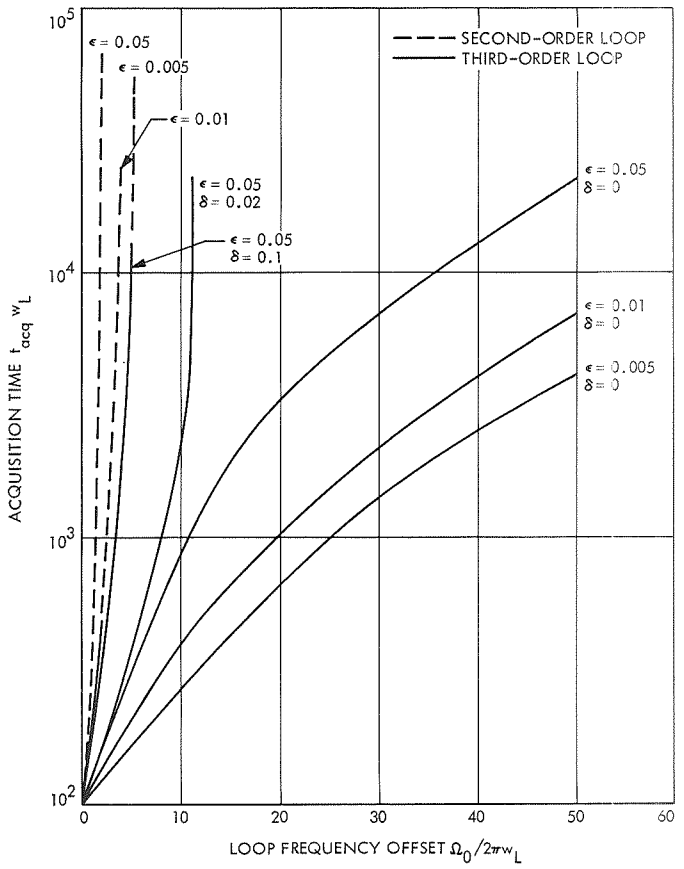

Figure 3. Measured acquisition time as a function of loop frequency offset (normalized axes)

Steady-State Errors

Due to imperfect integrations, there are steady-state phase errors that build up because of the instantaneous frequency detuning and the rate of change of this detuning. Compared with the corresponding expression for a second-order loop, the steady-state error ϕ_{ss} due to an instantaneous frequency offset is reduced by a factor of about δ, and the error caused by a frequency rate is diminished by a factor of about $\delta + (\epsilon/k)$. Such a comparison reflects the desirability not only of making ϵ and δ very small, but also of keeping k as large as other factors will permit. Figure 4 depicts the steady-state phase errors that result from frequency offsets and frequency rates.

Root Loci

For a given set of loop constants, the loop gain K or signal level A may be varied and the position of the poles of the transfer function $L(s)$ plotted. Since $r = AK\tau_2^2/\tau_1$ is proportional to both A and K, it may be used as the independent variable. The system roots start at the poles of $F(s)$ at $r = 0$ and finally terminate at the zeros of $F(s)$. These loci take on different characteristics, depending on the value of $k = \tau_2/\tau_3$.

The six loci illustrated in Figure 5 show, for various increasing k:

(a) When $k > k_{max}$, there are two underdamped (complex) and one overdamped (real) roots for all $r > r_{osc}$.

(b) When $k = k_{max}$, there are two underdamped and one overdamped roots for all $r > r_{osc}$ except at $r \approx 3$, at which point all three roots become equal.

(c) When $k_0 < k < k_{max}$, there is a region where two roots pass from underdamped to critically damped, to overdamped, to critically damped, and finally to underdamped.

(d) At $k = k_0$, the system roots are always critical or overdamped for $r > 3.375$.

(e) The $k < k_0$ case is similar to the $k = k_0$ case, except there is a root nearer the origin, indicating a more sluggish response when $k < k_0$.

(f) When $k = 0$, the zero cancels the pole near the origin, producing a second-order loop.

The cases illustrated in Figure 5b and 5d are of special interest. Figure 5b depicts the maximum value of k (i.e., k_{max}) that can be used when no underdamped roots are desired. In such a design, there is only one fixed operating signal level (i.e., $r = 3$). Figure 5d shows the maximum

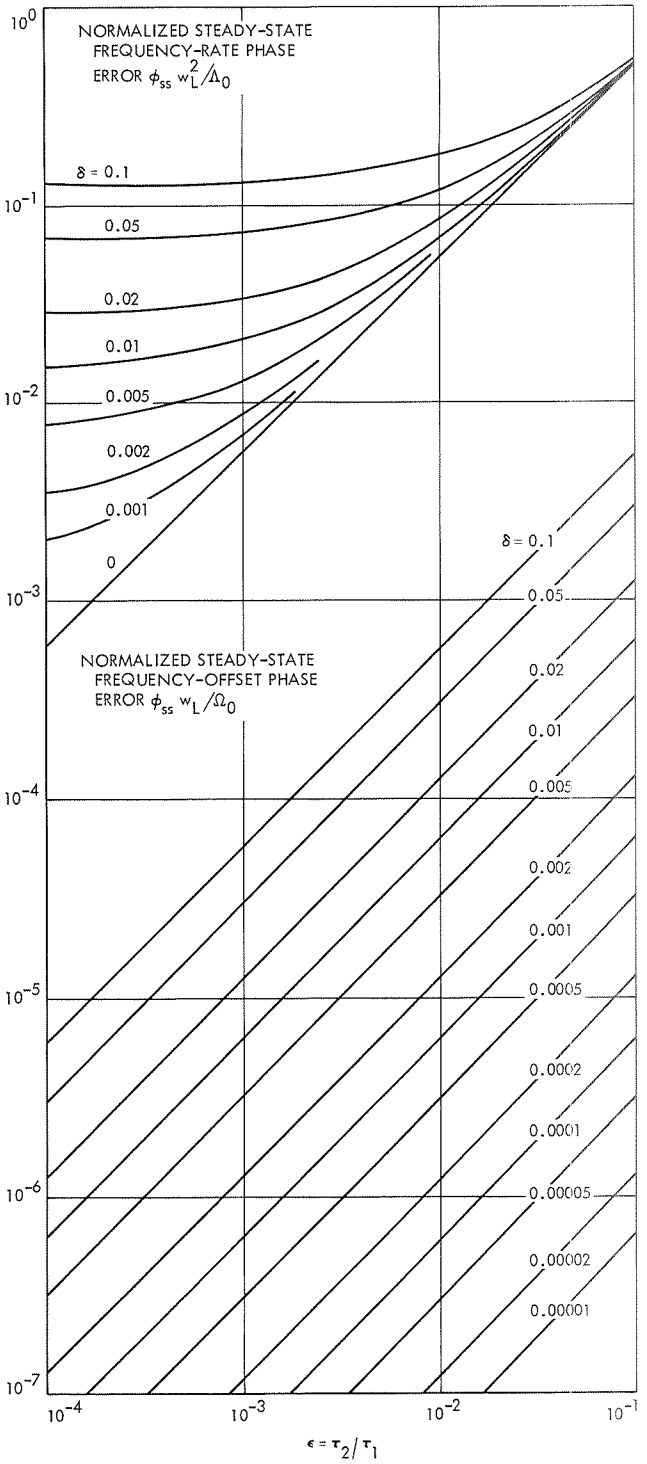

Figure 4. Normalized phase errors due to frequency offsets and frequency rates as functions of loop filter imperfections

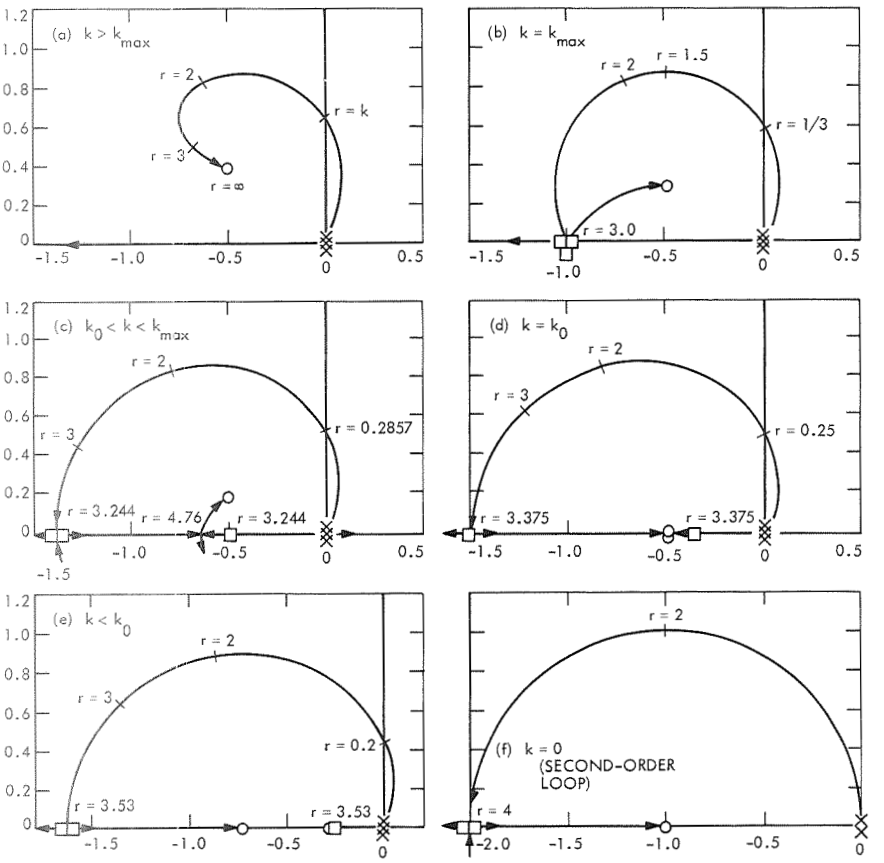

Figure 5. Root loci of the third-order loop as a function of $r = AK\tau_2^2/\tau_1$ for various values of the parameter $k = \tau_2/\tau_3$

value of k (i.e., k_0) that can be used if no underdamped roots are desired at any signal level above a design point producing $r_0 = 3.375$.

To minimize the possibility that acquisition is faulty, it is necessary that damping be critical or beyond; to minimize steady-state error once lock is achieved, k should be as large as possible. These two conditions are met in slightly different ways according to the type of signals to be tracked. If the design is to be for signals of a fixed level, then k should be set to k_{max} and r should be set to produce critical damping at this level (Figure 5b). If the design is to be for signals of various intensities, then k should be made equal to k_0 and r should be set for critical damping (Figure 5d) at the weakest expected signal level to ensure that the roots are never underdamped.

The gain margin is the ratio r/r_{osc}, which is about 22 dB for variable signal level designs, 19 dB for fixed signal level designs and 12 dB for hybrid designs.

Effect of Internal and VCO Noise

The effect of VCO and other noises internal to the loop can be modeled as an equivalent noise voltage, $n_v(t)$, appearing at the VCO input. The form of the phase-error it causes greatly resembles the corresponding equation for second-order loops, but the phase error variance is about 10 to 18% higher than that for the second-order case. Hence, there is no relaxation in the requirement for spectral purity in the VCO to be used. However, there are other effects in the VCO not well modeled spectrally; one such effect is a steady drift in rest frequency due to some change in the oscillator operating condition, such as temperature or bias voltage. These appear to the loop error detector as slight alterations to the frequency offset or rate of the incoming sinusoid. Such effects can be analyzed as part of the loop overall transient. Because the third-order loop minimizes the effect of such transients, the drift requirement on VCOs may be greatly relaxed.

Noise-Detuning of the VCO (Out of Lock)

When acquisition begins with the loop filter capacitors having the initial random charges as deposited in them by input noise prior to application of signal, there are random voltages which deviate the VCO from its rest frequency by perhaps $1/\delta$ times as far as that in a second-order loop with the same loop gain K. This comparison is somewhat unfair, as it fails to recognize the increased tracking capability of the third-order system. To judge performance between second- and third-order systems fairly, it is necessary to raise the gain of the second-order loop by this same $1/\delta$ to equate the static phase errors due to detuning. (There will be little change in the second-order loop's ability to track

an acceleration, however.) The frequency wanderings of the second-order system will then *always exceed those of the third-order system* by at least a factor $1 + (\epsilon/k\delta)$. When $k\delta$ is smaller than $\epsilon = \tau_2/\tau_1$, the advantage is obvious.

Concluding Remarks

This summary article has indicated the tracking performance gains that can be obtained by simple modifications or redesign of existing receivers. The interested reader desiring more detail may consult Reference 6, which develops the theoretical performance of practical third-order tracking systems; presents design methods and procedures by which they may be synthesized; discusses hardware configuration and implementation factors; and indicates, by actual observed data, that the design goals and performance measures are as specified by the theory.

References

1. Jaffee, R., and Rechtin, E., "Design and Performance of Phase-Lock Loops Capable of Near-Optimum Performance Over a Wide Range of Input Signal and Noise Levels," *Trans. IRE,* Vol. IT-1, pp. 66–76, Mar. 1955.

2. Tausworthe, R. C., *Theory and Practical Design of Phase-Locked Receivers,* Technical Report 32-819, Vol. I. Jet Propulsion Laboratory, Pasadena, Calif., Feb. 15, 1966.

3. Tausworthe, R. C., "A Second/Third-Order Hybrid Phase-Locked Receiver for Tracking Doppler Rates," in *Deep Space Network Progress Report for November–December 1970,* Technical Report 32-1526, Vol. I, pp. 42–45. Jet Propulsion Laboratory, Pasadena, Calif., Feb. 15, 1971.

4. Gardner, F. M., *Phaselock Techniques,* pp. 12, 15, 22, 31, 50, 52, 72, and 74. John Wiley and Sons, Inc., New York, 1966.

5. Viterbi, A. J., *Principles of Coherent Communications,* pp. 64–72. McGraw-Hill Book Company, Inc., New York, 1966.

6. Tausworthe, R. C., and Crow, R. B., *Practical Design of Third-Order Phase-Locked Loops,* JPL Internal Document 900-450. Jet Propulsion Laboratory, Pasadena, Calif., Apr. 27, 1971.

Non-orthogonal Redundant Configurations of Single-Axis Strapped-Down Gyros

A. K. Bejczy

Guidance and Control Division

The functional reliability of the inertial reference unit of a three-axis stabilized spacecraft for long lifetime missions is of specific concern. Realizing the highly efficient redundancy potential inherent to non-orthogonal emplacements of more than three single-axis strapped-down gyros, and considering practical implementation and performance criteria, 45-deg skew-symmetric six- and four-gyro configurations based on the geometry of a regular octahedron are presented in this article. These configurations result in optimum performance, exhibit unique simplicity in gyro output processing requirements, allow high-density packaging, and require reasonable fabrication and test procedures. The redundancy potential of an octahedron six-array gyro configuration is twice as high as that of six gyros in an orthogonal emplacement. An octahedron-based skew emplacement of four gyros can provide minimum redundancy for the inertial reference unit, which, for an orthogonal emplacement, could only be obtained by six gyros.

Introduction

For three-axis stabilized spacecraft designed for long lifetime (8-12 yr) missions, the functional reliability of the inertial reference unit (IRU) constructed of single-axis strapped-down gyros is of specific concern, since the IRU has an irreplaceable functional assignment in the following critical guidance and control system operations: celestial reference acquisition, commanded turns, midcourse thrusting, planet encounters, and celestial reference occultations or disturbances in the field-of-view of the electro-optical attitude reference sensors. In addition to the critical in-line functions, the IRU can also provide a significant backup for the celestial attitude reference sensors in any phase of a mission.

Because of the very mechanism of attitude sensing through single-axis strapped-down gyros, increasing the functional reliability of the IRU must be sought not only on the component level of the single gyro instruments, but also on the instrument level of the total IRU by employing a

redundant number of gyros. The physics of attitude sensing by single-axis strapped-down gyros indicates two geometrically different ways to employ a redundant number of gyros in the IRU: (1) paralleling two or more gyros on each of the three orthogonal control axes of the spacecraft, and (2) emplacing the sensitive axes of more than three gyros in a linearly independent non-orthogonal configuration. Simple combinatorial calculations show that the redundant non-orthogonal gyro configurations are *much more efficient* in increasing the functional reliability of the IRU than are conventional redundancy techniques that simply parallel two or more gyros on the spacecraft's three orthogonal control axes.

The highly effective redundancy in full attitude reference inherent to the non-orthogonal gyro configurations is physically based on the *coupled* properties of attitude information obtainable through a linearly independent non-orthogonal emplacement of the sensitive axes of a redundant ($n > 3$) set of gyros. In such configurations, *no one gyro is restricted to replace the function of any specified gyro.* For example, out of six gyros, *any three* can fail without losing full attitude reference. This would practically result in *triple* redundancy for attitude information on each of the three orthogonal control axes of a three-axis stabilized spacecraft.

General Properties of Non-Orthogonal Gyro Configurations

For $n > 3$ single-axis strapped-down gyros in a non-orthogonal configuration, the total measurement vector in a compact vector-matrix notation is

$$\mathbf{h} = \mathbf{A}\mathbf{w} \tag{1}$$

or, in component form,

$$h_1 = A_{1x}w_x + A_{1y}w_y + A_{1z}w_z \tag{1a}$$

$$h_2 = A_{2x}w_x + A_{2y}w_y + A_{2z}w_z \tag{1b}$$

$$\begin{array}{cccc} \cdot & \cdot & \cdot & \cdot \\ \cdot & \cdot & \cdot & \cdot \\ \cdot & \cdot & \cdot & \cdot \end{array}$$

$$h_n = A_{nx}w_x + A_{ny}w_y + A_{nz}w_z \tag{1n}$$

where

$\mathbf{h} = (h_1,\cdots,h_n)'$, an n-dimensional column vector representing the outputs of the n gyros. Depending on the mode of operation of the gyros, $\mathbf{h}$ is the angular rate or integrated rate (angular displacement) measured by the $1,2,\cdots,n$ gyros along the $1,2,\cdots,n$ gyro input-axis directions.

$\mathbf{A} = (A_{ij})$, an n-by-3 matrix of direction cosines relating the n gyro input-axis orientations to the x,y,z (pitch, yaw, roll) orthogonal control axes of the spacecraft (Figure 1).

$\mathbf{w} = (w_x,w_y,w_z)'$, a 3-dimensional column vector. Depending on the mode of operation of the gyros, $\mathbf{w}$ represents the three angular rates or integrated rates (angular displacement) along the x,y,z spacecraft control axes.[1]

The quantities of interest for attitude control are w_x,w_y,w_z, which now are not measured directly, but should be computed from Equations 1a–1n. Out of the n equations, only three are needed to determine the three "unknowns" w_x,w_y,w_z. In fact, *any group of three* linearly independent equations yield solutions for w_x,w_y,w_z. (Linear independency means that the input axes of the corresponding three gyros are not colinear or coplanar.)

[1]For rate integrating gyros, the linear relationship given by Equation 1 will accurately relate the measured angular increments h_i to the x,y,z body-axis angular increments w_x,w_y,w_z if the angular rates are low. This condition is satisfied for the intended application.

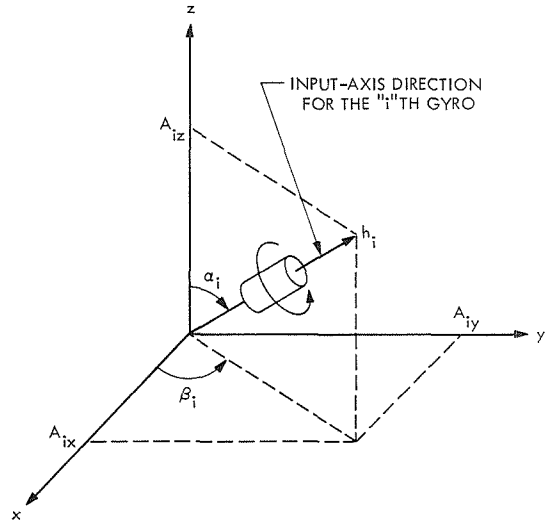

$$h_i = A_{ix}w_x + A_{iy}w_y + A_{iz}w_z$$

$$A_{ix} = \sin \alpha_i \cos \beta_i$$

$$A_{iy} = \sin \alpha_i \sin \beta_i$$

$$A_{iz} = \cos \alpha_i$$

Figure 1. Orthogonal projections of one gyro in a skew emplacement

Having a set of n linearly independent non-orthogonal gyro orientations, there are $n!/3!\,(n-3)!$ possible combinations of three out of n gyro measurements to determine w_x,w_y,w_z. That is, $n = 4$ gives 4, $n = 5$ gives 10, and $n = 6$ gives 20 different ways to determine the three quantities of interest. In contrast, an orthogonal emplacement of $n = 6$ gyros (paralleling two gyros on each of the three orthogonal control axes of the spacecraft) yields only 8 ways to determine w_x,w_y,w_z. Thus, in combinatorial terms, six gyros in a linearly independent non-orthogonal emplacement provide *2.5 times higher redundancy* for full attitude reference than six gyros in an orthogonal emplacement.

Selecting any three (h_i,h_j,h_k) out of the n gyro measurements, the computation of "equivalent" w_x,w_y,w_z measurements requires the implementation of three equations of the following general form:

$$\left.\begin{aligned} w_x &= B_{xi}h_i + B_{xj}h_j + B_{xk}h_k \\ w_y &= B_{yi}h_i + B_{yj}h_j + B_{yk}h_k \\ w_z &= B_{zi}h_i + B_{zj}h_j + B_{zk}h_k \end{aligned}\right\} \qquad (2)$$

where $B_{xi},\cdots,B_{zk}$ are elements of the inverse of the 3-by-3 $\mathbf{A}^{(ijk)}$ submatrix of $\mathbf{A}$, the elements of which are the direction cosines of the selected i,j,k gyro input-axis orientations. Clearly, each group of three gyros has its own transform matrix $\mathbf{B}^{(ijk)}$. It is noted that $B_{xi},\cdots,B_{zk}$ are *precomputed constants* determined by the fixed direction cosines $A_{ix},\cdots,A_{kz}$. The implementation of Equation 2 is depicted in Figure 2. For low angular rates and digital outputs of rate integrating gyros, Figure 2 can be interpreted as follows: Process the h_i,h_j,h_k gyro pulses as they occur and count them in the w_x,w_y,w_z adders according to the corresponding constant transform gains $B_{xi},\cdots,B_{zk}$.

Practical Criteria for Constructing Non-Orthogonal Redundant Gyro Configurations

Theoretically, for a selected number $n>3$ of single-axis strapped-down gyros, an unlimited variety of linearly independent non-orthogonal configurations is possible. Practical considerations, however, will substantially limit the possibilities of constructing appropriate configurations that also match mission requirements and spacecraft constraints. The practical construction criteria are as follows:

(1) Minimal transformation of the inherent (random and non-random) instrument errors to the computed equivalent w_x,w_y,w_z measurements. Assuming equal, independent, and normal *random* error characteristics for each gyro, the random error transformation in terms of the variance for the x axis is

$$\sigma_x^2 = (B_{xi}^2 + B_{xj}^2 + B_{xk}^2)\sigma_0^2 \qquad (3)$$

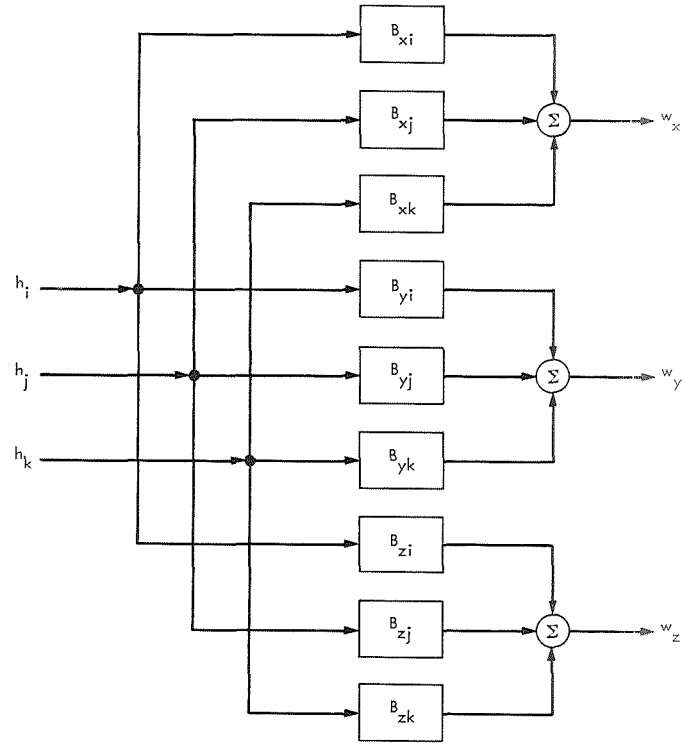

Figure 2. Mechanization scheme for measurement transformation

where σ_0^2 denotes the variance of a single gyro. The transformation of the *non-random* instrument errors (drift, misalignment) is, in the "worst case" and for the x axis, proportional to

$$|B_{xi}| + |B_{xj}| + |B_{xk}| \tag{4}$$

Clearly, similar expressions are valid for the y and z axes.

(2) Simple gyro output processing to obtain the equivalent w_x,w_y,w_z measurements. This requires some cyclic symmetry for the values of the transform gains. (For example, for six gyros in a linearly independent non-orthogonal but otherwise unrestricted emplacement, there exist *180 different* transform gain values through which to obtain equivalent w_x,w_y,w_z measurements from the 20 three-gyro combinations.)

(3) Possible compact packaging for thermal control of the gyros and economical use of spacecraft volume.

(4) Reasonable fabrication and test procedures.

References 1–5 represent the total reported works on non-orthogonal gyro configurations. With the exception of Reference 2, they mainly consider Criterion 1 and emphasize specific modes of operation or restrict

the configuration. Reference 1 considers only one four-gyro configuration and one five-gyro configuration. Reference 2 considers two orthogonal triads skewed relative to each other. References 3 and 4 describe the dodecahedron six-array configuration of the Massachusetts Institute of Technology. This work is the most elaborate and has reached the testing phase; however, its main emphasis is on a self-contained failure monitoring technique that can isolate any two failed gyros out of the six gyros, and it assumes that the IRU operation starts with six gyros turned on. Reference 5 considers mainly gyro arrays equally spaced on a 54.75-deg cone. The reported works do not emphasize Criterion 2 in any specific manner.

In this article, both Criteria 1 and 2 are basic concerns, and specific attention is paid to Criteria 3 and 4.

45-deg Emplacement Symmetry for Four and Six Gyros

A 45-deg emplacement symmetry for four and six gyros offers great advantages in processing gyro outputs to obtain the equivalent w_x,w_y,w_z measurements. Furthermore, such configurations provide optimal performance regarding instrument error transformation, require reasonable fabrication and test procedures, and can be emplaced in a high-density package.

Six-Gyro Case

Let the six gyro input-axis directions, taken one by one and identified with numbers 1 to 6, be oriented perpendicular to the opposite facing parallel edges of a regular octahedron. Let this octahedron be emplaced with its center at the origin of an x,y,z orthogonal reference system such that the octahedron's opposite facing corners are fixed to the x,y,z axes (Figure 3). The essential feature of this octahedron six-array emplacement geometry is a skew symmetry: each one of the three datum planes contains two gyro input axes aligned with 45-deg inclination to the two reference axes of the respective datum plane. Thus, each of the three reference axes obtains symmetric (45-deg) projections from four of six gyro input-axis directions. The direction cosine matrix of this configuration is then

$$A \longleftrightarrow \begin{array}{|c|c|c|c|} \hline \text{Gyro index} & x & y & z \\ \hline 1 & 0.707 & 0 & 0.707 \\ 2 & -0.707 & 0 & 0.707 \\ 3 & 0.707 & 0.707 & 0 \\ 4 & 0.707 & -0.707 & 0 \\ 5 & 0 & 0.707 & 0.707 \\ 6 & 0 & 0.707 & -0.707 \\ \hline \end{array} \qquad (5)$$

The gyro output transformations into equivalent w_x,w_y,w_z measurements are listed in Table 1 for all 16 useful three-gyro combinations. The four coplanar (hence, of no value) three-gyro combinations are also indicated. Each 3-by-3 block in Table 1 should be interpreted in a vector-matrix sense, having a mechanization scheme as depicted in general terms in Figure 2. The numbers above each block identify three gyros by their index numbers defined in Figure 3 and Equation 5. The values inside each block identify the constant transform gains relating the corresponding gyro outputs to the three (w_x,w_y,w_z) quantities of interest.

Table 1 clearly shows the unique advantage in measurement processing associated with the six-array configuration: *All gyro outputs in all three-gyro combinations have one common scaling factor, $c = 0.707$ [more precisely, $c = \cos(45\ \text{deg}) = 2^{-\frac{1}{2}}$]*. The common scaling factor of the gyro pulse signals can be considered as part of the instrument electronics of the gyros or as a designed property of the w_x,w_y,w_z adders. Thus, having scaled all gyro outputs by c, the elements in the sixteen 3-by-3 transform matrices are $0,\pm1,\pm2$. Moreover, there are many common rows and columns in the 16 transform matrices given in Table 1. For example, in

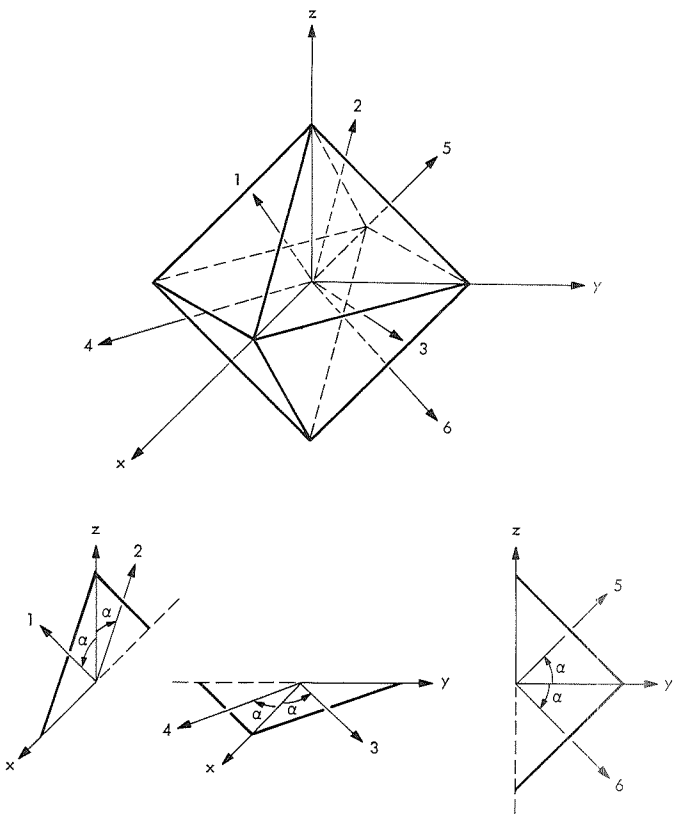

Figure 3. Octahedron six-array gyro configuration ($\alpha = 45$ deg)

Table 1. Transform gains for the three-gyro combinations of the octahedron six-array configuration (σ^2_{ir} = relative variance, c = 0.707)

	1	2	3	σ^2_{ir}	1	2	4	σ^2_{ir}	1	2	5	σ^2_{ir}	1	2	6	σ^2_{ir}
w_x	c	$-c$	0	1.0	c	$-c$	0	1.0	c	$-c$	0	1.0	c	$-c$	0	1.0
w_y	$-c$	c	$2c$	3.0	c	$-c$	$-2c$	3.0	$-c$	$-c$	$2c$	3.0	c	c	$2c$	3.0
w_z	c	c	0	1.0	c	c	0	1.0	c	c	0	1.0	c	c	0	1.0
	1	3	4	σ^2_{ir}	1	3	5	σ^2_{ir}	1	3	6	σ^2_{ir}	1	4	5	σ^2_{ir}
w_x	0	c	c	1.0	c	c	$-c$	1.5								
w_y	0	c	$-c$	1.0	$-c$	c	c	1.5	Coplanar combination				Coplanar combination			
w_z	$2c$	$-c$	$-c$	3.0	c	$-c$	c	1.5								
	1	4	6	σ^2_{ir}	1	5	6	σ^2_{ir}	2	3	4	σ^2_{ir}	2	3	5	σ^2_{ir}
w_x	c	c	c	1.5	$2c$	$-c$	c	3.0	0	c	c	1.0				
w_y	c	$-c$	c	1.5	0	c	c	1.0	0	c	$-c$	1.0	Coplanar combination			
w_z	c	$-c$	$-c$	1.5	0	c	$-c$	1.0	$2c$	c	c	3.0				
	2	3	6	σ^2_{ir}	2	4	5	σ^2_{ir}	2	4	6	σ^2_{ir}	2	5	6	σ^2_{ir}
w_x	$-c$	c	$-c$	1.5	$-c$	c	c	1.5					$-2c$	c	$-c$	3.0
w_y	c	c	c	1.5	$-c$	$-c$	c	1.5	Coplanar combination				0	c	c	1.0
w_z	c	c	$-c$	1.5	c	c	c	1.5					0	c	$-c$	1.0
	3	4	5	σ^2_{ir}	3	4	6	σ^2_{ir}	3	5	6	σ^2_{ir}	4	5	6	σ^2_{ir}
w_x	c	c	0	1.0	c	c	0	1.0	$2c$	$-c$	$-c$	3.0	$2c$	c	c	3.0
w_y	c	$-c$	0	1.0	c	$-c$	0	1.0	0	c	c	1.0	0	c	c	1.0
w_z	$-c$	c	$2c$	3.0	c	$-c$	$-2c$	3.0	0	c	$-c$	1.0	0	c	$-c$	1.0

the 1,2,3; 1,2,4; 1,2,5; and 1,2,6 combinations, the transform gains for w_x and w_z are unchanged, and only the polarities of the (numerically unchanged) gains for w_y are varying. Clearly, these structural features of the transform matrices imply very simple implementation.

The relative variances per reference axis ($\sigma^2_{ir} = \sigma^2_i/\sigma^2_0$) due to the error transformation of the skew geometry are also listed in Table 1 for each three-gyro combination. As may be seen, in most of the cases there is no error amplification; when error amplification does exist, the factor is insignificantly small (1.5 and 3). Furthermore, even the worst-case non-random error amplification factor is reasonably small, having a value 2.82. It is interesting to note that, for the three-gyro combinations of the dodecahedron configuration (References 3 and 4), the highest relative variance is 8.35, and the worst-case non-random error amplification factor is 5. Thus, *the octahedron six-array configuration tends to minimize the maximum error amplification inherent to a skew gyro emplacement.*

The six-array configuration also allows a high-density packaging, as shown in Figure 4. Moreover, *there is no difference between the packag-*

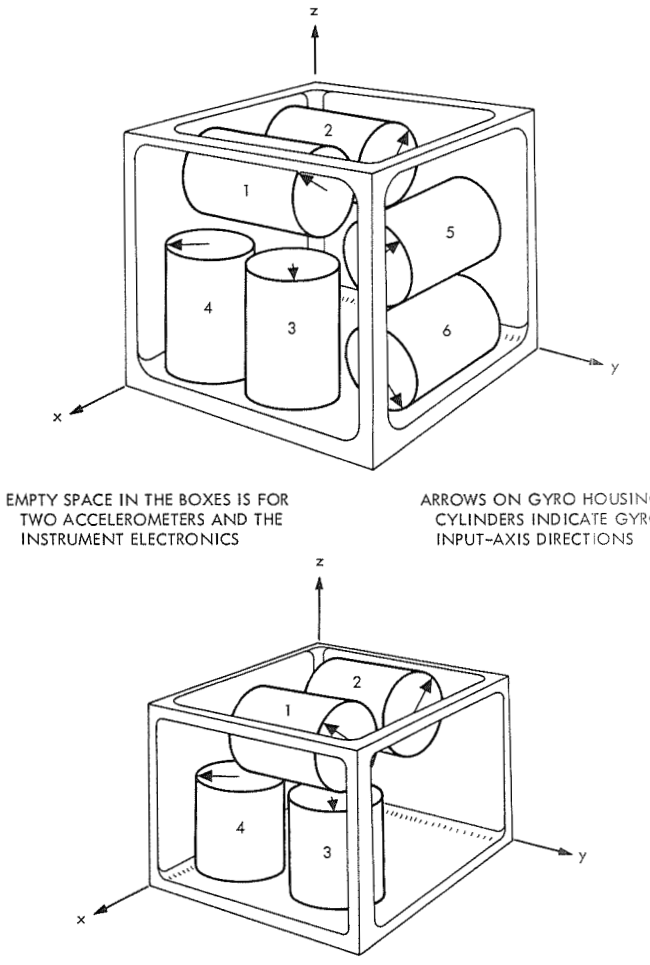

Figure 4. Packaging of six and four gyros in an octahedron-based emplacement

ing for the octahedron six-array configuration and that for an orthogonal emplacement of six gyros, as is apparent from Figure 4. Furthermore, the 45-deg emplacement symmetry implies substantial advantages in the fabrication process (making alignment fixtures, cutting angles in a metal) and in laboratory test procedures. In fact, system testing may be performed on a single-axis test pad basis.

Four-Gyro Case

When only minimum redundancy is required for the IRU, it can be provided by using four gyros in a non-orthogonal emplacement. (In an orthogonal emplacement, minimum redundancy can only be obtained by using six gyros.) Three different non-orthogonal emplacements of four gyros can very easily be constructed from the octahedron six-array configuration, *retaining all the advantages of that configuration.* The three

different non-orthogonal emplacements of four gyros will be equivalent to having gyros 1,2,3,4; 1,2,5,6; or 3,4,5,6 (Figure 3) in the IRU package. The transform gains corresponding to the relevant three-gyro outputs of those three four-gyro packages can easily be identified in Table 1. As may be seen, the only difference between the three four-gyro packages is that each package has a different preference axis where no error amplification occurs in all three-gyro combinations. It is interesting to note that the theoretically optimum four-gyro emplacement (Reference 1) yields a relative variance of 1.5 for all three reference axes in all three-gyro combinations, while, in the octahedron six-array-based four-gyro emplacement, the three-gyro combinations yield no error amplification on two reference axes and an error amplification factor of 3 on the third axis. This factor shifts its location between two axes for the different three-gyro combinations. A compact packaging arrangement for the octahedron six-array-based four-gyro emplacement is shown in Figure 4.

Reliability Merits

In the octahedron six-array configuration, the useful "three-out-of-six" gyro combinations for full attitude reference are reduced to 16 from 20, the maximum value achievable by a six-gyro skew configuration. It is felt, however, that the small reduction of the redundancy capability in the six-array configuration is compensated by the great simplicity in measurement processing. It is also noted that *the redundancy capability of the octahedron six-array configuration in combinatorial terms is still twice as high as the redundancy capability of six gyros in an orthogonal emplacement.*

The four coplanar three-gyro combinations of the octahedron six-array configuration have a small impact on the functional reliability of the octahedron six-array IRU, as may be seen in Figure 5, which displays the reliability functions of six different gyro configurations. Figure 5 was computed assuming perfect failure monitoring accomplished by external means (e.g., voltage sensing) and continuous operation of all gyros, with only failed gyros turned off. These assumptions have no significant effect on the *relative* reliability merits of different gyro configurations, provided: (1) failure monitoring has considerably higher reliability than that for the individual gyros, and (2) the shelf-life degradation of gyros is considerably smaller than the gyros' active wear-out rate. Additional reliability functions for different gyro configurations and operation modes and for different failure monitoring techniques can be found in Reference 6.

It is noted that the octahedron six-array-based four-gyro configurations possess the full redundancy capability that is available with a linearly independent four-gyro skew emplacement.

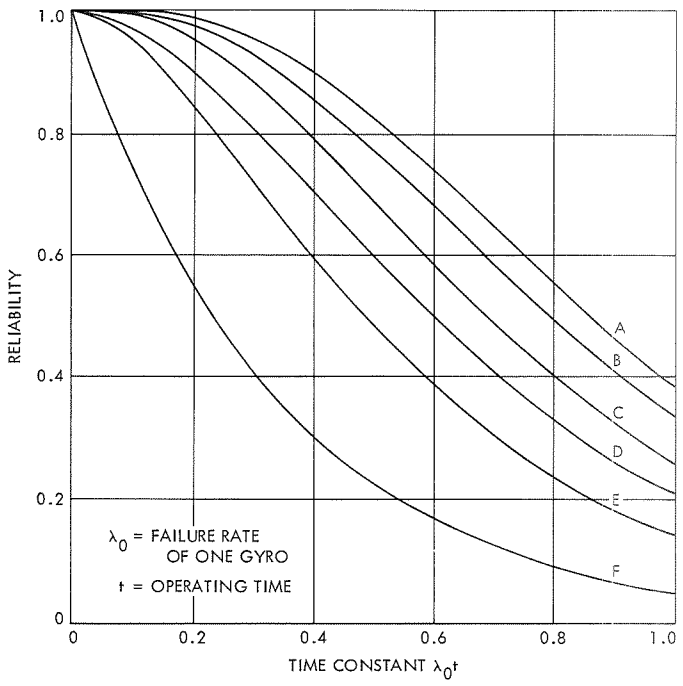

A OPTIMUM (SKEW) CONFIGURATION OF SIX GYROS
B OCTAHEDRON (SKEW) CONFIGURATION OF SIX GYROS
C SKEW CONFIGURATION OF FIVE GYROS
D ORTHOGONAL EMPLACEMENT OF TWO GYROS ON EACH AXIS
E SKEW CONFIGURATION OF FOUR GYROS
F NON-REDUNDANT IRU

Figure 5. Reliability functions of six gyro configurations

Concluding Remarks

Non-orthogonal redundant gyro configurations offer several useful operation options: (1) Operating four gyros at a given time, *instant* full attitude reference is available if *any one* of the four gyros has failed; (2) operating five gyros at a given time, one failed gyro can be identified by a data processing technique; and (3) even one skewed gyro is useful for in-line estimation of full attitude reference.

References

1. Barnhill, D. H., and Susens, D. C., "Digital Attitude Reference, Redundancy and Temperature Control Considerations," paper presented at the AIAA/JACC Guidance and Control Conference, Aug. 15–17, 1966.

2. Weiss, R., and Nathan, I., "An Ultra-Reliable Attitude Reference System for a Manned Orbiting Laboratory with Limited Sparing Capability," paper presented at the AIAA Guidance and Control Conference, Seattle, Wash., 1966.

References (contd)

3. Gilmore, J. P., *A Non-Orthogonal Gyro Configuration,* M.S. thesis. Massachusetts Institute of Technology, Cambridge, Jan. 1967.

4. Gilmore, J. P., and McKern, R. A., "A Redundant Strapdown Inertial System Mechanization—SIRU, paper presented at the AIAA Guidance and Control Conference, Santa Barbara, Calif., Aug. 17–19, 1970.

5. Pejsa, A. J., "Optimum Orientation and Accuracy of Redundant Sensor Arrays," paper presented at the AIAA 9th Aerospace Sciences Meeting, New York, N.Y., Jan. 25–27, 1971.

6. Bejczy, A. K., *Reliability Merits of Different Redundant Orthogonal and Non-Orthogonal Single-Axis Gyro Configurations,* JPL Internal Document EM 344-301-AKB. Jet Propulsion Laboratory, Pasadena, Calif., Jan. 21, 1971.

Analytically Determined Response of a 300-μm Silicon Detector to a Polyenergetic Beam of Neutrons[1]

M. Taherzadeh

Guidance and Control Division

Nuclear radiation from a radioisotope thermoelectric generator used as the prime energy source for electrical power in a space mission could severely affect scientific instruments or detectors on the spacecraft. Therefore, a thorough analysis and evaluation of the types of radiation and their effects on the detectors were necessary.

In this article, the response of a 300-μm silicon detector to an incident polyenergetic neutron beam emitted from a plutonium dioxide fuel power source is determined. The results indicate that the response of the detector is basically due to elastic scattering reactions, and the contribution from other reactions is very small. For neutron energies greater than 4.5 MeV, the (n,p) and (n,α) reactions contribute less than 2% to the total response. The maximum response for this detector is less than 4×10^{-3} counts/neutron within the range of bias energies of 25 to 250 keV. Moreover, this maximum value will decrease if consideration is given to the pulse height defect phenomenon.

Introduction

Nuclear radiation (mainly, neutrons and gamma rays) is emitted when a radioisotope thermoelectric generator is used as the prime energy source for electrical power on a spacecraft. The neutrons and photons are emitted from the plutonium fuel power source with a flux level that depends upon the impurities and the age of the fuel itself. The neutrons interact directly with the spacecraft's scientific instruments or detectors; also, when detectors are shielded against primary photons, additional radiation is generated by inelastic scattering and the radiative capture of the source neutrons within the shield. Since this radiation could severely affect the detectors, it is essential that the types of radiation and their effects on the detectors be thoroughly analyzed and evaluated.

[1]Based on Reference 1.

Response of a Bare Detector

The response of a bare 300-μm silicon detector to neutrons can be studied by an analytical scheme using the probability laws of interactions and energy and angular distributions. In the case of a bare, very thin detector such as discussed here and low-energy neutrons, the pulse height can be estimated easily using kinematical equations. This, of course, does not mean that the exact response can be calculated by such a simplified scheme. Nevertheless, if the response of a silicon detector is estimated for a worst case and shown to be much below the response to the primary gamma rays from the source, the importance of neutrons as far as additional shielding is concerned would be reduced. Since the main emphasis of this analysis is the response to neutrons emanated from a plutonium dioxide fuel power source, the neutron source spectrum is examined first.

The neutron flux and the flux spectrum of a typical plutonium dioxide fuel power source are presented in Figure 1. The fuel is a multihundred-watt (2-kW) power source that emits a total of 4.59×10^4 neutrons/g-s. At 50 cm from the center of the source and at zero angle with respect to the major axis of the fuel, the total flux is 5.43×10^3 neutrons/cm^2-s. From this flux distribution, it is concluded that the average neutron energy is about 2 MeV, and the maximum neutron energy can be as high as 10 MeV or more, but with a very small neutron abundance.

In order to limit the analysis to the number of nuclear reactions involved, a maximum can arbitrarily be set for the neutron energy so that the percent of neutrons to be ignored contributes an insignificant amount to the overall response of the detector. One such arbitrarily selected maximum energy is 6 MeV; the neutrons with energies above this value contribute less than 0.5%.

With a range of energies for the released neutrons having been selected, the response of a silicon detector to a beam of neutrons emitted from a plutonium dioxide fuel power source can now be calculated. The total and the partial neutron cross sections as functions of neutron energies up to 6 MeV (Reference 2) are presented in Figure 2. Elastic scattering (n,n) and inelastic scattering $(n,n'\gamma)$ reactions and (n,α), (n,p), and radiative capture (n,γ) reactions (the neutron disappearing reactions) are considered here. The significant features of these cross sections are:

(1) The (n,p) and (n,α) reactions become important beyond a neutron energy of about 4.5 MeV; however, at these high neutron energies, the neutron abundance diminishes very rapidly. For this reason, reactions that are kinematically possible but have high threshold energies, such as $(n,2n)$ reactions, are not included in this analysis,

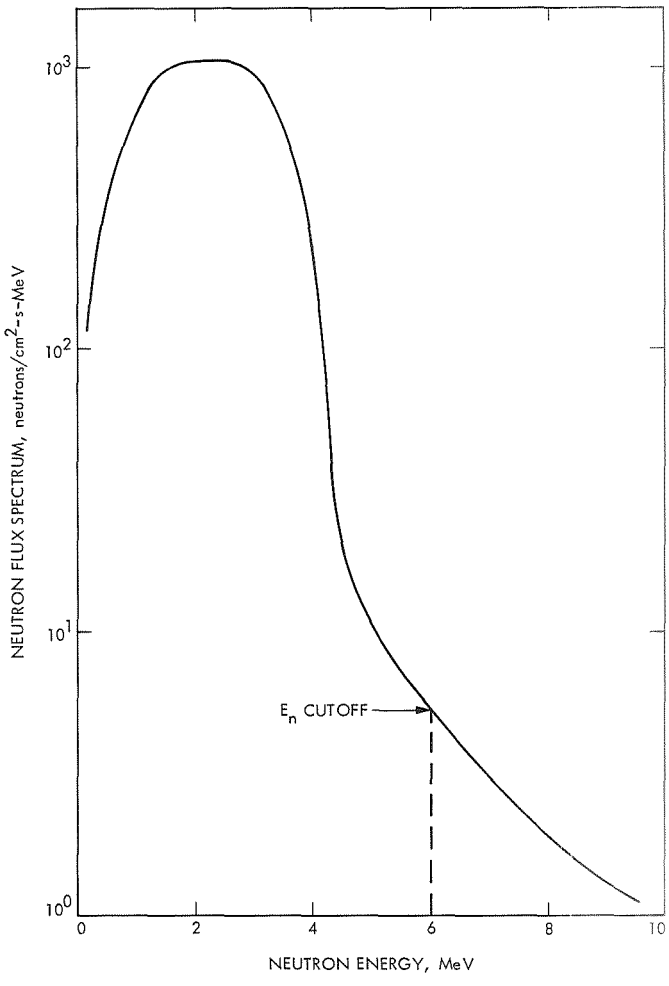

Figure 1. Neutron flux spectrum as a function of neutron energy

and the contributions from such reactions should be considered extremely small.

(2) At low neutron energies (i.e., below 1.5 MeV), only (n,n) and (n,γ) reactions are possible.

(3) In the medium range of neutron energies (i.e., 1.5 to 5 MeV), the difference between the total cross section and the elastic scattering cross section increases with energy, but the difference still remains small. This means that, in this neutron energy range, the (n,n) reaction is the most important.

Thus, the (n,p) and (n,α) reactions can be considered as a source of background, but the (n,n) reaction is by far the largest contributor. The (n,γ) and $(n,n'\gamma)$ reactions have much smaller cross sections, and the

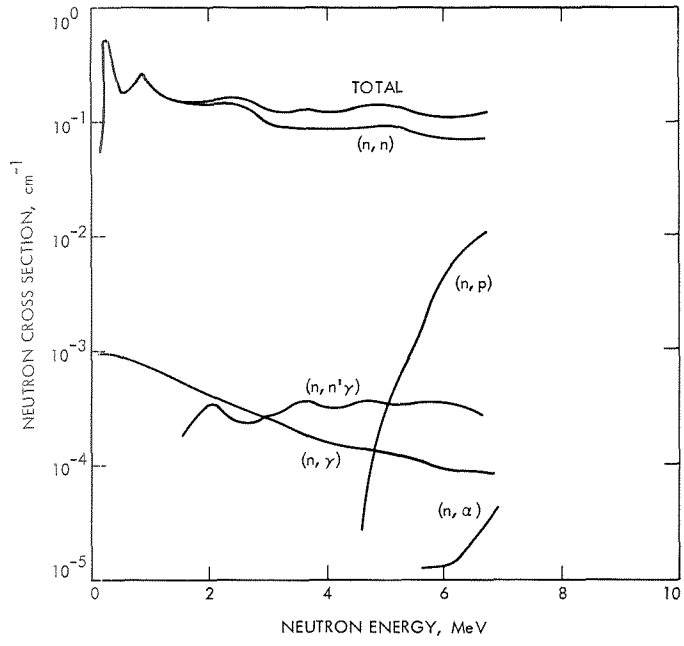

Figure 2. Neutron cross section as a function of neutron energy

emitted photons escape the detector's sensitive area before depositing any energy. In Table 1, the neutron–silicon reactions are listed with their corresponding emitted secondary particles and various characteristics of the reactions. The $(n,2n)$ reaction is included as an example of the reactions that will not be considered due to their high threshold energies and low neutron flux levels.

The response function of a detector medium at a given neutron energy E_n and when angular distribution in the center-of-mass (CM) system is assumed isotropic is given by

$$R(E_n,E_B) = \epsilon_D(E_n) \int_{E_B}^{(E_{Si})_{max}} \frac{dE_{Si}}{\gamma_D E_n} \left[\left(1 - \frac{< \Delta E >}{E_{Si}} \right) \sum_\nu \frac{2\nu + 1}{2} \right.$$

$$\left. \times \alpha_\nu (E_n) P_\nu \left(1 - \frac{2E_{Si}}{\gamma_D E_n} \right) \right] + \epsilon_{\alpha,p}(E_n)\, \delta_{\alpha,p} \qquad (1)$$

where E_B is the bias energy; ϵ terms are efficiency functions; $(E_{Si})_{max}$ is the maximum silicon recoil energy; γ_D is a constant that, for the silicon recoil, is 0.1332; and $< \Delta E > / E_{Si}$ is the fraction of non-ionizing energy dissipated in the medium and, thus, not contributing to the charge collection process of the detector. The P_ν term represents the Legendre polynomials of degree ν, with α_ν as their coefficients; these energy-dependent

Table 1. Characteristics of neutron–silicon reactions[a]

Type of reaction	Specific reaction	Quantity of heat Q, MeV	Threshold neutron energy $(E_n)_{th}$, MeV	Neutron abundance at $(E_n)_{th}$, %	Maximum energy of charged particles, MeV	Range of charged particles, μm	Reaction cross section,[b] $cm^2 \times 10^{-24}$ (=barns)
Neutron disappearing	$Si^{28}(n,\alpha)Mg^{25}$	−2.7	2.66	13	2.68	9	0
Neutron disappearing	$Si^{28}(n,p)Al^{28}$	−3.9	3.66	8.3	1.81	44	0
Elastic scattering	$Si^{28}(n,n)Si^{28}$	0	0	—	0.798	0.045	2.915
Inelastic scattering	$Si^{28}(n,n'\gamma)Si^{28}$	0	0	—	—	—	0.00364
Radiative capture	$Si^{28}(n,\gamma)Si^{29}$	8.47	0	—	—	—	0.0111
Other particle producing	$Si^{29}(n,2n)Si^{28}$	−8.47	8.81	0.14	—	—	0
Other particle producing	$Si^{28}(n,n'p)Al^{27}$	−11.6	12.06	—	—	—	0

[a]Maximum neutron energy $(E_n)_{max} = 6$ MeV.

[b]At 1.5 MeV.

coefficients are obtained from Reference 3, where up to a ninth-order polynomial was used to reproduce the angular distribution of the neutrons. All nine coefficients at any neutron energy are used in this calculation. The $\delta_{\alpha,p}$ term represents the fact that (n,α) and (n,p) reactions can contribute to the total response if $E_{\alpha,p} - < \Delta E >_{\alpha,p} \geq E_B$.

The detector's efficiency function for normal incidence, $\epsilon_D(E_n)$, is generally given by

$$\epsilon_D(E_n) = 1 - \exp\left[-\mu(E_n)t\right] \tag{2}$$

where $\mu(E_n)$ is the attenuation coefficient of the detector and t is the sensitive thickness. The curves for the efficiency functions for (n,n), (n,p), and (n,α) reactions and the curve for the total value for a 300-μm silicon detector are presented in Figure 3. The shape of the curve for the total

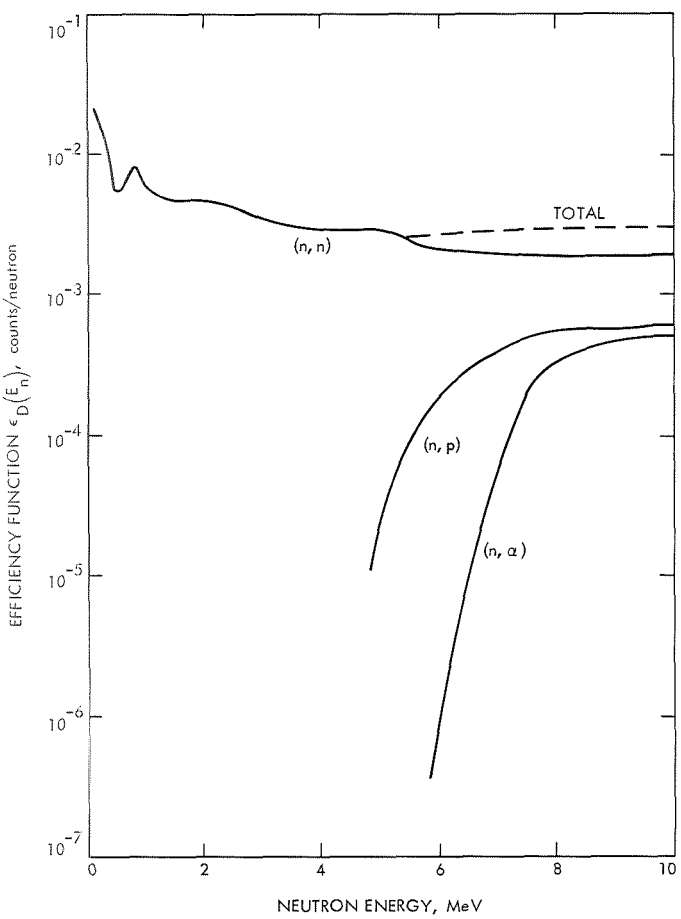

Figure 3. Efficiency function ϵ_D (E_n) as a function of neutron energy

value follows that for the total cross section because the effective thickness of the detector is small and

$$\epsilon_D(E_n) = tN\sigma\,(E_n) \tag{3}$$

where $N\sigma$ is the neutron cross section. Since the energy transferred to the silicon by neutrons is $0.133E_n \sin^2(\theta_{CM}/2)$, where θ_{CM} is the angle in the CM system, $(E_{Si})_{max}$ is obtained when $\nu = 0$, $\theta_{CM} = 180$ deg, and the energy distribution function for the silicon nuclei after collision is $1/(E_{Si})_{max}$. The probability function is given by $1 - [E_B/(E_{Si})_{max}]$, and the response function is

$$R(E_n,E_B) = \epsilon_D(E_n,t)\left(1 - \frac{E_B}{0.133E_{Si}}\right), \qquad \nu = 0 \tag{4}$$

In Figure 4, the response function is plotted for various values of E_n and E_B. The contribution from protons generated in (n,p) reactions and the contribution from alpha particles generated in (n,α) reactions are indeed small. At low E_n, these charged particles do not exist; at high E_n, the contribution from protons is more than one order of magnitude lower and the contribution from alpha particles is about five orders of magnitude lower than the pulse height generated by elastic scattering of neutrons. Therefore, at E_n up to 5 MeV, the major portion (~99%) of

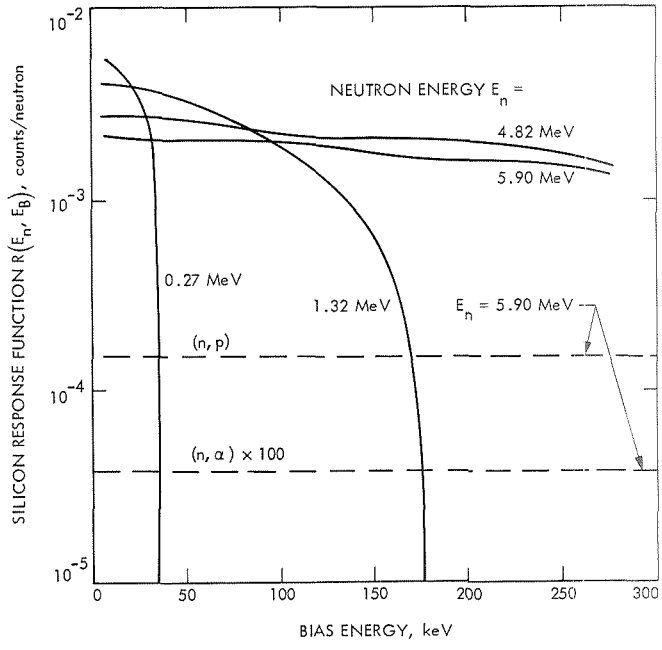

Figure 4. Silicon response function $R\,(E_n, E_B)$ as a function of bias energy

counts comes from the silicon nuclei after being struck by neutrons, and, at 6 MeV, nearly 90% of the response is due to this reaction. The protons and alpha particles generated within the detector are completely absorbed since the edge effects are small. For this reason, they must be included in the pulse height calculation since the time interval for the ionization process is much smaller than the charge collection time interval, and the deposited energy is equal to the maximum energy if it is above E_B.

The neutron flux ϕ from the fuel capsule can also be included in the response function; thus, in the $[0,(E_n)_{max}]$ energy interval, the response of the silicon detector at E_n is

$$\frac{dC(E_n)}{dE_n} = \frac{\phi(E_n)AR(E_n,E_B)}{\phi_0} \tag{5}$$

where A is the detector's cross-sectional area and $dC(E_n/dE_n$ is given in counts/(neutron/cm^2)-MeV. The total silicon counting rate for a polyenergetic neutron beam with energies up to $(E_n)_{max}$ is

$$C(E_n) = \int_{(E_n)_{min}}^{(E_n)_{max}} \phi(E_n)AR(E_n,E_B)dE_n \tag{6}$$

where $(E_n)_{min}$ is the minimum neutron energy allowed for a given E_B (i.e., $7.55E_B$).

Equation 6 is plotted in Figure 5 for the same E_n values used in Figure 4; $C(E_n)$ is given in counts/s for energies from $(E_n)_{min}$ up to $(E_n)_{max}$. The total counting rate at a given E_n depends upon E_B. At $E_B = 100$ keV and $E_n = 5$ MeV, the counting rate is about 20 counts/s when angular distribution is assumed isotropic; no pulse height defects are taken into account, and the total neutron flux for this case is only 151 neutrons/cm^2-s.

Response of a Detector Subject to Pulse Height Defects

The response function calculated in the previous section is yet subject to another restriction, namely, the pulse height defect. This effect is more pronounced in the case of silicon detectors because the pulse height is mainly due to the elastic scattering of neutrons.

Neutrons transfer their energies to the silicon-sensitive medium by atomic scattering and nuclear reactions, rather than through an electronic ionization process. The secondary charged particles produced by the neutron interaction, such as protons, alpha particles, and silicon nuclei,

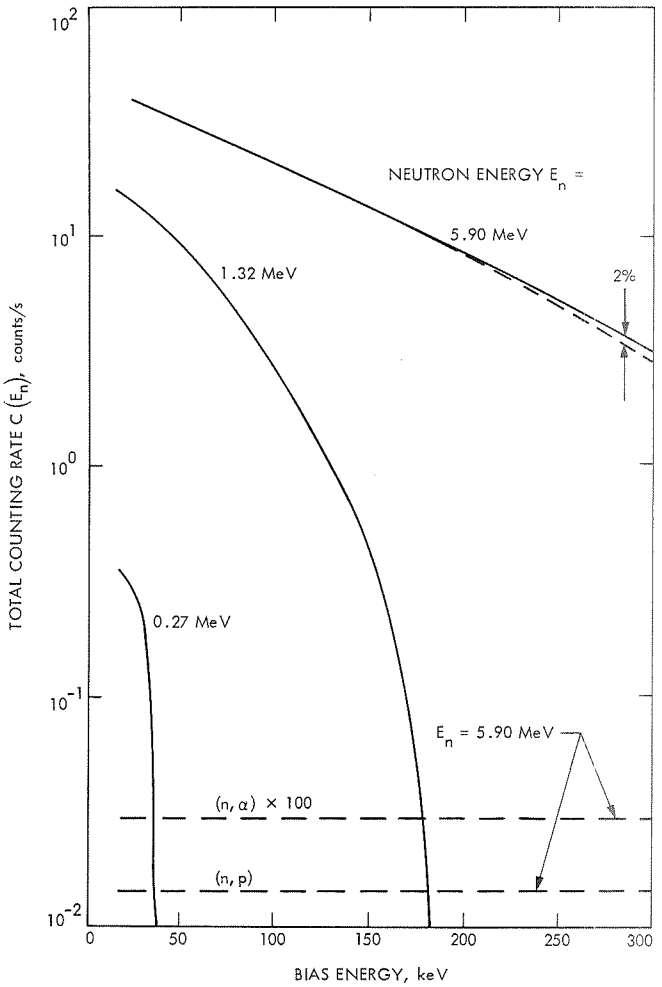

Figure 5. Total counting rate C (E_n) as a function of bias energy

in turn transfer their energies to the medium by ionization and nuclear charge scattering. The photons generated in the (n,γ) and $(n,n'\gamma)$ reactions escape the medium in most cases and thus will not deposit energy. The non-ionizing processes contribute to the pulse height defect. The ionization causes the displacement of electrons, while nuclear charge scattering (Rutherford scattering) causes the displacement of atoms from their equilibrium position and leaves vacancies in the lattice.

The maximum energies and ranges of the protons, alpha particles, and silicon nuclei were presented in Table 1. Since 300 μm was selected as the depletion depth of the detector, nearly all of these charged particles remain inside. The energy transferred to the silicon is $(E^i_{Si})_{max} \sin^2 (\theta_{CM}/2)$, where $(E^i_{Si})_{max}$ is the maximum transmitted energy. If r_i is the ratio of

the mass of the silicon atom to the mass of the ith charged particle (namely, proton, alpha particle, or silicon nucleus), then

$$E_{Si}^{i} = 4r_i E_i (1 + r_i)^{-2}$$

Since $r_p = 28$, $r_\alpha = 7$, and $r_{Si} = 1$,

$$(E_{Si}^{p})_{max} = 0.1332(E_p)_{max}$$

$$(E_{Si}^{\alpha})_{max} = 0.438(E_\alpha)_{max}$$

$$(E_{Si}^{Si})_{max} = (E_{Si})_{max}$$

If the maximum energies of the charged particles for a 6-MeV neutron beam from Table 1 are used, then

$$(E_{Si}^{p})_{max} = 240 \text{ keV}$$

$$(E_{Si}^{\alpha})_{max} = 1170 \text{ keV}$$

$$(E_{Si}^{Si})_{max} = 798 \text{ keV}$$

However, in the real case, only fractions of these energies are transmitted to the medium by ionizing processes, and the remainder contribute to the pulse height defect.

Figure 6 presents the fraction of the pulse height defect as a function of the charged particle energy and considers up to two neutron scatters. It may be seen that the pulse height defect is important only at low

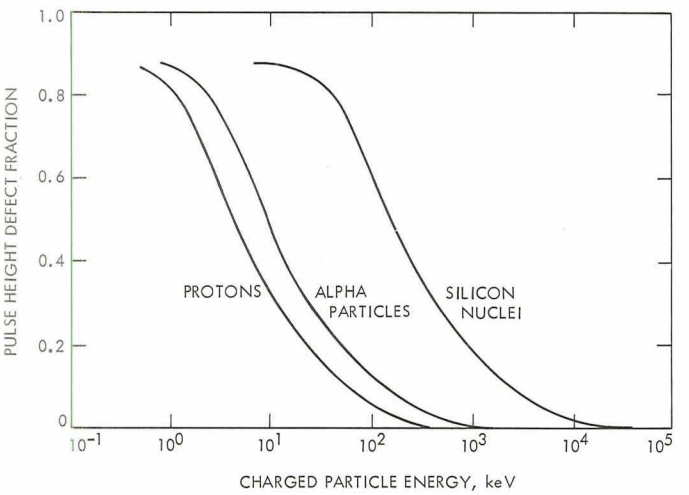

Figure 6. Pulse height defect fraction as a function of charged particle energy

energies, and, within this range, the pulse height defect due to the silicon nuclei is much greater than that due to protons or alpha particles. For example, for a 100-keV charged particle energy ($E_n = 4.5$ MeV for protons, 4.0 MeV for alpha particles, and 0.75 MeV for silicon nuclei), the pulse height defect due to protons is about 6 keV, that due to alpha particles is about 12 keV, and that due to silicon is about 60 keV.

The pulse height defects can now be included in the silicon responses presented in Figure 4. For $E_n = 1.32$ MeV, only silicon nuclei with a maximum energy of 175 keV need to be considered; if E_B is set at higher values, there would be no response. The pulse height defect at this energy (Figure 6) indicates that 58% of the energy is transmitted to the medium by the non-ionizing processes; thus, E_B needs to be set even lower (74 keV) if any response is desired. At high E_n (i.e., 6 MeV), the maximum energies of the charged particles are those given in Table 1, and the pulse height defects are 48 keV for protons, 159 keV for alpha particles, and 528 keV for silicon nuclei. This means that protons and alpha particles will contribute to the total response, but there will be no pulse height due to the (n,n) reaction if $E_B > 270$ keV.

Concluding Remarks

The following remarks summarize the results of this analysis:

(1) For the E_n range of 0.27 to 6 MeV and E_B range of 25 to 250 keV, the maximum response of a 300-μm silicon detector is about 4×10^{-3} counts/neutron.

(2) For an E_n or E_γ of 3 MeV and an E_B of 50 keV, the response of the silicon detector to neutrons is about 11% of the response to the source gamma rays (i.e., $R_n = 0.0029$ and $R_\gamma = 0.025$; Reference 4).

(3) For an E_B range of 50 to 250 keV and for a neutron flux emitted from a multihundred-watt (2-kW) plutonium dioxide fuel power source, the counting rate is estimated to be about 31 to 5 counts/s.

Acknowledgment

The author wishes to express his appreciation to Dr. M. Reier of the JPL Guidance and Control Division for his valuable remarks during this investigation.

References

1. Taherzadeh, M., and Anno, G., "The Response of a 300μ Silicon Detector to Monoenergetic Neutrons Determined by the Use of the

References (contd)

Monte Carlo Technique," paper presented at the National Symposium on Natural and Man-Made Radiation in Space, Las Vegas, Nevada, March 1–5, 1971, sponsored by AEC/NASA (proceedings to be published).

2. Ray, J. W., et al., *Neutron Cross Sections of Nitrogen, Oxygen, Aluminum, Silicon, Iron, Deuterium, and Beryllium,* UNC-5139. United Nuclear Corporation, Elmsford, N.Y., Nov. 1965.

3. Campbell, R. W., et al., *Compilation, Evaluation and Deduction of Neutron Differential Scattering Data, Vol. IV,* NAA-SR-11980. Atomic International, 1967.

4. Reier, M., *The Response of a Shielded 300μ Silicon Detector to Monoenergetic Gamma Rays From 0.279 to 2.75 MeV,* JPL Internal Document EM 342-118. Jet Propulsion Laboratory, Pasadena, Calif., Sept. 14, 1970.

Remote Examination of Rock Specimens

J. D. Burke

Advanced Technical Studies Office

R. Choate

Space Sciences Division

R. B. Coryell

Project Engineering Division

In JPL studies of prospects for post-*Apollo* lunar exploration, methods are being considered for extending the *Apollo* observations into a more complete understanding of the moon's bulk composition, mode of accretion, and thermal history. Based on *Apollo* samples to date, it appears that relatively simple remotely controlled methods may be adequate for characterizing lunar materials found along extended surface traverses. To investigate this possibility, studies and experiments have been made to determine (1) what performance can be expected from a minimum rover-borne system with imaging and sample manipulation, and (2) the advantages conferred by desirable additions, such as close-up color imaging, various types of microscopy, and chemical or mineral analysis using X-rays. Laboratory and field experiments reported in this article support the feasibility of this prospect and identify some characteristics of an automated system required to realize this technique.

Introduction

In JPL studies of prospects for post-*Apollo* lunar exploration, one objective has been to find methods for extending the *Apollo* observations into a more complete understanding of the moon's bulk composition, mode of accretion, and thermal history. With the suite of *Apollo* samples as a starting point, it appears that relatively simple remotely controlled methods may be adequate for characterizing lunar materials found along extended surface traverses. To investigate this possibility, studies and experiments have been made to determine (1) what performance can be expected from a minimum rover-borne system with imaging and sample

manipulation, and (2) the advantages conferred by desirable additions such as close-up color imaging, various types of microscopy, and chemical or mineral analysis using X-rays.

These remote techniques cannot, of course, equal the quality and variety of the analytical methods available on earth. However, because of the great amount of information provided by *Apollo* at isolated surface sites, extension to other regions may be feasible with more limited methods. The object of the tests reported here was to verify this prospect.

Laboratory Imaging Experiments

The first task was to determine the general performance limits of imaging systems required for the later work. By means of simple experiments in the Image Processing Laboratory, it was found that standard closed-circuit television systems available on loan from other JPL programs could be used with minor modifications to simulate the ranges of resolution and other picture parameters considered practical for transmission from lunar rovers (Reference 1). Samples of sand (Figure 1) with various particle sizes and shapes were used to define the limits of acceptable illumination, magnification, contrast, and so forth for identification of the material being viewed. Next, rock samples were examined and it

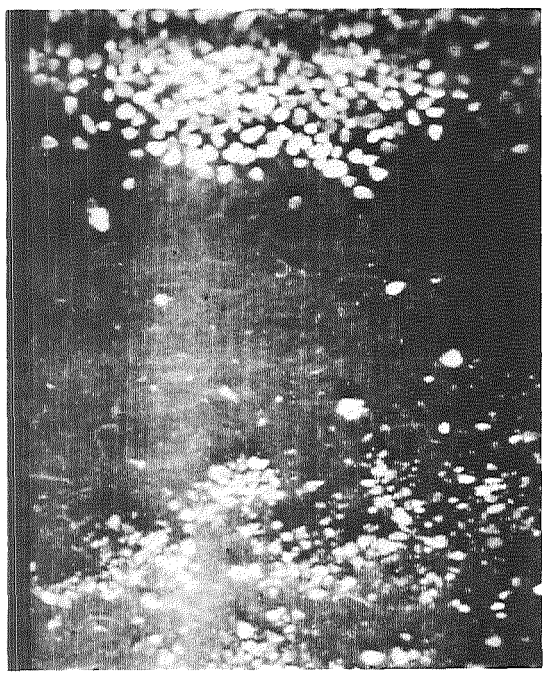

Figure 1. TV image of two sand samples; particle size 100–500 μm

was immediately evident that identification would require three more features:

(1) An ability to rotate the sample, the camera, and the direction of illumination relative to each other.

(2) A size calibration such as a scale in the field of view (or, if an internal reticle is used, a measurement of distance to the sample).

(3) A gray scale in the field of view.

These provisions were easily added in the Science Experiment Test Laboratory (SETL), and a series of identification tests were run using the setup shown in Figures 2 and 3. The samples, mounted on a pan-and-tilt stand and illuminated by the movable collimated light source built for *Surveyor* shadow simulations, were viewed via black-and-white television cameras (with various lenses) by several experienced geologists, petrologists, and mineralogists who recorded their observations, commented on the adequacy of picture parameters such as magnification and depth of field, and attempted to identify the rocks. Then, following the TV session, each observer viewed the samples directly and, if desired, with a hand lens to verify or correct his previous identifications. In this way the limits of required system performance were outlined for various

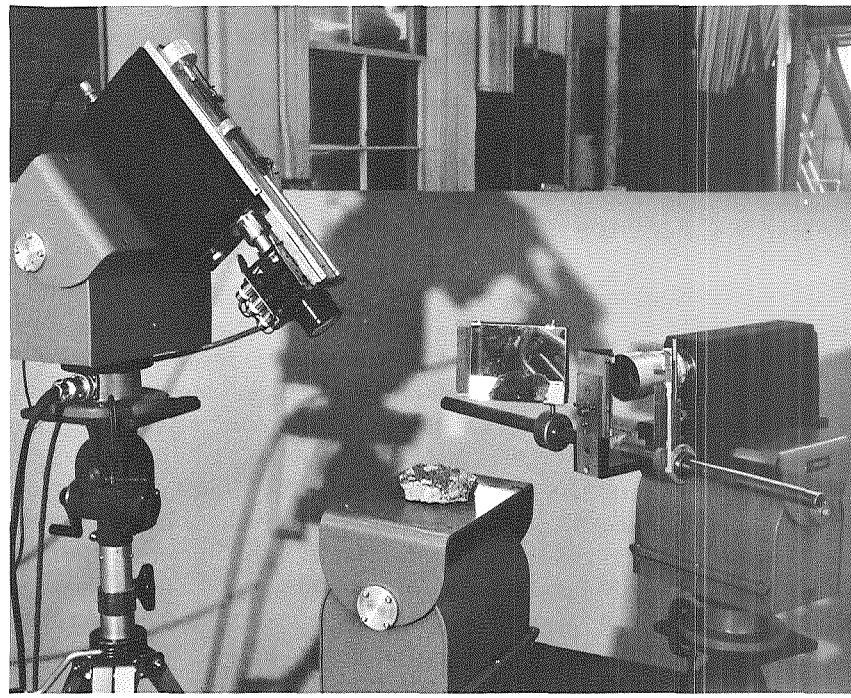

Figure 2. TV cameras with zoom and stereo attachments viewing sample illuminated by movable collimated light source. Pan-and-tilt stands and camera lenses are remotely controlled

Figure 3. Control console for remote manipulators and cameras. Window is curtained to prevent direct viewing during tests

classes of samples. As expected, freshly broken rock surfaces were preferred by all observers; an ability to break open the lunar samples is obviously desirable, particularly when the ubiquitous lunar dust is considered, and is feasible as shown by *Surveyor* experience (Reference 2). The results of this first test series are summarized in Table 1.

The observers were asked to evaluate their own ability at describing rock textures by use of the remote TV system in comparison to their ability with a hand-held specimen. Evaluations were mostly restricted to about five different rock specimens, ranging in type mainly from fine-grained basalt to medium-grained diorite. The specific textural features evaluated included the four principal ones listed by Tyrrell in *Principles of Petrology* (Reference 3). The ratings for the individual petrographers mostly ranged between 75 and 100%; the extreme values, based on individual specimens, ranged from 40 to 100%. The mean values for the principal textures (as averaged for the observers) are: degree of crystallinity, 85%; grain size, 95%; grain shape and crystal-face development, 85%; and intergrain relationships, 80% (Table 1). The average for all petrographers for these four principal textural features was 85%.

The observers' evaluation of their capability at mineral identification via remote TV ranged from 50 to 75% of their ability with a hand-held

Table 1. Quantitative evaluation of the petrographic data obtained by 300-line resolution TV in comparison to a hand-held specimen[a]

Petrographer	Textural features					Mineral identification features	
	Degree of crystallinity	Grain size	Grain shape and crystal face development	Intergrain relationship	Volcanic textures	Number of minerals present	Mineral identification
Number 1	100	100	75	75	75	50	75
Number 2	40 100	95 100	90 100	75 100	— 70	90 60	50 —
Number 3	75	100	75	50	—	—	50
Number 4	100	75	75	75	—	—	—
Number 5	90	100 100	100 80	90 80	—	50	—
Average for individual features	85	95	85	80	75	65	60
Average for major textural features	85						
Overall average	80						

[a]All values to nearest 5%.

specimen using a 10× hand lens. The average value for all petrographers was between 60 and 65%. The average for all seven textural and mineral identification features that were individually rated was 80% (Table 1).

The major difficulty in the evaluation program was inadequate resolution of the first TV system used, so that certain critical mineral phenomena, such as twinning, cleavage, and color differences, were either not visible or were not identifiable. Object resolution based on tests with high-contrast sand grains was approximately 50 μm. Center vertical and horizontal resolution of the TV pictures averaged approximately 300 lines. Substantially better resolution and much higher magnifications were available in the TV systems used in later tests; the data reported here are for the early system, representing about the minimum acceptable from a lunar rover.

Several observers emphatically stated that detailed visual examination should be not only the first but also the primary technique used in analysis of rock specimens on any automated long traverse. It was emphasized that it should be possible to determine 80 to 90% of the petrographic information in most rock specimens—pertaining to textures and to identification of the essential and main accessory minerals—from any technique equal to that of hand-specimen field examination with a 10-power hand lens. A major advantage of visual examination is that many specimens can be examined rapidly; during a lunar or planetary mission, the visual images and other data concerning these rock specimens would be recorded on magnetic tape for later detailed evaluation.

It is readily acknowledged that the study of textures, including all those discussed above, is best done in thin section under a petrographic polarizing microscope. However, the problems involved in the complex preparation of thin sections remotely on the moon, the cost in payload weight, and the probable consumption of substantial mission operations time all weigh against this procedure in the near future. A useful substitute for thin-section examination is the observation of freshly broken rock specimens in reflected light under high magnifications of 40 to 50 power. If the capability of examining mineral fragments under transmitted polarized light is also added, then powerful scientific tools indeed are available for use by the lunar or planetary geologist—tools both for rapid mineral identification and for textural description of the rocks encountered on a traverse.

Field Experiments

Following the tests with isolated specimens, the next logical step was to add the information that is available to an accomplished geologist when he views the surroundings in which the sample is found. On two occasions JPL has experimented with remotely controlled instruments in

the Southern California desert. The purpose of these experiments has been to identify functional and operational requirements for a remotely controlled mobile payload.

The first experiment, reported in References 4 and 5, used a battery of four TV cameras mounted on top of an electronics van (Figure 4). A geologist inside the van was provided an 80-deg field of view on four monitors (Figure 5). A fifth monitor allowed the geologist to direct the operation of the sampling TV camera and various sampling instruments outside the van (Figure 6).

Figure 4. Truck used for field tests, showing controllable array of TV cameras

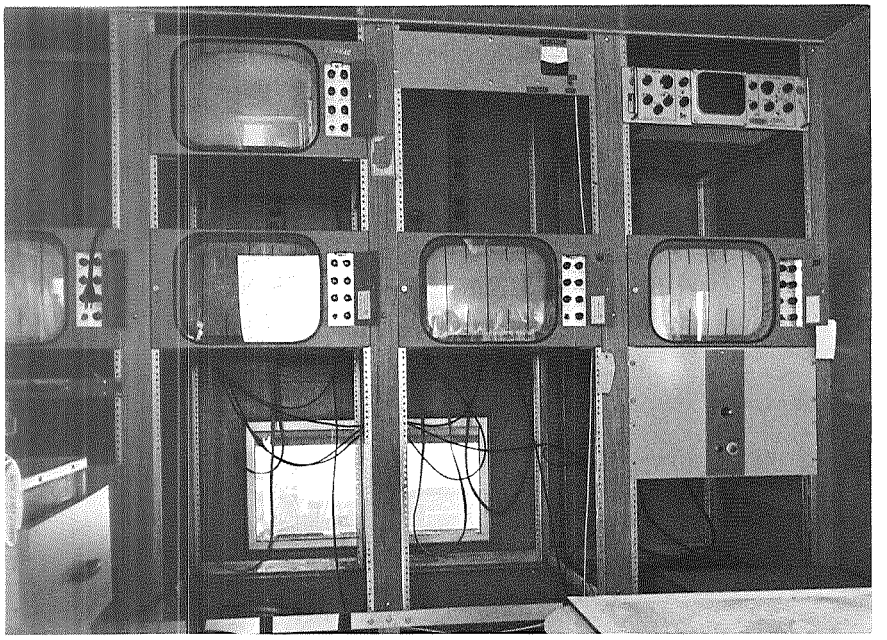

Figure 5. TV monitors inside truck for first test

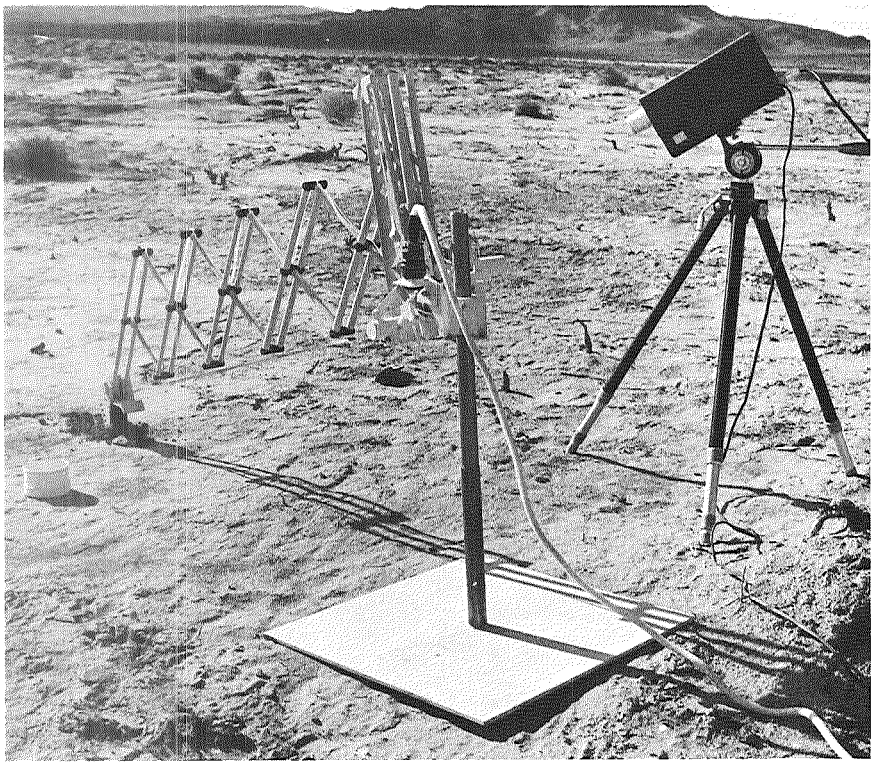

Figure 6. *Surveyor* sampler and sampling camera

Exercises in geological reconnaissance with TV imagery were conducted at 13 stations and sampling exercises at 9. Sample analysis was limited to imagery obtained by the sampling camera (zoom lens included). Conclusions made or confirmed by these exercises are listed in Table 2.

The second experiment, conducted in December 1970, used the same van. In place of TV cameras with overlapping field of view, film panoramas, simulating the images that would be obtained by a photofacsimile scanner on a lunar rover, were used. They were displayed by mounting an illuminated positive transparency above the TV monitors (Figure 7).

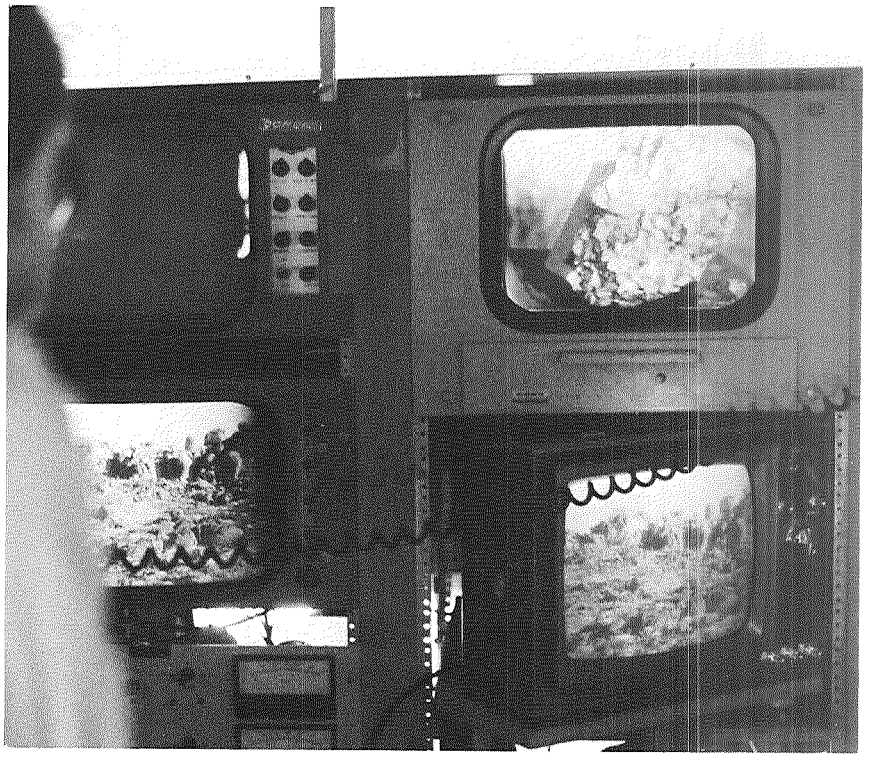

Figure 7. Displays used in second test: (top) panorama, (center) close-up of sample, (bottom) two views of near field

A surveillance TV camera (Figure 8) was mounted at the site from which the film panorama was made. A sample analysis TV camera was installed closer but exterior to the van, both cameras with zoom lenses and controlled remotely from inside the van. Rock specimens were mounted on a pan-and-tilt machine adjacent to the sample analysis camera (Figure 9).

Table 2. Resume of geological conclusions from field data

Operational procedure	Camera parameters	Ground system constraints
1. Direct sampling of surface material is required to supplement the TV data.	1. Some technique of ranging to observed features is required.	1. 360-deg panoramic display of both horizon and near-field should be displayed.
2. Reconnaissance geology requires data on the texture of surface material and either mineral phase data or elemental composition data or both.	2. Some technique of sizing observed features required.	2. High-resolution view of selected areas contained in panoramic view is required.
3. *Surveyor* surface sampler is preferred over drill or auger.	3. Color vision is not particularly important for reconnaissance observations; however, color vision is important in rock and mineral identification.	3. Panoramic view must first be displayed for observations of immediate interest and mapping. A permanent copy of imagery should be made for subsequent study.
4. Properly instrumented rover can perform geological reconnaissance, but not detailed geological mapping.	4. Stereo vision is not required but may be useful in showing relative range of features.	4. The reconnaissance map, with observed geology, will have to be kept up to date with vehicle progress.
5. In addition to data taken at stations, the geologist would like data taken en route between stations.	5. Resolution for observing panoramic display is not particularly critical; however, resolution for examining textures should be able to resolve grains as small as 0.05 mm in diameter.	
6. Geological observations will modify the traverse route and selection of stations.		

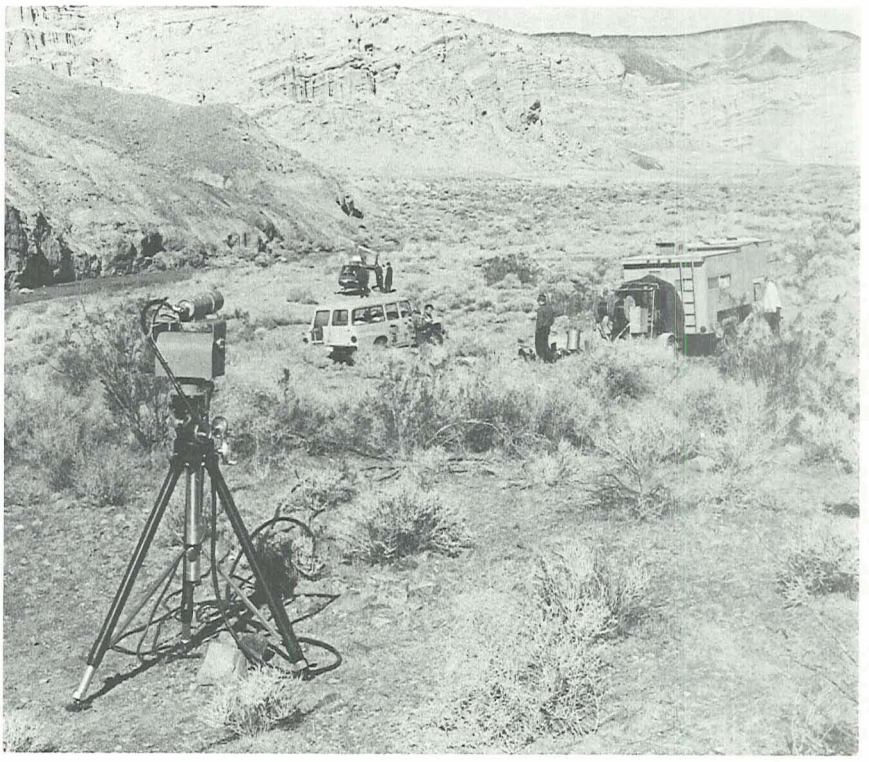

Figure 8. Surveillance TV camera and field test vehicles

To simulate a remote compositional analysis, some samples were analyzed following the field experiment by Mr. Sean Cary at Los Angeles City College using the X-ray diffraction technique. Correlation of petrographic data from the sample analysis camera and the X-ray diffractograms is currently in progress.

A team of three or four geologists in the van (Figure 8) performed geomorphologic analysis on the film panorama, examined distant features via the surveillance camera, selected rock specimens and fines with that camera, and made petrographic analyses of samples. Conclusions on geomorphology, rock units, and structure were then plotted on an aerial photograph of the area. The geologists were not permitted to view the test areas directly, either from the ground or from the air.

At seven stations, covering volcanic terrain, igneous intrusives, and sedimentary sequences, field exercises tended to confirm the earlier conclusions. Final conclusions await completion in the laboratory of the sample analysis. However, certain observations are very clear: Imagery made available to the geologists allowed them to select samples representative of the area. The gross geologic character of most areas

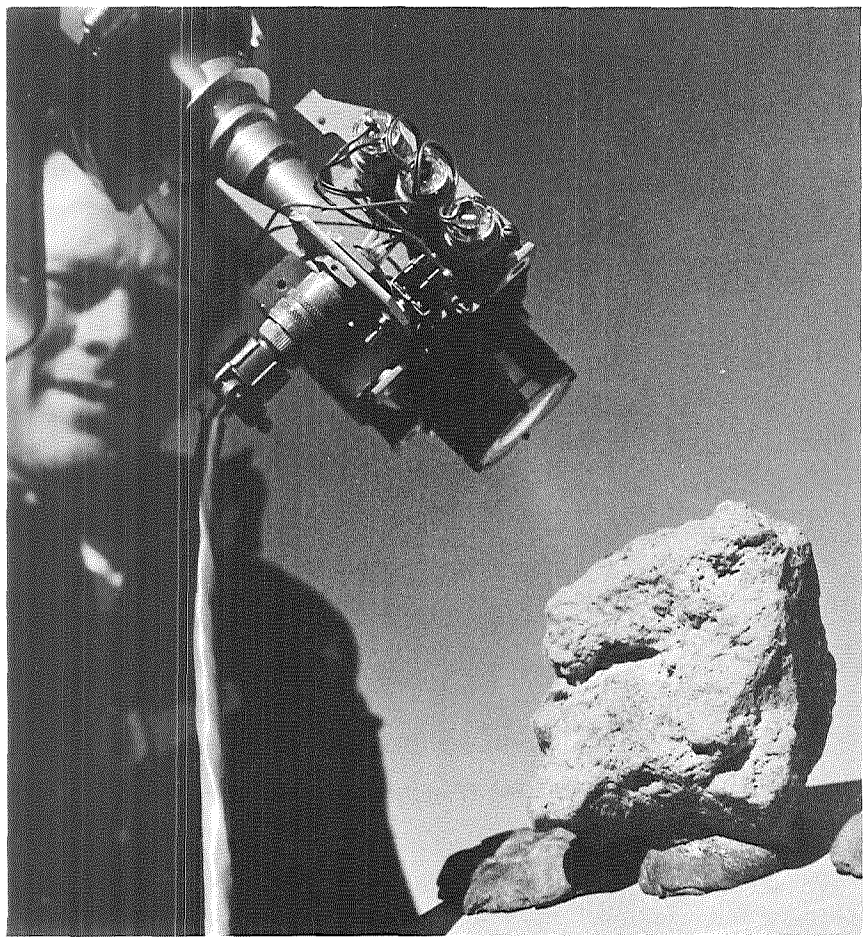

Figure 9. **Close-up camera and sample during second field test series**

was quite evident from the overhead photography and panoramas. Panoramic imagery was found to be very effective in locating sampling sites and providing an integrated view of geological features.

References

1. McCormick, C. W., and Bailey, G., *Remote Visual Examination of Rock Specimens,* JPL Internal Document 760-47. Jet Propulsion Laboratory, Pasadena, Calif., May 1970.
2. *Surveyor Project Final Report: Part I. Project Description and Performance, Vols. I and II,* July 1, 1969, and *Part II. Science Results,* June 15, 1968, Technical Report 32-1265. Jet Propulsion Laboratory, Pasadena, Calif.
3. Tyrrell, G. W., *The Principles of Petrology,* p. 394. Methuen & Co., Ltd., London, 1926.

References (contd)

4. Brereton, R. G., Coryell, R. B., Howard, E. A., and Rubin, D. K., *Experiments in Remote Geological Reconnaissance and Landmark Navigation,* JPL Internal Document 760-41. Jet Propulsion Laboratory, Pasadena, Calif., Oct. 15, 1969.

5. Brereton, R. G., and Howard, E. A., "Comments on Geological Observations From an Automated Vehicle (Field Test)," in *Supporting Research and Advanced Development,* Space Programs Summary 37-55, Vol. III, pp. 258–263. Jet Propulsion Laboratory, Pasadena, Calif., Feb. 28, 1969.

Bibliography of Current Reporting

Author Index With Abstracts

The appraisal of readings of relatively short static pressure probes in the vicinity of an oblique shock wave is discussed in this article. Such probes are used along with pitot tubes to determine the Mach number distribution in supersonic flow fields. In the absence of shock waves in the flow, an upstream length of 15-probe diameters from the hole to the tip has been found to be sufficient to allow the local static pressure upstream of the probe bow shock wave to recover within about 1%. However, when traversing the probe across an oblique shock wave, the interaction between the probe bow shock wave and the oblique shock wave can influence the flow field along the probe, particularly where the pressure is measured.

The purpose of the investigation reported here was to learn about the lateral extent of the interaction region so that measurements can be properly interpreted. There is usually no problem with obtaining accurate pitot tube measurements, because the pitot pressure is influenced by the bow shock-oblique shock wave interaction at distances less than one tip height; therefore, the region of influence can be reduced by using a probe with a small tip. However, the size of the static pressure probe is limited by strength considerations; in addition, the measured pressure is expected to be influenced at distances greater than a probe diameter because of the configuration of the probe and the oblique shock wave.

B02 Flow Coefficients for Supersonic Nozzles With Comparatively Small Radius of Curvature Throats

L. H. Back and R. F. Cuffel

J. Spacecraft Rockets, Vol. 8, No. 2, pp. 196–198, February 1971

This article discusses the determination of the mass flow rate through choked nozzles, with emphasis on comparatively small radius-of-curvature throats. In the flow regime investigated (throat Reynolds numbers larger than 10^6), viscous (boundary-layer) effects are not believed to be significant, so the flow field can be regarded as essentially isentropic. Mass flux nonuniformities for the air flows studies are then primarily caused by the throat configuration and result in reduced mass flow rates below the ideal one-dimensional flow value, since, in either the subsonic flow region near the centerline or the supersonic region near the wall, the mass flux is less than that at the sonic condition. The nozzles considered have circular-arc throats with values of r_c/r_{th}, the

ratio of throat radius of curvature to throat radius, extending from 2 down to nearly 0, corresponding to a sharp-edged throat.

Measured values of the mass flow coefficient are presented for nozzles recently tested at JPL and for nozzles previously tested in other investigations. Of interest is the relative correspondence of the earlier measurements by Durham that span a large range of r_c/r_{th} to the recent data, since there is some question about their absolute magnitude due to the accuracy of the measurements made in a blow-down facility. These measurements, taken collectively, provide a basis on which to evaluate the effect of r_c/r_{th} on the flow coefficient and to appraise existing and recently developed prediction methods for isentropic flow by other investigators.

BAHM, E.

B03 **A Magnetic Tape Recorder for Long Operating Life in Space**

E. Bahm

JPL Quarterly Technical Review, Vol. 1, No. 1, pp. 116–124, April 1971

In the past, magnetic tape recorders for space applications have caused many problems. However, they are still widely used because they are the only mass memory device acceptable for spacecraft. Most of the tape recorder problems have been associated with the mechanical tape transport, while the tape recorder electronics generally achieved a satisfactory performance record. This article describes a tape recorder which uses a very simple mechanical system to transport the tape with very few possible failure modes. The simplicity of the tape transport has been achieved at the expense of added complexity of the electronic system. The resulting tape recorder is better balanced in its mechanical and electronic reliability. The test results with a feasibility model have been very encouraging.

BARKER, E. S.

B04 **High-Dispersion Spectroscopic Observations of Venus: V. The Carbon Dioxide Band at 8689 Å**

L. D. G. Young, R. A. J. Schorn, E. S. Barker (University of Texas), and M. MacFarlane (University of Texas)

Icarus: Int. J. Sol. Sys., Vol. 11, No. 3, pp. 390–407, November 1969

For abstract, see Young, L. D. G.

B05 **High-Dispersion Spectroscopic Observations of Venus: VII. The Carbon Dioxide Band at 10 488 Å**

L. D. G. Young, R. A. J. Schorn, and E. S. Barker (University of Texas)

Icarus: Int. J. Sol. Sys., Vol. 13, No. 1, pp. 58–73, July 1970

For abstract, see Young, L. D. G.

BARTZ, D. R.

B06 **Characteristics, Capabilities, and Costs of Solar Electric Spacecraft for Planetary Missions**

D. R. Bartz and J. L. Horsewood (Analytical Mechanics Associates, Inc.)

J. Spacecraft Rockets, Vol. 7, No. 12, pp. 1379–1390, December 1970

Since 1965, when the feasibility of using solar-photovoltaic-powered, electrically propelled spacecraft for planetary missions was first suggested, the propulsion system technology has been developed to near-readiness; additionally, further studies have been made to gain a clear perspective of the mission applicability of solar–electric spacecraft. It was felt that a summary of the current characteristics, capabilities, and costs of solar–electric spacecraft for planetary missions might prove useful in suggesting: (1) those missions for which solar–electric propulsion is best suited, and (2) the advantages that can accrue from the multimission use of a given solar–electric spacecraft design. Such a summary is presented in this article.

BATHKER, D. A.

B07 **Predicted and Measured Power Density Description of a Large Ground Microwave System**

D. A. Bathker

Technical Memorandum 33-433, April 15, 1971

A comparison between predicted and measured microwave field strengths on, near, and in the far field of a large ground antenna system is given. The system consists of a high-power S-band transmitter and a parabolic reflector. Use of the radiations patterns of the feed system is adopted as accounting for the total power output. Estimates of secondary or stray radiation are given and discussed. A first-order tubular beam concept is introduced to simplify and provide a clear impression. It is concluded that certain

safety restrictions are necessary; a discussion of these restrictions is included.

BEERER, J. G.

B08 ***Mariner* Mission to Venus and Mercury in 1973**

R. D. Bourke and J. G. Beerer

Astronaut. Aeronaut., Vol. 8, No. 1, pp. 52–59, January 1971

For abstract, see Bourke, R. D.

BENOIT, R. E.

B09 **Microbial and Ecological Investigations of Recent Cinder Cones, Deception Island, Antarctica—A Preliminary Report**

R. E. Cameron and R. E. Benoit (Virginia Polytechnic Institute)

Ecology, Vol. 51, No. 5, pp. 802–809, Late Summer 1970

For abstract, see Cameron, R. E.

BENSON, G. S.

B10 **Resonances in the Neptune–Pluto System**

J. G. Williams and G. S. Benson (University of California, Los Angeles)

Astron. J., Vol. 76, No. 2, pp. 167–177, March 1971

For abstract, see Williams, J. G.

BERG, R. A.

B11 **A Preliminary Control Net of Mars**

M. E. Davies (Rand Corporation) and R. A. Berg (USAF Aeronautical Chart and Information Center)

J. Geophys. Res., Vol. 76, No. 2, pp. 373–393, January 10, 1971

For abstract, see Davies, M. E.

BIRD, E. F.

B12 **DSN [Deep Space Network] Progress Report for March–April 1971: GCF Television Assembly Design for the Systems Development Laboratory**

E. F. Bird

Technical Report 32-1526, Vol. III, pp. 187–189, June 15, 1971

The newly constructed Systems Development Laboratory (SDL) at the Jet Propulsion Laboratory will serve as an extension of the Space Flight Operations Facility (SFOF). The *Pioneer* Project will utilize the SDL for conducting the operations of the *Pioneer F* and *G* missions. The Ground Communications Facility (GCF) provides intercommunication between the SDL and the SFOF. One of the communication media is television. This article defines the requirements and the resulting design of the GCF Television Assembly in the SDL.

BOND, F. E., JR.

B13 DSN [Deep Space Network] Progress Report for January–February 1971: The Teletype Discipline of Data Transfer Designed for Support of *Mariner* Mars 1971 Missions

F. E. Bond, Jr.

Technical Report 32-1526, Vol. II, pp. 148–164, April 15, 1971

This article describes the overall teletype configuration that has been developed to support the ground communications requirements established for the *Mariner* Mars 1971 missions. Primary emphasis is placed on the worldwide distribution of mission traffic formatted in the teletype discipline, routed through the communications switching facilities, and provided to various analysis and control centers.

BOURKE, R. D.

B14 *Mariner* Mission to Venus and Mercury in 1973

R. D. Bourke and J. G. Beerer

Astronaut. Aeronaut., Vol. 8, No. 1, pp. 52–59, January 1971

The year 1973 presents an unusual opportunity to fly a single spacecraft to both Venus and Mercury. The *Mariner* Venus–Mercury 1973 Project, under which the spacecraft is being developed, has the following objectives:

(1) To conduct exploratory investigations of Venus and Mercury, measuring environmental, atmospheric, surface, and body characteristics. First priority is assigned to the Mercury investigations.

(2) To perform experiments in the interplanetary medium and to obtain experience with a dual-planet gravity-assist mission.

The project, being managed by JPL, is still in its early stages, with many key aspects of the mission yet to be decided. This article describes the preliminary mission planning phase, including the background of the project, the characteristics of the 1973 opportunity, and some possible mission options being considered.

BRERETON, R. G.

B15 **Lunar Traverse Missions**

R. G. Brereton, J. D. Burke, R. B. Coryell, and L. D. Jaffe

JPL Quarterly Technical Review, Vol. 1, No. 1, pp. 125–137, April 1971

The results of recent JPL studies on Lunar Traverse Missions are compared with the announced characteristics of the Soviet Lunokhod 1 rover, delivered to the Moon by the *Luna 17* spacecraft in November 1970. Except for some differences in emphasis among the scientific experiments, the Lunokhod mission is quite similar to those recommended in the JPL studies.

BRINKMANN, R. T.

B16 **Electron Impact Excitation of N_2**

R. T. Brinkmann and S. Trajmar

Ann. Géophys., Vol. 26, No. 1, pp. 201–207, January–March 1970

An experimental and theoretical study has been made of the excitation of molecular nitrogen under electron bombardment. Differential electron impact energy-loss spectra were obtained at scattering angles from 0 to 80 deg; incident energies of 15, 20, 30, 60, and 80 eV; and the entire possible energy-loss range. Resolution was typically 0.10 eV. The resulting cross-sections have been put on an absolute scale by normalizing to known cross-sections. Empirical and theoretical extrapolations have been made for higher incident energies. A computer program was written which uses the Monte Carlo method to calculate the energy deposited in the various states as a function of incident energy and distance from the source. If branching ratios and quenching efficiencies are assumed, the resultant emission intensities are readily calculated. Illustrative results are presented for 100-eV incident elec-

trons, this energy being intermediate between typical auroral and airglow cases of interest.

BRYAN, A.

B17 DSN [Deep Space Network] Progress Report for January–February 1971: DSIF Uplink Amplitude Instability Measurement

A. Bryan and G. Osborn

Technical Report 32-1526, Vol. II, pp. 165–168, April 15, 1971

A simple and inexpensive upper-bound technique for the measurement of Deep Space Instrumentation Facility (DSIF) effective radiated power is described. Test results verify the theoretical model and imply that DSIF uplink stability can satisfy *Pioneer F/G* attitude-control requirements.

BURKE, J. D.

B18 Lunar Traverse Missions

R. G. Brereton, J. D. Burke, R. B. Coryell, and L. D. Jaffe

JPL Quarterly Technical Review, Vol. 1, No. 1, pp. 125–137, April 1971

For abstract, see Brereton, R. G.

BUTCHER, L.

B19 DSN [Deep Space Network] Progress Report for January–February 1971: Tracking and Data System Near-Earth Telemetry Automatic Switching Unit

L. Butcher

Technical Report 32-1526, Vol. II, pp. 136–139, April 15, 1971

A hardware–software system is described that is capable of selecting the best data stream from among as many as six incoming data streams and switching it automatically to the Deep Space Instrumentation Facility (DSIF) telemetry system. The system has been implemented at the Cape Kennedy Compatibility Test Station to provide the best spacecraft telemetry stream to the DSIF telemetry system during the near-earth phase of a tracking mission, when as many as six Air Force Eastern Test Range stations are receiving spacecraft telemetry.

BUTMAN, S.

B20 Interplex Modulation

S. Butman and U. Timor

JPL Quarterly Technical Review, Vol. 1, No. 1, pp. 97–105, April 1971

In a conventional phase-shift-keyed/phase-modulated (PSK/PM) system, the receiver tracks the frequency and phase of the carrier by means of a phase-locked loop and coherently demodulates the data. However, due to the inherent nonlinearity of the phase-modulation process, some power is transmitted as cross modulation, which reduces the useful available power. This article describes a new PSK/PM modulation scheme, called Interplex, which reduces the cross-modulation power loss. The scheme can be implemented in existing systems without significant hardware changes and appears attractive in concept for improving the performance of deep space telecommunications systems.

B21 Rate Distortion Over Band-Limited Feedback Channels

S. Butman

IEEE Trans. Inform. Theor., Vol. IT-17, No. 1, pp. 110–112, January 1971

Although linear feedback is by itself sufficient to achieve capacity of an additive gaussian white noise (AGWN) channel, it can not, in general, achieve the theoretical minimum mean-squared error for analog gaussian data. This article gives the necessary and sufficient conditions under which this optimum performance can be achieved.

BUTTERWORTH, L. W.

B22 Structural Analysis of Silicon Solar Arrays

L. W. Butterworth and R. K. Yasui

Technical Report 32-1528, May 15, 1971

This report on the structural design of solar arrays includes discussions on thermal stresses in array components, mechanical stresses in solar arrays, analysis of a stress relief interconnect, and current material properties. Special emphasis has been placed on developing simple but accurate methods of analysis that will be of use to the designer.

CAMERON, R. E.

C01 Growth of Bacteria in Soils from Antarctic Dry Valleys

R. E. Cameron and E. L. Merek (NASA)

Technical Report 32-1522, February 1, 1971

This report presents the results of a study of microbial response in four cold desert surface soils following moist soil incubation. Soils were typical Antarctic dry valley saline sands, low in organic matter content and low in abundances and kinds of viable microorganisms. Moist soil incubation increased the viable counts of three of the four soils. Most of the bacteria could grow at temperatures of 8°C; however, they grew more rapidly at 25°C. Failure of isolants from three of the soils to grow in sea salts medium indicated that they were probably not marine contaminants. It is suggested that the organisms in the three soils are probably indigenous organisms. They have adapted to the cold desert Antarctic terrestrial ecosystem, which provides a soil microbial ecology as a Mars model.

C02 Survival of Antarctic Desert Soil Bacteria Exposed to Various Temperatures and to Three Years of Continuous Medium-High Vacuum

R. E. Cameron and H. P. Conrow

Technical Report 32-1524, February 1, 1971

Samples of cold desert soil containing viable bacteria from McKelvey Dry Valley, Southern Victoria Land, Antarctica, were subjected to 3 years of continuous medium-high vacuum of 10^{-3} to 10^{-4} torr at room temperature and storage for 4 years at −30, −5, and +20°C. Dependent upon storage temperatures, the survivability of bacteria decreased with increase in temperatures, with only 3 bacteria/g of soil surviving at room temperature in vacuum and 500 bacteria/g of soil surviving storage at −30°C. *Corynebacterium* sp., a soil diphtheroid, constituted approximately 90% of the surviving populations. *Arthrobacter* spp. and a *Micrococcus* sp. also survived, but no *Bacillus* spp. survived in any of the samples, although they were present in the soil when it was cultured soon after collection. The reduction in abundance and kinds of bacteria from this naturally harsh terrestrial environment is relevant to the importance of storage conditions for return of Martian soil samples. Based upon Antarctic soil microbial ecology as a Mars model, the most likely life forms for a Martian cold desert soil ecosystem are diphtheroid-like microorganisms.

C03 **Microbial and Ecological Investigations of Recent Cinder Cones, Deception Island, Antarctica—A Preliminary Report**

R. E. Cameron and R. E. Benoit (Virginia Polytechnic Institute)

Ecology, Vol. 51, No. 5, pp. 802–809, Late Summer 1970

Cinder cones that arose during December 1967 within Telefon Bay, Deception Island, Antarctica, were investigated 1 yr later to determine the establishment of microorganisms and cryptogams. Culture media were inoculated to determine the presence and abundance of algae, fungi, and heteorotrophic, chemoautotrophic, aerobic, microaerophilic, and anaerobic bacteria. No mosses or lichens had become established on the cones. Algae, fungi, and bacteria were generally most abundant around fumaroles emitting moisture and CO_2. Several samples contained few or no culturable microorganisms. "Soil" properties of coarse-textured, relatively unweathered acid volcanic materials were unfavorable for growth, despite the presence of moisture. Microorganisms were identified from the cinder cones and included primarily soil diphtheroids and *Bacillus* spp., *Chlorococcum humicola,* and *Penicillium* spp. Most of the bacteria could grow at 2°C as well as at 20°C.

CANNON, W.

C04 **Electric Space Potential in a Cesium Thermionic Diode**

K. Shimada and W. Cannon

Technical Memorandum 33-480, March 31, 1971

For abstract, see Shimada, K.

CERINI, D. J.

C05 **Liquid-Metal MHD Power Conversion**

D. J. Cerini

JPL Quarterly Technical Review, Vol. 1, No. 1, pp. 64–67, April 1971

A liquid-metal magnetohydrodynamic (MHD) power converter has been successfully operated with the generation of ac electrical power. Gaseous nitrogen is used to produce the closed-cycle flow of the liquid-metal (NaK) working fluid through the MHD generator where the fluid kinetic energy is converted to electrical energy. In this article the operational characteristics of the con-

verter are given and the results of the current series of tests are discussed.

CHAO, C. C.

C06 DSN [Deep Space Network] Progress Report for March–April 1971: An Additional Effect of Tropospheric Refraction on the Radio Tracking of Near-Earth Spacecraft at Low Elevation Angles

C. C. Chao and T. D. Moyer

Technical Report 32-1526, Vol. III, pp. 63–70, June 15, 1971

The current tropospheric calibration in the Double Precision Orbit Determination Program assumes that the direction of the ray path after it exits from the troposphere is parallel to the true line-of-sight. Such an assumption will induce a sizable error for near-earth tracking at low elevation angles. This article examines such effects and gives additional corrections to the present tropospheric calibration for near-earth tracking.

CHEN, C. J.

C07 Pumping Mechanism of CO_2 Laser and Formation Rate of CO_2 From CO and O

C. J. Chen

J. Appl. Phys., Vol. 42, No. 3, pp. 1016–1020, March 1, 1971

The pumping mechanism of a high-current-pulsed CO_2 laser has been investigated. It was found that there is a time delay of the laser pulse behind the current pulse. From the dependence of the time delay on the plasma parameters, such as electron density, electron temperature, gas temperature, gas pressure, and emission of oxygen atomic line (7771 Å), it can be shown that, during the current pulse, the CO_2 is totally dissociated into CO and O. The subsequent recombinations of CO and O into CO_2 are responsible for the pumping of the upper level of the CO_2 laser (10.6 and 9.4 μ). The time delay between the current pulse and laser pulse is thought to be due to the time required for CO and O to recombine to reach the threshold population for lasing for the particular optical cavity. The threshold upper level population is obtained by knowing the Q value of the optical cavity, wavelength of the laser line, and linewidth of the radiation line. By equating the amount of CO_2 formed during the delay time to the threshold

upper laser population, the reaction rate of $CO+O \rightarrow CO_2$ is thus obtained. The agreement between the rate obtained and that previously determined supports the proposed pumping mechanism.

CLELAND, E. L.

C08 **Measured Performance of Silicon Solar Cell Assemblies Designed for Use at High Solar Intensities**

R. G. Ross, Jr., R. K. Yasui, W. Jaworski, L. C. Wen, and E. L. Cleland

Technical Memorandum 33-473, March 15, 1971

For abstract, see Ross, R. G., Jr.

COLLINS, S. A.

C09 **Photometric Properties of the *Mariner* Cameras and of Selected Regions on Mars**

A. T. Young and S. A. Collins

J. Geophys. Res., Vol. 76, No. 2, pp. 432–437, January 10, 1971

For abstract, see Young, A. T.

C10 **Maximum Discriminability Versions of the Near-Encounter *Mariner* Pictures**

J. A. Dunne, W. D. Stromberg, R. M. Ruiz, S. A. Collins, and T. E. Thorpe

J. Geophys. Res., Vol. 76, No. 2, pp. 438–472, January 10, 1971

For abstract, see Dunne, J. A.

CONROW, H. P.

C11 **Survival of Antarctic Desert Soil Bacteria Exposed to Various Temperatures and to Three Years of Continuous Medium-High Vacuum**

R. E. Cameron and H. P. Conrow

Technical Report 32–1524, February 1, 1971

For abstract, see Cameron, R. E.

COOPER, M. A.

C12 A Detailed Evaluation of the Dependence of ^3J(H—H) on Bond Angle in Alkenes and Cycloalkenes

M. A. Cooper and S. L. Manatt

Org. Mag. Reson., Vol. 2, No. 5, pp. 511–525, October 1970

Newly determined and accurate data for the magnitudes of *cis* vinyl proton–proton spin–spin coupling constants in *cis*-dialkylethylenes and cycloalkenes have been obtained. With these new data and also values taken from the recent literature, it has proved possible to make a critical determination of the correlation between ^3J(H—H) and C=C—H bond angles in ethylenic systems. It is suggested that it is possible to obtain accurate estimates of bond angles using nuclear-magnetic-resonance coupling constants, even though much more data will be required to fully substantiate this proposal. Whereas *cis*-^3J(H—H) decreases rapidly with increasing C=C—H bond angles, evidence is presented that the opposite is the case for *trans*-^3J(H—H). A brief theoretical discussion of these trends in coupling constants is given.

CORYELL, R. B.

C13 Lunar Traverse Missions

R. G. Brereton, J. D. Burke, R. B. Coryell, and L. D. Jaffe

JPL Quarterly Technical Review, Vol. 1, No. 1, pp. 125–137, April 1971

For abstract, see Brereton, R. G.

CROW, R. B.

C14 DSN Progress Report for January–February 1971: Coherent Reference Generator for DSN Mark III Data System

R. B. Crow

Technical Report 32-1526, Vol. II, pp. 133–135, April 15, 1971

A new frequency generator/distribution subsystem is being developed to meet the increasing complexity of the Deep Space Network (DSN) Mark III data system. The coherent reference generator is an assembly that will accept the primary frequency standard from the hydrogen maser (or possible secondary standard from the rubidium, cesium, or remote standards) and furnish required reference frequencies for a deep space station. Preliminary design information and specifications for the coherent reference generator are given and discussed.

CUDDIHY, E. F.

C15 **Fatigue of Teflon Bladder Bag Materials**

E. F. Cuddihy

JPL Quarterly Technical Review, Vol. 1, No. 1, pp. 57–63, April 1971

A correlation between fatigue and stress–strain behavior of Teflon materials was observed during a study of the fatigue properties of liquid propellant expulsion Teflon bladder bag materials. This correlation requires only the knowledge of the ultimate breaking stress of the materials in order to obtain an estimate of the fatigue properties, and permits a rapid assessment of the expected fatigue behavior of candidate materials for bladder bags from only a comparison of their ultimate breaking stress. The general principles of this method of fatigue analysis is discussed, along with the recognition that this technique should have general application for other polymeric materials where stress–strain behavior is comparable to Teflon.

CUFFEL, R. F.

C16 **Static Pressure Measurements Near an Oblique Shock Wave**

L. H. Back and R. F. Cuffel

AIAA J., Vol. 9, No. 2, pp. 345–347, February 1971

For abstract, see Back, L. H.

C17 **Flow Coefficients for Supersonic Nozzles With Comparatively Small Radius of Curvature Throats**

L. H. Back and R. F. Cuffel

J. Spacecraft Rockets, Vol. 8, No. 2, pp. 196–198, February 1971

For abstract, see Back, L. H.

CUMMING, W. D.

C18 **The Conformational Preferences of the *N*-Trimethylsilyl and *O*-Trimethylsilyl Groups**

J. P. Hardy and W. D. Cumming

J. Am. Chem. Soc., Vol. 93, No. 4, pp. 928–932, February 24, 1971

For abstract, see Hardy, J. P.

CURKENDALL, D. W.

C19 DSN [Deep Space Network] Progress Report for March–April 1971: A First-Order Theory for Use in Investigating the Information Content Contained in a Few Days of Radio Tracking Data

V. J. Ondrasik and D. W. Curkendall

Technical Report 32-1526, Vol. III, pp. 77–93, June 15, 1971

For abstract, see Ondrasik, V. J.

CUTTS, J. A.

C20 The Surface of Mars: Pt. 1. Cratered Terrains

B. C. Murray (California Institute of Technology), L. A. Soderblom (California Institute of Technology), R. P. Sharp (California Institute of Technology), and J. A. Cutts (California Institute of Technology)

J. Geophys. Res., Vol. 76, No. 2, pp. 313–330, January 10, 1971

For abstract, see Murray, B. C.

C21 The Surface of Mars: Pt. 2. Uncratered Terrains

R. P. Sharp (California Institute of Technology), L. A. Soderblom (California Institute of Technology), B. C. Murray (California Institute of Technology), and J. A. Cutts (California Institute of Technology)

J. Geophys. Res., Vol. 76, No. 2, pp. 331–342, January 10, 1971

For abstract, see Sharp, R. P.

C22 The Surface of Mars: Pt. 3. Light and Dark Markings

J. A. Cutts (California Institute of Technology), L. A. Soderblom (California Institute of Technology), R. P. Sharp (California Institute of Technology), B. A. Smith (California Institute of Technology), and B. C. Murray (California Institute of Technology)

J. Geophys. Res., Vol. 76, No. 2, pp. 343–356, January 10, 1971

As discussed in this article, pictures taken by the *Mariner VI* and *VII* spacecraft have provided significant clues to the nature of the light and dark markings on Mars, but do not yet provide an ade-

quate foundation for any complete explanation of the phenomena. They display detail never before seen or photographed and demonstrate that there is no network of dark lines (i.e., canals) on the planet. A variety of shapes and of boundaries between major markings are recorded in the pictures. No substantial correlation of albedo markings with cratered or chaotic terrain has been recognized; featureless terrain conceivably may be genetically related to light areas. Within and surrounding the dark area Meridiani Sinus, there is evidence of local topographic control of albedo markings; light material is found in locally low areas. Also, characteristic patterns of local albedo markings are exhibited by craters there. Aeolian transportation of light material with deposition locally in low areas is suggested as an explanation of these markings and may be useful as a working hypothesis for subsequent exploration. Across some light/dark boundaries, crater morphologies are unchanged; across others, craters in the light area appear smoother. If there is a relationship between cratered-terrain modification and surface albedo, it is an indirect one.

C23 The Surface of Mars: Pt. 4. South Polar Cap

R. P. Sharp (California Institute of Technology),
B. C. Murray (California Institute of Technology),
R. B. Leighton (California Institute of Technology),
L. A. Soderblom (California Institute of Technology), and
J. A. Cutts (California Institute of Technology)

J. Geophys. Res., Vol. 76, No. 2, pp. 357–368, January 10, 1971

For abstract, see Sharp, R. P.

C24 Mercator Photomap of Mars

J. A. Cutts (California Institute of Technology),
G. E. Danielson, Jr., and M. E. Davies (Rand Corporation)

J. Geophys. Res., Vol. 76, No. 2, pp. 369–372, January 10, 1971

Television images of Mars obtained by high-resolution cameras on the *Mariner VI* and *VII* spacecraft have been converted to a photographic likeness of the planet in the Mercator projection by the use of computer image-processing techniques. Areodetic positions of features are established using the *Mariner VI* and *VII* control net. The representation, termed here a Mercator photomap, provides an authentic rendition of complex and subtle markings. The photomap and the techniques used in its development, as described in this article, have applications to the study of the seasonal variations on Mars, an objective of the *Mariner* Mars 1971 orbiter television experiment.

DANIELSON, G. E., JR.

D01 Mercator Photomap of Mars

J. A. Cutts (California Institute of Technology),
G. E. Danielson, Jr., and M. E. Davies (Rand Corporation)

J. Geophys. Res., Vol. 76, No. 2, pp. 369–372, January 10, 1971

For abstract, see Cutts, J. A.

D02 Calibration of the *Mariner* Mars 1969 Television Cameras

G. E. Danielson, Jr., and D. R. Montgomery

J. Geophys. Res., Vol. 76, No. 2, pp. 418–431, January 10, 1971

The purpose of an instrument calibration is to determine, as accurately as possible, the relationship between the input stimulus and the instrument's output signal. Each individual instrument has a unique calibration signature that must be accurately determined, in addition to its behavior characteristics in the environment in which it is predicted to operate. The philosophy adopted for calibration of the *Mariner* Mars 1969 television system was derived from the basic purpose of exploratory photography, as established by prior lunar and planetary missions, "to produce the most accurate and complete reproductions possible of the observed scenes, consistent with specific objectives and limitations of the particular experiment." This article presents a description of the *Mariner* Mars 1969 two-camera television system, following by discussions of the system, component, subsystem, and thermal–vacuum calibrations that were performed.

DAVIES, M. E.

D03 Mercator Photomap of Mars

J. A. Cutts (California Institute of Technology),
G. E. Danielson, Jr., and M. E. Davies (Rand Corporation)

J. Geophys. Res., Vol. 76, No. 2, pp. 369–372, January 10, 1971

For abstract, see Cutts, J. A.

D04 A Preliminary Control Net of Mars

M. E. Davies (Rand Corporation) and R. A. Berg (USAF Aeronautical Chart and Information Center)

J. Geophys. Res., Vol. 76, No. 2, pp. 373–393, January 10, 1971

A control net for Mars has been computed from measurements of 112 points identified on the *Mariner VI* and *VII* pictures, and areocentric coordinates of these points are presented. The coordinates of an initial point are determined, and the near-encounter frames of *Mariner VI* and the adjoining near-encounter frames of *Mariner VII* are tied to this initial point; then, the far-encounter pictures of *Mariners VI* and *VII* are joined to the near-encounter pictures. The near-encounter *Mariner VII* polar pass is located without reference to the far-encounter frames.

DAVIS, J. P.

D05 **Thermionic Reactor Ion Propulsion Spacecraft for Unmanned Outer Planet Exploration**

J. F. Mondt and J. P. Davis

J. Spacecraft Rockets, Vol. 8, No. 3, pp. 295–297, March 1971

For abstract, see Mondt, J. F.

DEO, N.

D06 **An Extensive English Language Bibliography on Graph Theory and Its Applications**

N. Deo

Technical Report 32-1413, Supplement 1, April 15, 1971

This report is a supplement to the original bibliography of linear graph theory and its applications that was published in October 1969. Most of the 841 entries in this supplement have appeared in the past two years. Some are papers that were overlooked in the original report. Dissertations or internal reports that were listed in the original bibliography but have since been published in journals are listed. Again, only those sources that are published in the English language (originally or in translation) are listed. Unpublished works, private communications, and technical reports not generally available have been omitted.

DETWEILER, H. K.

D07 **Calculation of Space-Charge Forces in the Analysis of Traveling-Wave Tubes**

H. K. Detweiler

JPL Quarterly Technical Review, Vol. 1, No. 1, pp. 106–115, April 1971

A comprehensive large-signal traveling-wave tube computer program has been developed for the study and design optimization of high-efficiency space-type tubes. Studies have been made previously with a theory which employs a "deformable-disk model" (DDM) for the electron beam, but neglects RF space-charge forces in the beam. That theory was found to yield accurate predictions for tubes in which RF space-charge forces are not the predominant factor in determining device performance. However, RF space-charge effects can be very important in tubes designed for space flight applications. Thus, it is essential to include them in the computer calculations if accurate predictions of device performance are to be obtained. Expressions for the space-charge fields, appropriate to the DDM representation of the electron beam, are presented in this article and the methods used in the calculations are described.

DEVINE, C. J.

D08 On the Computation of Debye Functions of Integer Orders

E. W. Ng and C. J. Devine

Math. Comp., Vol. 24, No. 110, pp. 405–407, April 1970

For abstract, see Ng, E. W.

DUNNE, J. A.

D09 Digital Processing of the *Mariner 6* and *7* Pictures

T. C. Rindfleisch, J. A. Dunne, H. J. Frieden, W. D. Stromberg, and R. M. Ruiz

J. Geophys. Res., Vol. 76, No. 2, pp. 394–417, January 10, 1971

For abstract, see Rindfleisch, T. C.

D10 Maximum Discriminability Versions of the Near-Encounter *Mariner* Pictures

J. A. Dunne, W. D. Stromberg, R. M. Ruiz, S. A. Collins, and T. E. Thorpe

J. Geophys. Res., Vol. 76, No. 2, pp. 438–472, January 10, 1971

Algorithms for the removal of various types of noises and for enhancement of some contrast and resolution were applied to the *Mariner VI* and *VII* composite analog video data to produce pictures optimal for the recognition of fine-scale surface features on

Mars. A set of these pictures is presented, along with a brief discussion identifying the types of processing procedures required to generate them.

EDMUNDS, R. S.

E01 **Development of a Strapdown Electrically Suspended Gyro Aerospace Navigation System: Final Report**

G. Paine, R. S. Edmunds, and B. S. Markiewcz

Technical Memorandum 33-471, April 1, 1971 (Confidential)

For abstract, see Paine, G.

EISENBERGER, I.

E02 **DSN [Deep Space Network] Progress Report for March–April 1971: Estimating the Parameters of the Distribution of a Mixture of Two Poisson Populations**

I. Eisenberger

Technical Report 32-1526, Vol. III, pp. 94–97, June 15, 1971

This article considers the problem of estimating the parameters of the distribution of a mixture of two Poisson populations. If a random variable is such that, with probability p, it comes from a Poisson distributed population with parameter γ_1 and, with probability $(1 - p)$, it comes from a Poisson-distributed population with parameter γ_2, its density function is given by

$$g(x) = \frac{p\gamma_1^x e^{-\gamma_1} + (1-p)\gamma_2^x e^{-\gamma_2}}{x!}, \qquad x = 0,1,2,\cdots$$

The problem of estimating p, γ_1, and γ_2 is considered with respect to a Deep Space Instrumentation Facility application involving certain types of equipment for which the density function of time to failure obeys the exponential law.

ELLEMAN, D. D.

E03 **Relative Rates and Their Dependence on Kinetic Energy for Ion–Molecule Reactions in Ammonia**

W. T. Huntress, Jr., M. M. Mosesman, and D. D. Elleman

J. Chem. Phys., Vol. 54, No. 3, pp. 843–849, February 1, 1971

For abstract, see Huntress, W. T., Jr.

ESHLEMAN, V. R.

E04 The Neutral Atmosphere of Venus as Studied With the *Mariner V* Radio Occultation Experiments

G. Fjeldbo, A. J. Kliore, and V. R. Eshleman (Stanford University)

Astron. J., Vol. 76, No. 2, pp. 123–140, March 1971

For abstract, see Fjeldbo, G.

FANALE, F. P.

F01 Potassium–Uranium Systematics of *Apollo 11* and *Apollo 12* Samples: Implications for Lunar Material History

F. P. Fanale and D. B. Nash

Science, Vol. 171, No. 3969, pp. 282–284, January 22, 1971

Apollo 11 and *12* lunar rock suites differ in their potassium–uranium abundance systematics. This difference indicates that relatively little exchange of regolith material has occurred between Mare Tranquillitatis and Oceanus Procellarum. The two suites appear to have been derived from materials of identical potassium and uranium content. It appears unlikely that bulk lunar material has the ratio of potassium to uranium found in chrondrites. However, systematic differences in the potassium–uranium ratio between *Apollo* samples and crustal rocks of the earth do not preclude a common potassium–uranium ratio for bulk earth and lunar material.

FINNEGAN, E. J.

F02 DSN [Deep Space Network] Progress Report for March–April 1971: A New High-Voltage Crowbar

E. J. Finnegan

Technical Report 32-1526, Vol. III, pp. 146–148, June 15, 1971

A crowbar is described which is capable of holding off very high voltage, 80 kV or greater, using two or more mercury-pool ignitrons connected in series. This system will replace a single high-voltage ignitron which has required lengthy processing prior to use and which failed to stand off voltages above 70 kV. It was necessary to perfect a higher voltage device in order to improve the reliability of the crowbar used to protect the high-powered (high voltage) klystron from self-destructive arcs. An experimental

version of the crowbar was built and operated. Also an experimental photon generator, using a light-emitting diode and fiber optics and a silicon-controlled rectifier with which to pulse the ignitron, was built and tested. Test results are presented, and the performance has been essentially as predicted. The device will be used on the 400-kW transmitting subsystem.

FINNIE, C.

F03 **DSN [Deep Space Network] Progress Report for January–February 1971: Design of Hydrogen Maser Cavity Tuning Servo**

C. Finnie

Technical Report 32-1526, Vol. II, pp. 86–88, April 15, 1971

The design of the hydrogen maser cavity tuning servo continues to be considered. In this article, the servo design details are described for a prototype hydrogen maser cavity tuner for use with the hydrogen maser frequency standards developed at JPL.

FJELDBO, G.

F04 **The Neutral Atmosphere of Venus as Studied With the *Mariner V* Radio Occultation Experiments**

G. Fjeldbo, A. J. Kliore, and V. R. Eshleman (Stanford University)

Astron. J., Vol. 76, No. 2, pp. 123–140, March 1971

The *Mariner V* radio occultation measurements at 423.3 and 2297 MHz (S band) are used to derive profiles in height of refractivity, molecular number density, pressure, temperature, and dispersive radio-frequency absorption for the atmosphere of Venus. The measurements cover heights between about 90 and 35 km (above a reference surface at a radius of 6050 km), over a pressure range from about 4×10^{-4} to 7 atm. Results obtained on the day and night sides are remarkably similar. The 90- to 60-km region contains inversion and thermal layers with the minimum temperature being at least as low as 180 K. The average temperature lapse rate is 4 K/km between 80 and 60 km. From 60 to 50 km the lapse rate is about 10 K/km, equal to the dry adiabatic rate for CO_2. No radio absorption was observed above 50 km. In the 50- to 35-km height region, the lower-frequency signal was not absorbed, but the S-band signal suffered an approximately constant loss of 4×10^{-3} dB per kilometer of propagation path. Assuming that the agent causing the microwave loss has negligible refractivity, there is a minimum in the temperature lapse rate

between 50 and 45 km altitude. Below this transition region, the atmosphere may be slightly superadiabatic with the temperature reaching approximately 500 K at the lowest level of measurement. The temperature and microwave loss profiles suggest the presence of two different cloud systems separated in altitude by about 10 km.

FLANAGAN, F. M.

F05 Deep Space Network Support of the Manned Space Flight Network for *Apollo*: 1969–1970

F. M. Flanagan, R. B. Hartley, and N. A. Renzetti

Technical Memorandum 33-452, Vol. II, May 1, 1971

This memorandum summarizes the Deep Space Network (DSN) activities in support of the *Apollo* Project during 1969 and 1970. Beginning with the *Apollo 9* mission and concluding with the *Apollo 13* mission, the narrative includes mission descriptions, NASA support requirements placed on the DSN, and comprehensive accounts of the support activities provided by each committed DSN deep space communication station. Associated equipment and activities of the three elements of the DSN (i.e., the Deep Space Instrumentation Facility, the Space Flight Operations Facility, and the Ground Communications Facility) in meeting the radio-metric and telemetry demands of the missions are documented. Recent scientific and engineering developments and plans that will have a direct effect on future DSN *Apollo* support plans are also discussed.

FLEISCHER, G. E.

F06 Multi-Rigid-Body Attitude Dynamics Simulation

G. E. Fleischer

Technical Report 32-1516, February 15, 1971

The results of attempts to put into practice the apparent advantages of the "barycenter formulation" of rigid-body rotational dynamics are described. The end product is a FORTRAN subroutine capable of computing the angular accelerations of each body in a system composed of several point-connected rigid bodies.

A 3-body system is used to illustrate the concept of the connection barycenter. Extension of the barycenter formulation of the dynamical equations to the general case of n bodies is then derived. Some discussion is devoted to the computational problem of handling interbody torques of constraint. An efficient proce-

dure for accommodating the presence of symmetric rotors in the system is also developed.

Two space vehicle attitude dynamics and control simulations of some interest are used to illustrate the application of the computer subroutine MLTBDY: one example is a spacecraft, under three-axis control, subject to the perturbations of a mechanically scanning platform, while the other is a rigid space vehicle hinged to four large solar-cell panels and under the influence of a trajectory-correcting rocket engine.

FOSTER, C. F.

F07 **DSN [Deep Space Network] Progress Report for March–April 1971: S-Band Demodulator**

C. F. Foster

Technical Report 32-1526, Vol. III, pp. 149–153, June 15, 1971

This article describes a portable S-band demodulator. The demodulator is a first-order phase-locked loop designed to work directly with the nominal levels out of the Deep Space Instrumentation Facility exciter and/or transmitter. This demodulator provides an independent means for verification of the exciter/transmitter performance. Its primary utilization is the measurement of exciter/transmitter amplitude stability, short-term phase stability, modulation index, bandpass, and modulation fidelity.

FOX, K.

F08 **Comment on: "On the Validity of Converting Sums to Integrals in Quantum Statistical Mechanics" [C. Stutz, *Am. J. Phys.*, Vol. 36, No. 9, pp. 826–829, September 1968]**

K. Fox

Am. J. Phys., Vol. 39, No. 1, pp. 116–117, January 1971

In the referenced document, Stutz discussed conditions sufficient to ensure that the conversion of a sum to an integral was valid. The author concurs with Stutz's feeling that such conversions may seem mysterious to the uninitiated and hereby points out that Stutz's results are simply a direct consequence of well-known formulas in the theory of *theta functions*. This theory has been treated in detail in the literature, and its relationship to Stutz's results is summarized here.

F09 **Simple Approximate Eigenfunctions for an Electron in a Finite Dipole Field**

K. Fox

Phys. Rev., Pt. A: Gen. Phys., Vol. 3, No. 1, pp. 13–15, January 1971

Ground-state energy eigenvalues for an electron in a stationary finite electric-dipole field are calculated by a novel variational approach. The physical model is taken to be a perturbed hydrogen atom. Accurate energy eigenvalues are obtained for a large range of dipole moments. The simple variational functions used compare favorably with more nearly exact eigenfunctions obtained in complex calculations.

FRIEDEN, H. J.

F10 **Digital Processing of the *Mariner 6* and *7* Pictures**

T. C. Rindfleisch, J. A. Dunne, H. J. Frieden, W. D. Stromberg, and R. M. Ruiz

J. Geophys. Res., Vol. 76, No. 2, pp. 394–417, January 10, 1971

For abstract, see Rindfleisch, T. C.

FYMAT, A. L.

F11 **Effect of Absorption on Scattering by Planetary Atmospheres**

A. L. Fymat and K. D. Abhyankar

J. Geophys. Res., Vol. 76, No. 3, pp. 732–735, January 20, 1971

Discrepancies between observed and theoretical values of intensity and polarization of light scattered by planetary atmospheres are usually attributed to Mie scattering by aerosols. It is shown that absorption by molecules or aerosols or both is another important contributor to such deviations.

GARY, B.

G01 **Circular-Polarization and Total-Flux Measurements of Jupiter at 13.1-cm Wavelength**

S. Gulkis and B. Gary

Astron. J., Vol. 76, No. 1, pp. 12–16, February 1971

For abstract, see Gulkis, S.

GEIGER, P. J.

G02 **Measurement of Organic Carbon in Arid Soils Using Hydrogen-Flame Ionization Detector**

P. J. Geiger and J. P. Hardy

Soil Sci., Vol. 111, No. 3, pp. 175–181, March 1971

This article discusses the technical feasibility of determining total organic carbon in soils with the hydrogen-flame ionization detector. Samples containing small concentrations of organic carbon are oxidized by one of two methods: hot oxygen if no appreciable amounts of carbonate are present, or a powdered chlorate eutectic mixture if carbonate is present. The method is particularly useful where samples are small and difficult to obtain, since only a few milligrams are necessary to complete an analysis. The determination takes but a few minutes. The apparatus can be built in almost any laboratory presently using gas chromatography.

GELLER, M.

G03 **On Some Indefinite Integrals of Confluent Hypergeometric Functions**

E. W. Ng and M. Geller

J. Res. NBS, Sec. B: Math. Sci., Vol. 74B, No. 2, pp. 85–98, April–June 1970

For abstract, see Ng, E. W.

GEORGEVIC, R. M.

G04 **Simplified Formulae for the Calculation of Perturbations of the Osculating Orbital Parameters and of the Range Rate of a Celestial Body**

R. M. Georgevic

Technical Memorandum 33-481, June 15, 1971

Although the results of the variation-of-parameters method in celestial mechanics are well-known, the final formulae for the time variations of the orbital parameters of the instantaneous osculating conic have, in most cases, quite different forms. There

exists a need for a set of final formulae in their simplest possible forms when using the variation-of-parameters method to solve a dynamical problem of close-to-Keplerian motion. A concise derivation of the simplest possible set of formulae for the variation-of-parameters method is presented in this memorandum.

Expressions are also presented for the disturbing effects on the geocentric range and range rate of a celestial body due to any disturbing force in the sense of a first-order perturbation theory. Lastly, an attempt is made to replace the mean anomaly as the sixth orbital parameter by a more convenient variable that asserts the consistency in the orders of magnitude of all six time variations of orbital parameters.

GOODWIN, P. S.

G05 DSN Progress Report for January–February 1971: *Helios* Mission Support

P. S. Goodwin

Technical Report 32-1526, Vol. II, pp. 18–27, April 15, 1971

This article relates the historical factors that led to the establishment of the *Helios* Project, a cooperative solar probe between the Federal Republic of West Germany and the United States. The project management relationships between the two countries, including the role of the Deep Space Network (DSN), are described. A description of the spacecraft and its telecommunications subsystem is also given.

G06 DSN Progress Report for March–April 1971: *Helios* Mission Support

P. S. Goodwin

Technical Report 32-1526, Vol. III, pp. 20–28, June 15, 1971

This is the second in a series of articles relating to Project *Helios* which, when used in conjunction with the first article, will give the reader an overall view of the project, its objectives and organization, and the support to be provided by the Deep Space Network (DSN). This article treats, in particular, the contemplated *Helios* trajectories. Both the near-earth phase and the deep

space phase of the mission are discussed, with particular emphasis being placed upon the tracking and data acquisition aspects.

GORDON, D. L.

G07 **Tracking and Data System Support for the *Mariner* Mars 1969 Mission: Planning Phase Through Midcourse Maneuver**

N. A. Renzetti, K. W. Linnes, D. L. Gordon, and T. M. Taylor

Technical Memorandum 33-474, Vol. I, May 15, 1971

For abstract, see Renzetti, N. A.

GREENWOOD, R. F.

G08 **Results of the 1969 Balloon Flight Solar Cell Standardization Program**

R. F. Greenwood

Technical Report 32-1530, May 1, 1971

High-altitude calibration of solar cells was accomplished during July and August 1969 with the aid of free-flight balloons. Flights were conducted to an altitude of 36,576 m (120,000 ft), a 12,192-m (40,000-ft) altitude increase over the 1968 flights. Solar cells calibrated in this manner are recovered and used as intensity references in solar simulators and in terrestrial sunlight. Balloon-calibrated standard solar cells were made available to NASA centers and other government agencies through a cooperative effort with JPL.

Comparison of solar cell data taken at altitudes of 24,384 m (80,000 ft) and 36,576 m (120,000 ft) was made. Solar cells with altered spectral response characteristics showed an approximate 1% increase in short-circuit current at the higher altitude. Normal, unaltered solar cells exhibited little, if any, change in output between the two altitudes.

Attempts to fly radiometers on two separate flights met with only partial success. The first flight was plagued with instrumentation troubles; the final flight was cancelled because of balloon damage.

A sky radiation experiment was also conducted as part of the 1969 balloon flights. Results indicate that no sky radiation is detectable at 36,576 m (120,000 ft) using normal balloon instrumentation and telemetry techniques.

GULKIS, S.

G09 A Brief Survey of the Outer Planets Jupiter, Saturn, Uranus, Neptune, Pluto, and Their Satellites

R. L. Newburn, Jr., and S. Gulkis

Technical Report 32-1529, April 15, 1971

For abstract, see Newburn, R. L., Jr.

G10 Circular-Polarization and Total-Flux Measurements of Jupiter at 13.1-cm Wavelength

S. Gulkis and B. Gary

Astron. J., Vol. 76, No. 1, pp. 12–16, February 1971

Circular-polarization and total-flux measurements of Jupiter at a wavelength of 13.1 cm were made during April and May 1969 with the 210-ft radio telescope at the Mars Deep Space Station in California. An upper limit to the net degree of circular polarization of 1% was established over the longitude range of the observations, 10–100° and 160–250° System III (1957.0). Total flux data have been used to derive a magnetosphere rotation period of $09^h55^m29^s.72 \pm 0.11$, which is 0.35 s longer than the standard International Astronomical Union System III (1957.0). The total flux data define a beaming curve which has north–south symmetry about the magnetic equator, whereas the beaming curve produced from 1964 observations shows an asymmetry.

HADEK, V.

H01 Cell for Measurement of Basic Electrical Properties of Amorphous and Polycrystalline Materials Under Pressure

V. Hadek

Rev. Sci. Instr., Vol. 42, No. 3, pp. 393–394, March 1971

The most common method of measuring electrical properties of amorphous and polycrystalline materials is to use samples in the form of pellets with vacuum-deposited metallic electrodes. Other techniques (e.g., the anvil technique) yield the resistivity vs pressure relationship, but the temperature range is limited. This article describes a simple and accurate instrument by means of which the resistivity and the Seebeck coefficient can be measured simultaneously as a function of temperature and pressure. With the technique described here, the need for pellet preparation and evaporation of electrode is obviated; also, the measurement of electrical properties is possible in a broad temperature range

much below room temperature. This technique is less time-consuming and allows close packing of the material and better contact than that obtained with the pellet technique.

HAFNER, F. W.

H02 **Computer Controlled Operating and Data Handling System for a Quadrupole Mass Spectrometer**

J. Houseman and F. W. Hafner

Technical Report 32-1518 (Reprinted from *J. Phys., Pt. E: Sci. Instr.*, Vol. 4, No. 1, pp. 46–50, January 1971)

For abstract, see Houseman, J.

HANSELMAN, R. G.

H03 **DSN Progress Report for January–February 1971: GCF Reconfiguration of the Goldstone DSCC Microwave Terminals for 50-kbit Data Transmission**

R. G. Hanselman

Technical Report 32-1526, Vol. II, pp. 129–132, April 15, 1971

The Ground Communications Facility (GCF) functional design for 1971–1972 specifies two 50-kbit/s data streams between the Deep Space Network (DSN) Space Flight Operations Facility and DSS 14 (Mars Deep Space Station), one stream being a backup to the other. This article describes the reconfiguration of the Goldstone Deep Space Communications Complex (DSCC) microwave terminals required for the transmission of dual 50-kbit/s digital data streams between DSS 14 and the Goldstone DSCC area communications terminal located adjacent to DSS 12 (Echo DSS).

HARDY, J. P.

H04 **The Conformational Preferences of the *N*-Trimethylsilyl and *O*-Trimethylsilyl Groups**

J. P. Hardy and W. D. Cumming

J. Am. Chem. Soc., Vol. 93, No. 4, pp. 928–932, February 24, 1971

O-Trimethylsilylcyclohexanol (I) and *N*-trimethylsilylcyclohexylamine (II) and the *cis*- and *trans*-4-methyl and *cis*- and *trans*-4-*tert*-butyl derivatives of these molecules have been synthesized. Measurements at 100 and 220 MHz of the nuclear-magnetic-

resonance chemical shifts of the α protons of the unsubstituted and *cis*- and *trans*-4-*tert*-butyl-substituted compounds were used to obtain values of 1.21 and 0.88 kcal/mol for the conformational free energy preferences (*A* values) of the $-NHSiMe_3$ and $-OSiMe_3$ groups, respectively. In addition, *A* values of 1.15 and 0.93 kcal/mol, respectively, for these same groups were estimated from the chemical shift data for the *cis*-4-methyl compounds, assuming an *A* value of 1.70 kcal/mol for the methyl group. The close agreement between these two methods suggests that, in the present case at least, accurate measurement of conformational preferences may be obtained by the chemical shift method. The present results are discussed in light of recent criticism of this method. An unusually large value for an HCNH proton–proton coupling of 10 Hz was observed for II.

H05 Photocatalytic Production of Organic Compounds From CO and H_2O in a Simulated Martian Atmosphere

J. S. Hubbard, J. P. Hardy, and N. H. Horowitz

Proc. Nat. Acad. Sci., Vol. 68, No. 3, pp. 574–578, March 1971

For abstract, see Hubbard, J. S.

H06 Measurement of Organic Carbon in Arid Soils Using Hydrogen-Flame Ionization Detector

P. J. Geiger and J. P. Hardy

Soil Sci., Vol. 111, No. 3, pp. 175–181, March 1971

For abstract, see Geiger, P. J.

HARTLEY, R. B.

H07 DSN Progress Report for January–February 1971: *Apollo* Mission Support

R. B. Hartley

Technical Report 32-1526, Vol. II, pp. 33–41, April 15, 1971

The *Apollo 14* mission began with launch on January 31, 1971, and ended with splashdown on February 9. The support provided by the Deep Space Network (DSN) to the Manned Space Flight Network (MSFN) during the mission is described. Support was provided from the three 26-m (85-ft) DSN/MSFN Wing stations, the Goldstone 64-m (210-ft) antenna, the Ground Communications Facility, and the Space Flight Operations Facility. Premission and mission activities are discussed, and the mission is briefly described.

H08 **Deep Space Network Support of the Manned Space Flight Network for *Apollo*: 1969–1970**

F. M. Flanagan, R. B. Hartley, and N. A. Renzetti

Technical Memorandum 33-452, Vol. II, May 1, 1971

For abstract, see Flanagan, F. M.

HASBACH, W. A.

H09 **Lightweight Solar Panel Development**

W. A. Hasbach

Technical Report 32-1519, March 15, 1971

This report describes the work performed by the Boeing Co., Aerospace Group, Space Division, Seattle, Washington, between July 1, 1969, and July 1970, on the Lightweight Solar Panel Development Program under JPL contract. The report contains technical information concerning the preliminary design, analysis, test article design, fabrication, and test of a lightweight solar panel made of a built-up beryllium structure with an active cell area of 29 ft^2. Evaluations are presented of the results of the modal survey, reverberant acoustic, random vibration, sinusoidal vibration, static load, thermal–vacuum–shock, substrate frequency, and power output tests.

H10 **Design and Development of a 66-W/kg, 23-m^2 Roll-Up Solar Array**

W. A. Hasbach

JPL Quarterly Technical Review, Vol. 1, No. 1, pp. 68–77, April 1971

Future space missions will require greater power output, lighter weight, and decreased stowed volume for solar arrays. To meet these requirements, a program was initiated to develop the technology for a roll-up solar array by preparing a detailed design, performing the associated analyses, fabricating an engineering development model, and subjecting the engineering model to a comprehensive test program consisting of both environmental and developmental tests. The design and testing of the 66-W/kg (30-W/lb), 23-m^2 (250 ft^2) roll-up solar array developed during this program is described in this article.

HONG, J. P.

H11 A Multiclass Sequential Hypothesis Test With Applications in Pattern Recognition

J. P. Hong

Technical Memorandum 33-482, June 15, 1971

This memorandum presents an algorithm that can be used to build a reading machine that will read impact printed characters and handwritten letters. Invariant features are extracted by random lines. The number of intersections and the total length of intersection that these lines produce are the random variable observations used as inputs to a hypothesis test. This method allows the pattern to be anywhere in the retina and eliminates the cost of fine alignment of the pattern before taking samples. The use of the whole probability distribution of the random variable allows the introduction of size invariant methods.

The sequential multiclass hypothesis test that is presented is Wald's sequential probability ratio test for the two-class problem. The form of this test allows rapid computation of the errors of the first and second kinds for each possible decision. Extensive experiments with block letters and handwritten numerals that verify the usefulness of the proposed test are reported. These experiments show that the error rates are under the control of the user and that the average length of the test can be predicted.

HOROWITZ, N. H.

H12 Photocatalytic Production of Organic Compounds From CO and H_2O in a Simulated Martian Atmosphere

J. S. Hubbard, J. P. Hardy, and N. H. Horowitz

Proc. Nat. Acad. Sci., Vol. 68, No. 3, pp. 574–578, March 1971

For abstract, see Hubbard, J. S.

HORSEWOOD, J. L.

H13 Characteristics, Capabilities, and Costs of Solar Electric Spacecraft for Planetary Missions

D. R. Bartz and J. L. Horsewood (Analytical Mechanics Associates, Inc.)

J. Spacecraft Rockets, Vol. 7, No. 12, pp. 1379–1390, December 1970

For abstract, see Bartz, D. R.

HORTON, T. E.

H14 **Shock-Tube Thermochemistry Tables for High-Temperature Gases: Carbon Dioxide**

W. A. Menard and T. E. Horton

Technical Report 32-1408, Vol. V, March 15, 1971

For abstract, see Menard, W. A.

HOUSEMAN, J.

H15 **Computer Controlled Operating and Data Handling System for a Quadrupole Mass Spectrometer**

J. Houseman and F. W. Hafner

Technical Report 32-1518 (Reprinted from *J. Phys., Pt. E: Sci. Instr.*, Vol. 4, No. 1, pp. 46–50, January 1971)

A computer-controlled operating and data handling system for a quadrupole mass spectrometer is described in this report. The overall system carries out on-line chemical analyses of combustion gases in a rocket chamber.

The computer-controlled mode of operation is based on supplying the quadrupole control console with an externally generated control voltage to tune the instrument to the mass numbers that are of interest. In this manner, only the peak heights of the mass numbers of interest need to be recorded, rather than a complete spectrum.

The operation consists of a calibration phase and a run phase. In the calibration phase, the exact control voltages for all mass numbers are determined. The control voltages drift with time, and, in the run phase, nine slightly different values are supplied around the calibrated control voltage to ensure that the peak is not missed. Thus, only nine data points are recorded for each preselected mass number. Immediately after each test series, a snapshot dump of one scan is printed out in the test area. The quadrupole output is recorded on digital tape and subsequently processed by an IBM 7094 computer to yield the relative concentrations of the desired components.

The system described here can be used in any application where the fast scanning capability of the quadrupole is of interest.

HUBBARD, J. S.

H16 **Photocatalytic Production of Organic Compounds From CO and H_2O in a Simulated Martian Atmosphere**

J. S. Hubbard, J. P. Hardy, and N. H. Horowitz

Proc. Nat. Acad. Sci., Vol. 68, No. 3, pp. 574–578, March 1971

$[^{14}C]CO_2$ and [^{14}C]organic compounds are formed when a mixture of [^{14}C]CO and water vapor diluted in $[^{12}C]CO_2$ or N_2 is irradiated with ultraviolet light in the presence of soil or pulverized vycor substratum. The $[^{14}C]CO_2$ is recoverable from the gas phase, and the [^{14}C]organic products, from the substratum. Three organic products have been tentatively identified as formaldehyde, acetaldehyde, and glycolic acid. The relative yields of $[^{14}C]CO_2$ and [^{14}C]organics are wavelength- and surface-dependent. Conversion of CO to CO_2 occurs primarily at wavelengths shorter than 2000 Å, apparently involves the photolysis of water, and is inhibited by increasing amounts of vycor substratum. Organic formation occurs over a broad spectral range below 3000 Å and increases with increasing amounts of substratum. It is suggested that organic synthesis results from adsorption of CO and H_2O on surfaces, with excitation of one or both molecules occurring at wavelengths longer than those absorbed by the free gases. This process may occur on Mars and may have been important on the primitive earth.

HUMPHREY, M. F.

H17 Solid-Propellant Burning-Rate Modification

M. F. Humphrey

JPL Quarterly Technical Review, Vol. 1, No. 1, pp. 29–34, April 1971

Low acceleration is one of the requirements for solid-propellant orbit insertion motors for future outer-planet missions. This article describes the research accomplished in reducing the low-pressure burning rates of modified solid propellants. Techniques developed with the saturated hydroxy-terminated polybutadiene system were successfully applied to the polyether system (JPL 540) and an unsaturated hydroxy-terminated polybutadiene propellant system. Burning-rate reductions up to 50% were obtained by the synergistic effects of increased oxidizer size, reduction of iron, and inclusion of flame retardants and endothermic combustion modifiers.

HUNTRESS, W. T., JR.

H18 Relative Rates and Their Dependence on Kinetic Energy for Ion–Molecule Reactions in Ammonia

W. T. Huntress, Jr., M. M. Mosesman, and D. D. Elleman

J. Chem. Phys., Vol. 54, No. 3, pp. 843–849, February 1, 1971

Ion-cyclotron-resonance techniques are used to measure the relative rates and their dependence on kinetic energy for the major ion–molecule reactions in ammonia. Charge transfer is shown to compete with proton transfer in the reaction of both NH_2^+ and NH_3^+ with ammonia over an energy range from thermal velocities to 50 eV:

$$\begin{array}{lll} & & NH_4^+ + NH_2 \\ & \overset{k_1}{\nearrow} & \\ NH_3^+ + NH_3 & & \\ & \underset{k_4}{\searrow} & \\ & & NH_3^+ + NH_3 \end{array}$$

$$\begin{array}{lll} & & NH_4^+ + NH \\ & \overset{k_2}{\nearrow} & \\ NH_2^+ + NH_3 & & \\ & \underset{k_3}{\searrow} & \\ & & NH_3^+ + NH_2 \end{array}$$

The rate for charge transfer increases with increasing kinetic energy, while the rate for proton transfer decreases with kinetic energy. At thermal kinetic energies, $k_2/k_1 = 0.6$ and $k_3/k_2 = 1.0$. Resonant charge transfer from NH_3^+ was observed only for translationally excited ions.

HURD, W. J.

H19 DSN [Deep Space Network] Progress Report for March–April 1971: A Wideband Digital Pseudo-Gaussian Noise Generator

W. J. Hurd

Technical Report 32-1526, Vol. III, pp. 111–115, June 15, 1971

A digital system has been constructed for the generation of wideband gaussian noise with a spectrum which is flat to within ±0.5 dB from 0 to 10 MHz. These characteristics are substantially better than those of commercially available analog noise generators, and are required in testing and simulation of wideband communications systems. The noise is generated by the analog summation of 30 essentially independent binary waveforms, clocked at 35 MHz, and low-pass filtered to 10 MHz.

HUTCHISON, R. B.

H20 Radiative Lifetimes of U.V. Multiplets in Atomic Carbon, Nitrogen and Oxygen

R. B. Hutchison (Northwestern University)

J. Quant. Spectrosc. Radiat. Transfer, Vol. 11, No. 1, pp. 81–91, January 1971

Ten multiplets in the spectral region 916–1742 Å of carbon, nitrogen, and oxygen have been measured using a modification of the phase-shift technique. Excitation of the emission was accomplished by the impact of 200-eV electrons with molecular gases containing the atom of interest. The electron beam was sinusoidally modulated at eight, logarithmically spaced, radio frequencies ranging from 0.55 to 28.0 MHz. The phase delay of the sinusoidally varying photon output was measured by comparison with a calibrated, variable delay line to determine the radiative lifetimes. Five of the multiplets were found to exhibit cascading effects, and corrections for these effects were obtained by the application of a one-level cascade model. The measured lifetimes ranged from 1.0 to 9.9 ns, with estimated accuracies of 0.4–1.0 ns.

INGHAM, J. D.

I01 Cyanate Ion and the Uremic Syndrome

J. D. Ingham

JPL Quarterly Technical Review, Vol. 1, No. 1, pp. 45–48, April 1971

A critical survey is made of the literature that logically provides an hypothesis that relates the symptoms of kidney failure (uremic syndrome) to the presence of cyanate ion derived from metabolic urea. If the hypothesis can be unequivocally verified, the consequences will provide a solution to the problem of defining the primary toxic factor in uremia and should lead to substantial improvements in the available treatment for patients with kidney failure.

JACKSON, E. B.

J01 DSN Progress Report for March–April 1971: DSN Research and Technology Support

E. B. Jackson

Technical Report 32-1526, Vol. III, pp. 154–158, June 15, 1971

Major activities in support of the Deep Space Network (DSN) research and technology program are presented for the last 6 mo. Work was performed at both the Venus Deep Space Station and the Microwave Test Facility. Progress and performance summaries are given in the following areas: radiometric observations (20–25 GHz); pulsars and planetary radar; 26-m antenna upgrade;

precision antenna gain measurements; weak source observations; and radio star observations (Cygnus A); the Mars Deep Space Station transmitter rework and testing; transmitter development; 100-kW clock synchronization (X-band); switched carrier experiment; 400-kW harmonic filter; dual 20-kW transmitters; horizontal mill installation; clock synchronization transmissions; and acceptance testing of Deep Space Instrumentation Facility klystrons.

JAFFE, L. D.

J02 **Lunar Traverse Missions**

R. G. Brereton, J. D. Burke, R. B. Coryell, and L. D. Jaffe

JPL Quarterly Technical Review, Vol. 1, No. 1, pp. 125–137, April 1971

For abstract, see Brereton, R. G.

J03 **Blowing of Lunar Soil by *Apollo 12: Surveyor 3* Evidence**

L. D. Jaffe

Science, Vol. 171, No. 3973, pp. 798–799, February 26, 1971

This article presents an analysis of discoloration patterns that were noted on the *Surveyor 3* (*Surveyor III*) television camera after the *Apollo 12* lunar module had landed nearby. Evidence indicates that lunar surface particles were eroded and entrained by lunar module exhaust during the landing and were ejected almost horizontally at 70 m/s or faster. These particles struck the *Surveyor* camera and whitened its surface.

JAWORSKI, W.

J04 **Measured Performance of Silicon Solar Cell Assemblies Designed for Use at High Solar Intensities**

R. G. Ross, Jr., R. K. Yasui, W. Jaworski, L. C. Wen, and E. L. Cleland

Technical Memorandum 33-473, March 15, 1971

For abstract, see Ross, R. G., Jr.

JET PROPULSION LABORATORY

J05 **Proceedings of the Third Annual Conference on Effects of Lithium Doping on Silicon Solar Cells (Held at the Jet Propulsion Laboratory, April 27 and 28, 1970)**

Jet Propulsion Laboratory
(P. A. Berman and J. Weingart, Editors)

Technical Memorandum 33-467, April 1, 1971

The Third Annual Conference on Effects of Lithium Doping on Silicon Solar Cells was sponsored by JPL to provide a forum for an in-depth review and discussion of the results of investigations being carried out by various organizations, under NASA/JPL sponsorship, as part of the Solar Cell Research and Development Program. Participating organizations included cell manufacturers and university and industrial research laboratories. The 15 formal presentations of the conference and a summary of the proceedings are presented.

JOHNSON, D.

J06 DSN [Deep Space Network] Progress Report for March–April 1971: Level Sets of Real Functions on the Unit Square

D. Johnson and E. Rodemich

Technical Report 32-1526, Vol. III, pp. 108–110, June 15, 1971

The problem of finding a level curve of f, a real-valued continuous function on the unit square, which joins opposite sides of the square is investigated. It is shown that while f need not have such a level curve, it at least always has a level connected set with the desired property. This problem is connected with the problem of minimizing the bandwidth of a certain matrix.

KATOW, M. S.

K01 DSN Progress Report for January–February 1971: Antenna Structures: Evaluation of Field Measurements of Reflector Distortions

B. Marcus and M. S. Katow

Technical Report 32-1526, Vol. II, pp. 113–121, April 15, 1971

For abstract, see Marcus, B.

KAWANO, K.

K02 DSN [Deep Space Network] Progress Report for March–April 1971: SFOF Mark IIIA User Terminal and Display Subsystem Design

K. Kawano

Technical Report 32-1526, Vol. III, pp. 171–174, June 15, 1971

The user terminal and display subsystem (UTD) provides various users with the means to communicate with the Central Processing System in the Space Flight Operations Facility (SFOF). Prints, plots, alphanumeric, and graphic displays are presented on various peripheral devices and on digital television. This article discusses the requirements, design considerations, and implementation of the UTD.

KIZNER, W.

K03 **DSN [Deep Space Network] Progress Report for January–February 1971: Optimal Frame Synchronization**

W. Kizner

Technical Report 32-1526, Vol. II, pp. 141–144, April 15, 1971

Optimal frame synchronization algorithms are developed that will reject bad data as well as provide high probabilities for obtaining correct frame synchronization with data that have an error rate within the allowable limits specified by the project. The exact analysis to obtain these probabilities is outlined. Since the amount of computation to obtain these quantities may be very large, easily computed approximations are also given.

KLIORE, A. J.

K04 **The Neutral Atmosphere of Venus as Studied With the *Mariner V* Radio Occultation Experiments**

G. Fjeldbo, A. J. Kliore, and V. R. Eshleman (Stanford University)

Astron. J., Vol. 76, No. 2, pp. 123–140, March 1971

For abstract, see Fjeldbo, G.

KLOC, I.

K05 **Mechanical Interaction of a Driven Roller (Wheel) on Soil Slopes: The Necessary Conditions for an Equilibrium–Velocity Solution**

I. Kloc

Technical Memorandum 33-477, Pt. I, June 15, 1971

The objective of the study reported here was to develop and provide a better understanding of mobility concepts for soft

sloping terrains as applied to lunar roving vehicles. A general solution is given for the mobility performance problem of a power-driven rigid cylindrical roller climbing a semi-infinite soft soil slope with uniform velocity. The roller axle is subjected to vertical and pull force components. A gravitating, cohesive-frictional soil is considered. Emphasis is placed on the application of the solution to lunar and planetary locomotion. The mechanics of soil–roller interaction is described and solved, considering both stress and velocity, as a mixed boundary-value problem. Kötter's quasi-static equilibrium equations are related to a plastic stress configuration satisfying Shield's velocity conditions along the characteristic lines. Solutions of the equilibrium equations yield the driving torque, slip, sinkage, and soil–roller interface stresses. Driving power requirements and thrust efficiency are determined.

A general concept of safety factor against immobilization is introduced. A computer program for the soil–wheel interaction performance (SWIP) was developed, and limited applications of this theory to rigid wheel tests on horizontal terrains indicate very reasonable agreement. The method was also applied to the *Apollo* and *Lunokhod 1* lunar roving vehicle wheels.

Part I of this memorandum presents the basic and necessary conditions satisfying the limiting equilibrium and velocity equations. Part II, to be published separately, will provide the concepts of sufficiency asserting the completeness of a given solution and the computer program.

KNOELL, A. C.

K06 Structural Design and Stress Analysis Program for Advanced Composite Filament-Wound Axisymmetric Pressure Vessels (COMTANK)

A. C. Knoell

Technical Report 32-1531, May 15, 1971

This report describes a computer program (COMTANK) that enables the user to design and analyze advanced composite filament-wound axisymmetric pressure vessels. Based on user input, the program develops a pressure vessel design using netting analysis theory and then analyzes the design considering the orthotropic construction of the vessel. The analysis consists essentially of determining the stress resultants that exist at a point in the tank wall and then the stresses that exist in each ply of the laminate at that point.

KOLBLY, R. B.

K07 **DSN [Deep Space Network] Progress Report for March–April 1971: Switched Carrier Experiments**

R. B. Kolbly

Technical Report 32-1526, Vol. III, pp. 133–145, June 15, 1971

This article describes experiments to produce a practical system for time-sharing a klystron amplifier between two up-link frequencies. Attempts to produce intermodulation products in the Deep Space Instrumentation Facility (DSIF) receiver passband and observations on intermodulation products at a DSIF station (Pioneer Deep Space Station) are described.

KROGH, F. T.

K08 **An Integrator Design**

F. T. Krogh

Technical Memorandum 33-479, May 15, 1971

The general design of a system of subroutines for solving the initial value problem in ordinary differential equations is given. An attempt has been made to design these subroutines in such a way that they will be easy to use on easy problems and still be flexible enough to treat any type of initial value problem with a high degree of efficiency. Emphasis is on the use of these subroutines, rather than on the mathematical algorithms, which, at this time, are not completely specified. Implementation of the design in FORTRAN IV suffers from deficiencies in the design of the multiple entry feature provided in some of the current FORTRAN IV compilers.

LAESER, R. P.

L01 **DSN Progress Report for March–April 1971: *Mariner* Mars 1971 Mission Support**

R. P. Laeser

Technical Report 32-1526, Vol. III, pp. 29–37, June 15, 1971

Implementation schedule tradeoffs caused the actual Deep Space Network (DSN) configuration for support of *Mariner* Mars 1971 launch/midcourse/cruise to be significantly different from the original plans. This article describes the actual configuration by network system.

LAWSON, D. D.

L02 Estimation of Polymer Molecular Weight via Refractive Index

R. A. Rhein and D. D. Lawson

Chem. Technol., Vol. 1, No. 2, pp. 122–126, February 1971

For abstract, see Rhein, R. A.

LEACH, G. E.

L03 DSN [Deep Space Network] Progress Report for March–April 1971: SFOF Digital Television Computer Subassembly

G. E. Leach

Technical Report 32-1526, Vol. III, pp. 175–178, June 15, 1971

The Space Flight Operations Facility (SFOF) digital television computer subassembly is part of the digital television assembly. It provides control functions and interfacing of two IBM 360/75's to 80 channels of television for real-time display of alphanumeric and graphic information. The subassembly consists of a dual computer configuration which is utilized in a primary/alternate mode. This provides the capability for rapid detection and correction of failures in the mission operations environment.

LEAHEY, C. F.

L04 DSN Progress Report for January–February 1971: Mark IIIA Simulation Center Interactive Alphanumeric Television System

C. F. Leahey

Technical Report 32-1526, Vol. II, pp. 100–107, April 15, 1971

The Deep Space Network (DSN) Mark IIIA Simulation Center is capable of simultaneously simulating two spacecraft and three deep space stations using the Univac 1108 and the EMR 6050 computers. The control consoles of the Mark II system were inadequate for controlling a simulation of the size required for the Mark IIIA system. A new control and display system was designed using interactive cathode-ray tube data terminals and high-speed printers. This design upgrades the control and display system for future use in more complex missions. Development, capabilities, and operation of this system are described.

LEIGHTON, R. B.

L05 **The *Mariner 6* and *7* Pictures of Mars: One Year's Processing and Interpretation—An Overview**

R. B. Leighton (California Institute of Technology) and
B. C. Murray (California Institute of Technology)

J. Geophys. Res., Vol. 76, No. 2, pp. 293–296,
January 10, 1971

In late July and early August 1969, 201 complete television frames of Mars were returned by *Mariners 6* and *7 (Mariners VI* and *VII)*. During the subsequent year, over 3500 different versions of those frames were generated by computer processing, involving the production of about 35,000 individual photographic prints and large amounts of computer printout as well. This extensive data processing and distribution required the significant participation of about 15 scientists, engineers, and technicians, mainly at JPL. During that same year, the processed data were analyzed and interpreted by approximately 25 scientists and technicians at six different institutions.

This article introduces a series of articles in this issue that present most of the scientific findings that accrued during the first year following the *Mariner VI* and *VII* flybys of Mars. The collection of articles constitutes a final report on the television experiment, although significant efforts are continuing. The nature of the data obtained, the results regarding the surface and atmosphere of Mars, and implications for subsequent Martian exploration are summarized in this overview.

L06 ***Mariner* Mars 1969: Atmospheric Results**

C. B. Leovy (University of Washington), B. A. Smith (New Mexico State University), A. T. Young, and R. B. Leighton (California Institute of Technology)

J. Geophys. Res., Vol. 76, No. 2, pp. 297–312,
January 10, 1971

For abstract, see Leovy, C. B.

L07 **The Surface of Mars: Pt. 4. South Polar Cap**

R. P. Sharp (California Institute of Technology),
B. C. Murray (California Institute of Technology),
R. B. Leighton (California Institute of Technology),
L. A. Soderblom (California Institute of Technology), and
J. A. Cutts (California Institute of Technology)

J. Geophys. Res., Vol. 76, No. 2, pp. 357–368, January 10, 1971

For abstract, see Sharp, R. P.

LEOVY, C. B.

L08 *Mariner* Mars 1969: Atmospheric Results

C. B. Leovy (University of Washington), B. A. Smith (New Mexico State University), A. T. Young, and R. B. Leighton (California Institute of Technology)

J. Geophys. Res., Vol. 76, No. 2, pp. 297–312, January 10, 1971

Results of investigation of probable atmospheric effects appearing in *Mariner* Mars 1969 television pictures that have undergone noise removal and preliminary decalibration are described. Two distinct types of haze are distinguished: *north polar haze*, seen prominently against the face of the planet in blue photographs, and *thin haze*, usually identified by its appearance on the limb and not strongly colored. Thin haze is surprisingly widespread, particularly in the southern hemisphere. Discrete bright features, which may be evidence for condensation on the ground or in the atmosphere, are described. These occur where bright features have often been seen from earth, in a region where very large multiple-ringed structures seem to dominate the surface morphology. The speculation that these may be evidence for local water-vapor exchange between ground and atmosphere is raised, and some constraints on local subsurface water-vapor sources in the Mars tropics are described. Finally, some implications of the *Mariner* Mars 1969 results pertinent to atmospheric exploration by the *Mariner* Mars 1971 spacecraft are briefly discussed.

LEVY, R.

L09 DSN [Deep Space Network] Progress Report for January–February 1971: A Reanalysis Program for Antenna Member Size Changes

R. Levy

Technical Report 32-1526, Vol. II, pp. 108–112, April 15, 1971

An efficient procedure is described for reanalysis of space-truss structural frameworks. The procedure has been programmed to operate as a post-processor to determine response changes from sets of displacements developed for the initial structure by an

independent structural analysis system. Examples given show substantial savings in computation time when operating in conjunction with the NASTRAN structural analysis system.

LEWICKI, G.

L10 **Electrical Characteristics of AlN Insulating Films in the Thickness Range 40 to 150Å**

G. Lewicki and J. Maserjian

Met. Trans., Vol. 2, No. 3, pp. 673–676, March 1971

Investigation of the electrical properties of metal–insulator–metal (MIM) capacitor structures prepared by nitriding freshly deposited aluminum films in a nitrogen glow discharge indicates that insulating films of AlN having thicknesses on the order of 100 Å could be useful in charge–storage devices. These films are sufficiently conductive at high fields to allow charging and discharging of a buried metal gate with relatively low and short voltage pulses (on the order of 10 V across the AlN for 10^{-7} s or less) and sufficiently insulating at lower values of electric field to store this charge for long periods of time. This article discusses the characteristics relating to steady-state current density, voltage, and insulator thickness for MIM capacitor structures (Au–AlN–Al) over the insulator thickness range 50 to 150 Å.

LIM, W. K.

L11 **Passive Damping of the Forced Precession Motion of a Two-Body Satellite**

W. K. Lim

J. Spacecraft Rockets, Vol. 8, No. 1, pp. 41–47, January 1971

The two-body satellite under study consists of two axisymmetric rigid bodies interconnected by a lossy universal joint that ensures a common axial spin but dissipates energy when there is lateral relative motion. The external torque acting on the system is assumed to be perpendicular to the symmetry axis of one body and an external fixed direction. This article is concerned with the analysis and analytical design of this system for fast damping of its transient oscillations. Two methods have been developed for the computation of the decay time of the forced precession cone angle: one is based on energy consideration, and the other, on angular momentum consideration. The dependences of the decay time on each of the physical parameters of the system were investigated. For an especially simple near-optimum configuration, an analytic solution for the decay time was obtained. The

newly developed theory was applied in an example to the design of a small sun-pointing interplanetary probe oriented by a solar sail.

LINNES, K. W.

L12 DSN Progress Report for March–April 1971: Radio Science Support

K. W. Linnes, T. Sato, and D. Spitzmesser

Technical Report 32-1526, Vol. III, pp. 46–51, June 15, 1971

Since 1967, radio scientists have used the Deep Space Network (DSN) 26- and 64-m antenna stations to investigate pulsars and the effects of the solar corona on radio signals. They have also observed radio emissions of X-ray sources, and have used very long baseline interferometry techniques for high-resolution studies of quasars. The various experiments are identified and summarized, and the published results are indicated.

L13 Tracking and Data System Support for the *Mariner* Mars 1969 Mission: Planning Phase Through Midcourse Maneuver

N. A. Renzetti, K. W. Linnes, D. L. Gordon, and T. M. Taylor

Technical Memorandum 33-474, Vol. I, May 15, 1971

For abstract, see Renzetti, N. A.

LIU, A.

L14 Method of Averages Expansions for Artificial Satellite Applications

J. Lorell and A. Liu

Technical Report 32-1513, April 1, 1971

For abstract, see Lorell, J.

LOBB, V.

L15 Bolted Joints Under Sustained Loading

V. Lobb and F. Stoller

J. Struct. Div., Proc. ASCE, Vol. 97, No. ST3, pp. 905–933, March 1971

A study of bolted structural joints under sustained loads (1000 h) was made to determine long-term joint slip. Joints representative of antenna structural joints were used. These joints were coated

with galvanize, Inorganic Zinc primer, red oxide zinc chromate primer, and mill scale. Interference bolts and hex-head bolts of two different grades were used (ASTM A325 and ASTM A490). The bolted structural joints were tested for long-term static shear stress, long-term static shear stress with a superimposed transverse vibration, and short-term static shear stress with repetitive load reversals. The effects of such variables as joint and fastener coatings, bolt design and strength level shear and tension stress, and balanced design tension-shear rates were studied. All of the faying surfaces tested reached a steady-state rate of slip under sustained loads. The amount and degree of total slip and slip rate were dependent principally on joint shear stress, faying-surface coating, and bolt type.

LORELL, J.

L16 **Method of Averages Expansions for Artificial Satellite Applications**

J. Lorell and A. Liu

Technical Report 32-1513, April 1, 1971

Formulas for the averaged potential in artificial satellite theory are derived. The potential due to gravity harmonics is developed for the general *nm* harmonic. That due to a third body is developed up to the fifth degree in R/R_3, the small distance ratio. The expressions given differ from ones generally available in the literature in that they do not depend on expansions in either eccentricity or inclination.

In addition, a discussion is included on the use of the method of averages for tesseral harmonics. In the case of the rapidly rotating planet Mars, the method is constrained to the evaluation of zonal harmonics. For more slowly rotating bodies such as the moon, all tesseral harmonics can be included.

LUDWIG, A.

L17 **Antenna Support Structure Aperture Blockage Loss**

A. Ludwig

JPL Quarterly Technical Review, Vol. 1, No. 1, pp. 86–96, April 1971

Loss in antenna gain caused by support structure aperture blockage is probably the most difficult loss factor to measure or calculate. In this article the loss is determined experimentally for aluminum and fiberglass structural configurations, and empirical formulas are developed to calculate the loss for other similar

configurations. Experimental and analytical data on the X-band RF transmission characteristics of thin fiberglass sheets are presented. It is concluded that fiberglass structures are far superior for minimizing gain loss.

LUSHBAUGH, W.

L18 DSN [Deep Space Network] Progress Report for January–February 1971: Information Systems: Hardware Version of an Optimal Convolutional Decoder

W. Lushbaugh

Technical Report 32-1526, Vol. II, pp. 49–55, April 15, 1971

A hardware version of an optimal convolutional decoder is described. This decoder implements the Viterbi algorithm for maximum-likelihood decoding of short-constraint-length convolutional codes. It is capable of decoding at data rates up to 1 megabit for codes of constraint length 3, 4, or 5 at code rate ½ or ⅓.

LUTES, G.

L19 DSN [Deep Space Network] Progress Report for January–February 1971: Improved Frequency Dividers

G. Lutes

Technical Report 32-1526, Vol. II, pp. 56–58, April 15, 1971

Frequency dividers with improved phase stability were recently developed for use in the hydrogen maser frequency standard. The commonly used methods of frequency division were found to have excessive phase noise and long-term drift and would thus seriously degrade the inherent stability of the frequency standard. An improvement in phase noise of nearly two orders of magnitude is indicated with the improved frequency dividers.

MacFARLANE, M.

M01 High-Dispersion Spectroscopic Observations of Venus: V. The Carbon Dioxide Band at 8689 Å

L. D. G. Young, R. A. J. Schorn, E. S. Barker (University of Texas), and M. MacFarlane (University of Texas)

Icarus: Int. J. Sol. Sys., Vol. 11, No. 3, pp. 390–407, November 1969

For abstract, see Young, L. D. G.

MACLAY, J. E.

M02 DSN Progress Report for January–February 1971: DSN Operations Control System

J. E. Maclay

Technical Report 32-1526, Vol. II, pp. 4–5, April 15, 1971

A new Deep Space Network (DSN) capability for high-speed transfer of operational control information has been implemented. A 24-fold increase in speed is realized by using the high-speed data line instead of teletype. Automatic inputting of source data yields an additional increase.

MADRID, G. A.

M03 DSN Progress Report for March–April 1971: Tracking System Analytic Calibration Support for the *Mariner* Mars 1971 Mission

G. A. Madrid

Technical Report 32-1526, Vol. III, pp. 52–62, June 15, 1971

The means by which calibrations for Deep Space Network (DSN) tracking data will be provided to the *Mariner* Mars 1971 Project is described. The scope and accuracy of calibrations for distinct error source components is stated and a description of the software to compute and provide calibrations for transmission media and platform observable errors is furnished. Utilization of these calibrations will permit the DSN to satisfy the project's navigational accuracy requirements of 250 km at encounter minus 30 days.

MANATT, S. L.

M04 A Detailed Evaluation of the Dependence of ^3J(H—H) on Bond Angle in Alkenes and Cycloalkenes

M. A. Cooper and S. L. Manatt

Org. Mag. Reson., Vol. 2, No. 5, pp. 511–525, October 1970

For abstract, see Cooper, M. A.

MARCUS, B.

M05 DSN Progress Report for January–February 1971: Antenna Structures: Evaluation of Field Measurements of Reflector Distortions

B. Marcus and M. S. Katow

Technical Report 32-1526, Vol. II, pp. 113–121, April 15, 1971

Field measurements of reflector distortions, using the theodolite angle differences and fixed arc lengths from the vertex of the paraboloid, are based on apparent displacements normal to the line of sight. Two computing methods are described that use directions information from the structural computer analysis to upgrade the readings in the pathlength errors sense. Comparative rms values of the 1/2 pathlength errors, after a paraboloid best fit, that result from the field measurements, the analytical analysis, and the rms equivalences to RF radio star measurements are overlayed on an rms surface tolerance versus elevation angle chart for the Deep Space Network (DSN) 64-m-diam antenna. Close rms agreements allow designation of an error tolerance of ± 0.08 mm (0.003 in.) for the field-measured rms values.

MARGOLIS, J. S.

M06 Self-Broadened Half-Widths and Pressure Shifts for the *R*-Branch *J*-Manifolds of the $3\nu_3$ Methane Band

J. S. Margolis

J. Quant. Spectrosc. Radiat. Transfer, Vol. 11, No. 1, pp. 69–73, January 1971

The self-broadening coefficients for the J-manifolds ($0 \leq J \leq 7$) of the R-branch of the $3\nu_3$ band of methane have been measured. These measurements were performed by comparing synthetic spectra with variable parameters to the measured ones. Measurements were made over a range of pressures of 500–1500 torr. Pressure shifts of the components within a J-manifold were also determined.

MARKIEWCZ, B. S.

M07 Development of a Strapdown Electrically Suspended Gyro Aerospace Navigation System: Final Report

G. Paine, R. S. Edmunds, and B. S. Markiewcz

Technical Memorandum 33-471, April 1, 1971 (Confidential)

For abstract, see Paine, G.

MARSH, H. E., JR.

M08 Oil-Absorbing Polymers

H. E. Marsh, Jr.

JPL Quarterly Technical Review, Vol. 1, No. 1, pp. 49–56, April 1971

A new research program has been started to develop technology needed to make practical use of a well-known characteristic of elastomeric cross-linked polymers. Such polymers, of which class modern solid-propellant binders are members, absorb large amounts of compatible solvents, and yet remain solid. Two goals are being considered in this program. One goal is a material that can be used as a dietary additive which will selectively absorb fats and oils in the digestive tract and hold them until elimination, thus preventing their assimilation. The other goal is a material that can be used in oil-slick mop-up operations. This article presents the interim results on the formulation and testing of three polymer types. Performances amounting to oleic acid absorption of up to 20 times the dry polymer weight have been measured. Higher values are expected. Both mineral oil and a cooking oil are also absorbed, but to a smaller extent.

MASEK, T. D.

M09 **Plasma Properties and Performance of Mercury Ion Thrusters**

T. D. Masek

AIAA J., Vol. 9, No. 2, pp. 205–212, February 1971

This article describes: (1) the electron bombardment ion thruster operation, (2) the relationship of the plasma to this operation, and (3) a consistent method for computing the discharge power per beam ion from the plasma properties for comparison with the measured value. A modified form of the Bohm stable sheath criterion is shown to apply for computing fluxes. The use of this criterion, along with calculations of ion production rates and electron fluxes, permits a more accurate and comprehensive picture of discharge losses than has been obtained previously. Langmuir probe measurements in conventional 15- and 20-cm-diam thrusters using mercury are presented. The 15-cm-diam thruster, of 1962 vintage, was operated at high flow rates (650-mA equivalent mercury flow rate) for comparison with previous lower flow-rate data and to establish reference thruster plasma characteristics.

MASERJIAN, J.

M10 **Electrical Characteristics of AlN Insulating Films in the Thickness Range 40 to 150Å**

G. Lewicki and J. Maserjian

Met. Trans., Vol. 2, No. 3, pp. 673–676, March 1971

For abstract, see Lewicki, G.

MASON, P. V.

M11 Effect of Tin Additive on Indium Thin-Film Superconducting Transmission Lines

P. V. Mason

J. Appl. Phys., Vol. 42, No. 1, pp. 97–102, January 1971

The effect of adding up to 23% tin to the indium film of a thin-film/tantalum-oxide/bulk-tantalum transmission line is described. Addition of tin reduces the velocity and increases the delay for fixed length by 1.4% for each percent of tin. Agreement with the predictions of Pippard's nonlocal theory when mean-free path is reduced is excellent. Pulse attenuation and shape degradation are not increased by addition of tin. Attenuation as low as 10 dB per microsecond of delay was observed at 1.25 K. The added tin reduces by 50% the sensitivity of velocity to temperature near the critical temperature and improves the reproducibility of velocity from line to line. Critical temperature is increased to 6 K for 23% tin, in good agreement with previous measurements.

McCLURE, J. P.

M12 DSN Progress Report for March–April 1971: Ground Communications Facility System Tests

D. Nightingale and J. P. McClure

Technical Report 32-1526, Vol. III, pp. 190–192, June 15, 1971

For abstract, see Nightingale, D.

McELIECE, R. J.

M13 DSN [Deep Space Network] Progress Report for January–February 1971: The Limits of Minimum Distance Decoding

R. J. McEliece

Technical Report 32-1526, Vol. II, pp. 59–61, April 15, 1971

Decoding algorithms that are based on the minimum distance of a block code cannot be used to achieve channel capacity. This degradation is compared with similar degradation caused by sequential decoding. The details of the calculations and assumptions used in this investigation are presented.

M14 DSN [Deep Space Network] Progress Report for January–February 1971: Symmetrically Decodable Codes

R. J. McEliece and J. E. Savage (Brown University)

Technical Report 32-1526, Vol. II, pp. 62–64, April 15, 1971

With the intention of finding binary block codes that are easily decoded, decoding functions consisting of one level of symmetric functions are examined. It is found that all codes so decodable with fixed error correction capability t have rate less than $1/(2t + 1)$ and that this rate is achieved by the repetition code that has two code words and length $2t + 1$. Decoding functions consisting of two or more levels of symmetric functions include all binary functions and can therefore decode arbitrarily good binary codes.

M15 DSN [Deep Space Network] Progress Report for March–April 1971: The Problem of Synchronization of Noisy Video

R. J. McEliece

Technical Report 32-1526, Vol. III, pp. 105–107, June 15, 1971

The problem of acquiring and maintaining TV line synchronization with the use of a pseudonoise (PN) prefix on each scan line, in the presence of random noise, is discussed. The currently proposed method of detecting a loss of TV line synchronization on the *Mariner* Mercury–Venus flight is to prefix each line with a 31-bit PN sequence, and to assume that a loss of synchronization has occurred if the PN appears to have suffered 9 or more bit errors. At high signal-to-noise ratios, this method behaves satisfactorily, but at low signal-to-noise ratios, which could occur at Mercury, the PN sequency can actually suffer 9 or more random bit errors with a significant probability. To reduce this probability to acceptable levels, a PN of length 63 is recommended for use on the *Mariner* Mercury–Venus flight.

M16 On Periodic Sequences From *GF(q)*

R. J. McEliece

J. Combin. Theor., Vol. 10, No. 1, pp. 80–91, January 1971

If $s(t)$ is a periodic sequence from $GF(q) = F$, and if N is the number of times a non-zero element from F appears in a period of s, a theorem presented in this article says $N \equiv 0 (\mathrm{mod}\ p^{\epsilon})$, where ϵ is an integer which depends upon the support of the

Fourier transform of s. An easy corollary deals with $G(f)$, the set of all sequences from F which satisfy the linear recurrence with characteristic polynomial $f \in F[x]$. It says that, for all $s \in G(f)$, $N \equiv 0 (\mathrm{mod}\ p^{\epsilon})$, where now ϵ depends upon the smallest integer ω for which it is possible to write 1 as a product of ω conjugates of roots of f.

McLAUGHLIN, F. D.

M17 DSN Progress Report for January–February 1971: Overseas DSIF 64-m Antenna Project Status

F. D. McLaughlin

Technical Report 32-1526, Vol. II, pp. 177–181, April 15, 1971

The status of construction of two Deep Space Instrumentation Facility (DSIF), 64-m-diameter, steerable, paraboloid, tracking antennas being installed near Canberra, Australia, and Madrid, Spain, is presented. These Deep Space Network (DSN) antennas are being constructed by the Collins Radio Company, Dallas, Texas, under JPL contract.

MENARD, W. A.

M18 Shock-Tube Thermochemistry Tables for High-Temperature Gases: Carbon Dioxide

W. A. Menard and T. E. Horton

Technical Report 32-1408, Vol. V, March 15, 1971

Equilibrium thermodynamic properties and species concentrations for carbon dioxide are tabulated for moving, standing, and reflected shock waves. Initial pressures range from 6.665 to 6665 N/m^2 (0.05 to 50.0 torr), and temperatures from 2,000 to over 80,000 K. In this study, 20 molecular and atomic species are considered.

M19 A Higher Performance Electric-Arc-Driven Shock Tube

W. A. Menard

JPL Quarterly Technical Review, Vol. 1, No. 1, pp. 17–28, April 1971

The results of an experimental study to improve the performance of electric-arc-driven shock tubes are presented. With only minor modifications to the driver, shock velocities have been increased by a factor of 3. The new driver has a conical internal design of small volume and uses a lightweight diaphragm that disintegrates

during the electrical discharge. Data obtained from a 15.2-cm-diameter driven tube, 11.3 m in length, show little shock wave attenuation in gases simulating the Jupiter and Saturn atmospheres. Shock velocities of 45 km/s with test times in excess of 4 μs have been attained. Because of the extended performance, the electric-arc-driven shock tube may now be used to study many outer-planet atmospheric entry problems.

MENNINGER, F.

M20 **DSN [Deep Space Network] Progress Report for March–April 1971: 26-m Antenna HA-dec Counter Torque Modifications**

F. Menninger

Technical Report 32-1526, Vol. III, pp. 245–247, June 15, 1971

A servo hydraulic control system is used to control the motion of the 26-m HA-dec Deep Space Instrumentation Facility antennas. This article describes the improvement in tracking performance of the 26-m antenna as a result of changes in the hydraulic circuit of the HA-dec servo subsystem. A discussion of previous problem areas and the results of the new modification are stated.

MEREK, E. L.

M21 **Growth of Bacteria in Soils from Antarctic Dry Valleys**

R. E. Cameron and E. L. Merek (NASA)

Technical Report 32-1522, February 1, 1971

For abstract, see Cameron, R. E.

MEYER, R.

M22 **DSN [Deep Space Network] Progress Report for March–April 1971: Stability Comparison of Three Frequency Synthesizers**

R. Meyer

Technical Report 32-1526, Vol. III, pp. 98–104, June 15, 1971

The HP 5100A/5110A, Dana 7030, and Fluke 644A synthesizers were evaluated to determine the typical drift and stability that can be expected in a control room environment. All synthesizers were judged equal in short-term drift, and the Dana synthesizer

was found to be superior in long-term drift. The HP and the Dana synthesizers were the most stable, while the Fluke synthesizers did not perform reliably.

MICCIO, J. A.

M23 DSN Progress Report for January–February 1971: DSN Traceability and Reporting Program

J. A. Miccio

Technical Report 32-1526, Vol. II, pp. 145–147, April 15, 1971

The Deep Space Network (DSN) Traceability and Reporting Program is a combination of three programs designed to coordinate and disseminate information needed by researchers, analysts, and managers concerning the DSN mission data record for a current and/or past mission. It also serves as a monitor or as an accounting device by providing status information relative to the generation of system, master, and experimenter data records. The program additionally functions as an index to the mission data captured on magnetic tape and microfilm retained in the DSN Operational Data Control Center.

MILLER, R. B.

M24 DSN Progress Report for March–April 1971: Radiometric Data Accountability, Validation, and Selection in Real-Time

R. B. Miller

Technical Report 32-1526, Vol. III, pp. 219–223, June 15, 1971

A principal responsibility of the Deep Space Network (DSN) Tracking System Analysis Group (TRAG) is to provide a source of validated radiometric data, with all associated information required for processing, for both flight projects and nonreal-time data users. This article describes the TRAG design goal for providing a complete and validated data source with a minimum of manual intervention. The functions described will be part of the Mark III A 360/75 tracking software subsystem.

MONDT, J. F.

M25 Thermionic Reactor Ion Propulsion Spacecraft for Unmanned Outer Planet Exploration

J. F. Mondt and J. P. Davis

J. Spacecraft Rockets, Vol. 8, No. 3, pp. 295–297, March 1971

The nuclear thermionic reactor power system is one of the leading nuclear power system candidates for electric propulsion applications for unmanned missions to Jupiter, Saturn, Uranus, and Neptune. This article presents the external-fuel thermionic reactor concept for development of a useful 70-lb/kWe, 70-kWe electric propulsion system. The side-thrust propulsion system isolates the science payload from the high temperature, the nuclear radiation, and the mercury exhaust environments. A spacecraft arrangement using side-thrust propulsion allows a 4π steradian field of view during the entire mission. The *Titan III-D/Centaur* launch vehicle, being developed for other unmanned missions, has the capability to launch the 70-kWe spacecraft to earth escape velocity.

MONTGOMERY, D. R.

M26 **Calibration of the *Mariner* Mars 1969 Television Cameras**

G. E. Danielson, Jr., and D. R. Montgomery

J. Geophys. Res., Vol. 76, No. 2, pp. 418–431, January 10, 1971

For abstract, see Danielson, G. E., Jr.

MOSESMAN, M. M.

M27 **Relative Rates and Their Dependence on Kinetic Energy for Ion–Molecule Reactions in Ammonia**

W. T. Huntress, Jr., M. M. Mosesman, and D. D. Elleman

J. Chem. Phys., Vol. 54, No. 3, pp. 843–849, February 1, 1971

For abstract, see Huntress, W. T., Jr.

MOYER, T. D.

M28 **DSN [Deep Space Network] Progress Report for March–April 1971: An Additional Effect of Tropospheric Refraction on the Radio Tracking of Near-Earth Spacecraft at Low Elevation Angles**

C. C. Chao and T. D. Moyer

Technical Report 32-1526, Vol. III, pp. 63–70, June 15, 1971

For abstract, see Chao, C. C.

M29 Mathematical Formulation of the Double-Precision Orbit Determination Program (DPODP)

T. D. Moyer

Technical Report 32-1527, May 15, 1971

This report documents the complete mathematical model for the double-precision orbit determination program (DPODP), a third-generation program recently completed at JPL. The DPODP processes earth-based doppler, range, and angular observables of the spacecraft to determine values of the parameters that specify the spacecraft trajectory for lunar and planetary missions. The program was developed from 1964 to 1968; it was first used operationally for the *Mariner VI* and *VII* spacecraft, which encountered Mars in August 1969.

The DPODP has more accurate mathematical models, a significant increase in numerical precision, and more flexibility than the second-generation single-precision orbit determination program (SPODP). Doppler and range observables are computed to accuracies of 10^{-5} m/s and 0.1 m, respectively, exclusive of errors in the tropospheric, ionospheric, and space plasma corrections.

MUDGWAY, D. J.

M30 DSN Progress Report for January–February 1971: *Viking* Mission Support

D. J. Mudgway

Technical Report 32-1526, Vol. II, pp. 28–32, April 15, 1971

Two *Viking* spacecraft, each consisting of an orbiter and a lander, will be launched on a mission to Mars in 1975. This article discusses the capabilities of the Deep Space Network (DSN) as significant factors in the radio frequency and data management design and the engineering requirements of the two orbiters and two landers. Also described is the DSN involvement in the extremely complex lander acquisition sequence, in which trade-offs are made between the total lander "on" period of 2 h and competing factors of round-trip light time and telemetry and command lockup times.

M31 DSN Progress Report for March–April 1971: *Viking* Mission Support

D. J. Mudgway

Technical Report 32-1526, Vol. III, pp. 38–45, June 15, 1971

This article discusses the capabilities of the Deep Space Network (DSN) as a factor in the design of the *Viking* telecommunications system. The problem of accommodating simultaneous downlinks from two orbiters and one lander with dual uplinks to one orbiter and one lander or two orbiters is discussed. Because the *Viking* encounter and subsequent orbital and landed operations take place near maximum earth–Mars separation (approximately 400×10^6 km), the signal-to-noise ratios on both up and downlinks are minimal to support the extensive command and data retrieval requirements. The tradeoffs between DSN capabilities and project requirements such as these are described in the context of the mission design.

MULHOLLAND, J. D.

M32 The System of Planetary Masses as Error Sources in Pulsar Timings

J. D. Mulholland

Astrophys. J., Vol. 165, No. 1, Pt. 1, pp. 105–107, April 1, 1971

Studies of the intrinsic variation of pulsar frequencies, related to the search for understanding of the physical processes occurring within these objects and to the search for planetary companions, require the reduction of the observations to the barycenter of the solar system. Uncertainties in planetary data will introduce corresponding uncertainties into the pulsar observations. The system of planetary masses, which presents such an error source, is shown to introduce potentially observable effects, but with sufficiently small rates as to represent nearly constant biases over extended periods of time. These effects could be misidentified as evidences of planetary companions, but can have no effect on the value of the braking parameter.

MURRAY, B. C.

M33 The *Mariner 6* and *7* Pictures of Mars: One Year's Processing and Interpretation—An Overview

R. B. Leighton (California Institute of Technology) and B. C. Murray (California Institute of Technology)

J. Geophys. Res., Vol. 76, No. 2, pp. 293–296, January 10, 1971

For abstract, see Leighton, R. B.

M34 The Surface of Mars: Pt. 1. Cratered Terrains

B. C. Murray (California Institute of Technology),
L. A. Soderblom (California Institute of Technology),
R. P. Sharp (California Institute of Technology), and
J. A. Cutts (California Institute of Technology)

J. Geophys. Res., Vol. 76, No. 2, pp. 313–330,
January 10, 1971

As described in this article, the pictures taken during the *Mariner VI* and *VII* missions show that craters are the dominant landform on Mars and that their occurrence is not correlated uniquely with latitude, elevation, or albedo markings. Two distinct morphological classes are recognized: small bowl-shaped and large flat-bottomed. The former show little evidence of modifications, whereas the latter appear generally more modified than lunar upland craters of comparable size. A regional maria/uplands dichotomy like the moon has not yet been recognized on Mars. Crater modification on Mars has involved much greater horizontal redistribution of material than that in the lunar uplands. It is possible that there are erosional processes only infrequently active. Analysis of the natures and fluxes of bodies that have probably impacted the moon and Mars leads to the conclusion that it is likely that most of the large flat-bottomed craters on Mars have survived from the final phases of planetary accretion. Significant crater modification, however, has taken place more recently on Mars. Inasmuch as the present small bowl-shaped craters evidence little modification, the postaccretion crater-modification process on Mars may have been primarily episodic rather than continuous. The size–frequency distribution of impacting bodies that produced the present small Martian bowl-shaped craters differs from the distribution of impacting bodies that produced the post-mare primary impacts on the moon by a marked deficiency of large bodies. Survival of crater topography from the end of planetary accretion would make any hypothetical earthlike phase with primitive oceans there unlikely. The traditional view of Mars as an earthlike planetary neighbor in terms of its surface history is not supported by the picture data.

M35 The Surface of Mars: Pt. 2. Uncratered Terrains

R. P. Sharp (California Institute of Technology),
L. A. Soderblom (California Institute of Technology),
B. C. Murray (California Institute of Technology), and
J. A. Cutts (California Institute of Technology)

J. Geophys. Res., Vol. 76, No. 2, pp. 331–342,
January 10, 1971

For abstract, see Sharp, R. P.

M36 **The Surface of Mars: Pt. 3. Light and Dark Markings**

J. A. Cutts (California Institute of Technology),
L. A. Soderblom (California Institute of Technology),
R. P. Sharp (California Institute of Technology),
B. A. Smith (California Institute of Technology), and
B. C. Murray (California Institute of Technology)

J. Geophys. Res., Vol. 76, No. 2, pp. 343–356,
January 10, 1971

For abstract, see Cutts, J. A.

M37 **The Surface of Mars: Pt. 4. South Polar Cap**

R. P. Sharp (California Institute of Technology),
B. C. Murray (California Institute of Technology),
R. B. Leighton (California Institute of Technology),
L. A. Soderblom (California Institute of Technology), and
J. A. Cutts (California Institute of Technology)

J. Geophys. Res., Vol. 76, No. 2, pp. 357–368,
January 10, 1971

For abstract, see Sharp, R. P.

NASH, D. B.

N01 **Potassium–Uranium Systematics of *Apollo 11* and *Apollo 12* Samples: Implications for Lunar Material History**

F. P. Fanale and D. B. Nash

Science, Vol. 171, No. 3969, pp. 282–284, January 22, 1971

For abstract, see Fanale, F. P.

NEWBURN, R. L., JR.

N02 **A Brief Survey of the Outer Planets Jupiter, Saturn, Uranus, Neptune, Pluto, and Their Satellites**

R. L. Newburn, Jr., and S. Gulkis

Technical Report 32-1529, April 15, 1971

A survey of current knowledge about Jupiter, Saturn, Uranus, Neptune, Pluto, and their satellites is presented. The best available numerical values are given for physical parameters, including orbital and body properties, atmospheric composition and structure, and photometric parameters. The more acceptable current theories of these bodies are outlined, with thorough referencing offering access to the details. The survey attempts to be complete through February 15, 1971.

NG, E. W.

N03 On Some Indefinite Integrals of Confluent Hypergeometric Functions

E. W. Ng and M. Geller

J. Res. NBS, Sec. B: Math. Sci., Vol. 74B, No. 2, pp. 85–98, April–June 1970

Analytical expressions and reduction formulas are developed for various indefinite integrals of the confluent hypergeometric functions. These integrals are of the type

$$\int f(a, b, z) z^p e^{\alpha z} dz,$$

where f is one of the two Kummer functions

$$M(a, b, z) \equiv {}_1F_1(a; b; z) \text{ or } U(a, b, z),$$

with real or complex a, b, z, and α, and real p.

N04 On the Computation of Debye Functions of Integer Orders

E. W. Ng and C. J. Devine

Math. Comp., Vol. 24, No. 110, pp. 405–407, April 1970

The Debye functions, which occur in thermodynamic problems in the context of, for example, crystallographic structure or radiation, are sometimes labeled radiation integrals. These functions, as defined in this article, are essentially incomplete Riemann's zeta functions. This article presents an efficient method for the computation of Debye functions of integer orders to 20 significant decimal digits.

N05 Recursive Algorithms for the Summation of Certain Series

M. M. Saffren and E. W. Ng

SIAM J. Math. Anal., Vol. 2, No. 1, pp. 31–36, February 1971

For abstract, see Saffren, M. M.

NIGHTINGALE, D.

N06 DSN Progress Report for March–April 1971: Ground Communications Facility System Tests

D. Nightingale and J. P. McClure

Technical Report 32-1526, Vol. III, pp. 190–192, June 15, 1971

The Ground Communications Facility substantially upgraded the High-Speed System and implemented a new Wideband

System for more comprehensive operational data transfers. Extensive tests were conducted prior to turning these systems over to operations personnel for integration into the Deep Space Network (DSN). This article summarizes the purpose and results of these tests, with the final objective of full committed support of *Mariner* Mars 1971 flight operations.

OAKLEY, E. C.

001 **DSN [Deep Space Network] Progress Report for March–April 1971: Digital Step Attenuator**

E. C. Oakley

Technical Report 32-1526, Vol. III, pp. 211–214, June 15, 1971

A 50-Ω digital step attenuator has been developed having 0.2-dB resolution and 51-dB maximum loss. This device has been tested from dc to 10 MHz, where a ±5-deg maximum differential phase shift was measured. Preliminary tests indicate that the attenuator may operate satisfactorily at frequencies as high as 100 MHz. No signal discontinuity occurs during switching, and positive confirmation of step activation is provided. The attenuator is constructed on a 14.5 by 3.2-cm (5.7 by 1.25-in.) double-sided etched circuit card, and occupies a volume of less than 74 cm^3 (4.5 $in.^3$).

OLIVER, R. E.

002 **Large Spacecraft Antennas: New Geometric Configuration Design Concepts**

R. E. Oliver

JPL Quarterly Technical Review, Vol. 1, No. 1, pp. 78–85, April 1971

Several unconventional approaches to the configurational design of high-gain microwave antenna reflectors are presented. These approaches provide means for improving the performance of nonfurlable antennas and for improving both aperture efficiency and stowed volume efficiency of furlable antennas.

The first class of design approaches involves relatively minor modifications of conventional dual-reflector (Cassegrain and Gregorian feed) antenna concepts. These modifications eliminate the loss of transmitted energy resulting from the reflection of energy

back into the feed from the subreflector as well as the loss due to interception of rays by the subreflector after reflection from the main reflector.

The second class of concepts involves the use of a conical main reflector and multiple reflections from this main reflector and from one or more subreflectors. These concepts offer the advantage of relative ease of fabrication, inspection, and furlability associated with a single curvature (conical) main reflector. In addition, they provide configurations with very small diameter subreflectors, resulting in low aperture area blockage and small furled antenna diameters.

ONDRASIK, V. J.

003 DSN [Deep Space Network] Progress Report for March–April 1971:
A First-Order Theory for Use in Investigating the Information Content Contained in a Few Days of Radio Tracking Data

V. J. Ondrasik and D. W. Curkendall

Technical Report 32-1526, Vol. III, pp. 77–93, June 15, 1971

An approximation to the topocentric range rate of a spacecraft is developed which is first order in both the time past epoch and the ratio between the distance of an observing station from the geocenter and the geocentric range. This approximation is compared with a numerical integrated trajectory to obtain some idea of the duration over which it may be reliable. The development is extended to include an analytical determination of the errors in the spacecraft state produced by errors in the range rate data. It is also shown how range data may be incorporated into this cursory error analysis. The partial derivatives of the gravitational geocentric acceleration with respect to range, declination, and right ascension are obtained analytically and shown graphically.

OSBORN, G.

004 DSN [Deep Space Network] Progress Report for January–February 1971:
DSIF Uplink Amplitude Instability Measurement

A. Bryan and G. Osborn

Technical Report 32-1526, Vol. II, pp. 165–168, April 15, 1971

For abstract, see Bryan, A.

OTOSHI, T. Y.

005 **DSN [Deep Space Network] Progress Report for January–February 1971: A Study of Microwave Transmission Through Perforated Flat Plates**

T. Y. Otoshi

Technical Report 32-1526, Vol. II, pp. 80–85, April 15, 1971

This article presents a simple formula and graph useful for predicting the transmission loss of a circular hole array in a metallic flat plate having either a 60- (staggered) or 90-deg (square) hole pattern. The formula is restricted to the case of an obliquely incident plane wave with the E-field polarized normal to the plane of incidence. The theoretical formula was experimentally verified by testing samples having hole diameters varying from 1.6 to 12.7 mm, porosities varying from 10 to 51%, and plate thicknesses varying from 0.08 to 2.3 mm. The agreement between theory and experiment was typically better than 1 dB at S-band and 2 dB at X-band.

006 **DSN [Deep Space Network] Progress Report for March–April 1971: Analysis of the Boresight Error Calibration Procedure for Compact Rotary Vane Attenuators**

T. Y. Otoshi

Technical Report 32-1526, Vol. III, pp. 126–132, June 15, 1971

In previous studies of the compact rotary vane attenuator, the possible error due to stator vane misalignment was not considered. It is shown in this article that even though the stator vanes are misaligned with respect to each other, the boresight error calibration procedure will tend to cause the residual attenuation error to reduce to a type B error which is generally negligible. This analysis applies to conventional as well as to compact rotary vane attenuators.

PAINE, G.

P01 **Development of a Strapdown Electrically Suspended Gyro Aerospace Navigation System: Final Report**

G. Paine, R. S. Edmunds, and B. S. Markiewcz

Technical Memorandum 33-471, April 1, 1971 (Confidential)

The Strapdown Electrically Suspended Gyro Aerospace Navigator (SEAN) is a developmental inertial system conceived in 1965. The

SEAN development program at JPL has proven the feasibility of employing electrically suspended gyros (ESGs) in a strapdown inertial navigation system with a high angular rate environment. Methods for accurately calibrating a strapdown ESG have also been demonstrated. This memorandum provides the objectives, accomplishments, recommendations, and conclusions of the program. Those areas requiring further development work to produce an operational system are detailed. A brief functional description of the system developed to prove the feasibility of an ESG strapdown navigator is also included.

PAINE, R. A.

P02 DSN Progress Report for January–February 1971: SFOF Cable Control

R. A. Paine

Technical Report 32-1526, Vol. II, pp. 122–124, April 15, 1971

The Space Flight Operations Facility (SFOF) experiences frequent reconfigurations in both its physical layout and its functional capabilities. These changes are necessary to meet new requirements placed on it by the Deep Space Network (DSN) and the flight projects. This article summarizes a cabling plan that maintains discipline in the installation and removal of cabling in the SFOF.

PENZO, P. A.

P03 Satellite Flyby Opportunities for the Multi-Outer-Planet Missions

P. A. Penzo

JPL Quarterly Technical Review, Vol. 1, No. 1, pp. 1–12, April 1971

In the proposed missions to the outer planets, observations of the planets' natural satellites will be of considerable scientific interest. In the study presented in this article, the satellite encounter opportunities are generated for two multiple-flyby missions which include all five of the major planets. Many favorable encounter opportunities are found for the large satellites of Jupiter, and some for Titan and Iapetus of Saturn. The opportunities for satellites of Uranus are least favorable. Opportunities also exist for multiple-satellite encounters on the same mission and examples are shown. Finally, for Jupiter, some arrival dates exist where very close flybys of certain satellites are possible. These opportunities, added to the multiple-planet missions, will enhance the scientific return significantly.

PHILLIPS, H.

P04 **DSN [Deep Space Network] Progress Report for March–April 1971: Development of the Heat Exchanger for the 64-m Antenna Hydrostatic Bearing**

H. Phillips

Technical Report 32-1526, Vol. III, pp. 193–196, June 15, 1971

Maintenance of oil temperature, as a means of viscosity control, is an essential requirement for the 64-m antenna hydrostatic bearing. Operational experience with the heat exchanger used for cooling the oil showed that it was not functioning adequately or in accordance with the design, and a resultant study showed a probable internal structural failure. A new heat exchanger was designed, with JPL assistance on the structural problem, and is now operating satisfactorily.

POWELL, W. B.

P05 **Thrust-Chamber Technology for Oxygen Difluoride/Diborane Propellants**

R. W. Riebling and W. B. Powell

J. Spacecraft Rockets, Vol. 8, No. 1, pp. 4–14, January 1971

For abstract, see Riebling, R. W.

RAKUNAS, R. R.

R01 **DSN Progress Report for March–April 1971: DSN Multiple-Mission Command System**

R. R. Rakunas and A. Schulze

Technical Report 32-1526, Vol. III, pp. 4–6, June 15, 1971

The Deep Space Network (DSN) Multiple-Mission Command System generates and transmits commands to one or two spacecraft simultaneously from a central location. All commands are originated at the Space Flight Operations Facility (SFOF) and can be sent to one or more Deep Space Stations for storage or transmission to the spacecraft. This article describes the DSN Multiple-Mission Command System and reflects the functions of the Deep Space Instrumentation Facility, Ground Communications Facility, and SFOF elements that support it.

REED, I. S.

R02 DSN [Deep Space Network] Progress Report for January–February 1971: Boolean Difference Calculus and Fault Finding

I. S. Reed (University of Southern California)

Technical Report 32-1526, Vol. II, pp. 65–71, April 15, 1971

This article describes a method for testing for a possible fault in a gate in a larger switching circuit. The feature of the method is that it does not require isolating the suspicious gate from the rest of the circuit. The techniques involve a Boolean difference calculus reminiscent of, but not identical to, ordinary difference calculus.

REID, M. S.

R03 DSN Progress Report for January–February 1971: Improved RF Calibration Techniques: System Operating Noise Temperature Calibrations

M. S. Reid

Technical Report 32-1526, Vol. II, pp. 89–91, April 15, 1971

The system operating noise temperature performance of the following low noise research cones in the Deep Space Network (DSN) Goldstone Deep Space Communications Complex is reported for the periods indicated:

(1) S-band polarization ultra cone at DSS 11 (Pioneer Deep Space Station): October 1970 through January 1971.

(2) S-band research operational cone at DSS 13 (Venus DSS): October 1970 through January 1971.

(3) Polarization diversity S-band cone at DSS 14 (Mars DSS): mid-September 1970 through January 1971.

(4) Multi-frequency X-band/K-band cone at DSS 14: mid-March 1970 through February 1971.

The operating noise temperature calibrations were performed using the ambient termination technique.

REIER, M.

R04 Absolute Gamma-Ray Intensity Measurements of a SNAP-15A Heat Source

M. Reier

Nucl. Sci. Eng., Vol. 43, No. 3, pp. 267–272, March 1971

A germanium crystal has been used to measure the absolute intensity of gamma rays from the decay of ^{238}Pu, ^{212}Pb, ^{212}Bi, and ^{208}Tl in a 1.5-W SNAP-15A (System for Nuclear Auxiliary Power 15A) heat source. In practically all cases, agreement with other measurements is excellent. In addition, the amount of ^{236}Pu impurity originally present in the sample can be measured with an accuracy of 4%. It is estimated that the ^{236}Pu content in a fuel sample that is several months old can easily be measured with an accuracy of 10%.

RENZETTI, N. A.

R05 DSN Progress Report for January–February 1971: DSN Functions and Facilities

N. A. Renzetti

Technical Report 32-1526, Vol. II, pp. 1–3, April 15, 1971

The Deep Space Network (DSN), established by the NASA Office of Tracking and Data Acquisition and under the system management and technical direction of JPL, is designed for two-way communications with unmanned spacecraft traveling approximately 16,000 km (10,000 mi) from earth to planetary distances. The objectives, functions, and organization of the DSN are summarized, and its three facilities—the Deep Space Instrumentation Facility, the Ground Communications Facility, and the Space Flight Operations Facility—are described.

R06 DSN Progress Report for March–April 1971: DSN Functions and Facilities

N. A. Renzetti

Technical Report 32-1526, Vol. III, pp. 1–3, June 15, 1971

The Deep Space Network (DSN), established by the NASA Office of Tracking and Data Acquisition and under the system management and technical direction of JPL, is designed for two-way communications with unmanned spacecraft traveling approximately 16,000 km (10,000 mi) from earth to planetary distances. The objectives, functions, and organization of the DSN are summarized, and its three facilities—the Deep Space Instrumentation Facility, the Ground Communications Facility, and the Space Flight Operations Facility—are described.

R07 Tracking and Data System Support for the *Pioneer* Project: *Pioneer VII*. Extended Mission: February 24, 1967–July 1, 1968

N. A. Renzetti

Technical Memorandum 33-426, Vol. VI, April 15, 1971

The Tracking and Data System supported the deep space phase of the *Pioneer VII* mission, which is in an outward trajectory from the earth in a heliocentric orbit. During the period of this memorandom, six scientific instruments aboard the spacecraft continued to register information relative to interplanetary particles and fields, and radio metric data generated by the network continues to improve our knowledge of the celestial mechanics of the solar system. In addition to detail network support activities, network performance and special support activities are covered.

R08 **Tracking and Data System Support for the *Pioneer* Project: *Pioneer VII*. Extended Mission: July 1, 1968–July 1, 1969**

N. A. Renzetti

Technical Memorandum 33-426, Vol. VII, April 15, 1971

The *Pioneer VII* mission (outward trajectory, heliocentric orbit) utilized six scientific instruments to accumulate information relative to interplanetary high-energy particles, solar phenomena, and plasma. The spacecraft also served as a celestial mechanics experiment reference point. The Tracking and Data System (comprised of the Air Force Eastern Test Range, Deep Space Network, Manned Space Flight Network, and NASA Communications Network) tracked the spacecraft from launch through near-earth and deep space phases. For near-earth communications and tracking, all Tracking and Data System facilities responded to mission, launch vehicle, and range requirements. For deep space communications and tracking, the Deep Space Network responded to tracking, telemetry, command, monitoring, simulation, and operations control requirements.

R09 **Tracking and Data System Support for the *Pioneer* Project: *Pioneer VIII*. Extended Mission: June 1, 1968–July 1, 1969**

N. A. Renzetti

Technical Memorandum 33-426, Vol. VIII, May 1, 1971

The *Pioneer VIII* mission (outward trajectory and heliocentric orbit) employed seven scientific instruments to accumulate information relative to interplanetary high-energy particles, solar phenomena, and plasma. The spacecraft also served as a celestial mechanics experiment reference point and carried aloft a "piggyback" satellite, called the *Test and Training Satellite*, to be used for *Apollo* ground station crew training and mission simulation. Deep space tracking for the first period of the extended flight phase

was made possible by the Deep Space Network, which responded to all tracking telemetry, command, monitoring, simulation, and operations control requirements.

R10 Deep Space Network Support of the Manned Space Flight Network for *Apollo*: 1969–1970

F. M. Flanagan, R. B. Hartley, and N. A. Renzetti

Technical Memorandum 33-452, Vol. II, May 1, 1971

For abstract, see Flanagan, F. M.

R11 Tracking and Data System Support for the *Mariner* Mars 1969 Mission: Planning Phase Through Midcourse Maneuver

N. A. Renzetti, K. W. Linnes, D. L. Gordon, and T. M. Taylor

Technical Memorandum 33-474, Vol. I, May 15, 1971

The Tracking and Data System support for the *Mariner* Mars 1969 Project that is described herein was planned and implemented in close cooperation with the Mission Operations and Spacecraft Systems of the project. The project requirements for tracking, telemetry, command, simulation, mission control, and compatibility testing were reviewed for matching to Deep Space Network (DSN) capabilities. The DSN capabilities to support the project were set forth in an operations plan describing the design of the DSN systems formulated for the support of this project. Each of the systems is described. Unusual new features were the multimission telemetry system, which eliminated the need for mission-dependent equipment at the tracking stations, and an experimental high-rate telemetry system operating at 16,200 bits/s. This unusually high rate, employed for the first time in deep space missions, permitted low-resolution pictures to be returned in real time and full-resolution pictures to be played back from the spacecraft tape recorder in less than 3 h. Normal techniques and rates would have required 7 to 8 days of playback.

Flight support was provided in the near-earth phase by the facilities of the Air Force Eastern Test Range and by the Ascension Island Station of the Manned Space Flight Network. The 26-m antenna stations of the DSN provided the deep space phase support throughout the mission. During the cruise portion of the deep space phase, the DSN 64-m antenna at the Mars Deep Space Station in California provided ranging data to planetary distances; during the planetary encounter, it provided the 16,200-bits/s capability by means of the block-coded, high-rate telemetry system.

Analysis of the support performance shows that virtually all tracking and telemetry data received on earth was acquired, processed,

and delivered to the project. All commands delivered to the DSN by the project for transmission to the spacecraft were transmitted successfully.

RHEIN, R. A.

R12 Estimation of Polymer Molecular Weight via Refractive Index

R. A. Rhein and D. D. Lawson

Chem. Technol., Vol. 1, No. 2, pp. 122–126, February 1971

The number-average molecular weight of polymers is ordinarily obtained by laborious methods, such as viscosity, osmometry, light-scattering, and gel permeation chromatography measurements. As discussed in this article, linear correlations, have now been demonstrated between inverse molecular weight and index of refraction for isobutylene and ethylene oxide polymers and telomers and for saturated hydrocarbons and nonconjugated dienes.

RIEBLING, R. W.

R13 Thrust-Chamber Technology for Oxygen Difluoride/Diborane Propellants

R. W. Riebling and W. B. Powell

J. Spacecraft Rockets, Vol. 8, No. 1, pp. 4–14, January 1971

Analyses of high-launch-energy unmanned outer-planet orbiter missions for 1970–1985 indicate that payloads probably will be severely constrained by the capabilities of economical launch vehicles. One way to increase the payload is to use high-energy propellants in the spacecraft propulsion system. System studies have led to the choice of oxygen difluoride (OF_2) and diborane (B_2H_6) as a promising candidate propellant combination because of: (1) the potentially high vacuum specific impulse (approximately 400 s at a thrust chamber expansion area ratio of 60) at a relatively low chamber pressure of about 100 psia, and (2) a relatively broad common liquidus range (105°F with a maximum vapor pressure of 100 psia). (A low chamber pressure is important because liquid chemical propulsion systems required by unmanned missions envisioned for the next decade or so will burn relatively small quantities of propellant at relatively low thrust levels.) Both constraints dictate a pressure-fed (low-chamber-pressure) propulsion system, rather than a pumped (high-chamber-pressure) system.

Such a propulsion system now under development at JPL is being designed to be capable of operating anywhere between the solar orbits of Venus and Pluto. This article surveys one aspect of this program: thrust chamber technology for the OF_2/B_2H_6 propel-

lants. Advanced development of three types of pressure-fed chambers is under way: (1) a film-cooled or mixture-ratio-stratified chamber made of an advanced carbonaceous or graphitic material, or possibly a metallic material; (2) a regeneratively cooled metallic chamber; and (3) a heat-pipe-cooled metallic chamber. It is planned to select the most promising thrust chamber concept for final development to flight-prototype status. Reviewed here is the technology effort in the key areas of heat transfer, propellant flow characteristics, solids deposition, vacuum ignition behavior, delivered vacuum performance, and materials development. Other areas in which further effort appears justified are identified.

RINDFLEISCH, T. C.

R14 **Digital Processing of the *Mariner 6* and *7* Pictures**

T. C. Rindfleisch, J. A. Dunne, H. J. Frieden, W. D. Stromberg, and R. M. Ruiz

J. Geophys. Res., Vol. 76, No. 2, pp. 394–417, January 10, 1971

The *Mariner* Mars 1969 television camera system was a vidicon-based digital system and included a complex on-board video encoding and recording scheme. The spacecraft video processing was designed to maximize the volume of data returned and the encoded discriminability of the low-contrast surface detail of Mars. The ground-based photometric reconstruction of the *Mariner 6* and *7* (*Mariner VI* and *VII*) photographs, as well as the correction of inherent vidicon camera distortion effects necessary to achieve television experiment objectives, required use of a digital computer to process the pictures. The digital techniques developed to reconstruct the spacecraft encoder effects and to correct for camera distortions are described, and examples of the processed results are shown. Specific distortion corrections that are considered include the removal of structured system noises, the removal of sensor residual image, the correction of photometric sensitivity nonuniformities and nonlinearities, the correction of geometric distortions, and the correction of modulation transfer limitations.

ROBERTSON, F. A.

R15 **Low Acceleration Rate Ignition for Spacecraft**

J. I. Shafer, L. D. Strand, and F. A. Robertson

JPL Quarterly Technical Review, Vol. 1, No. 1, pp. 35–44, April 1971

For abstract, see Shafer, J. I.

RODEMICH, E.

R16 DSN [Deep Space Network] Progress Report for March–April 1971: Level Sets of Real Functions on the Unit Square

D. Johnson and E. Rodemich

Technical Report 32-1526, Vol. III, pp. 108–110, June 15, 1971

For abstract, see Johnson, D.

ROSS, R. G., JR.

R17 Measured Performance of Silicon Solar Cell Assemblies Designed for Use at High Solar Intensities

R. G. Ross, Jr., R. K. Yasui, W. Jaworski, L. C. Wen, and E. L. Cleland

Technical Memorandum 33-473, March 15, 1971

This memorandum presents the results of an experimental program to evaluate the performance of three solar panel design approaches suitable for use at high solar intensities: the second-surface mirror mosaic approach, the selective bandpass filter approach, and the tilted panel approach. Extensive data are presented on the thermal and electrical characteristics of a number of specific cell/coverglass assemblies representative of these approaches. Included are data on electrical performance at intensities from 1 to 6 suns, data on thermal–optical properties both before and after long-term ultraviolet and proton radiation exposure, and data on the thermal–mechanical properties of a number of solar cell adhesives.

RUIZ, R. M.

R18 Digital Processing of the *Mariner 6* and *7* Pictures

T. C. Rindfleisch, J. A. Dunne, H. J. Frieden, W. D. Stromberg, and R. M. Ruiz

J. Geophys. Res., Vol. 76, No. 2, pp. 394–417, January 10, 1971

For abstract, see Rindfleisch, T. C.

R19 Maximum Discriminability Versions of the Near-Encounter *Mariner* Pictures

J. A. Dunne, W. D. Stromberg, R. M. Ruiz, S. A. Collins, and T. E. Thorpe

J. Geophys. Res., Vol. 76, No. 2, pp. 438–472, January 10, 1971

For abstract, see Dunne, J. A.

RUSCH, W. V. T.

R20 Applications of Two-Dimensional Integral-Equation Theory to Reflector-Antenna Analysis

W. V. T. Rusch

Technical Memorandum 33-478, May 15, 1971

The method of moments is applied to the solution of integral equations for the current induced on conducting cylinders immersed in an arbitrary two-dimensional field. The solution is outlined, and such scattering parameters as the induced-field ratio and the extinction cross section are defined. Numerical solutions are obtained for several geometries that are relevant to the problem of large reflector antenna analysis.

SAFFREN, M. M.

S01 Recursive Algorithms for the Summation of Certain Series

M. M. Saffren and E. W. Ng

SIAM J. Math. Anal., Vol. 2, No. 1, pp. 31–36, February 1971

In this article, the computation of the series

$$S_N = \sum_{n=0}^{N} d_n p_n$$

is studied by regarding it as a solution of an inhomogeneous difference equation. Since power series are often computed using first-order difference equations, an analysis for this type of computation is also presented.

SATO, T.

S02 DSN Progress Report for March–April 1971: Radio Science Support

K. W. Linnes, T. Sato, and D. Spitzmesser

Technical Report 32-1526, Vol. III, pp. 46–51, June 15, 1971

For abstract, see Linnes, K. W.

SAVAGE, J. E.

S03 **DSN [Deep Space Network] Progress Report for January–February 1971: Symmetrically Decodable Codes**

R. J. McEliece and J. E. Savage (Brown University)

Technical Report 32-1526, Vol. II, pp. 62–64, April 15, 1971

For abstract, see McEliece, R. J.

SCHORN, R. A. J.

S04 **High-Dispersion Spectroscopic Observations of Venus: V. The Carbon Dioxide Band at 8689 Å**

L. D. G. Young, R. A. J. Schorn, E. S. Barker (University of Texas), and M. MacFarlane (University of Texas)

Icarus: Int. J. Sol. Sys., Vol. 11, No. 3, pp. 390–407, November 1969

For abstract, see Young, L. D. G.

S05 **High-Dispersion Spectroscopic Observations of Venus: VII. The Carbon Dioxide Band at 10 488 Å**

L. D. G. Young, R. A. J. Schorn, and E. S. Barker (University of Texas)

Icarus: Int. J. Sol. Sys., Vol. 13, No. 1, pp. 58–73, July 1970

For abstract, see Young, L. D. G.

SCHULZE, A.

S06 **DSN Progress Report for March–April 1971: DSN Multiple-Mission Command System**

R. R. Rakunas and A. Schulze

Technical Report 32-1526, Vol. III, pp. 4–6, June 15, 1971

For abstract, see Rakunas, R. R.

ŚCIBOR-MARCHOCKI, R. I.

S07 **DSN [Deep Space Network] Progress Report for March–April 1971: Description of a Telemetry Procedural Language**

R. I. Ścibor-Marchocki

Technical Report 32-1526, Vol. III, pp. 159–167,
June 15, 1971

A procedural language and a compiler for it are being developed as an aid in the writing of programs which will process telemetry data received from spacecraft. This article describes the language. Also, the philosophy that leads to the choice of the language is briefly presented.

SHAFER, J. I.

S08 **Low Acceleration Rate Ignition for Spacecraft**

J. I. Shafer, L. D. Strand, and F. A. Robertson

JPL Quarterly Technical Review, Vol. 1, No. 1, pp. 35–44,
April 1971

A g-dot ignition system for solid-propellant motors has been designed to prevent damage to fragile sensors or structural members on a spacecraft by producing, from a starting transient for the spacecraft of 0.3 g, a controlled buildup in thrust, such as to give an acceleration rate of about 0.3 g/s. The system consists of a 3-s, regressive-burning, controlled-flow igniter and a highly inhibited progressive-burning charge in the main motor. The igniter must operate in a hard vacuum and sustain burning of the uninhibited portion of the propellant below its normal L^* combustion limit through mass addition and heat transfer until the propellant surface has increased sufficiently to provide a stable motor chamber pressure. A specific internal torus-shaped igniter is described, as well as potential methods of initiating burning in the hard vacuum with Pyrofuze.

SHARP, R. P.

S09 **The Surface of Mars: Pt. 1. Cratered Terrains**

B. C. Murray (California Institute of Technology),
L. A. Soderblom (California Institute of Technology),
R. P. Sharp (California Institute of Technology), and
J. A. Cutts (California Institute of Technology)

J. Geophys. Res., Vol. 76, No. 2, pp. 313–330,
January 10, 1971

For abstract, see Murray, B. C.

S10 **The Surface of Mars: Pt. 2. Uncratered Terrains**

R. P. Sharp (California Institute of Technology),
L. A. Soderblom (California Institute of Technology),

B. C. Murray (California Institute of Technology), and
J. A. Cutts (California Institute of Technology)

J. Geophys. Res., Vol. 76, No. 2, pp. 331–342,
January 10, 1971

The two types of uncratered terrain on Mars revealed by the *Mariner VI* and *VII* photographs are described in this article. The two terrains are descriptively termed chaotic and featureless. Chaotic terrain is younger than cratered terrain and displays features strongly suggestive of slump and collapse. The speculation is offered that it may be an expression of geothermal developments within Mars that only recently have begun to affect the surface. Featureless terrain, identified only within the large circular area Hellas, is devoid of any discernible topographic forms larger than the limit of resolution, about 500 m. *Mariner VII* data indicate that Hellas is a topographically low and structurally old basin. Smoothness of its floor could be the product of a recent event or of continuous processes that obliterate craters. Local processes of high efficacy, unusual surface materials, or both are probably involved. Through its chaotic terrain, the Martian surface displays a development that does not seem to be recorded, at least in the form of preserved recognizable evidence, on the moon or earth.

S11 The Surface of Mars: Pt. 3. Light and Dark Markings

J. A. Cutts (California Institute of Technology),
L. A. Soderblom (California Institute of Technology),
R. P. Sharp (California Institute of Technology),
B. A. Smith (California Institute of Technology), and
B. C. Murray (California Institute of Technology)

J. Geophys. Res., Vol. 76, No. 2, pp. 343–356,
January 10, 1971

For abstract, see Cutts, J. A.

S12 The Surface of Mars: Pt. 4. South Polar Cap

R. P. Sharp (California Institute of Technology),
B. C. Murray (California Institute of Technology),
R. B. Leighton (California Institute of Technology),
L. A. Soderblom (California Institute of Technology), and
J. A. Cutts (California Institute of Technology)

J. Geophys. Res., Vol. 76, No. 2, pp. 357–368,
January 10, 1971

As shown in the *Mariner VI* and *VII* photographs and described in this article, the south polar cap of Mars occupies a region of

cratered terrain. Immediately outside the shrinking cap, craters appear no more modified than those in areas farther north that are not annually frost-covered. Craters showing through the frost mantle are locally as abundant as elsewhere on Mars. Only in a central region close to the pole are craters sparse.

Both far- and near-encounter views reveal a highly irregular pole-cap edge. Pictures of the same sector taken six days apart are near duplicates, suggesting that the irregularity is primarily ground-controlled. No evidence of the classical polar collar is seen. Within the marginal zone, frost is preserved largely in crater bottoms and on slopes inclined away from the sun. Preferential retention in low spots supports the earlier suggestion that the Mountains of Mitchel may actually be depressions. An argument based on incoming solar radiation as the prime factor in frost wastage and the narrow width of the marginal zone suggests that slopes of topographic features therein are mostly gentle, on the order of a few degrees. The frost cover of the pole-cap interior may range widely in thickness, obscuring parts of some craters and seemingly enhancing topographic visibility elsewhere, possibly through variations in thickness and reflectivity. Unusually bright areas on the cap surface and differences in luminance between bright rims and the more somber floors of craters and other depressions may be due in large part to differences in related frost textures and to the local history of evaporation and sublimation. Irregularly angular depressions within the pole-cap frost, termed "etch pits," may be the product of differential ablation or the undermining by wind of a slabby surficial crust.

Encircling the south pole is a region of subdued relief with a paucity of craters that displays enigmatic quasi-linear markings believed to be ground features. Although no satisfactory explanation of these markings has been formulated, it seems likely that this region has been occupied repeatedly by perennial masses of CO_2 ice, formed and maintained during those phases of the Martian precessional cycle that resulted in short cool summers in the southern hemisphere. Such ice masses may play a role in producing the unusual features of the central polar region. Physical relationships suggest a local maximum frost thickness as great as tens of meters. The possibility should be kept in mind that remnants of perennial CO_2 ice of still greater thickness may exist locally, for example, in the etch pit area.

SHIMADA, K.

S13 **Electric Space Potential in a Cesium Thermionic Diode**

K. Shimada and W. Cannon

Technical Memorandum 33-480, March 31, 1971

The process of cesium ionization that is influenced strongly by the electric potential gradient is being studied to yield a minimum plasma-loss operation. A metal–ceramic device equipped with a movable Langmuir probe was constructed for use in investigating cesium plasma parameters required for a minimum plasma-loss operation of thermionic converters. To determine the space potentials and the electron energies in the plasma, the probe characteristics were examined for four different modes of cesium discharge: (1) extinguished mode, (2) anode glow mode, (3) ball-of-fire mode, and (4) plasma mode. This memorandum describes the test device, the experimental procedures, and the results obtained.

SIEGMETH, A. J.

S14 DSN Progress Report for January–February 1971: *Pioneer* Mission Support

A. J. Siegmeth

Technical Report 32-1526, Vol. II, pp. 6–17, April 15, 1971

The objective of the *Pioneer F* and *G* missions is to conduct, during the 1972–1973 Jovian opportunities, exploratory investigations beyond the orbit of Mars of the interplanetary medium, the nature of the asteroid belt, and the environmental and atmospheric characteristics of the planet Jupiter. This article describes the design profile of these missions. The characteristics of these flights that interface with Deep Space Network (DSN) tracking and data acquisition support are depicted. A delineation of the mission description and a summary of spacecraft systems and subsystems are given.

S15 DSN [Deep Space Network] Progress Report for March–April 1971: *Pioneer* Mission Support

A. J. Siegmeth

Technical Report 32-1526, Vol. III, pp. 7–19, June 15, 1971

This article continues the description of the *Pioneer F* and *G* missions. The tracking and data acquisition support requirements are correlated with the mission characteristics. A description of the spacecraft's telecommunications and antenna subsystems is given. The CONSCAN subsystem, which has an automatic earth-homing capability, is also delineated. The typical characteristics of the S-band telecommunications link during Jupiter encounter are depicted.

SIMON, H. S.

S16 **DSN [Deep Space Network] Progress Report for March–April 1971: *Mariner* Mars 1971 Launch Phase Study Using the SFOF Mark IIIA Central Processing System Model**

H. S. Simon

Technical Report 32-1526, Vol. III, pp. 179–182, June 15, 1971

Simulation models are currently being used for Space Flight Operations Facility (SFOF) development at the Jet Propulsion Laboratory. This article describes the results of three modeling runs made during April 1971 to evaluate the performance of the SFOF Mark IIIA Central Processing System, configured to support the launch phase of the *Mariner* Mars 1971 mission.

SMITH, B. A.

S17 ***Mariner* Mars 1969: Atmospheric Results**

C. B. Leovy (University of Washington), B. A. Smith (New Mexico State University), A. T. Young, and R. B. Leighton (California Institute of Technology)

J. Geophys. Res., Vol. 76, No. 2, pp. 297–312, January 10, 1971

For abstract, see Leovy, C. B.

S18 **The Surface of Mars: Pt. 3. Light and Dark Markings**

J. A. Cutts (California Institute of Technology), L. A. Soderblom (California Institute of Technology), R. P. Sharp (California Institute of Technology), B. A. Smith (California Institute of Technology), and B. C. Murray (California Institute of Technology)

J. Geophys. Res., Vol. 76, No. 2, pp. 343–356, January 10, 1971

For abstract, see Cutts, J. A.

SNIFFIN, R.

S19 **DSN Progress Report for March–April 1971: Implementation of an S-Band Microwave Link for Spacecraft Compatibility Testing**

R. Sniffin

Technical Report 32-1526, Vol. III, pp. 203–210, June 15, 1971

The Deep Space Network (DSN) requires all spacecraft that are to be tracked by its stations receive a compatibility test prior to launch. Two facilities are maintained for this purpose: one at Cape Kennedy (DSS 71) for pre-launch checkout of the spacecraft, and another at JPL in Pasadena (CTA 21) for engineering checkout of spacecraft and spacecraft subsystems before shipment to the launch facility. As a cost- and time-effective approach to compatibility testing of the *Pioneer F* and *G* spacecraft being constructed by TRW Inc., a microwave link between JPL and TRW has been installed. The performance of this link has been evaluated experimentally and test results are given.

SODERBLOM, L. A.

S20 The Surface of Mars: Pt. 1. Cratered Terrains

B. C. Murray (California Institute of Technology),
L. A. Soderblom (California Institute of Technology),
R. P. Sharp (California Institute of Technology), and
J. A. Cutts (California Institute of Technology)

J. Geophys. Res., Vol. 76, No. 2, pp. 313–330, January 10, 1971

For abstract, see Murray, B. C.

S21 The Surface of Mars: Pt. 2. Uncratered Terrains

R. P. Sharp (California Institute of Technology),
L. A. Soderblom (California Institute of Technology),
B. C. Murray (California Institute of Technology), and
J. A. Cutts (California Institute of Technology)

J. Geophys. Res., Vol. 76, No. 2, pp. 331–342, January 10, 1971

For abstract, see Sharp, R. P.

S22 The Surface of Mars: Pt. 3. Light and Dark Markings

J. A. Cutts (California Institute of Technology),
L. A. Soderblom (California Institute of Technology),
R. P. Sharp (California Institute of Technology),
B. A. Smith (California Institute of Technology), and
B. C. Murray (California Institute of Technology)

J. Geophys. Res., Vol. 76, No. 2, pp. 343–356, January 10, 1971

For abstract, see Cutts, J. A.

S23 **The Surface of Mars: Pt. 4. South Polar Cap**

R. P. Sharp (California Institute of Technology),
B. C. Murray (California Institute of Technology),
R. B. Leighton (California Institute of Technology),
L. A. Soderblom (California Institute of Technology), and
J. A. Cutts (California Institute of Technology)

J. Geophys. Res., Vol. 76, No. 2, pp. 357–368,
January 10, 1971

For abstract, see Sharp, R. P.

SPIER, G. W.

S24 **Design and Implementation of Models for the Double Precision Trajectory Program (DPTRAJ)**

G. W. Spier

Technical Memorandum 33-451, April 15, 1971

A common requirement for all lunar and planetary missions is the extremely accurate determination of the trajectory of a spacecraft. The Double Precision Trajectory Program (DPTRAJ) developed by JPL proved to be a very accurate and dependable tool for the computation of interplanetary trajectories during the *Mariner* Mars 1969 missions. This memorandum describes the mathematical models that are currently used in the DPTRAJ, with emphasis on the development of the equations.

SPITZMESSER, D.

S25 **DSN Progress Report for March–April 1971: Radio Science Support**

K. W. Linnes, T. Sato, and D. Spitzmesser

Technical Report 32-1526, Vol. III, pp. 46–51, June 15, 1971

For abstract, see Linnes, K. W.

STOLLER, F.

S26 **Bolted Joints Under Sustained Loading**

V. Lobb and F. Stoller

J. Struct. Div., Proc. ASCE, Vol. 97, No. ST3, pp. 905–933,
March 1971

For abstract, see Lobb, V.

STRAND, L. D.

S27 Low Acceleration Rate Ignition for Spacecraft

J. I. Shafer, L. D. Strand, and F. A. Robertson

JPL Quarterly Technical Review, Vol. 1, No. 1, pp. 35–44, April 1971

For abstract, see Shafer, J. I.

STROMBERG, W. D.

S28 Digital Processing of the *Mariner 6* and *7* Pictures

T. C. Rindfleisch, J. A. Dunne, H. J. Frieden, W. D. Stromberg, and R. M. Ruiz

J. Geophys. Res., Vol. 76, No. 2, pp. 394–417, January 10, 1971

For abstract, see Rindfleisch, T. C.

S29 Maximum Discriminability Versions of the Near-Encounter *Mariner* Pictures

J. A. Dunne, W. D. Stromberg, R. M. Ruiz, S. A. Collins, and T. E. Thorpe

J. Geophys. Res., Vol. 76, No. 2, pp. 438–472, January 10, 1971

For abstract, see Dunne, J. A.

SWARD, A.

S30 DSN [Deep Space Network] Progress Report for January–February 1971: New Developments in the Hydrogen Maser Frequency Standard

A. Sward

Technical Report 32-1526, Vol. II, pp. 72–74, April 15, 1971

Measurements have been made on the JPL hydrogen masers to determine the average fractional frequency departure versus averaging time. In addition, the receiver section has been modified with a newly developed frequency synthesizer that will not only improve the performance and reliability of the receiver but also decrease its size and complexity.

TAYLOR, T. M.

T01 **Tracking and Data System Support for the *Mariner* Mars 1969 Mission: Planning Phase Through Midcourse Maneuver**

N. A. Renzetti, K. W. Linnes, D. L. Gordon, and T. M. Taylor

Technical Memorandum 33-474, Vol. I, May 15, 1971

For abstract, see Renzetti, N. A.

THORPE, T. E.

T02 **Maximum Discriminability Versions of the Near-Encounter *Mariner* Pictures**

J. A. Dunne, W. D. Stromberg, R. M. Ruiz, S. A. Collins, and T. E. Thorpe

J. Geophys. Res., Vol. 76, No. 2, pp. 438–472, January 10, 1971

For abstract, see Dunne, J. A.

TIMOR, U.

T03 **DSN [Deep Space Network] Progress Report for January–February 1971: Sequential Ranging With the Viterbi Algorithm**

U. Timor

Technical Report 32-1526, Vol. II, pp. 75–79, April 15, 1971

The performance of the sequential ranging system can be improved by using a maximum-likelihood receiver; however, the complexity grows exponentially with the number of components N needed to determine the range unambiguously. A new truncated maximum-likelihood receiver, based on the Viterbi decoder for convolutional codes, is presented and is shown to achieve a maximum-likelihood performance while having a fixed complexity independent of N. The improvement in signal-to-noise ratio, compared to the present receiver, is 1.5 db for an error probability of less than 10^{-2}.

T04 **Interplex Modulation**

S. Butman and U. Timor

JPL Quarterly Technical Review, Vol. 1, No. 1, pp. 97–105, April 1971

For abstract, see Butman, S.

TRAJMAR, S.

T05 Electron Impact Excitation of N_2

R. T. Brinkmann and S. Trajmar

Ann. Géophys., Vol. 26, No. 1, pp. 201–207, January–March 1970

For abstract, see Brinkmann, R. T.

TURNER, J. A.

T06 DSN Progress Report for March–April 1971: Operational Capabilities of the SFOF Mark IIIA User Terminal and Display Subsystem

J. A. Turner

Technical Report 32-1526, Vol. III, pp. 228–238, June 15, 1971

The Space Flight Operations Facility (SFOF) Mark IIIA Central Processing System has been developed to meet requirements for independent and simultaneous operation of multiple missions flown by an array of increasingly complex and sophisticated spacecraft. The Deep Space Network (DSN) Operations and Mission Support Areas must all be supported by the same computer system and therefore have been equipped with identical user input/output devices. The user input/output devices and their capabilities are described with the suggestion that operating techniques be developed and adapted to the improved and more interactive input/output capabilities of the new User Terminal and Display Subsystem.

TUSTIN, D. G.

T07 DSN Progress Report for January–February 1971: DSN Discrepancy Reporting Subsystem

D. G. Tustin

Technical Report 32-1526, Vol. II, p. 140, April 15, 1971

The Deep Space Network (DSN) discrepancy reporting subsystem for collecting and cataloging all documented reports of operational discrepancies facilitates rapid retrieval of required information using varied selection criteria. The discrepancy reporting subsystem and the results of the first year's discrepancy reporting operation using a computerized data management system are briefly described. The general problems encountered and the steps being taken to solve them are discussed.

URECH, J. M.

U01 **DSN Progress Report for January–February 1971: Processed Data Combination for Telemetry Improvement—DSS 62**

J. M. Urech

Technical Report 32-1526, Vol. II, pp. 169–176, April 15, 1971

Telemetry improvement proposals for the Deep Space Network (DSN) 26-m antenna network are being considered. Of the four possible methods of improving telemetry bit error rate performance by combining data with common time tags from two stations, this article discusses the method of *a posteriori* combination of processed telemetry data. The theory is presented and the results of a scheduled test with a *Pioneer* spacecraft are shown to be in good agreement.

Although the method is ideally applicable to two deep space stations (DSSs) with the same configuration [two ground operational equipment (GOE) or two multiple-mission telemetry (MMT) stations], the computer program was developed at DSS 62 (Cebreros DSS) for application to DSS 61 (Robledo DSS) with a GOE configuration and DSS 62 with an MMT configuration. The computer program is described in an appendix.

VOLKOFF, J. J.

V01 **DSN [Deep Space Network] Progress Report for January–February 1971: Photon Energies of a Cathode-Ray Tube System**

J. J. Volkoff

Technical Report 32-1526, Vol. II, pp. 92–99, April 15, 1971

Light emitted from a cathode-ray tube (CRT) is comprised of reflected environmental light incident upon the CRT system and light generated at the phosphor screen and transmitted through the CRT system. The total photon energy that leaves the system and those energies that are dissipated in the various elements of the CRT system are derived. An expression for the contrast ratio of the CRT system is also presented and discussed.

VON ROOS, O. H.

V02 **DSN Progress Report for January–February 1971: Second Order Charged Particle Effects on Electromagnetic Waves in the Interplanetary Medium**

O. H. von Roos

Technical Report 32-1526, Vol. II, pp. 42–48, April 15, 1971

Possible influences on the measurements of the total electron content due to magnetic fields, spatial inhomogeneities, and pulse shape distortions are investigated. The higher-order effects of the interplanetary plasma on radio signals as utilized in the Deep Space Network (DSN) are shown to be negligible as far as a determination of the electron content is concerned. It is seen that a lateral change in electron concentration engenders very small angular deviations of the ray path and leads to a negligible change in the apparent range.

V03 **DSN [Deep Space Network] Progress Report for March–April 1971: Analysis of the DRVID and Dual Frequency Tracking Methods in the Presence of a Time-Varying Interplanetary Plasma**

O. H. von Roos

Technical Report 32-1526, Vol. III, pp. 71–76, June 15, 1971

An analysis is made of two different methods for determining the total electron content of the plasma existing between a spacecraft and the earth. It is shown that the two methods complement each other. The dual frequency method is capable of measuring the structure of a plasma inhomogeneity, whereas the differenced range versus integrated doppler (DRVID) method is capable of locating this inhomogeneity within the ray path of the electromagnetic tracking signal.

WAHLQUIST, H. D.

W01 **Applications of FORMAC in the Mathematics of General Relativity**

H. D. Wahlquist

JPL Quarterly Technical Review, Vol. 1, No. 1, pp. 13–16, April 1971

The use of FORMAC (formula manipulation by computer) to perform symbolic analysis on the computer in the field of general relativity is described. FORMAC will accept symbolic analytical expressions involving complex algebraic functions, elementary transcendental functions, user-defined functions, and unspecified functions of any number of dependent variables. In particular, FORMAC programs have now been written to implement the non-commutative calculus of exterior differential forms. Applications of this new capability to Hamiltonian cosmology and the theory of partial differential equations are discussed.

WALLACE, K. B.

W02 **DSN [Deep Space Network] Progress Report for March–April 1971: Noise Diode Evaluation**

K. B. Wallace

Technical Report 32-1526, Vol. III, pp. 121–125, June 15, 1971

Noise diodes are installed in all R&D microwave receiver systems to check broadband receiver performance required for radiometric applications, such as radio astronomy and atmospheric studies. An application to which noise sources are particularly suited is the noise-adding radiometer; another application being studied is automated system performance evaluation. In this article, noise diodes similar to those in use at Deep Space Stations 13 and 14 are evaluated for variations in noise output due to temperature.

WEBER, R.

W03 **DSN Progress Report for March–April 1971: MSFN/DSN Integration Program for the DSS 11 26-m Antenna Prototype Station**

R. Weber

Technical Report 32-1526, Vol. III, pp. 197–202, June 15, 1971

A plan was proposed in mid-1971 wherein unique Deep Space Network (DSN) equipment would be installed in the 26-m antenna Manned Space Flight Network (MSFN) operations control room and integrated to function with pre-existing MSFN equipment. This effort was initiated at the Pioneer Deep Space Station (DSS 11) site in November 1970 and shortly thereafter at the two overseas sites. This plan allows the 26-m antenna DSN tracking capability to exist at these sites while the 64-m antenna is in the process of being built and integrated into the original 26-m antenna DSN control room. The details of the integration efforts at the DSS 11 prototype station are outlined, and significant accomplishments and milestones are indicated. The equipment layout in the operations control room is illustrated and the unique operational and electrical interfaces between the DSN equipment and the MSFN equipment are described.

WEIDNER, J. H.

W04 DSN Progress Report for March–April 1971: Software for the DSN Video Subsystem

J. H. Weidner

Technical Report 32-1526, Vol. III, pp. 239–244, June 15, 1971

The Deep Space Network (DSN) video subsystem provides the flight projects at JPL with a real-time and near real-time tonal image (picture) processing and display capability. The software of the subsystem controls all components and processes the picture data which it receives from the DSN Telemetry System. The video software is designed to give the flight projects the capability to automatically process, display, and record the picture data as they are received from the spacecraft. Its design also includes an interactive capability for selective picture processing and display.

WEINER, E. O.

W05 Computation of Structural Modes of a Rollout Array Spacecraft for Attitude Control Study

E. O. Weiner

Technical Memorandum 33-476, May 1, 1971

A study is presented of the structural modes required to determine the interaction between an attitude control system and a flexible structure. The flexible structure considered has a low stiffness that leads to natural frequencies in the range of the frequency response of the attitude control system, producing a coupling between the response of the structure and the attitude control system.

WEIR, C. E.

W06 DSN [Deep Space Network] Progress Report for March–April 1971: Rotating Antenna Tests at DSS 12

C. E. Weir

Technical Report 32-1526, Vol. III, pp. 215–218, June 15, 1971

The *Pioneer F* spacecraft will utilize a conical scan system to allow automatic pointing of its antenna at the earth. The spacecraft will rotate continuously about the roll axis during the mission, and will consequently present some characteristics to a

ground station not seen on previous missions. Tests were conducted using a rotating antenna on the collimation tower at DSS 12 (Echo Deep Space Station) to simulate the rotating *Pioneer F* spacecraft. Specific measurements were taken to determine the degradation in telemetry bit error rate and doppler quality as a result of the rotation and misalignment of the rotating antenna relative to the receiving antenna.

WELLS, R. A.

W07 **DSN [Deep Space Network] Progress Report for January–February 1971: Diagnostics for the SFOF Mark IIIA Central Processing System: Pre-Mission CPS/Facility Checkout Procedures**

R. A. Wells

Technical Report 32-1526, Vol. II, pp. 125–128, April 15, 1971

Prior to critical periods of data processing during a mission, comprehensive diagnostic tests of the Space Flight Operations Facility (SFOF) central processing system (CPS) are conducted to detect and correct equipment deficiencies before they can affect the continuity of the data processing. This article describes the test methods employed and their relationships to the current dual IBM 360/75 computer configuration. By preparing a test "script" in advance, the hardware checkout process is formalized and the results documented.

WEN, L. C.

W08 **Measured Performance of Silicon Solar Cell Assemblies Designed for Use at High Solar Intensities**

R. G. Ross, Jr., R. K. Yasui, W. Jaworski, L. C. Wen, and E. L. Cleland

Technical Memorandum 33-473, March 15, 1971

For abstract, see Ross, R. G., Jr.

WILLIAMS, J. G.

W09 **Resonances in the Neptune–Pluto System**

J. G. Williams and G. S. Benson (University of California, Los Angeles)

Astron. J., Vol. 76, No. 2, pp. 167–177, March 1971

Pluto's orbit has been integrated for 4.5 million years. The previously discovered libration of $3\lambda - 2\lambda_N - \tilde{\omega}$, where λ and λ_N are

the mean longitudes of Pluto and Neptune and $\tilde{\omega}$ is Pluto's longitude of perihelion, is confirmed and has an average period of 19 951 yr. It was also found that the argument of perihelion ω librates about 90 deg with an amplitude of 24 deg and a period of $3\ 955\ 000 \pm 20\ 000$ yr. There is an indication that both the difference between the nodes and the difference between the longitudes of perihelia of Neptune and Pluto may be locked on to the ω libration. All of the above effects are found to improve the stability of the Neptune–Pluto system by increasing the minimum distance of approach between the two bodies.

YASUI, R. K.

Y01 Structural Analysis of Silicon Solar Arrays

L. W. Butterworth and R. K. Yasui

Technical Report 32-1528, May 15, 1971

For abstract, see Butterworth, L. W.

Y02 Measured Performance of Silicon Solar Cell Assemblies Designed for Use at High Solar Intensities

R. G. Ross, Jr., R. K. Yasui, W. Jaworski, L. C. Wen, and E. L. Cleland

Technical Memorandum 33-473, March 15, 1971

For abstract, see Ross, R. G., Jr.

YEH, C.

Y03 Arbitrarily Shaped Dual-Reflector Antennas

C. Yeh

Technical Report 32-1503, May 1, 1971

An analysis based on geometrical optics for a dual-reflector antenna system with two arbitrarily shaped reflectors is carried out. Formulas for the phase and amplitude distribution in the aperture of the second reflector are obtained when the source function and the reflector surfaces are given. A design technique based on the derived formulas is also discussed.

YOUNG, A. T.

Y04 *Mariner* Mars 1969: Atmospheric Results

C. B. Leovy (University of Washington), B. A. Smith (New Mexico State University), A. T. Young, and R. B. Leighton (California Institute of Technology)

J. Geophys. Res., Vol. 76, No. 2, pp. 297–312, January 10, 1971

For abstract, see Leovy, C. B.

Y05 Photometric Properties of the *Mariner* Cameras and of Selected Regions on Mars

A. T. Young and S. A. Collins

J. Geophys. Res., Vol. 76, No. 2, pp. 432–437, January 10, 1971

The reciprocity principle was found to be a very effective test of linearity in the *Mariner VI* and *VII* television data. For the testing, areas on Mars were selected that were reasonably uniform, so as to avoid resolution-dependent effects. The areas were also selected so as to avoid any obvious diurnal "cloud" phenomena. As described in this article, in spite of serious problems with the photometric data, significant variations were found in limb-darkening from place to place on Mars. These variations enable a new parameter of the Martian surface (most probably the grain size or degree of compaction) to be studied.

YOUNG, L. D. G.

Y06 High-Dispersion Spectroscopic Observations of Venus: V. The Carbon Dioxide Band at 8689 Å

L. D. G. Young, R. A. J. Schorn, E. S. Barker (University of Texas), and M. MacFarlane (University of Texas)

Icarus: Int. J. Sol. Sys., Vol. 11, No. 3, pp. 390–407, November 1969

The average rotational temperature of the Cytherean atmosphere above the "cloudtops" was found to be 238 ± 1 K (standard deviation) based on 23 plates of the 8689-Å CO_2 band. If the temperatures found from the 8689-, 7820-, and 7883-Å bands are averaged for each plate on which these bands appear, an average rotational temperature of 242 ± 2 K (standard deviation) is obtained. This latter temperature is based on 31 plates taken of Venus between March and December 1967. The variation of the equivalent width of the 8689-Å band with Venus phase is seen to agree generally with the observations of Kuiper; the equivalent width decreases with increasing phase angles.

Y07 High-Dispersion Spectroscopic Observations of Venus: VII. The Carbon Dioxide Band at 10 488 Å

L. D. G. Young, R. A. J. Schorn, E. S. Barker (University of Texas), and M. MacFarlane (University of Texas)

Icarus: Int. J. Sol. Sys., Vol. 13, No. 1, pp. 58–73, July 1970

Observations of the 10,488-Å band of carbon dioxide in the spectrum of Venus were made from January 1965 through December 1967. The spectra were obtained at the coudé focus of the Struve reflector at dispersions of 2.8, 3.8, and 5.4 Å/mm. The 31 *best* plates were used to derive rotational temperatures by two methods. In the first method, linear least-squares fits to a square-root absorption law were made, and temperatures ranging from 193 to 284 K were derived; the average temperature was 244 K. The second method also required a linear least-squares fit, this time to the curve of growth. This fit gave slopes from 0.38 to 0.58, corresponding to rotational temperatures of 202 to 250 K, with an average temperature of 236 K. The rotational temperatures derived by both methods showed no significant variation with the phase angle i of Venus for $26 \leqslant i$, deg $\leqslant 164$. Finally, averaging the measurements obtained by three individuals and using the curve-of-growth method of data reduction gives a value for rotational temperature of 237 ± 3 K (formal standard deviation).

A search was made for spatial and temporal variations in the apparent amount of carbon dioxide in the absorption path. The amount appeared to vary significantly with the phase of Venus and also with the time of observation.

ZANDELL, C.

Z01 DSN [Deep Space Network] Progress Report for March–April 1971: Diagnostics for the SFOF Mark IIIA Central Processing System: Real-Time Background Routines

C. Zandell

Technical Report 32-1526, Vol. III, pp. 168–170, June 15, 1971

The on-line diagnostics for the Space Flight Operations Facility (SFOF) Central Processing System (CPS) have been modified to provide real-time diagnosis of equipment performance. Real-time diagnostics can be run while mission flight support continues. This is possible since any diagnostic can now run as an independent task under the mission real-time job step. The real-time capability allows certification of CPS hardware elements immediately preceding their commitment to mission flight support.

ŽMUIDZINAS, J. S.

Z02 Self-Consistent Green's-Function Approach to the Electron-Gas Problem

J. S. Žmuidzinas

Phys. Rev., Pt. B: Solid State, Vol. 2, No. 11, pp. 4445–4460, December 1, 1970

The electron-gas problem is investigated by means of a self-consistent Green's-function formalism with the aim of developing practical approximation schemes for metallic densities. The work is based on the Dyson equation for the single-particle propagator $G[U]$ as a functional of an external potential U. The self-energy functional $\Sigma[U]$, appearing in the Dyson equation, is evaluated by perturbation theory in terms of the exact $G[U]$, thereby leading to a self-consistent problem. A hierarchy of approximations is generated by summing successively larger sets of graphs for $\Sigma[U]$. The Dyson equation is expanded in a functional Taylor series in U and yields a nonlinear integral equation for the $U = 0$ propagator, as well as linear integral equations for the $U = 0$ higher-order Green's functions, with kernels dependent on $\delta\Sigma/\delta U$. In applications of the theory, the emphasis is on calculating the longitudinal dielectric function ϵ in terms of the contracted four-point Green's function. The linear integral equation for the latter is solved after making a low-momentum dominance approximation to the kernel. The result is a general, but approximate, closed-form expression for ϵ which can be used for different choices of Σ. The following five approximations for ϵ, based on different approximations for Σ, are presented: Hartree–Fock, random-phase, generalized random-phase, second-stage random-phase, and low-density–high-density approximations. The last approximation is designed to work well at the two extremes of the density spectrum and, hopefully, also at metallic densities. The long-wavelength plasmon dispersion relations obtained from two different versions of the generalized random-phase approximation for ϵ agree closely with the results reported by Kanazawa and Singwi.

ZOHAR, S.

Z03 DSN [Deep Space Network] Progress Report for March–April 1971: Matched Filters for Binary Signals: A Correction and Elaboration

S. Zohar

Technical Report 32-1526, Vol. III, pp. 116–120, June 15, 1971

This article is a correction and elaboration of "DSN Progress Report for November–December 1970: Matched Filters for Binary Signals," Technical Report 32-1526, Vol. I, pp. 52–62, February 15, 1971. That article described the design of matched filters for the optimal high-speed detection of binary signals and investigated their performance as a function of their complexity.

Subject Index

Subject Categories

Safety Engineering
Scientific Instruments
Soil Sciences
Solid-State Physics
Spectrometry
Standards, Reference
Structural Engineering
Surveyor Project
Telemetry and Command
Temperature Control
Test Facilities and Equipment
Thermodynamics
Tracking
Viking Project
Wave Propagation

Subjects

Publication Index

Technical Reports

DSN Progress Report for January–February 1971 (Technical Report 32-1526, Vol. II)

Technical Memorandums

JPL Quarterly Technical Review, Vol. 1, No. 1

Open Literature Reporting

NASA — JPL — Coml., L.A., Calif.